Thin-film Engineering of Solution Processable N-Type Silicon Phthalocyanines for Organic Thin-Film Transistors

---

Rosemary Cranston

Thesis submitted to the University of Ottawa in partial Fulfillment of the requirements for the Doctorate of Philosophy Degree in Chemical Engineering

Department of Chemical and Biological Engineering

Faculty of Engineering

University of Ottawa

PhD in Chemical Engineering (2024)

Chemical and Biological Engineering

University of Ottawa

TITLE:	Thin-film Engineering of Solution Processable N-Type Silicon Phthalocyanines for Organic Thin-Film Transistors
AUTHOR:	Rosemary Cranston (Chemical Engineering)
SUPERVISOR:	Benoît H. Lessard
PAGES:	207

Abstract

Despite significant advances in the field of organic electronic devices, there remains a critical need for soluble, stable, and high performing n-type organic semiconductors. Understanding how molecular design and thin-film fabrication conditions impact the formation, microstructure, morphology, and electronic properties of thin-films is crucial to expanding the application of organic thin-film transistors (OTFTs) in commercial electronics. Axially substituted silicon phthalocyanines (SiPcs) are promising organic electronic materials as a result of their favourable intermolecular stacking, crystallinity, chemical versatility, and compatibility with solution fabrication techniques. Here, SiPc derivatives with axial substituted alkyl chains of varying length, symmetry, and branching position were studied in OTFTs, establishing relationships between molecular structure, film morphology and device performance. Through low surface energy dielectric modifications, and the exploitation of fluorine-fluorine interactions at the dielectric-semiconductor interface, SiPc films with large area crystalline domains were achieved, yielding improved OTFT performance. Differences between sublimation and solution deposition methods were further investigated to understand the nucleation, crystallization, and film formation processes of SiPcs. Using a scalable high throughput printing platform for thin-film deposition highlighted the challenges of transitioning from lab scale fabrication to techniques compatible with commercial manufacturing. Finally, fabrication parameters play an important role in thin-film formation and resultant OTFT performance, with key parameters such as deposition rate, time, solvent, temperature, and post fabrication processing identified, examined, and controlled to obtain high performing devices. The works presented herein demonstrate the effectiveness of molecular substitutions and fabrication tuning as strategies to control crystal packing and the charge transport properties of semiconducting molecules, furthering our understanding of solution processable n-type semiconductors.

Résumé

Malgré l'advient d'avancées significatives dans le domaine de l'électronique organique, il y a un besoin persistent pour le développement de semiconducteurs organiques de type N ayant une meilleure solubilité, stabilité et performance. Une meilleure compréhension des impacts de la conception moléculaire sur la formation, la microstructure, la morphologie et les propriétés électroniques des couches-minces est cruciale pour promouvoir l'utilisation des transistors à couche-mine organique (*organic thin-film transistor*, OTFT) dans les dispositifs électroniques commerciaux. Les phthalocyanines de silicium (SiPc) à substitution axiales sont des matériaux prometteurs pour le développement de dispositifs électroniques organiques en raison de leur empilement moléculaire favorable, leur cristallinité, leur versatilité chimique et leur compatibilité avec des techniques de fabrication à base de solutions. Cette thèse porte sur l'utilisation de dérivées de SiPc ayant différentes longueurs de chaînes alkyles, symétries et positions de ramifications dans le but de fabriquer des OTFTs, puis d'établir des relations entre leur structure moléculaire, la morphologie des couches minces et la performance des dispositifs. La réduction l'énergie de surface du diélectrique et l'exploitation des interactions fluor-fluor à l'interface entre le diélectrique et le semiconducteur ont permis d'obtenir des couches de SiPc ayant de grands domaines cristallins, permettant ainsi d'améliorer la performance des OTFTs. Les différences entre les méthodes de dépôt en phase vapeur et en solution ont été étudiées afin de mieux comprendre les procédés de nucléation, de cristallisation et de formation de couches minces des SiPc. L'utilisation d'une plateforme d'impression à débit variable pour le dépôt de couches minces a permis de mettre en valeur les défis qui surviennent lors de la transition d'un procédé de fabrication à échelle de laboratoire à une échelle industrielle. Les paramètres de fabrication, tels que la vitesse de dépôt, la durée, le solvant utilisé, la température et le traitement suivant le dépôt, ont également joué un rôle important dans la formation des couches minces et dans la performance des OTFTs correspondants. Les travaux présentés dans cette thèse démontrent que les substitutions moléculaires et le réglage des paramètres de fabrication sont des stratégies efficaces pour le contrôle de l'empilement cristallin et des propriétés de transport de charges des molécules semiconductrices, contribuant ainsi aux connaissances des semiconducteurs de type N qui se prêtent à des techniques de fabrication à base de solutions.

Acknowledgments

I would first like to thank my thesis supervisor, Dr. Benoît Lessard. Your support and guidance have not only shaped this thesis but have also greatly influenced my growth as a researcher. Thank you for allowing me to have the independence I desired while giving me so many amazing opportunities to travel and learn throughout my studies. I am very grateful for all the time and effort you invested in me and for your constant faith in my abilities.

Thank you to all past and present members of the Lessard Research Group for always making the lab a fun, supportive, and welcoming place. I would especially like to thank Dr. Mario Vebber for synthesizing so many of the materials critical for my research, and Dr. Joseph Manion for providing excellent advice and for keeping the lab so well maintained.

I would also like to thank all the collaborators and support staff that I've worked with for their knowledge and expertise. Thank you to beamline scientists Dr. Adam Leontowich, Dr. Sufal Swaraj, and Dr. Arnaud Hemmerle for always ensuring our trips to synchrotron facilities are a success. Thank you to Dr. Chase Radford for your expertise and help in conducting experiments and interpreting results. Thank you to Dr. Jeffery Ovens and Dr. Spyridon Ntais at the University of Ottawa for keeping so many key pieces of equipment functioning.

Thank you so much to my friends and family for everything you do for me. Thank you to Kaitlin, Ben and Halynne for being my best friends and lab mates. Thank you to Zach for always keeping me well fed and happy. Special thank you to my parents Peter and Catherine and my brothers Henry and George, as well as my cat Pearl. I am endlessly grateful for all your love and support.

Finally, thank you to my thesis committee for your consideration of this report.

Table of Contents

List of Figures

List of Tables

List of Key Abbreviations

Abbreviation	Definition
AFM	Atomic force microscopy
DSC	Differential scanning calorimetry
DFT	Density functional theory
EA	Electron affinity
GIWAXS	Grazing-incidence wide-angle X-ray scattering
GIXS	Grazing-incidence X-ray scattering
HOMO	Highest-occupied molecular-orbital
LUMO	Lowest-unoccupied molecular-orbital
MPc	Metal phthalocyanine
MOSFET	Metal-oxide semiconductor field-effect transistor
NEXAFS	Near-edge X-ray absorption fine structure spectroscopy
OPV	Organic photovoltaic
OLED	Organic light emitting diode
OTFT	Organic thin-film transistor
PVD	Physical vapour deposition
STXM	Scanning transmission X-ray microscopy
SAMs	Self-assembled monolayers
SiPc	Silicon phthalocyanine
TGA	Thermogravimetric analysis
UV-vis	Ultraviolet-visible spectroscopy
XRD	X-ray diffraction

List of Key Variables

Variable	**Definition**
β	Angle of molecules relative to the substrate
C_i	Capacitance density
E_{HOMO}	HOMO energy level
E_{LUMO}	LUMO energy level
ΔE	Vertical transition energies
f	Oscillator strengths
H_m	Melting enthalpy
H_c	Crystallization enthalpy
$I_{on/off}$	On/off current ratio
I_{SD}	Source-drain current
J_k	Transfer integrals
L	Channel length
N_i	Interface charge trap density
T_s	Substrate temperature
T_b	Solvent boiling point at atmospheric pressure
T_m	Melting temperature
T_c	Crystallization temperature
V_T	Threshold voltage
V_{SD}	Source-drain voltage
V_{GS}	Gate source voltage
W	Channel width
μ_h	Hole mobility
μ_e	Electron mobility
γ_s	Surface energy of the substrate
γ^*	Interfacial surface energy between the deposited material and substrate
γ_d	Surface energy of the deposited material
λ	Reorganization energies
θ_w	Water contact angle

Chapter 1: Introduction

A portion of this chapter is adapted from: ***Cranston, R. R****. & Lessard, B. H. Metal phthalocyanines: thin-film formation, microstructure, and physical properties. RSC Adv. 11, 21716-21737 (2021).*

Organic Semiconductors

Organic semiconductors are carbon based materials with the ability to conduct charge due to their highly conjugated molecular structures. The alternating single and double bonds between covalently bound carbon atoms causes the delocalization of valence electrons in the conjugated system and enables the transport of charge along a molecule.[1–3] Each carbon atom in the conjugated system is sp^2 hybridized, with three sp^2 orbitals created per atom and one un-hybridized p_z orbital.[2,4] The sp^2 orbitals result in strong σ-bonds within the system while the p_z orbitals form weaker C-C π-bonds. The overlapping p_z orbitals of adjacent carbon atoms result in the delocalization of the π-electron density and result in π-bonding and π* anti-bonding orbitals.[2,4] The π* anti-bonding orbital is called the lowest unoccupied molecular orbital or LUMO energy level while the π-bonding orbital is known as the highest occupied molecular orbital or HOMO energy level. This HOMO-LUMO energy level gap decreases with increasing molecular conjugation and is analogous to the valence and conduction bands of inorganic semiconductors.[2,4] Due to the weak intermolecular bonds in organic solids, charge transport is localized to a finite number of molecules within the film and thus charge mobility is determined by the ease in which charge is transported from one molecule to another.[1–3] Charge transport in organic semiconductors is therefore described by hopping, band bending, or trap and release models which all depend on the degree of orbital overlap.[2,5] Thus the degree of order within organic solids, such as thin-films, often dictates the efficiency of charge transport with amorphous films yielding lower mobilities compared to poly- or semi-crystalline films.

Organic Electronics

Organic electronic devices using carbon based semiconducting materials have gained significant industrial and scientific interest as a complementary technology to traditional silicon based electronics. Due to moderate processing conditions and the ability to exploit solution fabrication techniques, organic materials facilitate the realization of low cost, high throughput manufacturing of large area electronics with minimal material consumption and waste production. Additionally, solution based manufacturing is compatible with non-traditional materials, such as polymers and textiles, providing a route towards the development of light weight, flexible, and wearable electronics for innovative applications in medicine, artificial skin, bendable displays, and highly sensitive point-of-need sensors.[6–8] The versatility of organic semiconducting materials have enabled their use in a myriad of device applications including organic light emitting diodes (OLEDs), organic photovoltaics (OPVs), and organic thin-film transistors (OTFTs). In particular, OLEDs have found significant commercial success as reduced power consumption, ease of manufacturing, and improved colour quality have resulted in their adoption for many displays.[9,10] Similarly, OPVs have recently achieved power conversion efficiencies similar to that of inorganic photovoltaics, paving the way for their commercial use.[11,12] OTFTs offer the largest array of possible applications, however their commercialization has been hindered by low performance, instability, manufacturing inconsistencies, and the synthetic complexity of many organic semiconducting materials. Through fundamental research, the relationships between molecular design, OTFT fabrication, and electrical performance can be better understood in order to improve OTFT use and enable the advancement of state of the art technologies.

Organic Thin-Film Transistors

Operation and Charge Transport

OTFTs are a type of three terminal device consisting of a gate electrode, insulating dielectric layer, organic semiconducting layer, and source-drain electrodes (**Figure 1.1a**). During operation, voltage is applied to the gate and drain electrodes, while the source electrode is grounded. The potential difference between the source-drain electrodes (I_{SD}) is therefore a function of the applied gate voltage (V_{GS}) across the dielectric layer. With a small applied bias, there is negligible current flow across the semiconductor channel and the device is in the off state. With a bias greater than a threshold voltage (V_T), charge is induced at the dielectric-semiconductor interface, creating a conducting channel which increases the current flow between the source-drain electrodes, at which point the transistor is considered to be in the on state.

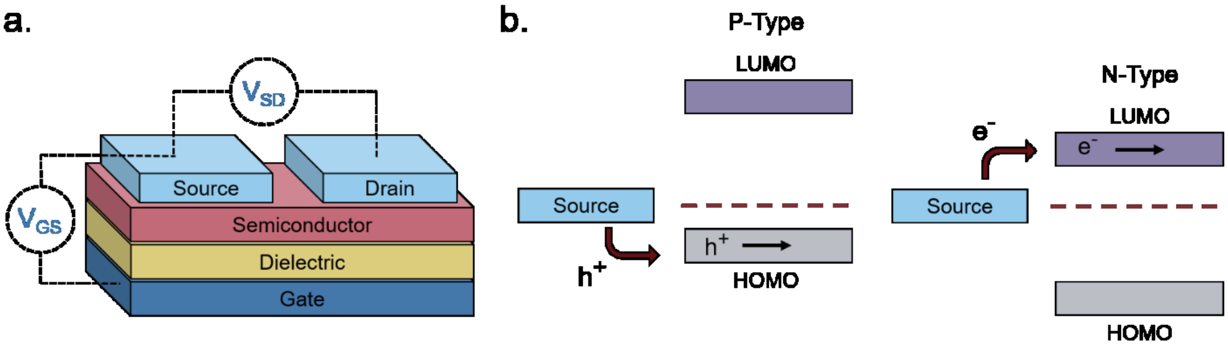

Figure 1.1. (a) Cross section diagram of a bottom-gate top-contact OTFT. (b) Energy level diagram of p- and n-type charge injection.

OTFTs can operate as either p-type, n-type or ambipolar devices depending on the semiconductor and electrode material used. For p-type operation, an applied negative bias injects holes, or positive charges, from the source to the semiconductor creating a conducting channel where charge is driven from the source to the drain. Conversely, n-type operation uses a positive bias to transport electrons, or negative charges, between the source and drain electrodes. The work function of the source-drain electrode material should be well aligned with the highest occupied molecular orbital (HOMO, p-type) or lowest unoccupied molecular orbital (LUMO, n-type) of the organic semiconductor to promote efficient charge injection (**Figure 1.1b**). Ambipolar devices display both p- and n-type charge transfer characteristics, though one mode of transport is typically favoured and results in better performing transistors. P-type organic semiconductors typically demonstrate higher mobilities and better chemical and environmental stability compared to n-type materials which are often air sensitive and insoluble. The fabrication of n-type OTFTs poses unique challenges due to the presence of radical anions that occur when a positive voltage is applied.[13,14] These anions can react with water and oxygen, inhibiting charge transfer, and forcing fabrication and operation within an inert environment, rendering them impractical for many applications.[15,16] The development of high performing n-type materials is critical for the advancement of organic electronic devices that use complementary p- and n-type circuits.[15,16] Thus, the need for high performing n-type materials has caused increased interest in the synthesis and characterization of novel n-type semiconductors which can achieve comparable electrical performance to leading p-type OTFTs.

Electrical Characterization

Electrical characterization is performed by varying source-drain biases (V_{SD}) or V_{GS} to obtain I_{SD} measurements resulting in an output curve (**Figure 1.2a**) or a transfer curve (**Figure 1.2b**) respectively. Output curves display the change in I_{SD} with V_{SD} taken at discreet V_{GS} intervals while transfer curves display the change in I_{SD} with V_{GS} taken at a constant V_{SD} in either the linear or saturation operating regimes, and are typically performed as a forward and reverse sweep in order to determine device hysteresis. At low V_{SD}, the charge carrier concentration in the transistor channel is uniform and the current increases linearly following Ohm's law. This is the linear operating regime in which the current flowing through the channel is directly proportional to V_{SD}. As V_{SD} is further increased the saturation operating regime is reached where the current becomes independent of V_{SD}.

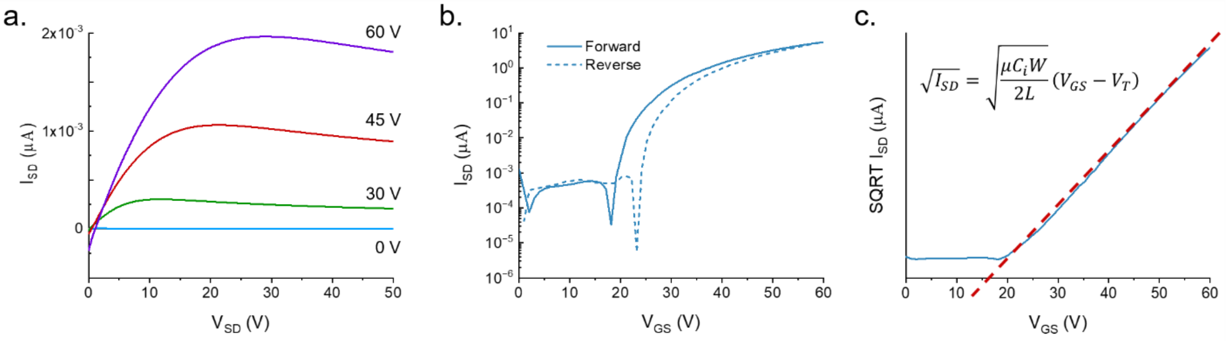

Figure 1.2. (a) Output curve, (b) forward and reverse transfer curves, and (c) plot of $\sqrt{I_{SD}}$ versus V_{GS} with dashed line representing the tangent used to calculate μ and V_T for an n-type OTFT.

OTFT performance can be characterized by a number of metrics with the most common being field-effect mobility (μ), V_T, and on/off current ratio ($I_{on/off}$). The μ of a device is a function of the rate of charge transfer through the semiconducting channel, and in the current literature calculated using a metal-oxide semiconductor field-effect transistor (MOSFET) model despite the physics of charge transport being different between these two device types.[1–3] Traditional MOSFETs use doped silicon to invert the conductivity at the dielectric-semiconductor interface to generate charge carriers.[1–3] However, OTFTs use intrinsic semiconducting materials that make direct contact with the electrodes where charge carriers accumulate at the interface.[1–3] OTFT μ can be calculated in either the saturation or linear operating regimes using the I_{SD} measurements from the transfer curve and **Equation 1.1** and **Equation 1.2** respectively.[1–3] Here, W is the channel width, L is the channel length, and C_i is the capacitance density calculated using the thickness of the dielectric layer and relative dielectric constant. For the saturation operating regime, μ is thus calculated by taking the square root of **Equation 1.1** to obtain a linear relationship between $\sqrt{I_{SD}}$ and V_{GS}. By plotting $\sqrt{I_{SD}}$ against V_{GS}, μ and V_T are calculated by the slope and x-intercept of the tangent line taken in the characterized V_{GS} range, represented in **Figure 1.2c**.

$$I_{SD,saturation} = \frac{\mu C_i W}{2L}(V_{GS} - V_T)^2 \tag{1.1}$$

$$I_{SD,linear} = \frac{\mu C_i W}{L}\left[(V_{GS} - V_T)V_{SD} - \frac{V_{SD}^2}{2}\right] \tag{1.2}$$

The aforementioned V_T of an OTFT is the V_G at which current starts to flow between the source-drain electrodes and the transistor is considered to be in the on state. OTFT V_T depends strongly on the semiconductor and dielectric materials used, with higher capacitance dielectrics enabling the use of lower operating V_G thus reducing V_T. Additionally, the V_T of organic devices is often not constant over time, and this bias stress behaviour is observed by a positive shift in V_T, resulting in hysteresis between the forward and reserve transfer curves (**Figure 1.2b**).[1–3] Bias stress can result from charge traps at the dielectric-semiconductor interface which themselves originate from impurities, defects, and grain boundaries in the semiconducting layer and greatly influence V_T.[17–19] Finally, $I_{on/off}$ is defined as the ratio of measured current in the on and off states at a particular V_G, and should be as large as possible to ensure efficient switching behaviour.[1–3] High performing OTFT operation is characterized by a high μ and a V_T close to 0 V, typically observed in highly-ordered low-defect crystalline films which promote efficient charge transport pathways between source-drain electrodes.[2] As such, μ, V_T, and $I_{on/off}$ are not only dependent on the materials and OTFT architecture used, but also the formation of the thin-film semiconducting layer and the molecular arrangement of molecules in the film.

Metal Phthalocyanine Semiconductors

In the simplest form, metal phthalocyanines (MPcs, $C_{32}H_{18}N_8M$) consist of four isoindole groups connected by nitrogen atoms forming an 18 π-electron ring structure, with two covalent bonds and two coordination bonds chelating a metal or metalloid center (**Figure 1.3**). With the possibility of over 70 central metal ions and 16 reactive sites in the peripheral and bay positions, an astonishing number of MPc complexes are possible.[20,21] Additionally, trivalent and tetravalent metal cations allow for the introduction of axial substituents providing an additional handle for tuning material properties. The choice of metal and the inclusion of peripheral, bay, or axial functionalization groups can strongly influence the physical and chemical properties of MPcs facilitating specific material tailoring. The extensive delocalization of the π-electron system and the exceptional stability of MPcs has resulted in their use for a myriad of applications since their discovery in 1907 and the first patent in 1929.[20,21] Historically, due to their vibrant blue, purple, or green colour, MPcs have been, and are still, used as commercial colourants in paints, plastics, textiles, printing inks, dyes, and even some food colouring.[22] Non-colourant applications have included catalysts, lubricants, indicators, and semiconductors, with recent interest focusing on more advanced applications.[22] The ability of MPcs to form highly ordered thin-films coupled with their chemical and mechanical stability has led to their use as the active layer in a number of electrochemical and photo-electrochemical sensors for drug analysis and the detection of pharmaceutical products,[23] gas sensing including the detection of alcohol vapours,[24–27] cannabinoid sensing,[28] and gamma radiation sensing[29]. MPc thin-films are a vastly growing area of research for emerging organic electronic devices having found promising success in OPVs,[30,31] OTFTs,[32,33] and OLEDs[34].

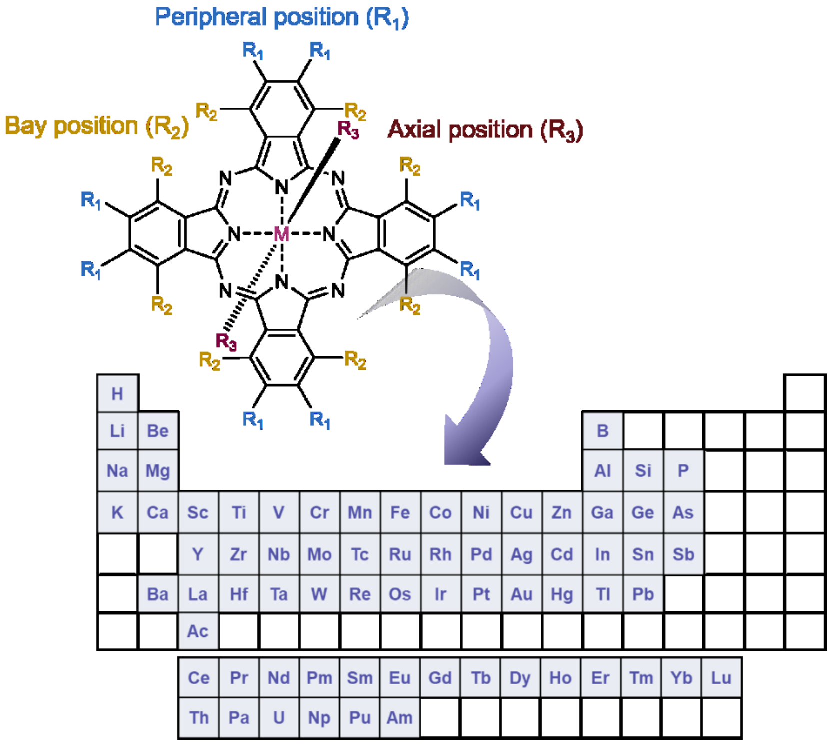

Figure 1.3. Schematic diagram of MPc structure with elements that form phthalocyanine complexes.

Silicon phthalocyanines (SiPcs) are a promising subset of the MPc family as their tetravalent metal center allows for additional chemical tunability of their axial positions. These chemical handles facilitate the use of axial groups such as phenoxy and benzoate substituents which have been shown to alter the processability, solid state properties, and performance of electronic devices.[35,36] Additionally, the ability to incorporate solubilizing alkyl chains to the axial positions makes SiPcs ideal for engineering solution processable semiconductors that are compatible with the large scale, low cost, and high throughput manufacturing that is required for commercial applications.[37] SiPc derivatives can often be prepared from straightforward synthetic routes which minimizes the overall complexity of the active layer material, and enables facile low-cost synthesis.[38] Since SiPcs predominantly demonstrate n-type charge transport characteristics whereas most MPcs act as p-type materials, the need for high performing stable n-type organic semiconducting materials makes SiPcs of particular interest for use in solution processable organic electronic devices and their components.

Thin-Film Growth by Solution Deposition

Deposition Techniques

Solution deposition of organic small molecules involves the dissolution of the deposit material into an organic solvent where it can then be deposited onto a substrate by one of four main methods: drop casting, spin coating, printing, and meniscus guided coating (**Figure 1.4**). As the solvent evaporates, the solution becomes supersaturated, driving nucleation and crystal growth, to form a thin-film. The nucleation and growth of solution deposited materials is complicated by solvent-vapour, solvent-substrate, solute-solvent, and solute-substrate interactions.[39] Additionally, controlling the formation of thin-films by solution processes is limited due to the rapid progression of nucleation, crystallization, and growth stages that can occur in a matter of seconds.[40]

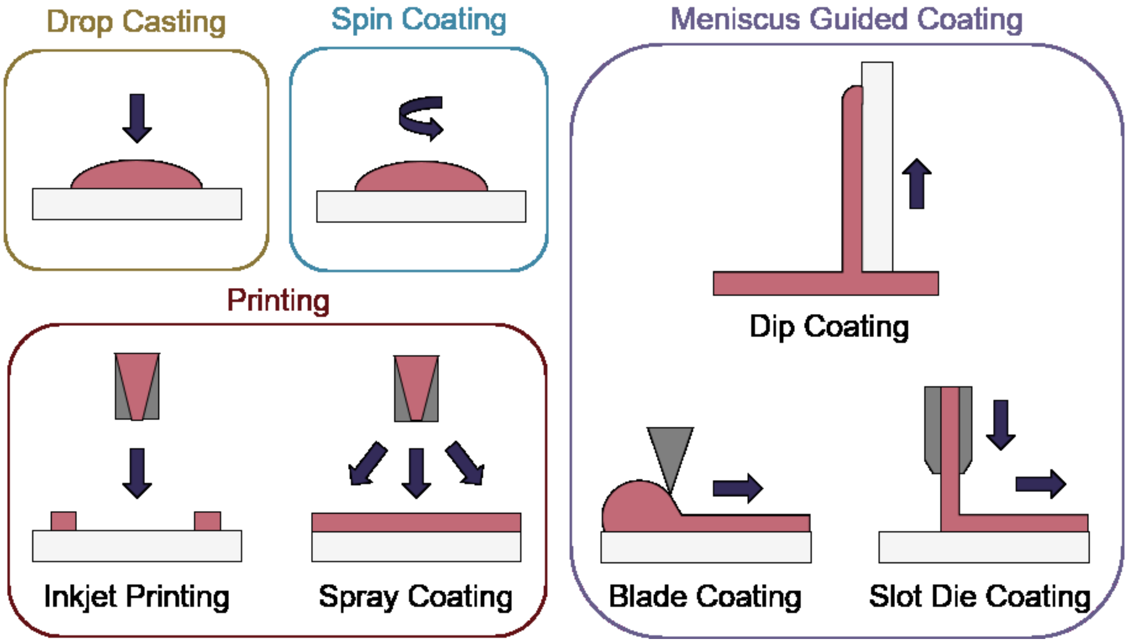

Figure 1.4. Diagram of various solution deposition methods.

Drop casting and spin coating are common lab scale techniques used to deposit material on small area substrates. Drop casting involves depositing solution droplets onto a stationary substrate with controlled droplet size and momentum, where the solvent is left to slowly evaporate, leading to the formation of a thin-film.[39] As no outside forces are applied, nucleation begins along the edge of the droplet with crystal growth occurring in the direction of the contact line recession. Drop casting can often lead to non-uniform deposition since the recession of the contact line is typically irregular. Spin coating is a more consistent fabrication method used to create uniform thin-films by dropping solution onto a rotating substrate which simultaneously spreads the solution by rotational forces while quickly evaporating the solvent.[39]

Printing is a broad definition of different deposition techniques, however it typically refers to large area solution processing methods that do not primarily rely on directional shear-induced alignment such as meniscus guided coating.[39] Inkjet printing is one of the most common and popular printing methods where a jet of solution is ejected from a chamber by a piezoelectric or thermal actuator and is deposited onto a substrate.[39] Similar to inkjet printing, spray coating ejects solution from a nozzle where small droplets are formed by aerosolization with an inert gas and are deposited onto the substrate.[39] Inkjet printing and spray coating are particularly useful as their compatibility with roll-to-roll manufacturing facilitates effective high throughput fabrication.

Meniscus guided coating methods are scalable large area techniques that use the linear movement of either the substrate, or coating tool, to fabricate thin-films with uniformly aligned crystal growth.[39,41] Dip coating, involving the vertical withdrawal of a substrate from a solution bath, blade coating, involving the use of a flat rectangular edge to spread solution across a substrate, and slot die coating, involving the flow of solution through an orifice and shaping device onto a horizontally moving substrate are common examples of meniscus-guided coating methods.[39,41] The alignment and size of the growing crystallites relies on the shear force directing solution flow and is largely influenced by the speed at which movement occurs.

Thermodynamics and Kinetics

When a solution is introduced onto a substrate surface, solvent evaporates, increasing the concentration of the solution until it becomes supersaturated and the dissolved molecules begin to precipitates to form a thin-film. The formation of precisely controlled thin-films with specific grain structures and morphologies remains a challenge for solution processing due to the rapid nucleation and growth steps. The thermodynamic driving force for nucleation is the difference between the chemical potential of organic molecules in the liquid phase (μ_l) and crystalline phase (μ_c).[42] In the case of solution deposition, $\Delta\mu$ corresponds to the difference between the concentration of the solution at equilibrium (C_∞) and the concentration during growth (C), which can be expressed as a function of the substrate temperature (T_s) in **Equation 1.3**.[42]

$$\Delta\mu = \mu_c - \mu_l = kT_s \ln\left(\frac{C_\infty}{C}\right) \tag{1.3}$$

Thermodynamically, C and T_s are the two parameters that determine the nucleation and growth of crystallites during solution deposition, however, solution deposition methods are largely governed by kinetic processes and rates of crystallization.[43] In the case of solution deposition, the kinetic driving force for nucleation is the rate of solvent evaporation which directly determines the rate of crystallization, and is thus key to the fabrication of consistent small molecule thin-films.[39,44] Due to variations in the respective solution processing methods the governing principals for the rate of solvent evaporation will be method specific.

Drop casting and printing techniques use the release, impact, and spreading of one or more solution droplets that may form a continuous thin-film before drying or may dry individually to create a thin-film composed of many islands. Controlling the rate of solvent evaporation, and thus the nucleation and growth stages, depends solely on the solvent and substrate properties as no external rotational or shear forces are applied.[45–47] The solution and substrate surface properties can influence the deposition by causing splashing, spreading, receding, and/or rebounding.[48–50] Additionally, temperature and concentration gradients within solution droplets can lead to coffee ring and Marangoni effects, leading to poorly controlled film formation.[46,47]

Thin-film formation by spin coating can be accurately represented when the evaporation rate of the solvent, the viscosity increase resulting from the increase in solute concentration, the surrounding vapour phase above the substrate, and the solvent's properties are taken into account.[51,52] The simplest and earliest models describing liquid flow on a rotating surface are formulated with three main assumptions: (i) the gas and liquid phases are Newtonian fluids; (ii) the fluid flow is axially symmetric and laminar; and (iii) the rotating surface is flat and extends infinitely.[51,52] It is widely accepted that the early stages of spin coating are flow dominated while late stages are dominated by the rate of solvent evaporation. At the transition point, when evaporation and flow become equal, the evaporation rate (ν_e) depends on the rotational speed (ω), yielding **Equation 1.4**.[51–55]

$$\nu_e = \omega^{1/2} \tag{1.4}$$

This simple relationship has been observed experimentally using polymer thin-films with only small reported variations in the exponent value.[51,52,55–59] However, as solvent evaporates the physical properties of the solution change, inducing non-Newtonian behavior. More rigorous models describing the spin coating process take into account heat and momentum transfer by including the effects of solution viscosity and solvent volatility.[52,57,58] The two stage flow dominated and evaporation dominated process of spin coating has been corroborated with *in situ* experimental data from spin coated small molecule thin-films.[60,61] These experiments show how the rapid flow dominated crystallization stage, which occurs over a sub-second time scale, is independent of the rotational speed, and the slower more gradual evaporation dominated stage is rotation speed dependant.[60,61] Therefore, the rate of solvent evaporation during spin coating can be described by **Equation 1.4**.

Meniscus guided coating methods depend mainly on solvent properties and coating speed. Solvent evaporation is dominant in the meniscus region leading to supersaturation, precipitation, and ultimately to nucleation. However, most meniscus-guided methods use an external shear force to enhance thin-film uniformity and crystallite alignment. The intensity of this force, determined by the coating speed (v_c), can be divided into two categories: fast coating speeds ($v_c \approx 1$ mm s^{-1}) and slow coating speeds ($v_c \approx 1$-100 µm s^{-1}). Fast coating speeds where solution is spread out by shear forces and solvent evaporation is separated from the meniscus region is known as the Landau-Levich-Derjaguin deposition regime where solvent evaporation is a function of v_c.[62–64] At slow coating speeds deposition corresponds to the evaporation regime where v_c is approximately equal to v_e of a pinned drop of solution that is receding primarily due to evaporative mass loss.[62] Thus, in contrast to the Landau-Levich-Derjaguin regime where solvent evaporation is separate from thin-film deposition, the evaporation regime is complicated by the interactions between solvent evaporation, fluid flow, and film formation.[62–64] A number of models have been proposed to describe v_e most of which take on the general form of **Equation 1.5**.[41,62,65]

$$v_e = AV_m T_s^{0.7} \exp\left(-\frac{\Delta S_{vap} T_b}{RT_s}\right) \tag{1.5}$$

Here V_m is the molar volume of the liquid solvent, ΔS_{vap} is the entropy of vapourization of the solvent, T_b is the boiling point of the solvent at atmospheric pressure, and A is a single fitting parameter combining all temperature independent varaibles.[62,65]

Effect of Deposition Parameters

Solution deposition processes can produce wide variations in thin-film microstructure depending on solution concentration, solvent type, substrate temperature, and substrate surface chemistry. Solution concentration influences thin-film coverage, such that at low concentrations low coverage sub-monolayer formation is observed, whereas at increasing concentrations the coverage and interconnectivity increase with the formation of mesh layers and multilayers. This phenomena has been documented in spin coated copper phthalocyanine (CuPc) thin-films where, at low solution concentration, CuPc molecules form a sub-monolayer of interconnected ribbons (**Figure 1.5**).[66–68] As the concentration of CuPc in the deposited solution increases, multilayer formation is observed, however complete coverage for a single layer is never achieved due to the anisotropic nature of CuPc which effects surface diffusion and subsequent nucleation.[66–68]

Solvent choice plays an important role in the formation of thin-films by solution deposition. The rate of solvent evaporation directly determines the crystallization rate, dictating the final thin-film morphology and microstructure. Solvents with a faster rate of evaporation generally lead to films with a greater surface roughness due to the occurrence of well separated clusters. Solvents with high evaporation rates, such as chloroform, can lead to the formation of these clusters since the rapidly evaporating solvent leaves little time for surface mobility or diffusion of the molecules on the substrate. This often results in lower aggregation and films with a non-coalesced morphology. Solvents with low evaporation rates, such as dimethylformamide, facilitate greater molecular mobility on the surface due to the longer evaporation time and often results in a more highly packed and ordered film. This has been demonstrated with tetrakis-(isopropoxy-carbonyl)-CuPc (TIP-CuPc) and a number of other semiconducting small molecules.[45,69–71]

The choice of solution processing method will have significant influence on thin-film microstructure. A study by Gojzewski et al., exhibited the differences in CuPc film formation by drop casting, spin coating, dip coating, and spray coating (**Figure 1.5**).[66] The authors used CuPc dissolved in trifluoroacetic acid that immediately spreads to cover the hydrophilic substrate surface to form a liquid film. Upon drop casting, outward capillary flow from the center of the drop brings dissolved CuPc molecules to the edge, creating the morphology shown in **Figure 1.5**. Spin coating using the same solution produced a multi-layer formation of nanoribbons similar to that of drop casting, however the added rotational force increases the rate of solvent evaporation creating a rougher film surface.[66] Dip coating yielded similar film characteristics (roughness, coverage and film volume) to drop casted films, however exhibited a unique morphology consisting of a sub-monolayer mesh-like film made of long, asymmetrically curved and interconnected nanoribbons where the CuPc molecules were orientated in-plane to the substrate.[66] Spray coated films displayed a similar morphology and comparable surface roughness, coverage, and film volume to spin coated films with large rod-like CuPc aggregates.[66] Due to the added rotational force during spin coating, noticeable differences in film morphology between the two fabrication methods are expected. However, as discussed, morphology is dependent on the rate of solvent evaporation. The specific fabrication parameters used for spray coating and spin coating in this case allows for sufficient solvent evaporation to create films of large rod-like CuPc aggregates.[66] This further corroborates the relationship between thin-film microstructure and solvent evaporation as the driving force for the nucleation and growth of solution deposited thin-films.

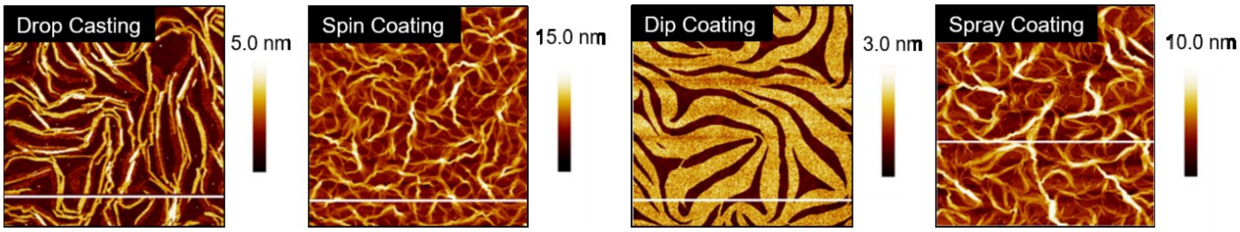

Figure 1.5. AFM images (5 μm x 5 μm) of CuPc thin-films fabricated by drop casting, spin coating, dip coating, and spray coating. Adapted with permission from ref 66. Copyright © 2020 the Authors under the Creative Commons Attribution Non-Commercial No Derivatives 4.0 License.

Thin-Film Microstructure of Metal Phthalocyanines

Packing Motifs

The growth mode and packing structure of inorganic thin-films is well understood by reason of the strong covalent bonds, and the inherent isotropic shape of inorganic atoms. In contrast, due to the anisotropic geometry and weak van der Waals forces of organic molecules more variable crystallite growth, molecular packing structures, thin-film textures, and morphologies are observed.[72,73] Molecular packing can not only impact the solid state properties of organic molecules but it can also effect the thermodynamic, kinetic, mechanical, electrical, and optical properties of the final thin-film.[74] The identification and classification of different packing structures is therefore crucial for applications in various industries including pharmaceuticals,[75] organic semiconductors,[76] pigments,[77] and explosives[78]. Conjugated aromatic small molecules have been known to form two main crystal packing structures: herringbone and π-stacked (**Figure 1.6**).[79] The herringbone structure exhibits altering face-to-edge and face-to-face molecular packing, and mainly occurs in planar MPcs, whereas the π-stacked configuration exhibits face-to-face packing and is adopted by non-planar MPcs.[79]

Polymorphism refers to the ability of molecules to form multiple distinct crystal structures. Controlling polymorphism in organic thin-films is challenging since π-conjugated molecules typically have similar cohesive energies and a low kinetic barrier to solid-solid transformations, making polymorphs difficult to isolate and stabilize.[74] Common methods of obtaining different polymorphs in thin-films is through varying film thickness, temperature, surface chemistry and post-deposition processes such as thermal and solvent annealing.[74] The identification of polymorphs and the differences in morphological, structural, and spectroscopic properties have been documented through electrical conductivity measurements[80,81], optical absorption spectra[82–

[84], electron paramagnetic resonance spectroscopy (EPR)[80], nuclear magnetic resonance (NMR)[77], Raman spectroscopy[77,83,85], and surface imaging[82–84].

The polymorphic character of MPcs was first reported by Hamm and Norman in 1948 for CuPc[86] and has since been extensively studied in a number of MPcs.[85,87–94] MPcs are known to exists in various polymorphic forms identified as α, β, γ, δ, ε, and x-phases with the metastable α-phase and stable β-phase being the most common and commercially significant.[80,85,95] The phase transition from α to β occurs in most MPc thin-films through exposure to temperature (200-300°C)[83,84,89,95] or organic solvents[96,97], and is characterized by a change in tilt angle between planes and the degree of π-electron overlap.[82,98] The stable β-phase is monoclinic in structure and forms long crystallite needles[99], whereas the metastable α-phase has been reported to be tetragonal[100], orthorhombic[101], or monoclinic[80] in structure, and generally forms into spherical crystallites. As an example, **Figure 1.6** highlights some of the differences between α- and β-phase CuPc polymorphs. For both polymorphs the CuPc molecules align in the herringbone packing structure with a 65° angle between molecules and the b axis for α-phase CuPc and a 45° angle for β-phase CuPc.[82] The larger angle of α-phase CuPc results in increased π-electron overlap and is likely the reason for the higher conductivity displayed by this polymorph.[80,81] Differences in CuPc packing structure determine solid state properties such as conductivity, optical absorbance, and even colour which are critical for determining appropriate use in some applications. α- and β-phase CuPc are often used as organic semiconductors in electronic devices with particular interest in α-phase CuPc due to the high carrier mobility and high-frequency capacitance and conductance demonstrated by α-phase CuPc OTFTs[102], and α-phase CuPc-Si hetero-structures[103]. Additionally, in the ink industry the most widely used blue pigments are CuPc based, with α- (purple), β- (green-blue), and ε-phase (red) CuPc being the most popular in printing inks, paints, plastics, and textiles.[77,104]

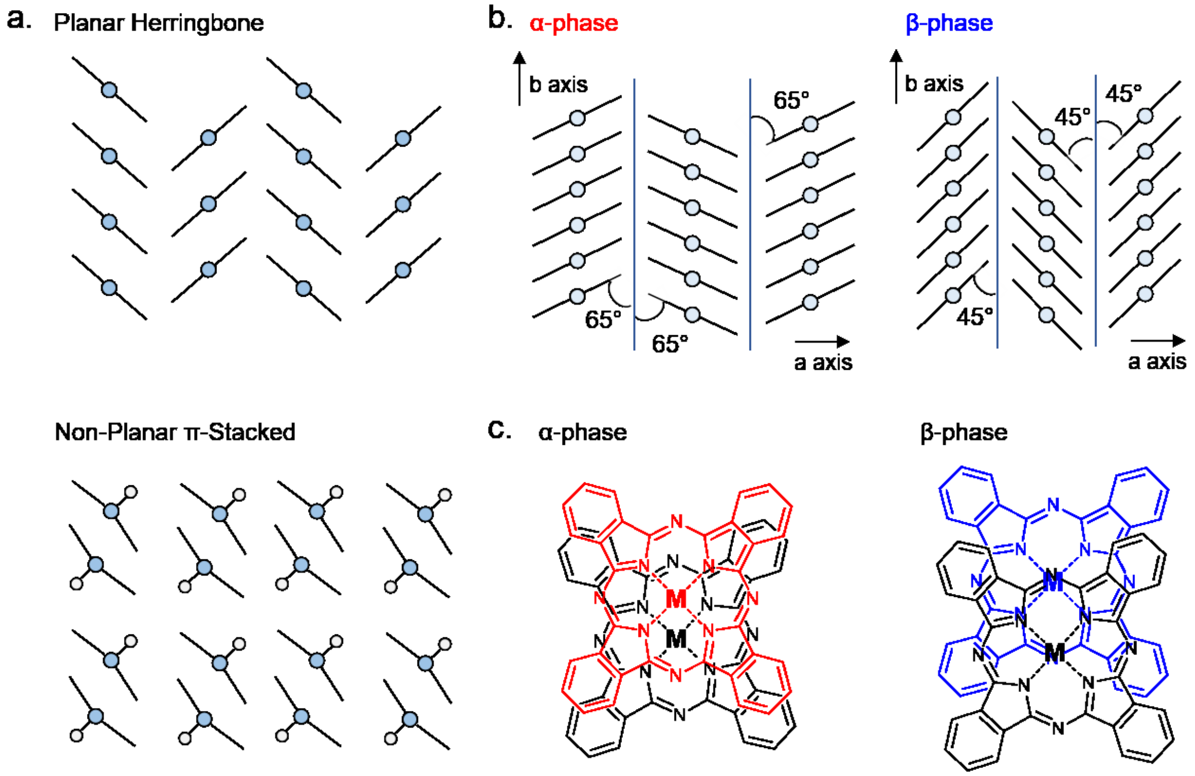

Figure 1.6. (a) Schematic diagram of herringbone and π-stacked crystal packing. (b) Crystal packing structure of α-phase and β-phase CuPc. Reproduced with permission from ref 98. Copyright © 2017 Elsevier B.V. (c) α-phase and β-phase superposition of phthalocyanine molecules along the b axis. Reproduced with permission from ref 95. Copyright © 1988 American Chemical Society.

Thin-Film Morphologies

MPcs can form a myriad of film morphologies depending on the molecular structure, packing motif, and fabrication conditions (**Figure 1.7**). Planar divalent MPcs, such as zinc, copper, cobalt, iron, and magnesium phthalocyanine (ZnPc, CuPc, CoPc, FePc, MgPc) exhibit morphologies with ribbon-like grains of similar structure and shape with only small variations in grain size.[105] Typically, ribbon-like grain morphologies are observed for films deposited on heated substrates whereas smaller more cylindrical shapes are observed at lower substrate surface temperatures.[87,106–108] Non-planar trivalent and tetravalent MPcs, such as aluminum chloride, titanium oxide, lead, and vanadyl phthalocyanine (AlClPc, TiOPc, PbPc, VOPc) have much larger rectangular plate-like features owing to their different π-stacked packing structure.[105] Additionally, these four MPc thin-films have a greater surface roughness and lower surface area to volume ratio compared to the planar divalent MPc thin-films.[105,109–112]

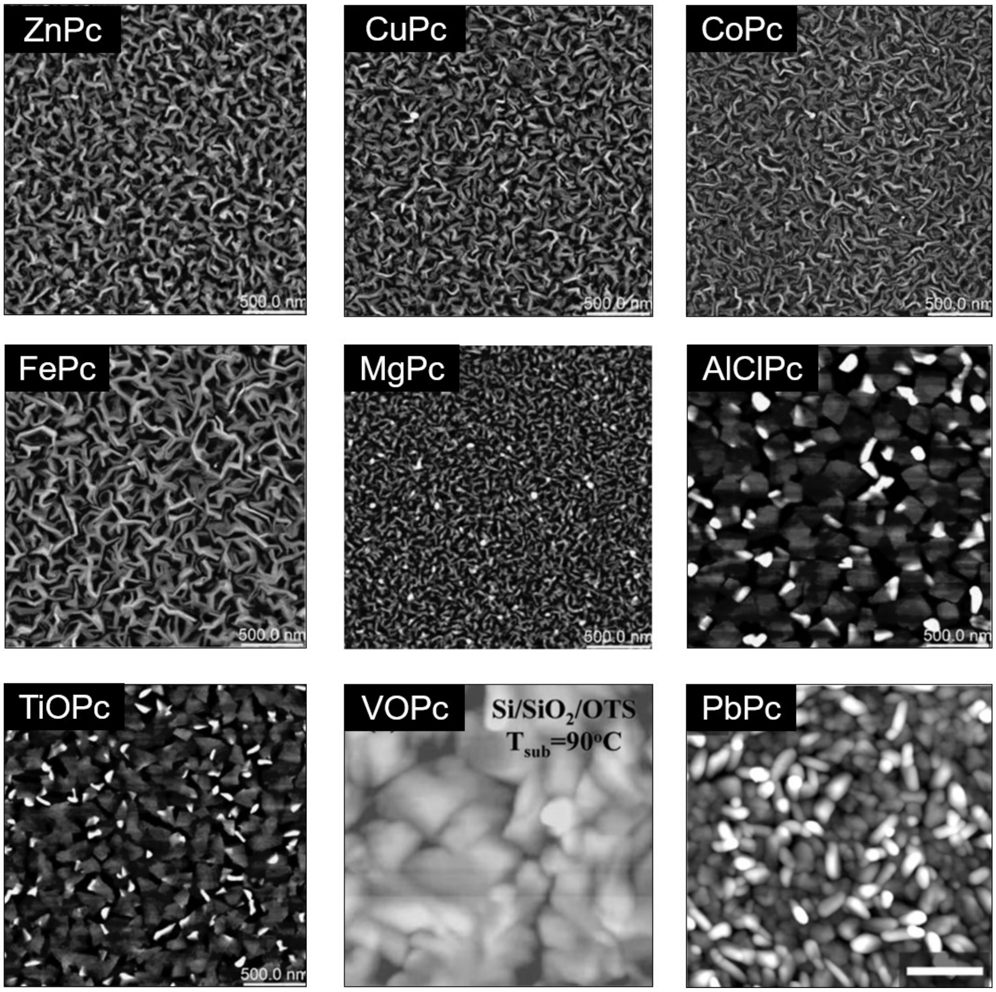

Figure 1.7. AFM images (2.5 μm x 2.5 μm) of CoPc, AlClPc, FePc, MgPc, TiOPc, ZnPc, CuPc. Adapted with permission from ref 105. Copyright © 2019 The Royal Society of Chemistry. AFM images (1 μm x 1 μm) of VOPc. Adapted with permission from ref 109. Copyright © 2008 American Chemical Society. AFM image (2 μm x 2 μm) of PbPc. Adapted with permission from ref 110. Copyright © 2011 American Chemical Society.

The thin-film morphology of MPcs can also be altered through the inclusion of axial substituents as demonstrated by SiPc films (**Figure 1.8**). SiPc thin-films with phenoxy and fluorophenoxy groups show two distinct morphologies either consisting of small regular circular grains or more elongated rectangular grains depending on the structure of the phenoxy substituent.[35,113] In electronic devices, morphology has been shown to impact the charge carrier mobility of transistors[114–116], the power conversion efficiency of solar cells[117–119], and the performance of light emitting diodes[120]. Additionally, the mechanical stability of thin-films, including the flexibility and sensitivity to stress and strain, will affect the degree of reorganization in film morphology with mechanical deformation.[121–123] In particular, films with large grains and broad boundaries are more susceptible to mechanical deformation as the formation of wide interconnected cracks are more prevalent compared to films with smaller grains and a smoother surface morphology.[121,123,124]

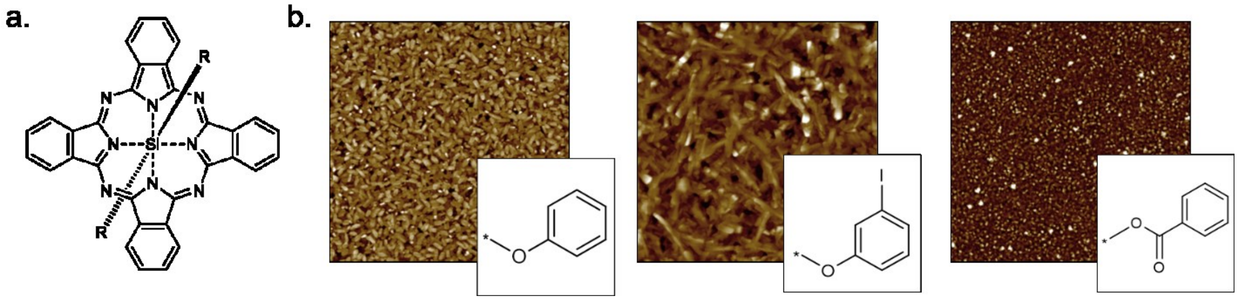

Figure 1.8. (a) Structure of axially substituted SiPc. (b) AFM images (2.5 µm x 2.5 µm) of SiPcs with phenoxy axial substituents. Adapted with permission from ref 35. Copyright © 2020 American Chemical Society.

Thin-Film Characterization

High performing organic thin-film devices rely on the specific interfacial orientation and alignment of molecules to achieve optimum opto-electric properties and thus the characterization of these molecular interfaces is critical to the development of advanced devices. Minor fabrication variations in organic thin-films can lead to an imbalance in property optimization where the ability to fine tune molecular structure to optimize nano-scale properties, such as intermolecular charge transfer, negatively impacts large-scale thin-film formation. From molecular packing to crystallite formation and surface morphology, analysis must be performed at various size scales in order to fully characterize the films. **Figure 1.9** illustrates the relevant size scales and corresponding structural characteristics important to organic thin-films and the characterization techniques which can be used to provide information at each scale. Surface morphology characterization is frequently used to access how material structure and fabrication parameters affect grain formation, and surface homogeneity, which are often correlated to electrical characterization. Unlike surface characterization, characterizing packing structure and crystallite formation requires X-ray based techniques which provide additional information not possible with other methods like optical microscopy, and scanning probe techniques. X-ray methods allow for the determination of packing motifs, molecular orientation and orientation mapping, and degree of crystallinity. These methods also provide a more complete quantitative picture of the film in comparison to surface imaging.

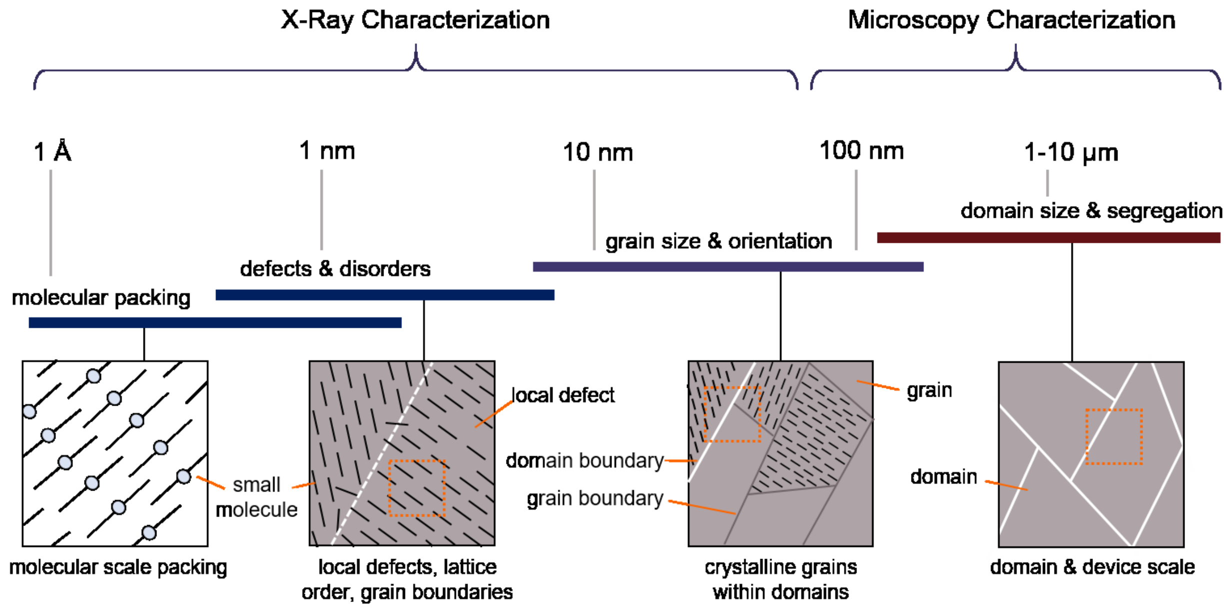

Figure 1.9. Size scales, structural features, and relevant characterization techniques for organic thin-films.

Microscopy Techniques

Atomic force microscopy (AFM) is a type of scanning probe microscopy with the ability to obtain high resolution topography images of a sample surface in the nanometer range. AFM uses a cantilever mounted with a sharp probe tip to create a raster scan of a sample. During operation the x, y, and z coordinates of the probe tip are recorded to create a 3D pseudo-colour plot of the surface.[125,126] AFM operation is typically described by one of three modes: (i) contact mode, (ii) tapping mode, and (iii) non-contact mode. Non-contact mode does not require the probe to contact the surface and therefore does not suffer from probe or sample degradation making it preferable for soft samples such as organic thin-films. In non-contact mode the probe tip is brought close to the sample surface resulting in strong intermolecular forces between the sample and the probe tip. These intermolecular forces cause the cantilever to deflect by repulsive or attractive forces from the sample, allowing for precise height measurements by reflecting a laser off the cantilever to a detector.[125,126] AFM images of organic thin-films can be used to obtain information about grain size and shape, grain boundaries, surface roughness, and surface homogeneity to relate surface morphology to device performance.

Raman microscopy uses the vibrational properties of MPcs to elucidate changes in the configuration of the macrocycle as a result of substituent groups, central metal, and orientation and packing structure of molecules relative to the substrate.[85,127–131] MPc thin-films exhibit a distinctive band pattern with vibrations under 600 cm^{-1} attributed to the deformation of the macrocycle ring, N-M stretching, and the deformation of isoindoles.[132–134] The 600-900 cm^{-1} vibrations are generally due to the deformation of the benzene and isoindole rings, with 1330-1445 cm^{-1} assigned to isoindole stretching and vibrations of the N-M and C-H bonds.[132–134] The most intense vibrational band observed in MPcs is around 1500 cm^{-1} which exhibits a clear sensitivity to changes in the central metal with a definite trend correlating metal size to shifts in vibration.[127–129,131,132] Through polarized Raman microscopy the intensity of this band can be used to determine the orientation MPc molecules to the substrate in order to ascertain the effects of fabrication parameters and to identify polymorphic phases and film order.[85,130,135] Additionally, the spectra region from 1350-1500 cm^{-1}, known as the finger print region, changes depending on the individual MPc and can display up to six unique bands.[127,128] This region has been known to change depending on the metal center, degree of fluorination, and the inclusion of substituent groups.[127,128,132] Through Raman microscopy the vibrational properties of MPc thin-films can be used to determine fundamental thin-film characteristics such as molecular alignment and film homogeneity, and identify MPc films by their metal ion and polymorphic forms.

X-Ray Techniques

X-ray scattering techniques employ the use of incident X-rays at a sample where a fraction of the waves are diffracted and collected creating distinct diffraction patterns with high intensity peaks characteristic to the specific film properties. The angle of the diffracted peaks provides information on the spacing between molecular planes in the film, whereas the direction of the peaks correspond to the orientation of the planes. X-ray diffraction (XRD) is a rapid non-destructive characterization technique primarily used to ascertain the crystal structure and atomic spacing of crystalline and semi-crystalline materials. XRD is based on the constructive interference of monochromic X-rays with a crystalline sample that satisfies Bragg's Law to produce a plot of all possible diffraction directions and their intensity (**Figure 1.10a**).[136–138] Monochromic X-rays are generated by a cathode ray tube and filtered to produce monochromatic radiation which are then concentrated and directed at a sample surface.[136–138] The interaction between the incident X-rays and sample produces constructive interference and diffracted X-rays which are then recorded. Bragg's Law is used to relate the wavelength and diffracted angle to the lattice d-spacing of molecules in the sample. In terms of organic thin-film characterization, analyzing an XRD patterned in terms of peak location, width, and intensity can be used to determine the crystalline structure of a film, average crystallite size, degree of crystallinity, and identify polymorph formation.[136–138]

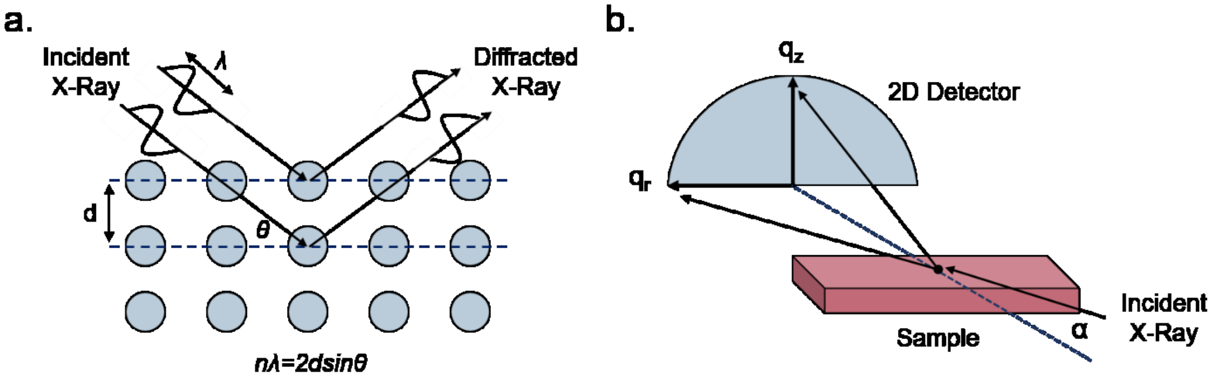

Figure 1.10. Schematic diagram of (a) the principals of XRD and (b) GIWAXS experimentation.

Grazing-incidence X-ray scattering (GIXS) is a common synchrotron based X-ray scattering technique where the scattering vector is directed along the sample plane and the diffracting planes are perpendicular to the sample plane.[139] GIXS can be used to analyze the bulk or surface film properties depending on the chosen incident angle and detection method, for example signal can be collected by a point detector for high accuracy or more commonly using a 2D detector for rapid data collection over a large area with minimal sample damage (**Figure 1.10b**).[139] Grazing-incidence wide-angle X-ray scattering (GIWAXS) is one of the most commonly used synchrotron techniques to investigate organic thin-films with the ability to resolve features in the range of approximately 1 Å-100 nm.[139] 2D GIWAXS patterns can be used to determine crystal packing through the size and symmetry of the unit cell by analysing peak position and intensity, crystallite size and disorder by analysing peak width, and the degree of crystallinity by analysing the integrated diffraction intensity.[139] Additionally, the molecular orientation and alignment can be determined by performing an azimuthal scan where a diffraction peak is selected and the intensity recorded while the sample is rotated about the substrate normal to determine the orientation distribution.[139]

Scope of Thesis

This thesis focuses on the development and advancement of solution fabrication methodologies to produce n-type OTFTs, with the aim to better understand the complex relationships of crystallite nucleation, thin-film formation, and small molecule deposition on the electrical performance of transistors. In **Chapter 2**, eight axially substituted SiPc derivatives with different alkyl chain lengths, symmetries, and branching points were used as the semiconductor layer in OTFTs fabricated by spin coating. The development of structure-property relationships between axial substituent, thin-film surface morphology, and device performance helped realize molecule design rules for solubilizing SiPcs. Additionally, the effects of thermal annealing and spin coating time on film formation, two key processing steps in OTFT fabrication, were investigated by X-ray techniques to elucidate the relationship between thin-film microstructure and device performance.

Using a unique SiPc derivative, compatible with both sublimation and solution processes, **Chapter 3** compares OTFTs fabricated by spin coating and physical vapour deposition, characterizing microstructure, morphology and device performance to assess how deposition processes effect film formation and device functionality. Building off the work presented in **Chapter 3**, **Chapter 4** documents the use of polarized Raman microscopy as a quick and robust technique to determine the influence of deposition method and post deposition thermal annealing on the thin-film properties of the same SiPc derivative. Comparing physical vapour deposition and spin coating, the orientation of molecules in films were determined and further characterized by XRD to assess variations in microstructure and polymorph formation due to annealing temperature.

Chapter 5 investigates the use of asymmetric axial fluorination to achieve high performance n-type OTFTs through controlled self-assembly by fluorine-fluorine interactions. Two novel asymmetric SiPc derivatives consisting of one axially substituted fluorine and one tri-alkyl silane group were synthesized and characterized in OTFTs. The effect of surface energy and fluorination were investigated at the dielectric-semiconductor interface by XRD, AFM, microscopy, and GIWAXS to assess alterations in film conformation, microstructure, and morphology.

Chapter 6 illustrates the use of high throughput meniscus guided printing for larger scale fabrication to further understand property-performance relationships in organic semiconductors. High throughput thin-film deposition by printing reduces the required time and material costs, enabling rapid analysis of materials, fabrication parameters, and device components compared to lab scale spin coating. OTFTs were fabricated using three SiPc derivatives with different alkyl chain length solubilizing groups and the deposition parameters were investigated in a multidimensional variable space to determine optimal processing conditions.

Chapter 7 presents the main conclusions realized from each work and highlights recommendations for future research concerning the fabrication of solution processable high performing n-type OTFTs. Finally, **Chapter 8** provides a summary of the additional publications that I have contributed to throughout my doctoral work, focusing on my expertise in thin-film characterization by AFM, XRD, GIWAXS, and Raman microscopy, and my work on the fabrication of other MPc based OTFTs.

References

1 Zaumseil, J. & Sirringhaus, H. Electron and Ambipolar Transport in Organic Field-Effect Transistors. Chem. Rev. 107, 1296–1323 (2007).

2 Klauk, H. Organic thin-film transistors. Chem. Soc. Rev. 39, 2643 (2010).

3 Horowitz, G. Organic thin film transistors: From theory to real devices. J. Mater. Res. 19, 1946–1962 (2004).

4 Myers, J. D. & Xue, J. Organic Semiconductors and their Applications in Photovoltaic Devices. Polym. Rev. 52, 1–37 (2012).

5 Troisi, A. & Orlandi, G. Dynamics of the Intermolecular Transfer Integral in Crystalline Organic Semiconductors. J. Phys. Chem. A 110, 4065–4070 (2006).

6 Liao, C. et al. Flexible Organic Electronics in Biology: Materials and Devices. Adv. Mater. 27, 7493–7527 (2015).

7 Song, J., Liu, H., Zhao, Z., Lin, P. & Yan, F. Flexible Organic Transistors for Biosensing: Devices and Applications. Adv. Mater. (2023).

8 Liu, K., Ouyang, B., Guo, X., Guo, Y. & Liu, Y. Advances in flexible organic field-effect transistors and their applications for flexible electronics. npj Flex. Electron. 6, 1 (2022).

9 Hong, G. et al. A Brief History of OLEDs—Emitter Development and Industry Milestones. Adv. Mater. 33, (2021).

10 Lee, J. et al. Recent Progress on Quantum Dot Patterning Technologies for Commercialization of QD-LEDs: Current Status, Future Prospects, and Exploratory Approaches. Small Methods (2024).

11 Solak, E. K. & Irmak, E. Advances in organic photovoltaic cells: a comprehensive review of materials, technologies, and performance. RSC Adv. 13, 12244–12269 (2023).

12 Zheng, X. et al. Versatile organic photovoltaics with a power density of nearly 40 W g −1. Energy Environ. Sci. 16, 2284–2294 (2023).

13 Facchetti, A. Gels excel. Nat. Mater. 7, 839–840 (2008).

14 Lan, S. et al. Improving device performance of n-type organic field-effect transistors via doping with a p-type organic semiconductor. J. Mater. Chem. C 7, 4543–4550 (2019).

15 Griggs, S., Marks, A., Bristow, H. & McCulloch, I. n-Type organic semiconducting polymers: stability limitations, design considerations and applications. J. Mater. Chem. C 9, 8099–8128 (2021).

16 Quinn, J. T. E., Zhu, J., Li, X., Wang, J. & Li, Y. Recent progress in the development of n-type organic semiconductors for organic field effect transistors. J. Mater. Chem. C 5, 8654–8681 (2017).

17 Padma, N., Sawant, S. N., Sudarsan, V., Sen, S. & Gupta, S. K. Comparison of the role of holes and electrons in hysteresis and threshold voltage stability of organic field effect transistors. Phys. status solidi 210, 2111–2120 (2013).

18 Bolognesi, A. et al. Effects of Grain Boundaries, Field-Dependent Mobility, and Interface Trap States on the Electrical Characteristics of Pentacene TFT. IEEE Trans. Electron Devices 51, 1997–2003 (2004).

19 Park, J. H. et al. Origin of Bias-Stress Induced Instability in Organic Thin-Film Transistors with Semiconducting Small-Molecule/Insulating Polymer Blend Channel. ACS Appl. Mater. Interfaces 5, 1625–1629 (2013).

20 Thomas, A. L. Phthalocyanine Research and Applications. (CRC Press, 1990).

21 McKeown, N. B. Phthalocyanine Materials: Sythesis, Structure and Function. (Cambridge University Press, 1998).

22 Moser, T. The Phthalocyanines: Manufacture and Applications. (CRC Press, 1983).

23 Gonçalves, J. M., Iglesias, B. A., Martins, P. R. & Angnes, L. Recent advances in electroanalytical drug detection by porphyrin/phthalocyanine macrocycles: Developments and future perspectives. Analyst 146, 365–381 (2021).

24 Newton, M. I., Starke, T. K. H., Willis, M. R. & McHale, G. NO2 detection at room temperature with copper phthalocyanine thin film devices. Sensors Actuators B Chem. 67, 307–311 (2000).

25 Li, X. et al. Copper phthalocyanine thin film transistors for hydrogen sulfide detection. Sensors Actuators, B Chem. 176, 1191–1196 (2013).

26 Miyata, T. & Minami, T. Chlorine gas sensors with high sensitivity using Mg-phthalocyanine thin films. Appl. Surf. Sci. 244, 563–567 (2005).

27 Spadavecchia, J., Ciccarella, G., Siciliano, P., Capone, S. & Rella, R. Spin-coated thin films of metal porphyrin-phthalocyanine blend for an optochemical sensor of alcohol vapours. Sensors Actuators, B Chem. 100, 88–93 (2004).

28 Comeau, Z. J. et al. On-the-Spot Detection and Speciation of Cannabinoids Using Organic Thin-Film Transistors. ACS Sensors 4, 2706–2715 (2019).

29 Arshak, K., Arshak, A., Zleetni, S. & Korostynska, O. Thin and thick films of metal oxides and metal phthalocyanines as gamma radiation dosimeters. IEEE Trans. Nucl. Sci. 51, 2250–2255 (2004).

30 Williams, G., Sutty, S., Klenkler, R. & Aziz, H. Renewed interest in metal phthalocyanine donors for small molecule organic solar cells. Sol. Energy Mater. Sol. Cells 124, 217–226 (2014).

31 Grant, T. M. et al. Boron Subphthalocyanines and Silicon Phthalocyanines for Use as Active Materials in Organic Photovoltaics. Chem. Rec. 19, 1093–1112 (2019).

32 Melville, O. A., Lessard, B. H. & Bender, T. P. Phthalocyanine-Based Organic Thin-Film Transistors: A Review of Recent Advances. ACS Appl. Mater. Interfaces 7, 13105–13118 (2015).

33 Zhou, W., Yutronkie, N. J., Lessard, B. H. & Brusso, J. L. From chemical curiosity to versatile building blocks: unmasking the hidden potential of main-group phthalocyanines in organic field-effect transistors. Mater. Adv. 2, 165–185 (2021).

34 Plint, T., Lessard, B. H. & Bender, T. P. Assessing the potential of group 13 and 14 metal/metalloid phthalocyanines as hole transport layers in organic light emitting diodes. J. Appl. Phys. 119, 145502 (2016).

35 King, B. et al. Silicon Phthalocyanines for n-Type Organic Thin-Film Transistors: Development of Structure-

Property Relationships. ACS Appl. Electron. Mater. 3, 325–336 (2021).

36 Melville, O. A., Grant, T. M. & Lessard, B. H. Silicon phthalocyanines as N-type semiconductors in organic thin film transistors. J. Mater. Chem. C 6, 5482–5488 (2018).

37 Vebber, M. C., Grant, T. M., Brusso, J. L. & Lessard, B. H. Bis(trialkylsilyl oxide) Silicon Phthalocyanines: Understanding the Role of Solubility in Device Performance as Ternary Additives in Organic Photovoltaics. Langmuir 36, 2612–2621 (2020).

38 Grant, T. M., Dindault, C., Rice, N. A., Swaraj, S. & Lessard, B. H. Synthetically facile organic solar cells with >4% efficiency using P3HT and a silicon phthalocyanine non-fullerene acceptor. Mater. Adv. 2, 2594–2599 (2021).

39 Diao, Y., Shaw, L., Bao, Z. & Mannsfeld, S. C. B. Morphology control strategies for solution-processed organic semiconductor thin films. Energy Environ. Sci. 7, 2145–2159 (2014).

40 Lee, S. S. et al. Controlling Nucleation and Crystallization in Solution-Processed Organic Semiconductors for Thin-Film Transistors. Adv. Mater. 21, 3605–3609 (2009).

41 Lu, Z. et al. Meniscus-guided coating of organic crystalline thin films for high-performance organic field-effect transistors. J. Mater. Chem. C 8, 9133–9146 (2020).

42 Sunagawa, I. Crystals: Growth, Morphology, and Perfection. (Cambridge University Press, 2005).

43 Li, R. et al. Heterogeneous nucleation promotes carrier transport in solution-processed organic field-effect transistors. Adv. Funct. Mater. 23, 291–297 (2013).

44 Wedl, B. et al. Crystallisation kinetics in thin films of dihexyl-terthiophene: the appearance of polymorphic phases. RSC Adv. 2, 4404 (2012).

45 Kim, C. S., Lee, S., Gomez, E. D., Anthony, J. E. & Loo, Y.-L. Solvent-dependent electrical characteristics and stability of organic thin-film transistors with drop cast bis(triisopropylsilylethynyl) pentacene. Appl. Phys. Lett. 93, 103302 (2008).

46 Kaliyaraj Selva Kumar, A., Zhang, Y., Li, D. & Compton, R. G. A mini-review: How reliable is the drop casting technique? Electrochem. commun. 121, 106867 (2020).

47 Yang, X., Chhasatia, V. H., Shah, J. & Sun, Y. Coalescence, evaporation and particle deposition of consecutively printed colloidal drops. Soft Matter 8, 9205 (2012).

48 Yarin, A. L. DROP IMPACT DYNAMICS: Splashing, Spreading, Receding, Bouncing…. Annu. Rev. Fluid Mech. 38, 159–192 (2006).

49 Josserand, C. & Thoroddsen, S. T. Drop Impact on a Solid Surface. Annu. Rev. Fluid Mech. 48, 365–391 (2016).

50 Rein, M. Phenomena of liquid drop impact on solid and liquid surfaces. Fluid Dyn. Res. 12, 61–93 (1993).

51 Ohara, T., Matsumoto, Y. & Ohashi, H. The film formation dynamics in spin coating. Phys. Fluids A Fluid Dyn. 1, 1949–1959 (1989).

52 Norrman, K., Ghanbari-Siahkali, A. & Larsen, N. B. Studies of spin-coated polymer films. Annu. Reports Prog. Chem. - Sect. C 101, 174–201 (2005).

53 Schubert, D. W. & Dunkel, T. Spin coating from a molecular point of view: its concentration regimes, influence of molar mass and distribution. Mater. Res. Innov. 7, 314–321 (2003).

54 Sahu, N., Parija, B. & Panigrahi, S. Fundamental understanding and modeling of spin coating process: A review. Indian J. Phys. 83, 493–502 (2009).

55 Meyerhofer, D. Characteristics of resist films produced by spinning. J. Appl. Phys. 49, 3993–3997 (1978).

56 Lai, J. H. An investigation of spin coating of electron resists. Polym. Eng. Sci. 19, 1117–1121 (1979).

57 Chen, B. T. Investigation of the solvent-evaporation effect on spin coating of thin films. Polym. Eng. Sci. 23, 399–403 (1983).

58 Spangler, L. L., Torkelson, J. M. & Royal, J. S. Influence of solvent and molecular weight on thickness and surface topography of spin-coated polymer films. Polym. Eng. Sci. 30, 644–653 (1990).

59 Daughton, W. J. & Givens, F. L. An Investigation of the Thickness Variation of Spun-on Thin Films Commonly Associated with the Semiconductor Industry. J. Electrochem. Soc. 129, 173–179 (1982).

60 Wei Chou, K. et al. Late stage crystallization and healing during spin-coating enhance carrier transport in small-molecule organic semiconductors. J. Mater. Chem. C 2, 5681–5689 (2014).

61 Manley, E. F., Strzalka, J., Fauvell, T. J., Marks, T. J. & Chen, L. X. In Situ Analysis of Solvent and Additive Effects on Film Morphology Evolution in Spin-Cast Small-Molecule and Polymer Photovoltaic Materials. Adv. Energy Mater. 8, 1–20 (2018).

62 Janneck, R., Vercesi, F., Heremans, P., Genoe, J. & Rolin, C. Predictive Model for the Meniscus-Guided Coating of High-Quality Organic Single-Crystalline Thin Films. Adv. Mater. 28, 8007–8013 (2016).

63 Shaw, L. et al. Microstructural Evolution of the Thin Films of a Donor–Acceptor Semiconducting Polymer Deposited by Meniscus-Guided Coating. Macromolecules 51, 4325–4340 (2018).

64 Janneck, R., Karagiannis, D., Heremans, P., Genoe, J. & Rolin, C. Influence of Solute Concentration on Meniscus-Guided Coating of Highly Crystalline Organic Thin Films. Adv. Mater. Interfaces 6, 1900614 (2019).

65 Chen, M., Peng, B., Huang, S. & Chan, P. K. L. Understanding the Meniscus-Guided Coating Parameters in Organic Field-Effect-Transistor Fabrications. Adv. Funct. Mater. 30, 1–8 (2020).

66 Gojzewski, H., Ghani, F. & Szybowicz, M. Thin films of copper phthalocyanine deposited by solution processing methods. Mater. Sci. 38, 79–90 (2020).

67 Ghani, F., Gojzewski, H. & Riegler, H. Nucleation and growth of copper phthalocyanine aggregates deposited from solution on planar surfaces. Appl. Surf. Sci. 351, 969–976 (2015).

68 Ghani, F., Bochukov, I., Fostiropoulos, K. & Riegler, H. Hybrid solution/vacuum-processed bilayer heterojunction organic solar cells: Structural characterization and performance. Thin Solid Films 525, 177–181 (2012).

69 Lee, J.-H., Kim, S., Kim, H. & Lee, J. Solvent-dependent performance of

solution-processed small-molecule organic field-effect transistors. Org. Electron. 52, 184–189 (2018).

70 Kim, Y.-H., Lee, Y. U., Han, J.-I., Han, S.-M. & Han, M.-K. Influence of Solvent on the Film Morphology, Crystallinity and Electrical Characteristics of Triisopropylsilyl Pentacene OTFTs. J. Electrochem. Soc. 154, H995 (2007).

71 Rubinger, C. P. L. et al. Influence of solvent additives on the morphology and electrical properties of diF-TES ADT organic field-effect transistors. Org. Electron. 68, 205–211 (2019).

72 Gentry, K. P., Gredig, T. & Schuller, I. K. Asymmetric grain distribution in phthalocyanine thin films. Phys. Rev. B 80, 174118 (2009).

73 Yang, J. & Yan, D. Weak epitaxy growth of organic semiconductor thin films. Chem. Soc. Rev. 38, 2634 (2009).

74 Diao, Y. et al. Understanding Polymorphism in Organic Semiconductor Thin Films through Nanoconfinement. J. Am. Chem. Soc. 136, 17046–17057 (2014).

75 Hilfiker, R. & Raumer, M. von. Polymorphism in the Pharmaceutical Industry. (Wiley-VCH Verlag GmbH & Co. KGaA, 2018).

76 Chung, H. & Diao, Y. Polymorphism as an emerging design strategy for high performance organic electronics. J. Mater. Chem. C 4, 3915–3933 (2016).

77 Shaibat, M. A., Casabianca, L. B., Siberio-Pérez, D. Y., Matzger, A. J. & Ishii, Y. Distinguishing Polymorphs of the Semiconducting Pigment Copper Phthalocyanine by Solid-State NMR and Raman Spectroscopy. J. Phys. Chem. B 114, 4400–4406 (2010).

78 Miller, G. R. & Garroway, A. N. A Review of the Crystal Structures of Common Explosives Part 1: RDX, HMX, TNT, PETN, and Tetryl. Security 1–30 (2001).

79 Li, L. et al. Organic thin-film transistors of phthalocyanines. Pure Appl. Chem. 80, 2231–2240 (2008).

80 Achar, B. N. & Lokesh, K. S. Studies on polymorphic modifications of copper phthalocyanine. J. Solid State Chem. 177, 1987–1993 (2004).

81 Wihksne, K. & Newkirk, A. E. Electrical Conductivities of α- and β-Phthalocyanine. J. Chem. Phys. 34, 2184–2185 (1961).

82 Ai, X. et al. Phase modification of copper phthalocyanine semiconductor by converting powder to thin film. Appl. Surf. Sci. 428, 788–792 (2018).

83 Zou, T. et al. Controllable Molecular Packing Motif and Overlap Type in Organic Nanomaterials for Advanced Optical Properties. Crystals 8, 22 (2018).

84 Karan, S. & Mallik, B. Effects of annealing on the morphology and optical property of copper (II) phthalocyanine nanostructured thin films. Solid State Commun. 143, 289–294 (2007).

85 Szybowicz, M., Bała, W., Fabisiak, K., Paprocki, K. & Drozdowski, M. The molecular structure ordering and orientation of the metallophthalocyanine CoPc, ZnPc, CuPc, and MgPc thin layers deposited on silicon substrate, as studied by micro-Raman spectroscopy. J. Mater. Sci. 46, 6589–6595 (2011).

86 Hamm, F. A. & Van Norman, E. Transformations in Organic Pigments. J. Appl. Phys. 19, 1097–1109 (1948).

87 Senthilarasu, S., Hahn, Y. B. & Lee, S.-H. Structural analysis of zinc phthalocyanine (ZnPc) thin films: X-ray diffraction study. J. Appl. Phys. 102, 043512 (2007).

88 Louis, J. S., Lehmann, D., Friedrich, M. & Zahn, D. R. T. Study of dependence of molecular orientation and optical properties of zinc phthalocyanine grown under two different pressure conditions. J. Appl. Phys. 101, 013503 (2007).

89 Gaffo, L. et al. The effects of temperature on the molecular orientation of zinc phthalocyanine films. J. Mater. Sci. 45, 1366–1370 (2010).

90 Senthilarasu, S., Sathyamoorthy, R. & Kulkarni, S. K. Substrate temperature effects on structural orientations and optical properties of ZincPthalocyanine (ZnPc) thin films. Mater. Sci. Eng. B 122, 100–105 (2005).

91 Chowdhury, A., Biswas, B., Majumder, M., Sanyal, M. K. & Mallik, B. Studies on phase transformation and molecular orientation in nanostructured zinc phthalocyanine thin films annealed at different temperatures. Thin Solid Films 520, 6695–6704 (2012).

92 Ebert, A. A. & Gottlieb, H. B. Infrared Spectra of Organic Compounds Exhibiting Polymorphism. J. Am. Chem. Soc. 74, 2806–2810 (1952).

93 Yoon, Y. et al. Surface-guided polymorphism control of titanyl phthalocyanine single crystals. Inorg. Chem. Front. 7, 2178–2187 (2020).

94 Schoch, K. F., Greggi, J. & Temofonte, T. A. Morphology of metal phthalocyanine thin films. J. Vac. Sci. Technol. A Vacuum, Surfaces, Film. 6, 155–158 (1988).

95 Hassan, A. K. & Gould, R. D. Structural Studies of Thermally Evaporated Thin Films of Copper Phthalocyanine. Phys. Status Solidi 132, 91–101 (1992).

96 Iwatsu, F., Kobayashi, T. & Uyeda, N. Solvent effects on crystal growth and transformation of zinc phthalocyanine. J. Phys. Chem. 84, 3223–3230 (1980).

97 Iwatsu, F. Crystal Behaviour of Zinc Phthalocyanine Films in Alcohols. J. Cryst. Growth 71, 629–638 (1985).

98 Iwatsu, F. Size effects on the alpha-beta transformation of phthalocyanine crystals. J. Phys. Chem. 92, 1678–1681 (1988).

99 Robertson, M. An X-Ray Study of the Structure of the Phthalocyanines. Part I The Metal-free, Nickel, Copper, and Platinum Compounds. J. Chem. Soc. 1, 615 (1934).

100 Robsinson, M. T. & Klein, G. E. Unit Cell Constants of α-Copper Phthalocyanine. J. Am. Chem. Soc. 74, 6294 (1952).

101 Assour, J. M. On the Polymorphic Modifications of Phthalocyanines. J. Phys. Chem. 69, 2295–2299 (1965).

102 Xiao, K. et al. Metastable copper-phthalocyanine single-crystal nanowires and their use in fabricating high-performance field-effect transistors. Adv. Funct. Mater. 19, 3776–3780 (2009).

103 Popielarski, P. et al. Admittance spectroscopy of CuPC-Si and CoPC-Si heterostructures. Electrochim. Acta 104, 496–504 (2013).

104 Defeyt, C. et al. Contribution to the identification of α-, β- And μ-copper phthalocyanine blue pigments in modern artists' paints by X-ray powder diffraction, attenuated total reflectance micro-fourier transform infrared spectroscopy and micro-Raman

spectroscopy. J. Raman Spectrosc. 43, 1772–1780 (2012).

105 Boileau, N. T., Cranston, R., Mirka, B., Melville, O. A. & Lessard, B. H. Metal phthalocyanine organic thin-film transistors: changes in electrical performance and stability in response to temperature and environment. RSC Adv. 9, 21478–21485 (2019).

106 Hussein, M. T., Aadim, K. A. & Hassan, E. K. Structural and Surface Morphology Analysis of Copper Phthalocyanine Thin Film Prepared by Pulsed Laser Deposition and Thermal Evaporation Techniques. Adv. Mater. Phys. Chem. 06, 85–97 (2016).

107 Rani, V., Sharma, A., Kumar, P., Singh, B. & Ghosh, S. Charge transport mechanism in copper phthalocyanine thin films with and without traps. RSC Adv. 7, 54911–54919 (2017).

108 Bao, B. Z. & Lovinger, A. J. Highly Ordered Vacuum-Deposited Thin Films of Metallophthalocyanines and Their Applications in Field-Effect Transistor. Adv. Mater. 9, 42–44 (1997).

109 Li, L., Tang, Q., Li, H. & Hu, W. Molecular Orientation and Interface Compatibility for High Performance Organic Thin Film Transistor Based on Vanadyl Phthalocyanine. J. Phys. Chem. B 112, 10405–10410 (2008).

110 Vasseur, K., Rand, B. P., Cheyns, D., Froyen, L. & Heremans, P. Structural evolution of evaporated lead phthalocyanine thin films for near-infrared sensitive solar cells. Chem. Mater. 23, 886–895 (2011).

111 Madhuri, K. P., Santra, P. K., Bertram, F. & John, N. S. Current mapping of lead phthalocyanine thin films in the presence of gaseous dopants. Phys. Chem. Chem. Phys. 21, 22955–22965 (2019).

112 Liu, T. J. et al. Thin-film growth behavior of non-planar vanadium oxide phthalocyanine. Chinese Phys. B 28, 4–11 (2019).

113 Melville, O. A. et al. Ambipolarity and Air Stability of Silicon Phthalocyanine Organic Thin-Film Transistors. Adv. Electron. Mater. 5, 1900087 (2019).

114 Virkar, A. A., Mannsfeld, S., Bao, Z. & Stingelin, N. Organic Semiconductor Growth and Morphology Considerations for Organic Thin-Film Transistors. Adv. Mater. 22, 3857–3875 (2010).

115 Locklin, J., Roberts, M. E., Mannsfeld, S. C. B. & Bao, Z. Optimizing the Thin Film Morphology of Organic Field-Effect Transistors: The Influence of Molecular Structure and Vacuum Deposition Parameters on Device Performance. J. Macromol. Sci. Part C Polym. Rev. 46, 79–101 (2006).

116 Katz, H. E. & Bao, Z. The Physical Chemistry of Organic Field-Effect Transistors. J. Phys. Chem. B 104, 671–678 (2000).

117 Silva Sousa, D. F., Rosso Dotto, M. E., Eccher, J., Bock, H. & Bechtold, I. H. Blending with a phthalocyanine leads to improved P3HT donor layers for OPVs. Synth. Met. 263, 116367 (2020).

118 Kato, M. et al. Morphological and optical properties of α- and β-phase zinc (‖) phthalocyanine thin films for application to organic photovoltaic cells. J. Chem. Phys. 153, 144704 (2020).

119 Liu, F. et al. Characterization of the morphology of solution-processed bulk heterojunction organic photovoltaics. Prog. Polym. Sci. 38, 1990–2052 (2013).

120 Tadayyon, S. M. et al. CuPc buffer layer role in OLED performance: A study of

the interfacial band energies. Org. Electron. 5, 157–166 (2004).

121 Cosseddu, P., Tiddia, G., Milita, S. & Bonfiglio, A. Continuous tuning of the mechanical sensitivity of Pentacene OTFTs on flexible substrates: From strain sensors to deformable transistors. Org. Electron. 14, 206–211 (2013).

122 Chortos, A. et al. Highly Stretchable Transistors Using a Microcracked Organic Semiconductor. Adv. Mater. 26, 4253–4259 (2014).

123 Cosseddu, P., Milita, S. & Bonfiglio, A. Strain sensitivity and transport properties in organic field-effect transistors. IEEE Electron Device Lett. 33, 113–115 (2012).

124 Lai, S. et al. Morphology Influence on the Mechanical Stress Response in Bendable Organic Field-Effect Transistors with Solution-Processed Semiconductors. Adv. Electron. Mater. 4, 1–9 (2018).

125 Voigtländer, B. Atomic Force Microscopy. (Springer International Publishing, 2019).

126 Haugstad, G. Atomic Force Microscopy: Understanding Basic Modes and Advanced Applications. (John Wiley & Sons, Ltd, 2012).

127 Tackley, D. R., Dent, G. & Ewen Smith, W. Phthalocyanines: structure and vibrations. Phys. Chem. Chem. Phys. 3, 1419–1426 (2001).

128 Klyamer, D. D., Basova, T. V., Krasnov, P. O. & Sukhikh, A. S. Effect of fluorosubstitution and central metals on the molecular structure and vibrational spectra of metal phthalocyanines. J. Mol. Struct. 1189, 73–80 (2019).

129 Liu, Z., Zhang, X., Zhang, Y. & Jiang, J. Theoretical investigation of the molecular, electronic structures and vibrational spectra of a series of first transition metal phthalocyanines. Spectrochim. Acta - Part A Mol. Biomol. Spectrosc. 67, 1232–1246 (2007).

130 Szybowicz, M. & Makowiecki, J. Orientation study of iron phthalocyanine (FePc) thin films deposited on silicon substrate investigated by atomic force microscopy and micro-Raman spectroscopy. J. Mater. Sci. 47, 1522–1530 (2012).

131 Zhang, Y., Zhang, X., Liu, Z., Xu, H. & Jiang, J. Comparative density functional theory study of the structures and properties of metallophthalocyanines of group IV B. Vib. Spectrosc. 40, 289–298 (2006).

132 Zhang, X., Lin, W., Zhao, H. & Wang, R. Raman spectra study of p -tert-butylphenoxy-substituted phthalocyanines with different central metal and substitution positions. Vib. Spectrosc. 96, 26–31 (2018).

133 Jiang, J., Bao, M., Rintoul, L. & Arnold, D. P. Vibrational spectroscopy of phthalocyanine and naphthalocyanine in sandwich-type (na)phthalocyaninato and porphyrinato rare earth complexes. Coord. Chem. Rev. 250, 424–448 (2006).

134 Abe, M., Kitagawa, T. & Kyogoku, Y. Resonance Raman spectra of octaethylporphyrinato-Ni(II) and meso-deuterated and 15 N substituted derivatives. II. A normal coordinate analysis. J. Chem. Phys. 69, 4526–4534 (1978).

135 Szybowicz, M. et al. High temperature study of FT-IR and Raman scattering spectra of vacuum deposited CuPc thin films. J. Mol. Struct. 704, 107–113 (2004).

136 Pandey, A., Dalal, S., Dutta, S. & Dixit, A. Structural characterization of polycrystalline thin films by X-ray diffraction techniques. J. Mater. Sci. Mater. Electron. 32, 1341–1368 (2021).

137 Widjonarko, N. Introduction to Advanced X-ray Diffraction Techniques for Polymeric Thin Films. Coatings 6, 54 (2016).

138 Birkholz, M. Thin Film Analysis by X-Ray Scattering. (John Wiley & Sons, Ltd, 2006).

139 Rivnay, J., Mannsfeld, S. C. B., Miller, C. E., Salleo, A. & Toney, M. F. Quantitative Determination of Organic Semiconductor Microstructure from the Molecular to Device Scale. Chem. Rev. 112, 5488–5519 (2012).

Chapter 2. Thin-Film Engineering of Solution Processable N-Type Silicon Phthalocyanines for OTFTs

This chapter is adapted from: ***Cranston, R. R.****, Vebber, M. C., Berbigier, J. F., Rice, N. A., Tonnelé, C., Comeau, Z. J., Boileau, N. T., Brusso, J. L., Shuhendler, A. J., Castet, F., Muccioli, L., Kelly, T. L., Lessard, B. H. Thin-Film Engineering of Solution-Processable n-Type Silicon Phthalocyanines for Organic Thin-Film Transistors. ACS Appl. Mater. Interfaces 13, 1008-1020 (2021).*

Context

During the first phase of my graduate studies, I expanded the protocols and procedures for the fabrication of small molecule MPc based OTFTs by solution processes. Previously in our research group, MPc OTFTs were fabricated primarily by physical vapour deposition. I implemented a range of newly synthesized soluble SiPc derivatives as the active layer in bottom-gate top-contact OTFTs and characterized the electrical performance in relation to molecular design and fabrication parameters. As discussed in **Chapter 1**, the inclusion of alkyl chains to the axial position of the SiPc molecule can be used to increase the solubility of a material to enhance compatibility with solution deposition techniques. Using eight SiPc derivatives, the influence of alkyl chain length, symmetry, and branching position was studied, establishing a structure-property-performance relationship. Additionally, key fabrication parameters including deposition time and post deposition thermal annealing were analyzed and optimized for device performance. This work demonstrated that SiPc OTFTs fabricated from solution processes can achieve promising device performance and served as the foundation for my future projects.

Contributions of Authors

This work was completed through contributions of all authors. For this work, I fabricated and characterized all OTFTs, conducted XRD experiments, preformed all data analysis and wrote the manuscript. M.C.V. synthesized all $(OR)_2$-SiPc materials, and obtained thermal characteristics, DSC data, and TGA data. J.F.B conducted GIWAXS experiments with analysis. C.T and L.M. conducted DFT calculations with analysis. N.A.R conducted AFM imaging. Z.J.C assisted with XRD experiments. N.T.B assisted with OTFT characterization. A.J.S., F.C., T.K., J.B., and B.H.L., provided supervision for the project.

Abstract

Metal and metalloid phthalocyanines are an abundant and established class of materials widely used in the dye and pigment industry as well as in commercial photoreceptors. Silicon phthalocyanines (SiPcs) are among the highest performing n-type semiconductor materials in this family when used in organic thin-film transistors (OTFTs) as their performance and solid-state arrangement is often increased through axial substitution. Herein, we study eight axially substituted SiPcs and their integration into solution processed n-type OTFTs. Electrical characterization of the OTFTs, combined with atomic force microscopy (AFM), determined that the length of the alkyl chain affects device performance and thin-film morphology. The effects of high temperature annealing and spin coating time on film formation, two key processing steps for fabrication of OTFTs, were investigated by grazing-incidence wide-angle X-ray scattering (GIWAXS) and X-ray diffraction (XRD) to elucidate the relationship between thin-film microstructure and device performance. Thermal annealing was shown to change both film crystallinity and SiPc molecular orientation relative to the substrate surface. Spin time affected film crystallinity, morphology, and interplanar d-spacing, and thus ultimately modifying device performance. Of the eight materials studied, bis(tri-*n*-butylsilyl oxide) SiPc exhibited the greatest electron field-effect mobility (0.028 $cm^2\ V^{-1}\ s^{-1}$, threshold voltage of 17.6 V) of all reported solution processed SiPc derivatives.

Introduction

Organic thin-film transistors (OTFTs) have been used in applications such as chemical and biological sensors,[1,2] wearable electronics,[3] and flexible displays.[4,5] A primary advantage of organic semiconductors is that inexpensive solution based processing techniques such as inkjet printing and spin coating can be used for low-cost, large area manufacturing.[6–9] High performing solution processable p-type polymeric and small molecule semiconductors have been studied in OTFTs, with reported hole mobilities (μ_h) in excess of 5 $cm^2\ V^{-1}\ s^{-1}$.[10–12] Conversely, n-type semiconductors are often air sensitive and insoluble, rendering them incompatible with high throughput and low-cost solution processing techniques.[13] To achieve high mobility solution processable transistors, non-conjugated side chains must be engineered to simultaneously increase solubility while providing close intermolecular packing, facilitating the formation of highly crystalline thin-films.[14–16] Substituted alkyl chains have previously been reported to increase the solution processability of both p-type conjugated polymer[14,17,18] and small molecule[6,19,20] semiconductors. Changes in thin-film morphology, which often result in related electrical performance changes in OTFTs, have been attributed to alkyl chain length, branching point, chain flexibility, and chain position.[16]

Metal and metalloid containing phthalocyanines (MPcs) are a versatile family of small molecule semiconductors with favourable chemical, thermal, and opto-electronic properties.[21] Silicon phthalocyanines (SiPcs) have recently attracted significant interest due to their ease of synthesis and chemical tunability, leading to their integration into optoelectronic devices,[22–24] but also in more exotic applications such as photodynamic therapy,[25,26] or near infrared photo polymerization.[27,28] By exploiting axial substituents which can change solid state organization, SiPcs have recently demonstrated μ_e of 0.54 cm^2 V^{-1} s^{-1} in OTFTs, which is among the best reported performance for all MPc semiconductors.[29–31] Axial substituents can be used to change the solubility, crystal structure, and the energy of crystallization of a material, thus affecting thin-film formation and morphology. Recently, by taking advantage of these axial substituents, we developed solution processable bis(tri-*n*-hexylsilyl oxide) SiPc and bis(tri-*n*-butylsilyl oxide) SiPc based n-type transistors.[32]

Among processing methods, spin coating is a widely used lab scale technique for the deposition of thin organic semiconductor films on flat substrates. Thin-film formation via spin coating occurs as the residual solvent evaporates, in the optimal case driving and leading to crystal nucleation and formation.[33] The effectiveness of spin coating is largely dependent on the crystallization kinetics of the semiconductor and the employed fabrication conditions.[33,34] Compared to lengthy evaporative methods, such as physical vapour deposition, this process occurs in seconds as the solvent is ejected from the film at high rotational speeds and can be applied to a wider range of materials, including polymers.[33] However, due to the rapid rate of film crystallization, consistent film morphology, uniform grain sizes, and edge-on molecular orientation can be difficult to achieve.[7] Fabrication parameters such as solvent viscosity, spin speed, and annealing time and temperature also affect the morphology, packing, and crystallinity of spin coated thin-films.[6,33] Chou et al., found that when processing 6,13-bis(triisopropylsilylethynyl)-pentacene semiconductor solutions, slower spin speeds increase solvent evaporation time, which led to increased film crystallinity and improved μ_h.[33] Additionally, Zhang et al., reported how thermal annealing can tune the grain size of branched alkyl chain naphthalene diimides fused with 2-(1,3-dithiol-2-ylidene)malononitrile groups to achieve a higher μ_h.[6] It is therefore critical to study the effect of processing on film formation and to be cognizant that even small changes in molecular structure can have significant effects on final device performance.

Herein, the characterization of six axially-substituted bis(tri-alkylsilyl oxide) SiPcs are reported in bottom-gate top-contact solution processed OTFTs; previously studied bis(tri-*n*-hexylsilyl oxide) SiPc and bis(tri-*n*-butylsilyl oxide) SiPc are also included for comparison (**Figure 2.1**). The semiconducting properties of each material were evaluated by the crystal structures through density functional theory (DFT) calculations and in thin films by experimental electrical characterization of transistors. The effects of processing and molecular structure were elucidated through post-deposition characterization by atomic force microscopy (AFM), grazing-incidence wide-angle X-ray scattering (GIWAXS) and X-ray diffraction (XRD). The findings of this study will be critical in the development of MPc-based solution-processable OTFTs.

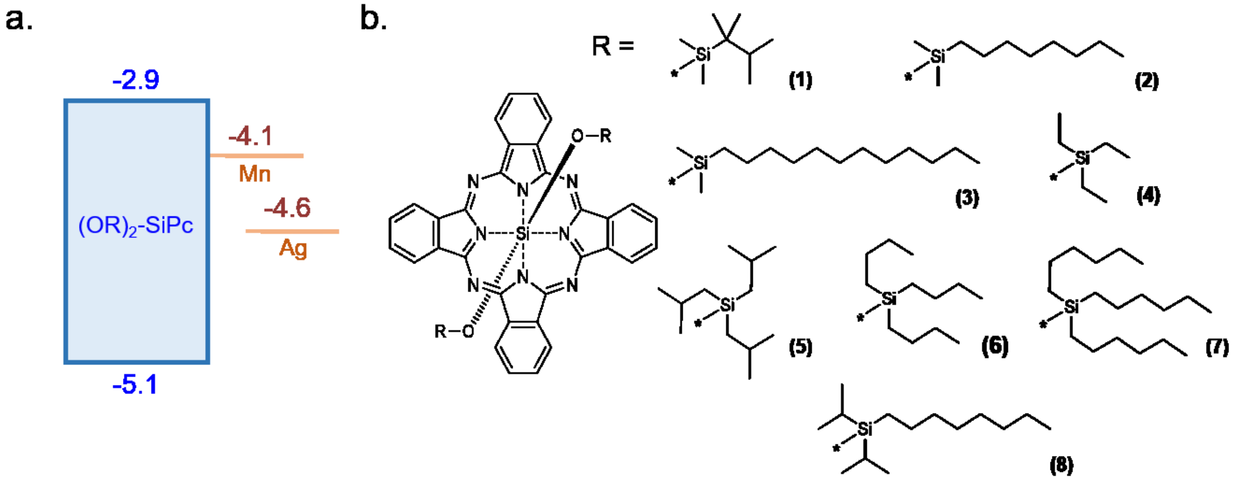

Figure 2.1. (a) Energy level diagram of $(OR)_2$-SiPc, manganese (Mn), and silver (Ag). (b) Structure of $(OR)_2$-SiPc with axial groups used in this study. Energy levels of Mn and Ag reported in reference 35.

Results and Discussion

Quantum Chemical Calculations

DFT calculations were performed at the B3LYP/6-31G(d) level to determine energy levels and charge transport parameters of each material. **Table 2.1** collects the HOMO, LUMO, and LUMO+1 energies, along with the electron affinities (*EA*s), TD-DFT transition energies and oscillator strengths towards the two nearly-degenerate singlet excited states S_1 and S_2, and charge transfer internal reorganization energies (λ) calculated for the eight phthalocyanine molecules. The *EA*s calculated in the gas phase lie in the range of 1.93-2.07 eV, with a weak dependence on the chemical nature of the axial substituents. Note that theoretical values systematically underestimate compared to experimental ones obtained from measurements on thin films, in which local charges are stabilized by the polarizable environment.[36] LUMO and LUMO+1 energies, as well as the S_1 and S_2 excited states are expected to be degenerate for unsubstituted MPcs[37] or substituted $(OR)_2$-MPcs with a centrosymmetric structure. In crystalline environments, geometrical distortions due to intermolecular interactions and positioning of the axial substituents reduce the symmetry of the wave function and partially lift the degeneracy of the two LUMOs. However, the two levels remain very close and can both contribute to electron transport, in practice doubling the number of available pathways. Moreover, internal reorganization energy values for the bimolecular electron transfer process $MPc^- + MPc \rightarrow MPc + MPc^-$ are rather favorable (the lower the better, see rate **Equation 2.6**), with values particularly low for small-sized molecules, and only 50-100 meV higher than those of typical fullerene and non-fullerene acceptors with much larger aromatic cores.[38]

Table 2.1. DFT energy values of the HOMO, LUMO, LUMO+1, electron affinity (*EA*, obtained from differences in the total energies of the charged and neutral molecules in their optimized geometries), internal reorganization energies (λ) and TD-DFT vertical transition energies (ΔE_{01} and ΔE_{02}), and oscillator strengths (f_{01} and f_{02}) from the ground state S_0 towards the nearly-degenerate singlet states S_1 and S_2, calculated at the B3LYP/6-31G(d) level. All energy values are in eV.

Material	E_{HOMO}	E_{LUMO}	E_{LUMO+1}	EA	ΔE_{01} (f_{01})	ΔE_{02} (f_{02})	λ
1	-5.08	-2.88	-2.88	1.94	2.07 (0.35)	2.07 (0.35)	0.215
2	-5.06	-2.87	-2.86	1.94	2.07 (0.36)	2.07 (0.35)	0.251
3	-5.06	-2.87	-2.86	1.94	2.07 (0.36)	2.07 (0.35)	0.254
4	-5.07	-2.87	-2.87	1.93	2.06 (0.35)	2.07 (0.35)	0.213
5	-5.12	-2.94	-2.93	2.02	2.05 (0.33)	2.06 (0.32)	0.221
6	-5.12	-2.93	-2.92	2.03	2.05 (0.35)	2.06 (0.34)	0.241
7	-5.14	-2.95	-2.94	2.07	2.05 (0.36)	2.06 (0.34)	0.266
8	-5.09	-2.90	-2.90	1.98	2.06 (0.33)	2.06 (0.33)	0.213

Figure 2.2 depicts the top views of the molecular dimers giving rise to the largest electronic couplings (J_k), again calculated with DFT utilizing the experimental crystal structures. Single crystals of **1-5** and **8** were obtained as outlined in the Experimental section and their structures

successfully determined through single crystal XRD as shown in **Figure S2.1**. Numerical values of the main transfer integrals are collected in **Table S2.1** for all crystals. The electron mobilities, which depend on the square of the couplings (**Equation 2.6**), were estimated for each material in the hopping transport regime and the ideal case of zero energetic disorder along each crystallographic axis, and reported in **Table 2.2** together with the qualitative estimate of the dimensionality of transport. These values correspond to the maximum mobility achievable for a defect-free single crystal, and thus an upper limit to experimentally measured mobilities. All compounds show as expected[39] mainly 1D or partial 2D transport and in principle could exhibit decent mobilities in crystal phase, with **2**, **3**, and **6** showing the most encouraging results, because of the larger electronic coupling (**Figure 2.2**). Conversely, **7**, **4**, and **8** show less promise than the others.

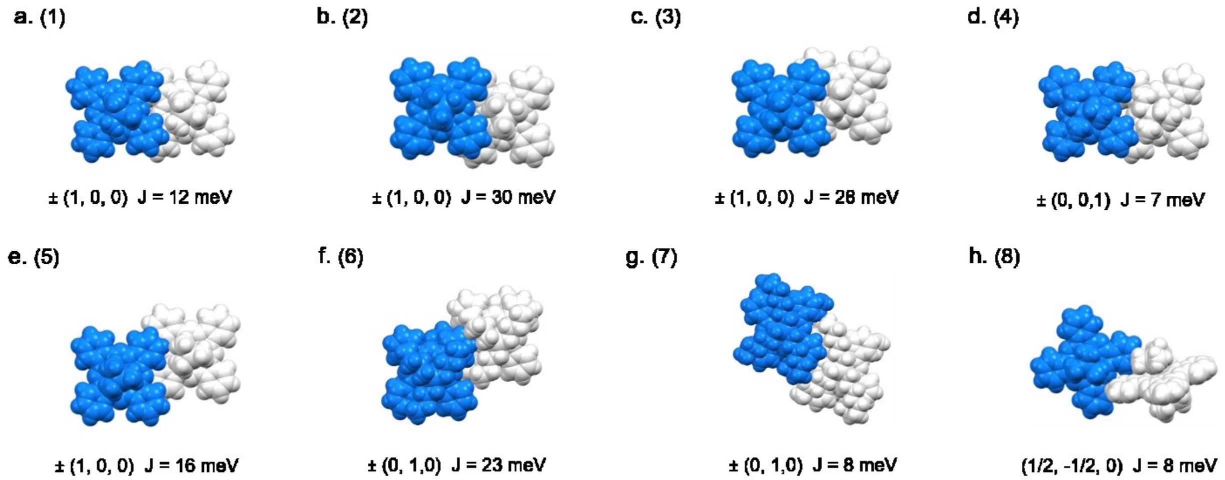

Figure 2.2. Top views of the molecular dimers giving rise to the largest electronic couplings for materials **1-8** (a-h), as extracted from periodic replicas of experimental crystal structures. In all structures, axial groups have been truncated to trimethyl silyl oxide for clarity.

Table 2.2. Computed electron mobilities along the crystal axes (μ_i with i = a, b, c; see Equation 2.6) in the eight phthalocyanine crystals, average mobility ($\mu_{e,avg} = (\mu_a + \mu_b + \mu_c) / 3$), and dimensionality (D) of the electron transport (ref 38).

Material	μ_a (cm^2 V^{-1} s^{-1})	μ_b (cm^2 V^{-1} s^{-1})	μ_c (cm^2 V^{-1} s^{-1})	$\mu_{e,\ avg}$ (cm^2 V^{-1} s^{-1})	D
1	0.300	0.112	0.034	0.149	2D
2	1.049	0.101	0.070	0.407	1D
3	0.914	0.115	0.009	0.346	1D
4	0.022	0.059	0.127	0.069	2D
5	0.532	0.030	0.029	0.197	1D
6	0.051	0.811	0.100	0.321	1D
7	0.012	0.092	0.054	0.053	2D
8	0.188	0.070	0.008	0.088	2D

Organic Thin-Film Transistor Performance

The eight axially substituted $(OR)_2$-SiPcs described in **Figure 2.1** were used as the semiconductor in bottom-gate top-contact OTFTs. N-doped silicon wafers with a thermally grown silicon oxide dielectric layer were treated with trichloro(octyl)silane (OTS) to form an ordered monolayer surface to improve thin-film formation.[29] The semiconducting layer was deposited by spin coating SiPc chloroform solutions on OTS treated wafers, followed by annealing at room temperature in air or at 100°C under vacuum for 1 hr. Characterization was performed in nitrogen at atmospheric pressure, to determine the saturation regime electron field-effect mobility (μ_e) by **Equation 2.2**, threshold voltage (V_T), and on/off current ratio ($I_{on/off}$). **Figure 2.3** shows a characteristic transfer curve for each material that exhibits semiconducting characteristics in devices, alongside a diagram of the bottom-gate top-contact OTFT architecture used in this work. Characteristic output curves, and the forward and reverse transfer curves of all functional materials are displayed in **Figures S2.2** and **Figure S2.3**, respectively.

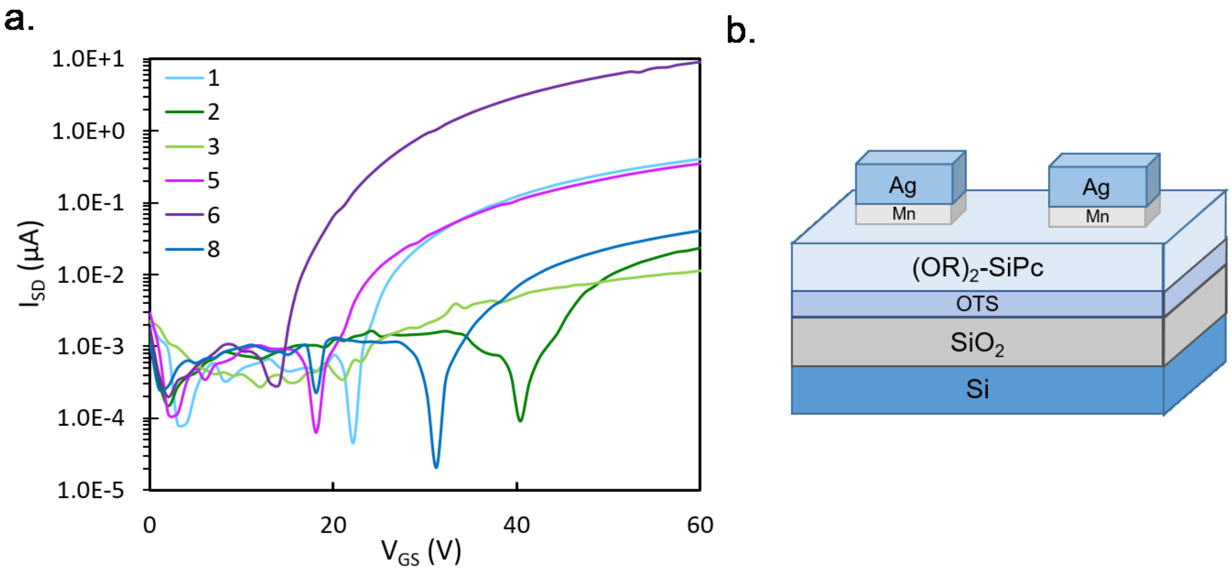

Figure 2.3. (a) Characteristic transfer curves of $(OR)_2$-SiPc transistors characterized at room temperature in nitrogen. $(OR)_2$-SiPc films were spun from chloroform at 1500 RPM for 90 sec and annealed at 100°C under vacuum for 1 hr. (b) Schematic diagram of bottom-gate top-contact OTFT architecture used in this study. **4** and **7** were found to be non-functional and are therefore excluded.

Electrical characteristics of each material for both annealing conditions are summarized in **Table 2.3**. **6** was found to have the highest $\mu_{e,\ avg}$ for both annealing at 25°C and under vacuum at 100°C of 7.3 x 10^{-3} $cm^2\ V^{-1}\ s^{-1}$ and 2.8 x 10^{-2} $cm^2\ V^{-1}\ s^{-1}$, respectively. **6** also displayed the third lowest V_T of 32.6 V before annealing and the second lowest (17.6 V) after annealing at 100°C. **4** and **7** were found to be non-functional as semiconductors in OTFTs with the fabrication conditions utilized in this study, as they did not exhibit semiconducting characteristics and therefore resulted in non-functional devices. This result is not completely unexpected given the low transfer integral values and correspondingly low calculated mobilities for these compounds (see **Table 2.2** and **Figure 2.2**). In literature, **7** was shown to be functional in bottom-gate bottom-contact OTFTs fabricated by drop-casting and characterized using the same conditions, with an average μ_e of 7.3 x 10^{-6} $cm^2\ V^{-1}\ s^{-1}$.[32] In the same work, OTFTs made with **6** resulted in an average μ_e of 5.6 x 10^{-5} $cm^2\ V^{-1}\ s^{-1}$, three orders of magnitude lower than the value obtained in the present study (2.8 x 10^{-2} $cm^2\ V^{-1}\ s^{-1}$). These variations in electrical performance are unsurprising due to the differences in transistor architecture and semiconductor deposition, emphasizing the importance of optimization of fabrication conditions on the electrical performance of solution processable small molecule OTFTs.

Table 2.3. Summary of $(OR)_2$-SiPc transistor characteristics, measured at room temperature in nitrogen atmosphere. Averages were calculated from forty unique transistors.

Material	Annealing Temp (°C)	$\mu_{e,\,max}$ (x 10^{-2} cm^2 V^{-1}s^{-1})	$\mu_{e,\,avg}$ (x 10^{-2} cm^2 V^{-1} s^{-1})	V_T (V)	$I_{on/off}$
1	25	0.208	0.137 ± 0.044	27.3 ± 1.6	10^4
	100	0.247	0.175 ± 0.025	24.9 ± 2.0	10^3
2	25	0.0322	0.0171 ± 0.0079	43.1 ± 1.2	10^2
	100	0.0321	0.0151 ± 0.014	42.4 ± 9.4	10^3
3	25	0.0300	0.0256 ± 0.0049	38.8 ± 0.3	10^2
	100	0.00320	0.00210 ± 0.00038	35.7 ± 10.4	10^2
4	25	-[a]	-[a]	-[a]	-[a]
	100	-[a]	-[a]	-[a]	-[a]
5	25	0.141	0.0820 ± 0.021	22.8 ± 2.4	10^4
	100	0.202	0.163 ± 0.023	16.8 ± 2.4	10^4
6	25	0.888	0.734 ± 0.094	32.6 ± 3.5	10^5
	100	4.34	2.80 ± 0.53	17.6 ± 2.3	10^5
7	25	-[a]	-[a]	-[a]	-[a]
	100	-[a]	-[a]	-[a]	-[a]
8	25	0.0405	0.0284 ± 0.0091	39.1 ± 0.8	10^3
	100	0.0356	0.0111 ± 0.0023	30.6 ± 8.2	10^3

a. non-functional device

As shown in **Table 2.3**, annealing at 100°C had little effect on the electrical characteristics of most of the SiPc transistors. For **1**, **2**, **5**, and **8**, the changes in μ_e and V_T are within the standard deviation and therefore no significant change in performance is correlated to annealing. However, for **6** the V_T decreased significantly by 15 V, with a μ_e increase of 2.1 x 10^{-2} cm^2 V^{-1} s^{-1} after annealing. Interestingly, annealing at 100˚C resulted in an order of magnitude decrease (4.6 x 10^{-5} cm^2 V^{-1} s^{-1}) in μ_e for **3**. AFM images of **3** and **6** before and after annealing are shown in **Figure S2.4**. Annealing **6** resulted in a more homogenous thin-film morphology compared to the non-annealed films, which could account for the observed increase in device performance. The effect of thermal annealing on **6** is further discussed in an upcoming section. After annealing, **3** exhibited a drastic morphology change with much larger plate-like features, potentially due to the exceptionally low crystallization temperature (89°C reported in **Table S2.2**). These large features are typically ideal for charge transport;[6,7] however, the formation of large grain boundaries could in turn increase charge trapping, resulting in a lower μ_e.[40–42] Thermogravimetric analysis (TGA) and differential scanning calorimetry (DSC) was run on all $(OR)_2$-SiPc derivatives (**Figure S2.5** and **Figure S2.6**). Melting and crystallization temperatures are reported in **Table S2.2**, and range from 61-231°C and 60-219°C, respectively. Due to the low melting temperature of the $(OR)_2$-SiPc derivatives, these materials are incompatible with physical vapour deposition (PVD) fabrication. Additionally, ultraviolet-visible spectroscopy (UV-vis) was performed on $(OR)_2$-SiPc thin-films and compared to the solution spectra[43] with results shown in **Figure S2.7** and **Table S2.3**. All $(OR)_2$-SiPcs, with the exception of **7**, exhibited significant red shifts of 16.9-30.5 nm, indicating a shift via J-type aggregation in thin-films.

Thin-film Morphology

AFM was performed to correlate the effects of SiPc molecular structure, and corresponding thin-film morphology, to OTFT performance, with results displayed in **Figure 2.4** and **Figure S2.8**. Of the best performing semiconductors (**1**, **5**, and **6**), **1** and **6** show well-ordered homogenous film morphology with small cylindrical features. **5** exhibits larger interconnected features with more distinct grain boundaries compared to **6**. The elongated features and more densely packed films of these materials likely contribute to the high μ_e exhibited in OTFTs. Of the worse performing materials (**2**, **3**, and **8**), **2** and **8** have a similar film morphology with small point-like features. Although these materials make homogenous films, they exhibit a much lower μ_e of 1.5 x 10^{-4} cm^2 V^{-1} s^{-1} and 1.1 x 10^{-4} cm^2 V^{-1} s^{-1}, and the two highest V_T of 42.4 V and 30.6 V, respectively. The spotted point-like features may represent more grain boundaries and increase charge trapping. As already mentioned, **3** has a unique morphology with very large plate-like features and large grain boundaries. These large grain boundaries have been shown to reduce charge carrier μ_e and result in worse electrical performance in OTFTs.[40–42,44] Accordingly, **3** shows the lowest μ_e of 2.1 x 10^{-5} cm^2 V^{-1} s^{-1} and on/off current ratio of 10^2 as seen by the transfer curve in **Figure 2.3**. **4** and **7** resulted in films with the largest height differences (**Figure 2.4**) and poor grain interconnectivity, which corresponds to non-functional OTFTs.

As shown by **Figure 2.4**, the nature of the axial substituents greatly affects thin-film morphology, directly impacting transistor performance. The worst performing semiconductors (**2**, **3**, and **8**) have a longer alkyl chain, resulting in highly asymmetric axial substituents. These long chains may hinder molecular packing and subsequently charge transfer yielding poor semiconducting performance characteristics (**Table 2.3**). The importance of molecular packing and thin-film formation on device performance is highlighted through material **2**. From DFT calculations (**Table 2.2**), **2** exhibited the highest calculated $\mu_{e,\ avg}$, however displayed low μ_e and high threshold voltage in OTFTs, likely due to thin-film characteristics and morphology. Of the best performing semiconductors (**1**, **5**, and **6**), **1** and **5** have axial substituents with asymmetric short branched chains, whereas **6** has symmetric trialkyl linear chains six carbons in length. Since **6** exhibited the highest μ_e in OTFTs, this may suggest an optimum median chain length for linear trialkyl substituents which promotes molecular packing. The other symmetric trialkyl materials (**4** and **7**) were non-functional as semiconductors. Materials **4** and **7** may have been non-functional due to the length of their alkyl chains, resulting in poor crystal growth and non-uniform morphologies.

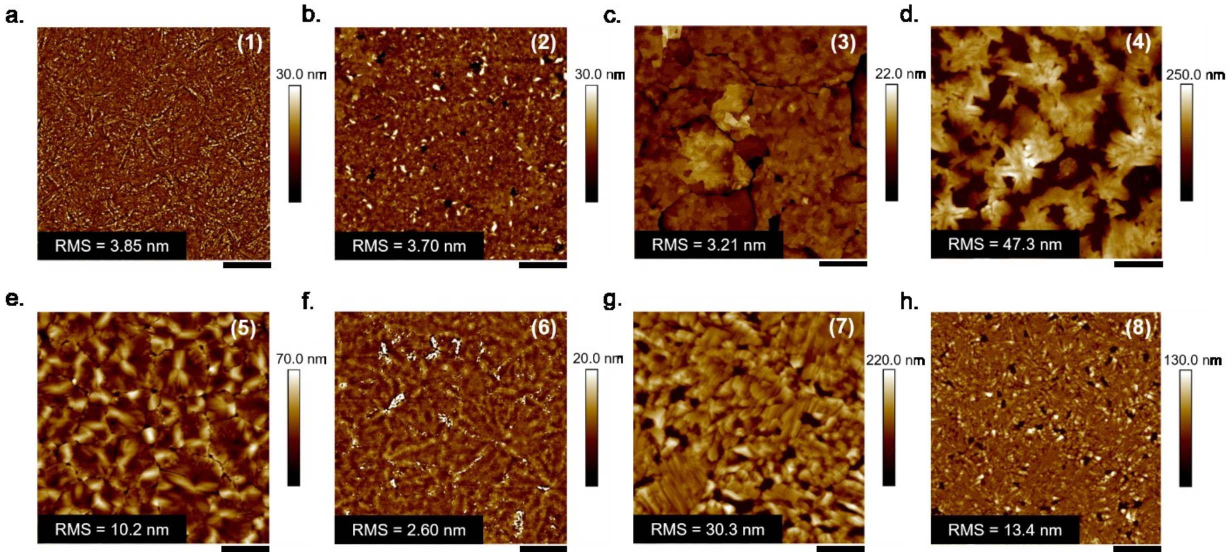

Figure 2.4. AFM images (10 µm x 10 µm) of materials **1-8** (a-h) with a scale bar of 2.0 µm. All films were spun from chloroform at 1500 RPM for 90 sec and annealed at 100°C for 1 hr.

Effect of Annealing Temperature

Using **6** as the semiconductor, the effect of annealing on OTFT performance was further investigated by characterizing transistors annealed at different temperatures. The devices were annealed for 1 hr under vacuum at 100°C or 185°C, and compared to un-annealed devices which were left at room temperature in nitrogen. **Figure 2.5a** shows the change in μ_e and V_T with increasing annealing temperature. Annealing at 100°C results in a μ_e increase of 2.1×10^{-2} cm^2 V^{-1} s^{-1} from an initial value of 7.3×10^{-3} cm^2 V^{-1} s^{-1}, with a V_T decrease of 15.0 V from an initial value of 32.6 V. However, upon annealing at 185°C the μ_e decreases by 2.6×10^{-2} cm^2 V^{-1} s^{-1} with a very large V_T increase of 39.8 V. As explained in the next section, the observed reduction in

OTFT performance can be explained by changes in thin-film crystallinity and molecular orientation which do not favour charge transport.[33,40,44,45]

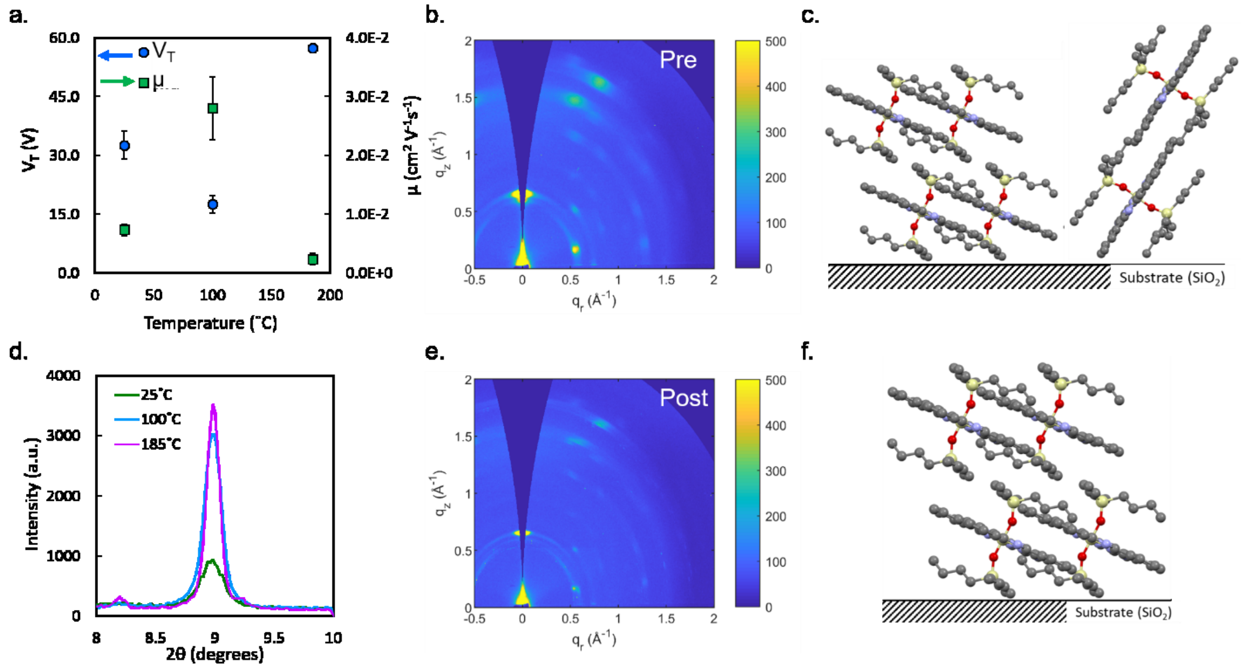

Figure 2.5. Change in (a) μ_e and V_T for **6** OTFTs annealed at 25°C, 100°C, and 185°C. (d) X-ray diffraction pattern of films. 2D scattering patterns for films annealed at (b) 25°C α = 0.02° and (e) 185°C α = 0.03° determined by GIWAXS. Diagram of (c) a combination of pseudo-face on and pseudo-edge on orientations, and (f) pseudo-face on orientation to the substrate determined by GIWAXS. All films were spun from chloroform at 1500 RPM for 90 sec and annealed at the indicated temperature for 1 hr.

Through grazing-incidence wide-angle X-ray scattering (GIWAXS) the crystallinity and orientation of the molecules in relation to the substrate was analyzed before and after thermal annealing. **Figure 2.5b** shows the 2D scattering pattern of **6** when annealed at room temperature. The film is highly crystalline, with a structure strongly correlated to the single crystal as shown by the similarities in the diffraction patterns in **Figure S2.9**. The partial arcs observed throughout the pattern also indicate a high degree of preferential orientation with respect to the substrate.[44] The alignment of the (100) peak, q = 0.65 Å^{-1}, along the q_z axis indicates that one major molecular orientation is with the (100) plane preferentially aligned parallel to the substrate surface (pseudo-face on). The (010) peak at q = 0.60 Å^{-1} reveals additional information; there are two distinct partial arcs at χ = 0 and 74° (where χ is the angle between q and the q_z axis), indicating two distinct orientations relative to the substrate. In addition to the pseudo-face on orientation described previously, there is a secondary population in a pseudo-edge on orientation with the (010) plane oriented parallel to the substrate. The pseudo-face on and pseudo-edge on orientations are depicted in **Figure 2.5c**, and all other features in the scattering pattern are consistent with these two orientations.

After annealing at 185°C for 1 hr the scattering pattern shows a change in the degree of preferential orientation (**Figure 2.5e**), indicated by a narrowing of the partial arcs and a disappearance of the second (010) reflection along q_z. The narrower arcs show an overall stronger degree of preferential orientation, while the presence of only a single (010) reflection at $\chi = 74°$ shows that all crystallites are now in a pseudo-face on orientation (**Figure 2.5c**). **Figure 2.5d** shows the XRD pattern of **6** annealed at each temperature. As the annealing temperature increases the intensity of the peaks increase with a slight decrease in peak width. The sharper more intense peaks indicate a larger crystalline coherence length and a more crystalline film.[6,44,46] The increase in peak intensity from 25°C to 100°C indicates a more ordered crystalline film, which may correspond to the increase in μ_e and decrease in V_T observed in OTFT performance. In literature, annealing has been shown in the most favorable cases to improve film crystallinity, reduce intermolecular spacing, and decrease the number of film defects, thus increasing the μ.[6,47] For **6**, annealing had no effect on the intermolecular spacing between crystal planes as observed by the consistent peak location at $2\theta = 9°$. AFM images of the films show that the film morphology becomes more uniform with smaller vertical ridges after annealing at 100°C (**Figure S2.4**), which supports the increase in device performance. However, after annealing at 185°C OTFT performance decreases despite the further improvement in film crystallinity. Annealing at a high temperature may facilitate large crystallite formation that results in worse charge transfer, and therefore decreased electrical performance, due to grain-boundary effects.[47,48]

In addition to grain size dependency, the decrease in OTFT performance after annealing at 185°C may be due to the molecular orientation relative to the substrate.[44] The disappearance of the (010) peak along the q_z axis at 185°C indicates that, after annealing, there is a stronger preference for the SiPc molecules to align in the pseudo-face on orientation shown in **Figure 2.5f**. As indicated by the calculation results in **Table 2.1** and **Figure 2.2**, having all crystallites with the (100) planes parallel to the substrate is undesirable for high μ_e OTFTs due to the lack of π-π stacking along this direction, resulting in ineffective charge transport from the source to the drain.[33,40,45] Therefore, the lower μ_e and higher V_T observed at a high annealing temperature is due to changes in film morphology and crystallite orientation. This result highlights a feature of materials with high mobility anisotropy (1D or 2D): since only specific crystal directions allow for efficient charge transport, increasing the crystallinity of the semiconducting film improves the transistor characteristics only if those directions lay parallel to the source-drain channel. Otherwise, more amorphous films can give rise to better performance.

Effect of Spin Time

In addition to annealing temperature, the effect of spin time on OTFT performance was investigated using un-annealed OTFTs fabricated with deposition times of 30 sec, 60 sec, and 90 sec, again using **6** as the semiconductor. **Figure 2.6a** demonstrates the change in μ_e and V_T with increasing deposition spin time. OTFTs fabricated at a longer spin time exhibited a small μ_e increase, of 2.9 x 10^{-3} cm^2 V^{-1} s^{-1} from an initial μ_e of 4.4 x 10^{-3} cm^2 V^{-1} s^{-1}, while experiencing a significant V_T reduction of 18.7 V from an initial value of 30.0 V, suggesting increased homogeneity of the semiconducting film and a decrease of surface traps at the interface with the dielectric.[49] This trend was also observed for annealed OTFTs with results shown in **Figure S2.10**.

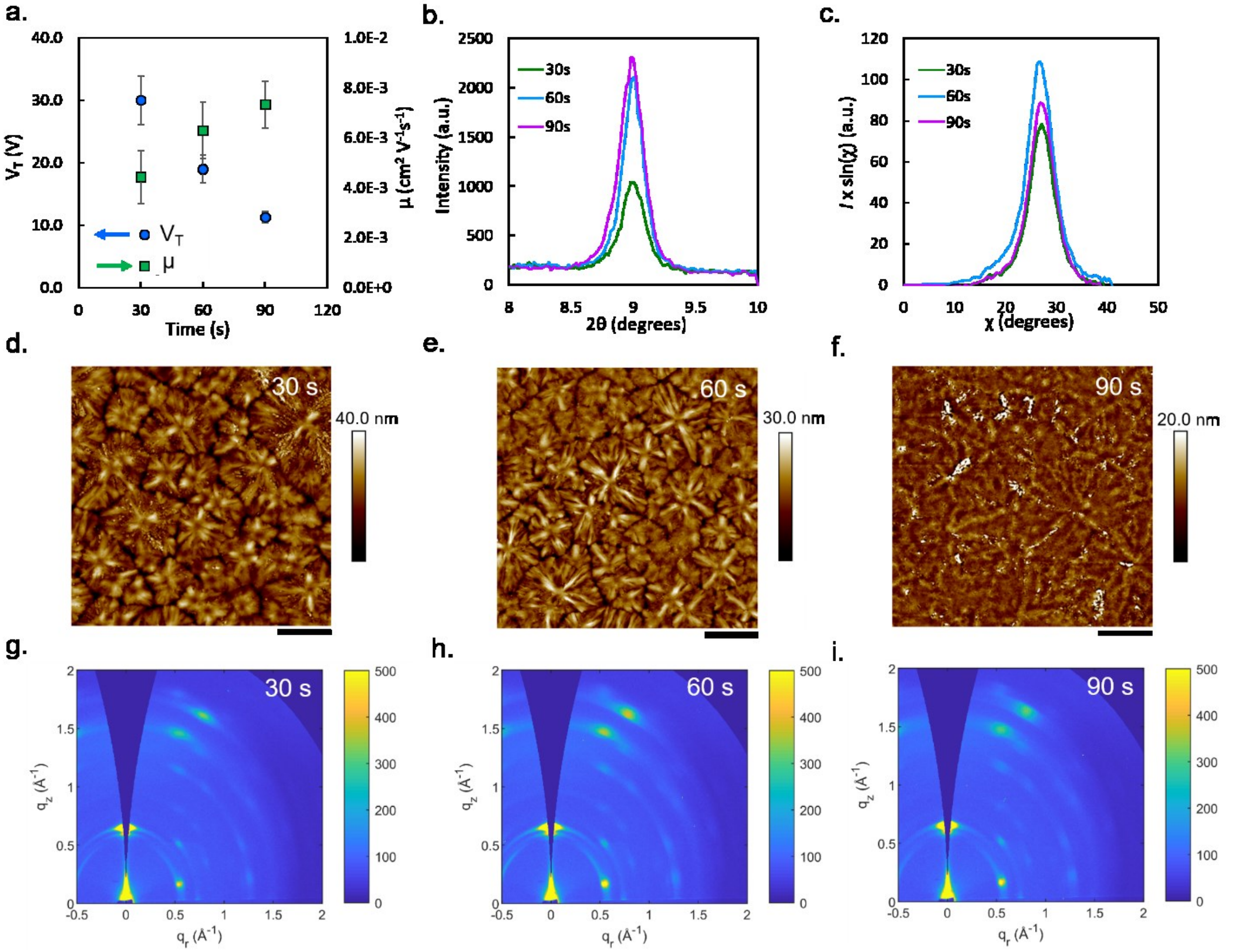

Figure 2.6. Change in (a) μ_e and V_T for **6** OTFTs spun at 30 sec, 60 sec, and 90 sec. (b) X-ray diffraction pattern of films. (c) Partial pole figures constructed from the (211) scattering feature, determined from GIWAXS data. AFM images (10 µm x 10 µm) of (d) 30 sec, (e) 60 sec, and (f) 90 sec spin times with a scale bar of 2.0 µm. 2D scattering patterns for films spun at (g) 30 sec α = 0.02°, (h) 60 sec α = 0.03°, and (i) 90 sec α = 0.03° determined by GIWAXS.

AFM images (**Figure 2.6d-f**) show that as the spin time increases from 30 sec to 90 sec, the crystallites appear to reduce in size and become more homogenous, which corresponds to the observed improvement in OTFT performance. **Figures 2.6g-i** show the 2D scattering pattern of the films fabricated at each spin time determined by GIWAXS. Unlike annealing temperature, spin time has no effect on the preferred molecular orientation of the $(OR)_2$-SiPc molecule relative to the substrate surface. The (100) and (010) peaks along the q_z axis are present at all spin times, indicating the presence of both pseudo-face on and pseudo-edge on orientations. Additionally, using the (211) peak as a reference (q = 1.8 Å^{-1}), there is little change in the distribution of crystallite orientations (**Figure 2.6c**).[44] The XRD patterns in **Figure 2.6b** show that a longer spin time results in a greater (100) (2θ = 9°) peak intensity, therefore indicating a more crystalline thin film. However, the increase in peak intensity observed at a longer spin time may also be attributed to differences in film thickness. It can be concluded that increasing spin time up to 90 sec results in a more homogenous film morphology while maintaining the same crystal orientation to the surface.

To further elucidate the effects of spin time on OTFT performance, additional characterization was performed with transistors fabricated using **3** as the semiconductor. **3** has very large axial substituents and a unique thin-film morphology, making it an interesting candidate for characterization. **Figure 2.7a** and **3.7b** show how μ_e and V_T change with increasing spin time. From 30 sec to 60 sec the μ_e trends upward with a small V_T increase of 3.2 V. However, in opposition to the trend observed for **6**, at 90 sec μ_e decreases significantly by 5.3 x 10^{-4} cm^2 V^{-1} s^{-1} from 7.8 x 10^{-4} cm^2 V^{-1} s^{-1} with an increase in V_T of 8.7 V, from 24.5 V to 33.2 V.

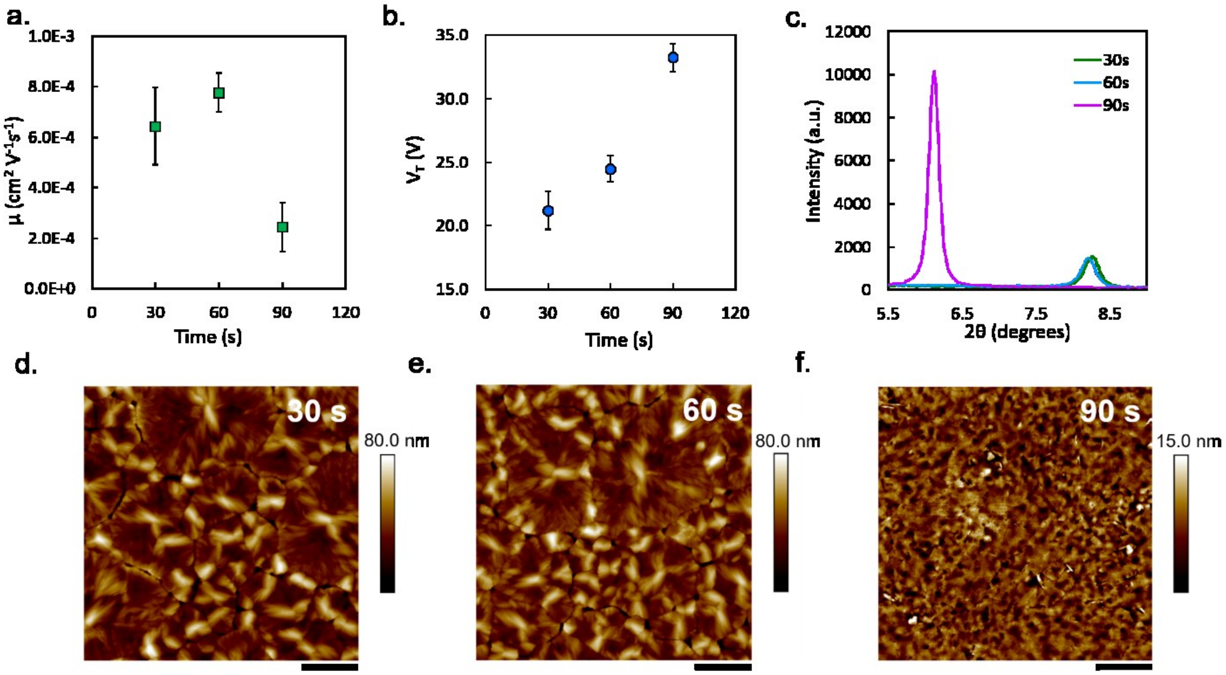

Figure 2.7. Change in (a) μ_e and (b) V_T for **3** OTFTs spun at 30 sec, 60 sec, and 90 sec. (c) X-ray diffraction pattern of films. AFM images (10 µm x 10 µm) of (d) 30 sec, (e) 60 sec, and (f) 90 sec spin times with a scale bar of 2.0 µm. All films were spun from chloroform at 1500 RPM for the indicated time and annealed at 25°C.

Figure 2.7c shows that the sudden variation in the device characteristics is associated with an abrupt change in the diffraction pattern of **3** spun at 30 sec or 60 sec to 90 sec. The 30 sec and 60 sec trials exhibit peaks of similar intensity at 2θ = 8.2°, whereas for the 90 sec trial this peak disappears and a new one with much higher intensity is present at 2θ = 6.1°. The distance between crystal planes was determined by **Equation 2.3** to be 10.8 Å for the 30 sec and 60 sec trials, and 14.4 Å for 90 sec. The shift in peak location and interplanar spacing is likely a preference towards a different crystal polymorph, changing the molecular packing and the ability of the molecules to transfer charge, resulting in worse electrical performance in OTFTs spun for 90 sec. This is further corroborated by the AFM images in **Figures 2.7d-f**, demonstrating that film morphology greatly changes at a spin time of 90 sec. The 30 sec and 60 sec trials have similar sized and shaped features, which corroborates the similar electrical characteristics exhibited in OTFTs, while the 90 sec trial has smaller features of a different shape compared to the 30 sec and 60 sec trials. Thus, it is likely that the larger grains and smaller interplanar spacing obtained at 30 sec and 60 sec improve charge transport through the film due to a decrease in charge trapping defects and enhanced π overlap between molecules.[6,7,50,51]

Furthermore, GIWAXS analysis of **3** spun at 90 sec determined that the observed scattering pattern does not match the pattern predicted by the single crystal data (**Figure S2.11**), implying the formation of a different polymorph.[52] Consistent with the XRD data shown in **Figure 2.7c**, the 2D scattering pattern also shows a highly crystalline film; additionally, there is a high degree of preferential orientation, as exhibited by the strong speckle pattern in **Figure S2.8a**. The structural differences between single crystals and thin-films highlights once again the importance of fabrication methods and processing conditions on OTFT performance.

In the literature it has been demonstrated that crystal formation during spin coating occurs in two stages. First a short period of fast crystallization takes place, followed by a slower crystallization that depends on the spin speed.[33] Chou et al. demonstrated how spin speed influences the crystallization stages of bottom-gate top-contact 6,13-bis(triisopropylsilylethynyl) (TIPS)-pentacene OTFTs, and concluded that to achieve high μ_h transistors a long period of slow crystallization is needed. It was hypothesized that longer spin time allows for an increased period of slow crystallization associated to residual solvent evaporation, which in turn promotes grain growth and defect healing, and increases device performance. For the $(OR)_2$-SiPcs studied in this work, the length of the alkyl chain affects the crystallization kinetics due to differences in material properties (e.g. solubility, diffusivity and viscosity), and thus affects the duration of each crystallization stage. This is supported by the different results obtained for **3** and **6**. **6** exhibited reduced V_T and increased film crystallinity with increasing spin time, whereas **3** showed little change in OTFT performance and film morphology with the exception of the 90 sec trial. At 90 sec there is potentially more time to reach equilibrium and therefore a more stable polymorph can crystallize, which may result in the differences in device performance. Further investigation into the kinetics and stages of crystallization will help to understand how the processing conditions can be used to control thin-film formation of organic semiconductors for solution processable techniques.

Conclusions

In this work eight axially-substituted silicon phthalocyanines were compared as n-type semiconductors in bottom-gate top-contact OTFTs fabricated by spin coating. Six of these materials are reported in OTFTs for the first time. Bis(tri-*n*-ethyl oxide) and and bis(tri-*n*-hexylsilyl oxide) silicon phthalocyanines (**4** and **7**, respectively) were found to be non-functional as semiconductors in OTFTs, in line with DFT calculations on crystal structures indicating that the packing of these materials determines small electron transfer integrals. The transistors fabricated with all the other compounds showed promising performances, with electron mobilities in the 10^{-4}-10^{-2} cm^2 V^{-1} s^{-1} range, and threshold voltages of a few tens of volts. After thermal annealing, bis(tri-*n*-butylsilyl oxide) SiPc (**6**) was found to have the highest μ_e of 0.028 cm^2 V^{-1} s^{-1}, and the highest on/off current ratio of 10^5, making it the best performing semiconductor out of all reported solution processable SiPc materials.

For the best performing material (**6**), and for bis(*n*-dodecyldimethylsilyl oxide) SiPc (**3**) which showed a peculiar thin-film structure with large plate-like features, the correlation between morphology and transistor transfer properties was thoroughly investigated by means of AFM and X-ray scattering, as a function of two key preparation parameters, spin coating time and annealing temperature. It was demonstrated that for SiPcs thermal annealing can be used to control both film crystallinity and the orientation of the molecules relative to the substrate surface to possibly achieve higher μ_e OTFTs with reduced V_T. Additionally, spin time was shown to have the potential of being complimentary to annealing, since it can be used to tune thin-film crystallinity without affecting the orientation of the molecules. These encouraging results show the effectiveness of axial substitution as a strategy to control crystal packing and charge transport properties of SiPcs, and the potential of these materials as n-type semiconductors in OTFTs, whose performance can be optimized by exploiting the effects of fabrication conditions on thin-film structures.

Experimental

Materials

Bis(thexyldimethylsilyl oxide) silicon phthalocyanine (**1**), bis(*n*-octyldimethylsilyl oxide) silicon phthalocyanine (**2**), bis(*n*-dodecyldimethylsilyl oxide) silicon phthalocyanine (**3**), bis(tri-*n*-ethyl oxide) silicon phthalocyanine (**4**), bis(triisobutylsilyl oxide) silicon phthalocyanine (**5**), bis(tri-*n*-butylsilyl oxide) silicon phthalocyanine (**6**), bis(tri-*n*-hexylsilyl oxide) silicon phthalocyanine (**7**), and bis(diisopropyloctylsilyl oxide) silicon phthalocyanine (**8**) were synthesized as described in literature.[43]

OTFT Fabrication

OTFTs were fabricated on n-doped silicon substrates (15 mm x 20 mm) with a 300 nm thermally grown silicon oxide dielectric from Ossila. Substrates were first cleaned by sonication in sequential baths (5 min each) of soapy water, distilled water, acetone and methanol, then dried with nitrogen gas. Cleaned substrates were treated with air plasma for 15 min. After which, substrates were rinsed with distilled water and isopropanol, then dried with nitrogen, before submersion in 1% v/v trichloro(octyl)silane (OTS) in toluene for 24 hrs at 70°C. Upon removal from the silane surface treatment bath, substrates were rinsed with toluene and isopropanol and dried under vacuum at 70°C for 1 hr. $(OR)_2$-SiPc solutions were prepared in a nitrogen environment at a concentration of 10 mg ml^{-1} in chloroform (see **Table S2.4** for solubility of 6 in common organic solvents). Solutions were heated at 50°C for 1 hr, filtered through 0.2 µm pore size PTFE membranes, and deposited onto the substrates by spin coating 60 µl of solution at 1500 RPM for 90 sec in nitrogen. The substrates were then annealed at room temperature in nitrogen or under vacuum at 100°C for 1 hr. Top contact electrodes were formed using shadow masks with a channel width $W = 1000$ µm and length $L = 30$ µm, creating 20 individual transistors per substrate. 10 nm of manganese and 50 nm of silver were deposited through the masks by physical vapour deposition using an Angstrom EvoVac thermal evaporator with target rates of 0.5 Å s^{-1} and 1.0 Å s^{-1} respectively. Manganese was used as an electrode interlayer to reduce the contact barrier between the electrodes and semiconducting layer, resulting in lower threshold voltage and improved field-effect mobility.[53]

OTFT Characterization

OTFT electrical characterization was performed using a custom built automatic multi-tester. The tester is composed of 48 gold plated (20 nm) nickel probe tips which simultaneously make contact with the source-drain electrodes of the individual transistors, along with the gate electrode. Results were obtained from 40 individual transistors across two substrates fabricated by the method outlined above. The multi-tester introduces an approximate resistance of 750 mOhm to the testing apparatus. A Keithley 2614B and a MCC USB DAQ were used to control the source-drain voltage (V_{SD}) and gate voltage (V_{GS}) to obtain source-drain current (I_{SD}) measurements. The tester was kept in a controlled nitrogen environment at atmospheric pressure for the duration of characterization as these materials are not air stable. By setting the V_{SD} constant at 50 V and varying the V_{GS}, I_{SD} measurements were obtained to determine the saturation regime field-effect mobility, threshold voltage, and on/off current ratio. The following equation was used to relate the saturation regime field-effect mobility and threshold voltage to V_{GS} and I_{SD} measurements.

$$I_{SD} = \frac{\mu_e C_i W}{2L}(V_{GS} - V_T)^2 \tag{2.1}$$

Where μ_e is the field-effect mobility, V_T is the threshold voltage, W is the channel width, L is the channel length, and C_i is the capacitance density. The capacitance density was calculated by $C_i = (\varepsilon_0\varepsilon_r)/t$, where t is the thickness of the dielectric (300 nm), and ε_r is the relative dielectric constant of SiO_2 equal to 3.9. The μ_e and V_T were determined by taking the square root of **Equation 2.1** to obtain a linear relationship between $\sqrt{I_{SD}}$ and V_{GS} as shown by the following equation.

$$\sqrt{I_{SD}} = \sqrt{\frac{\mu_e C_i W}{2L}}(V_{GS} - V_T) \tag{2.2}$$

By plotting the square root of I_{SD} against V_{GS} the μ_e and V_T are determined by the slope and x-intercept, respectively (**Figure S2.12**). Lastly, the on/off current ratio is defined as the ratio of the highest and lowest currents measured in the characterized V_{GS} range.

Determination of Thermal Characteristics

TGA of $(OR)_2$-SiPc samples were performed in nitrogen, at a 5°C min^{-1} heating rate, with a Discovery 5500 equipment from TA instruments. DSC spectra were obtained with a Discovery

2500 equipment from TA instruments, where each sample was cycled between 0-250˚C three times with a heating/cooling rate of 5°C min^{-1}.

Thin-Film UV-vis

Square glass microscope slides (25.4 mm, VWR) were cleaned in a sonication bath, following the same procedure described for silicon substrates. The clean slides were treated with air plasma (15 min) and then submerged in a 1% v/v OTS solution in toluene for 4 hrs. After rinsing the substrates with isopropanol, the $(OR)_2$-SiPc thin-films were deposited by spin coating 300 µl from 10 mg ml^{-1} chloroform solutions, at 500 RPM for 30 sec. Thin-film UV-vis spectra were then recorded in an Ocean Optics Flame spectrophotometer.

Single Crystal Preparation

Single-crystals for XRD analysis were grown from solution, by dissolving each $(OR)_2$-SiPc in a minimal amount of dichloromethane (DCM). The solutions were filtered through 0.2 µm pore size PTFE membranes into glass vials capped with aluminum foil. A needle was used to create a small hole in the foil cap, and the solvent was allowed to slowly evaporate, away from vibrations, over the course of 24 hrs.

XRD

XRD measurements of thin-films were obtained using a Rigaku Ultima IV powder diffractometer with a Cu Kα (λ = 1.5418 Å) source. Measurements were taken directly from thin-films deposited on silicon substrates with a scan range of $3° < 2θ < 15°$, and a rate of 0.5° min^{-1} with no spin, with results shown in **Figure S2.13**. The interplanar spacing (d-spacing) between lattice plans was calculated using Bragg's Law shown by the following equation.

$$n\lambda = 2dsin\theta \qquad (2.3)$$

Where λ is the wavelength of the incident wave equal to 1.54056 Å, d is the spacing between planes, θ is the angle of incidence in degrees, and n is a positive integer equal to 1 for this study.

Computational

All molecular geometries were optimized using density functional theory (DFT) with the B3LYP functional and the 6-31G(d) basis set. Each structure was verified to be a minimum of the potential energy surface on the basis of its all real harmonic vibrational frequencies. Internal reorganization energies (λ_i) were calculated at the same level, using the expression derived from the four-point adiabatic potential approach.

$$\lambda_i = E^{(-)}(M) - E^{(0)}(M) + E^{(0)}(M^-) - E^{(-)}(M^-) \tag{2.4}$$

Where $E^{(0)}(M)$ and $E^{(-)}(M^-)$ denote the ground-state energy of the neutral state and of the negatively charged state, respectively; $E^{(-)}(M)$ is the energy of the neutral molecule in the optimized geometry of the anion and $E^{(0)}(M^-)$, the energy of the anion in the optimized geometry of the neutral molecule. Transition energies towards the few first optically allowed excited states were also computed by means of time-dependent DFT at the B3LYP/6-31G(d) level.

Transfer integrals (J_k) characterizing the electron coupling between molecular pairs (k) were obtained by employing the projection method involving the LUMOs of monomers.[54] Since all molecules possess nearly degenerate LUMO (L) and LUMO+1 (L+1) levels which both contribute to the transport, the effective transfer integrals for electron transport were computed as geometric averages in line with previous works.[39]

$$J_k = \frac{1}{\sqrt{2}}\{J_{L,L}^2 + J_{L+1,L}^2 + J_{L,L+1}^2 + J_{L+1,L+1}^2\}^2 \tag{2.5}$$

The relative electron mobilities along the crystal axes i = a, b, c were evaluated at zero field neglecting energetic disorder in the transport level energies, using the expression:

$$\mu_i = \frac{q}{h}\left(\frac{\pi}{k_B T}\right)^{3/2} \frac{1}{\sqrt{\lambda}} \exp\left(-\frac{\lambda}{4k_B T}\right) \sum_k J_k^2 \left(\vec{r}_k \cdot \vec{e}_i\right)^2 \tag{2.6}$$

where the sum runs over all pairs of molecular neighbours separated by the distance vector $\vec{r}_k$, $\vec{e}_i$ is a cell axis unit vector. Variables q, h and k_B are respectively the elementary charge, the Planck, and Boltzmann constants, and T = 300 K. **Equation 2.6** combines Marcus formula for the hopping rate (ν_k) between two neighbouring sites with the equation for the diffusion coefficient in one dimension, $D = \frac{1}{2}\sum_k \nu_k \left(\vec{r}_k \cdot \vec{e}_i\right)^2$, and Einstein's equation relating mobility with diffusion, $\mu = \frac{qD}{k_B T}$.[55] Quantum chemical calculations were performed with the ORCA[56] and Gaussian[57] programs.

GIWAXS

GIWAXS experiments were performed at the Canadian Light Source (CLS) using the Hard X-ray MicroAnalysis (HXMA) beamline. A photon energy of 12.69 keV was selected using a Si(111) monochromator. The beam size was defined by slits having a 0.2 mm vertical gap and a 0.3 mm horizontal gap, and the angle of incidence was set in the range of 0.02 – 0.07°, as indicated. The sample was deposited on a ⟨100⟩ silicon wafer by spin coating from chloroform at 1500 RPM. GIWAXS patterns were collected with a Rayonix SX165 CCD detector (80 µm pixel size; 16.3 cm diameter), which was placed 214 mm from the sample center. The GIWAXS data were calibrated against a silver behenate standard and analyzed using the GIXSGUI software package.[58] Both polarization and solid-angle corrections were applied.

AFM

AFM images were taken using a Bruker Dimension Icon AFM with ScanAsyst-Air tips. Tapping mode was used to collect all images with a scan rate of 1 Hz. Image processing and editing was performed with NanoScope Analysis v.1.8 software.

Associated Content

Acknowledgments

The Natural Sciences and Engineering Research Council of Canada (NSERC, RGPIN-2017-03732 to T.L.K.; RGPIN/2015-509 03987 and STPGP 506661-17 to B.H.L) and the University of Ottawa and the University of Saskatchewan are acknowledged for financial support. T.L.K. and B.H.L. are Canada Research Chairs. The research was undertaken, in part, thanks to funding from the Canada Research Chair program. The Canadian Light Source (CLS) is supported by CFI, NSERC, the University of Saskatchewan, the Government of Saskatchewan, Western Economic Diversification Canada, the National Research Council Canada, and the Canadian Institutes of Health Research. N.T.B also thanks NSERC for the PGS-D.Technical support from HXMA beamline scientist Dr. Chang-Yong Kim is gratefully acknowledged. Computer time was provided by the Mésocentre de Calcul Intensif Aquitain (MCIA) of the University of Bordeaux and financed by the Conseil Régional d'Aquitaine and the French Ministry of Research and Technology. We also thank Centre for Research in Photonics at the University of Ottawa (CRPuO) for access to the AFM and Dr. Ovens for performing single crystal X-ray diffraction on the SiPc derivatives.

Supporting Information

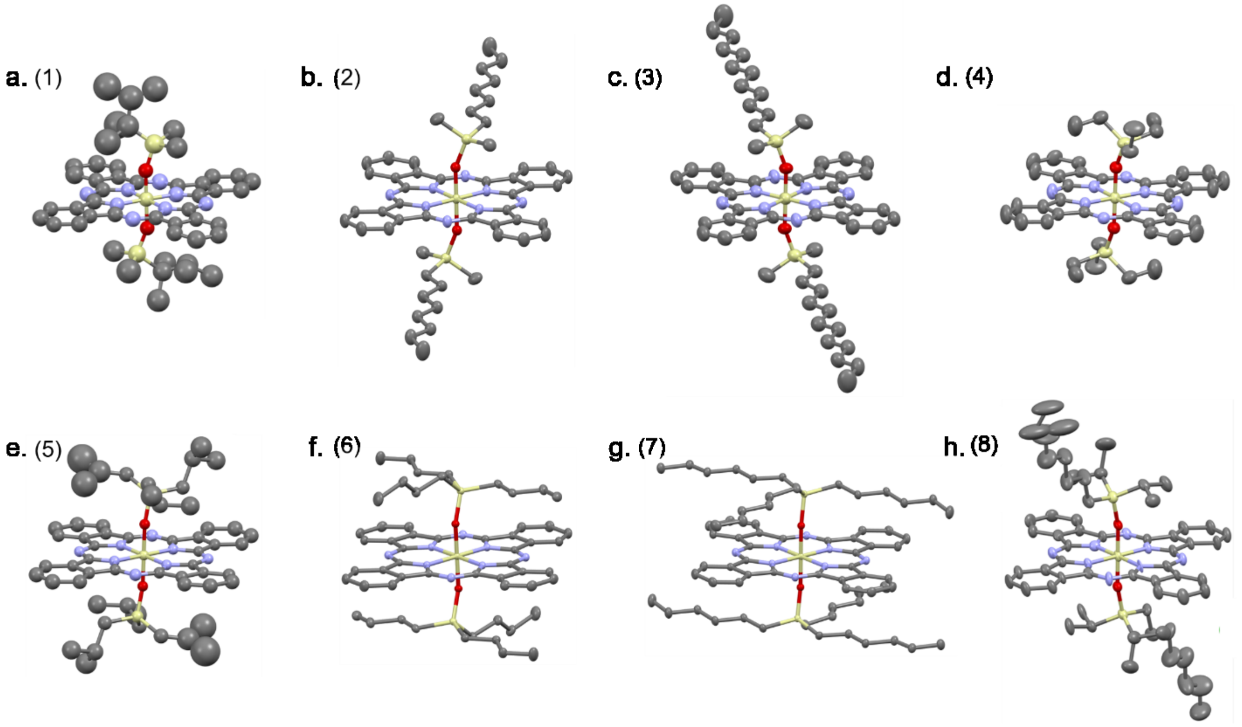

Figure S2.1. Crystal structures of materials **1-8** determined by single crystal X-ray diffraction. CCDC numbers for all materials are (a) 1987218, (b) 1987214, (c) 1987215, (d) 1987219, (e) 1987217, (f) 1522758, (g) 988974, and (h) 1987216. Data for **6** and **7** reproduced with permission from reference 32. Copyright 2019 ACS Applied Electronic Materials.

Table S2.1. Non-negligible electron transfer integrals ($J_k \geq 1$, in units of meV), calculated between a reference molecule and its first neighbours, using the experimental crystal structure. The crystallographic directions corresponding to intermolecular vectors joining the reference molecule with its neighbours are given in the basis of direct lattice vectors.

Crystal	Direction	J_k
1	± (1, 0, 0)	12
	(± 1/2, ± 1/2, 0)	5
	(0, 1/4, 1/2)	5
	(± 1/2, -1/4, 1/2)	1
2	± (1, 0, 0)	30
	± (0, 1, 0)	1
	± (-1, 1, 0)	9
	± (-1, 0, 1)	1
3	± (1, 0, 0)	28
	± (0, 1, 0)	1
	± (1, 1, 0)	11
4	± (1, 0, 0)	2
	± (0, 0, 1)	7
	± (0, 1/2, 1/2)	4
	± (0, -1/2, 1/2)	4
	± (1, 1, 0)	4
5	± (1, 0, 0)	16
	(0, ± 1/2, ± 1/2)	2
6	± (1, 0, 0)	1
	± (0, 1, 0)	23
	± (0, 0, 1)	7
7	± (1, 0, 0)	3
	± (0, 1, 0)	8
	± (0, 0, 1)	5
8	(± 1/2, ± 1/2, 0)	8
	± (0, 1, 0)	1

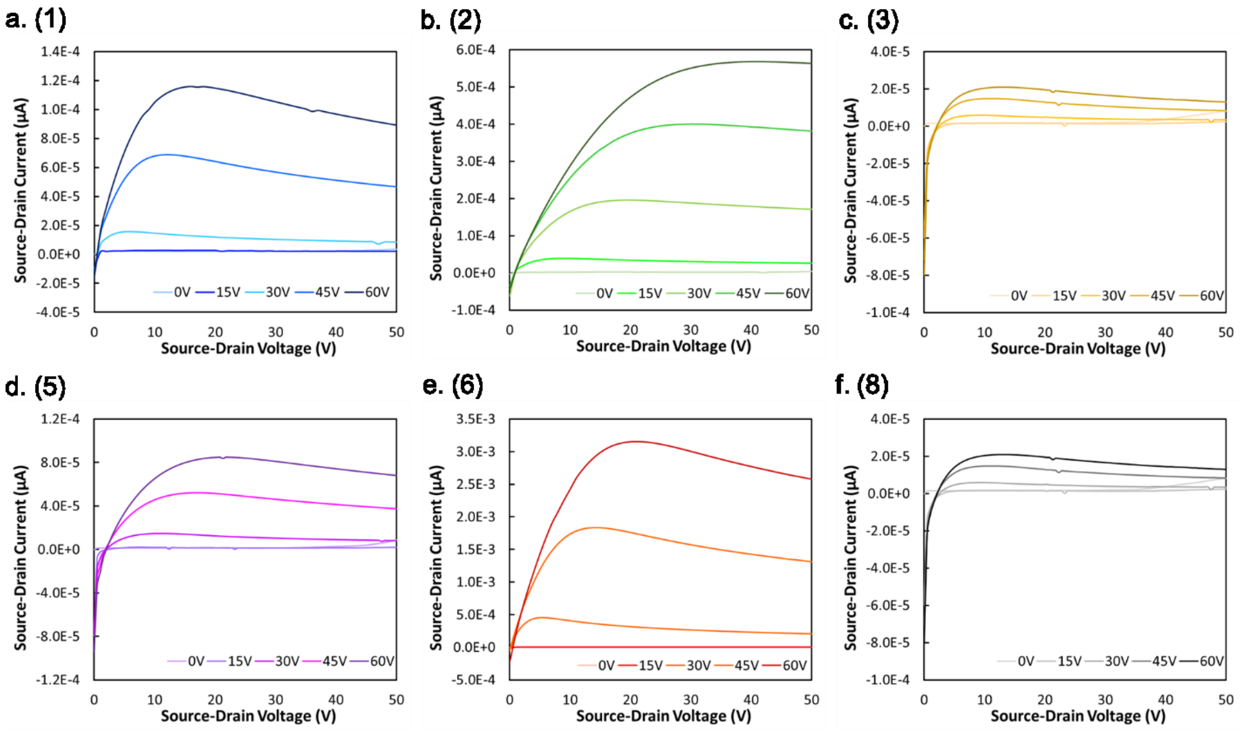

Figure S2.2. Characteristic output curves of materials (a) **1**, (b) **2**, (c) **3**, (d) **5**, (e) **6**, and (f) **8** characterized at room temperature in nitrogen. $(OR)_2$-SiPc films were spun from chloroform at 1500 RPM for 90 sec and annealed at 100°C under vacuum for 1 hr.

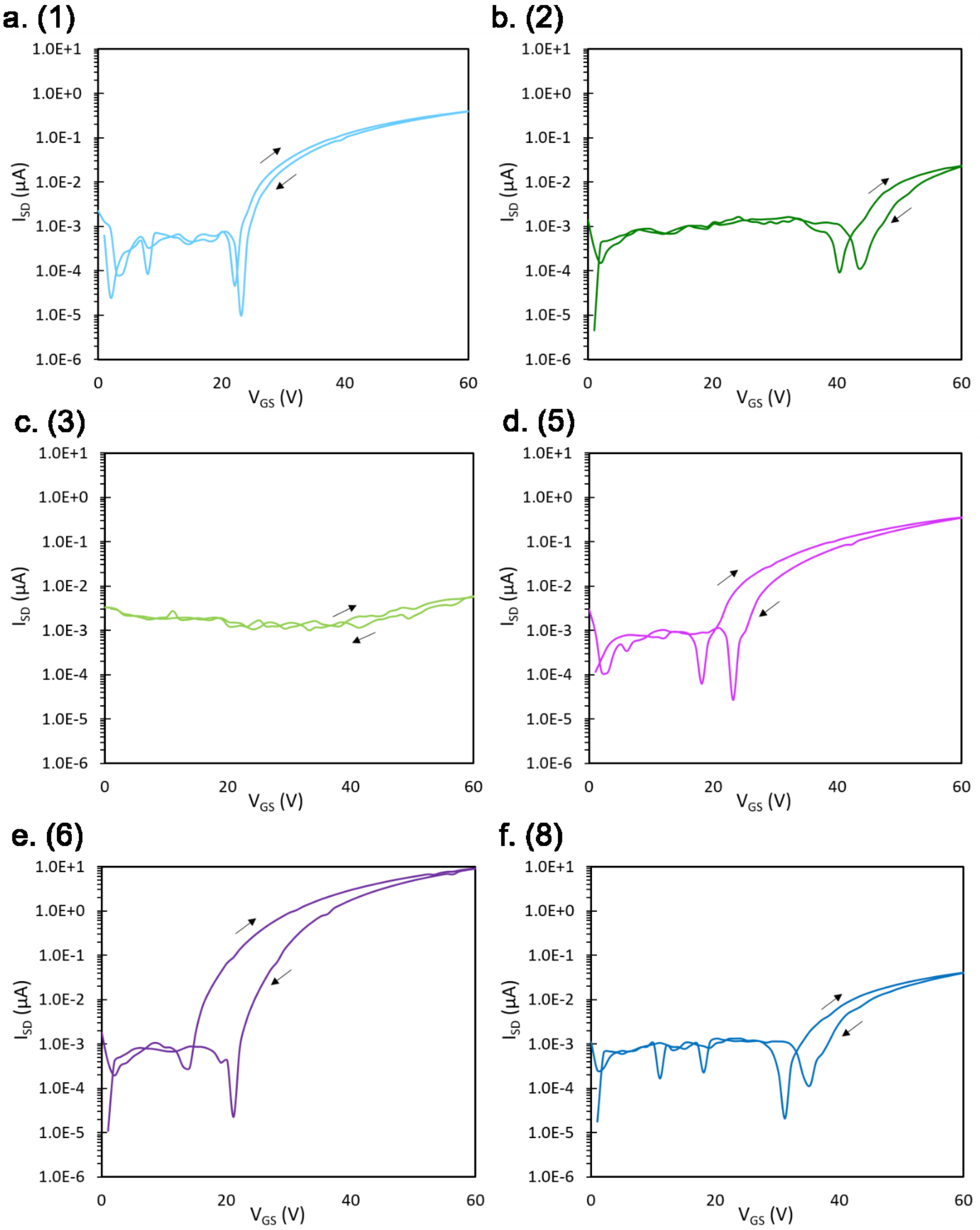
a. (1)

b. (2)

c. (3)

d. (5)

e. (6)

f. (8)

Figure S2.3. Characteristic forward and reverse transfer curves for materials (a) **1**, (b) **2**, (c) **3**, (d) **5**, (e) **6**, and (f) **8**, characterized at room temperature in nitrogen. $(OR)_2$-SiPc films were spun from chloroform at 1500 RPM for 90 sec and annealed at 100°C under vacuum for 1 hr.

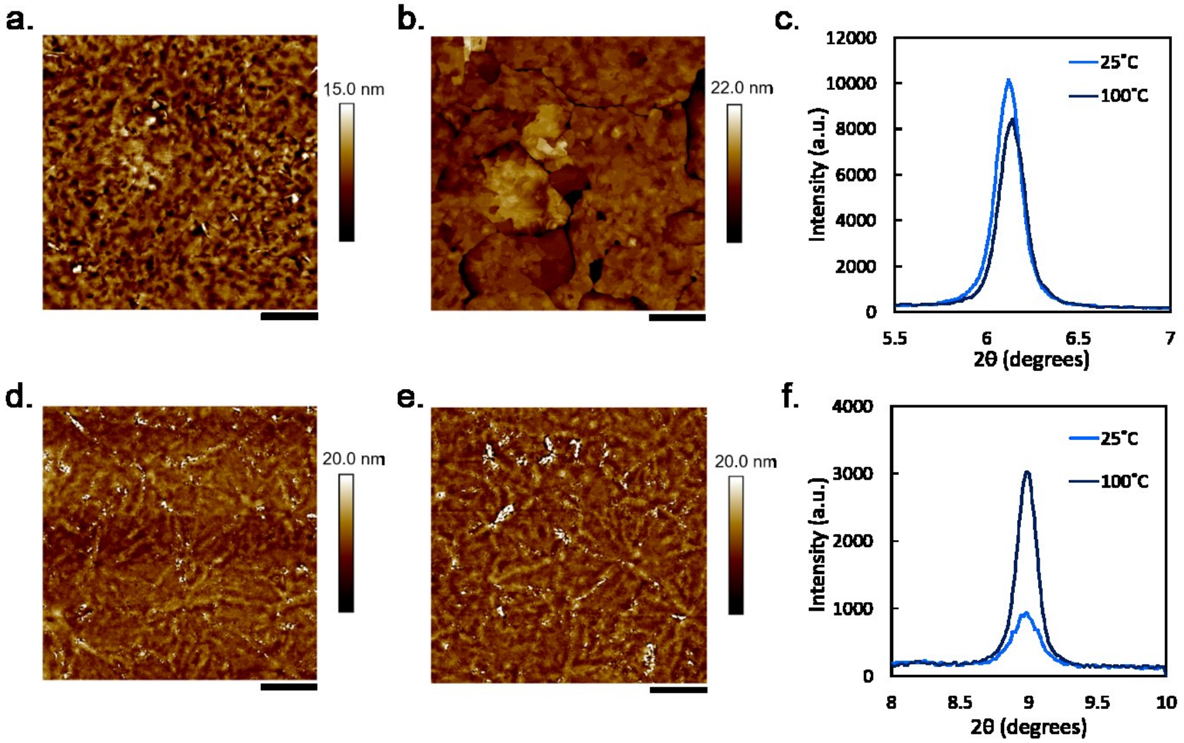

Figure S2.4. AFM images (10 µm x 10 µm) of material **3** annealed at (a) 25°C and (b) 100°C, and material **6** annealed at (d) 25°C, and (e) 100°C with a scale bar of 2.0 µm. XRD pattern of (c) material **3** and (f) material **6** annealed at each temperature. All films were spun from chloroform at 1500 RPM for 90 sec and annealed at the indicated temperature for 1 hr.

Table S2.2. Thermal characteristics of materials **1**-**8**.

Material	T_m[a] (°C)	T_c[b] (°C)	H_m[c] (J/g)	H_c[d] (J/g)
1	-[e]	-[e]	-[e]	-[e]
2	178	153	38.2	46.7
3	87/127	89/60	44.4	48.7/31.2
4	-[e]	-[e]	-[e]	-[e]
5	-[e]	-[e]	-[e]	-[e]
6	231/61[31]	219[31]	36.1[31]	30.7[31]
7	173[31]	110[31]	26.9[31]	23.5[31]
8	148	88	28.8	20

a. melting temperature, taken from the peak of DSC heating cycle
b. crystallization temperature, taken from the peak of DSC cooling cycle
c. melting enthalpy, calculated by the integration of the DSC peak referent to melting processes
d. crystallization enthalpy, calculated by the integration of the DSC peak
e. no observed thermal events in the assessed range

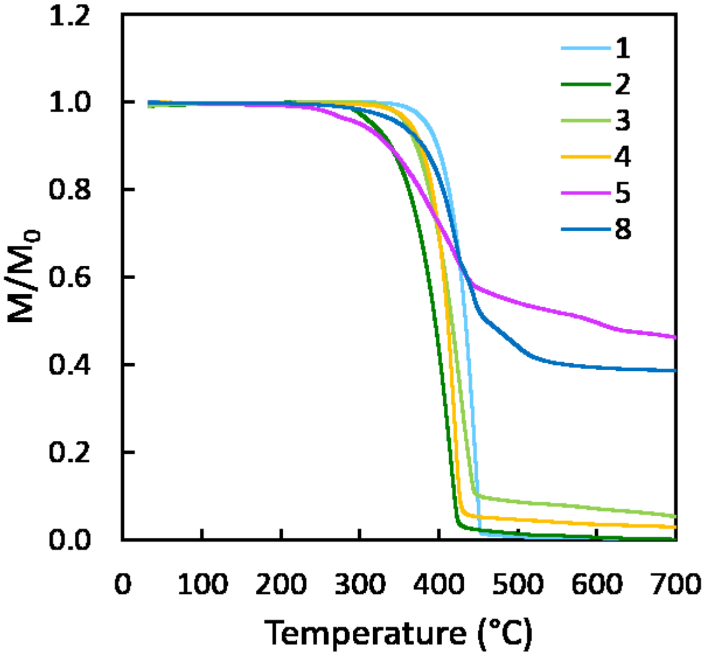

Figure S2.5. Thermogravimetric analysis (TGA) trace of $(OR)_2$-SiPcs.

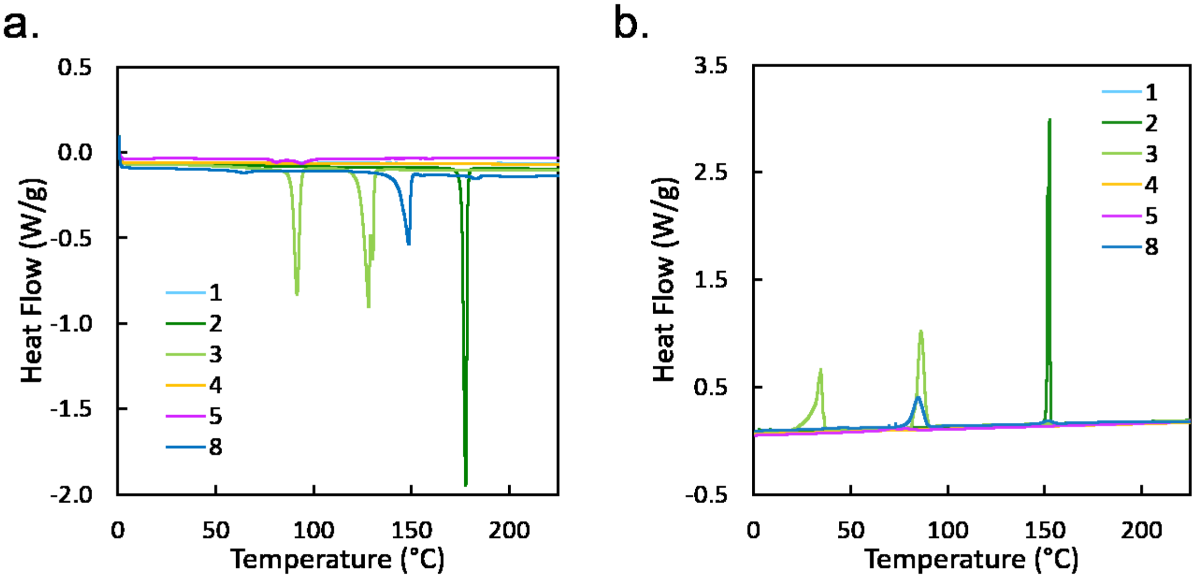

Figure S2.6. Differential scanning calorimetry (DSC) curves of (a) heating and (b) cooling of $(OR)_2$-SiPcs.

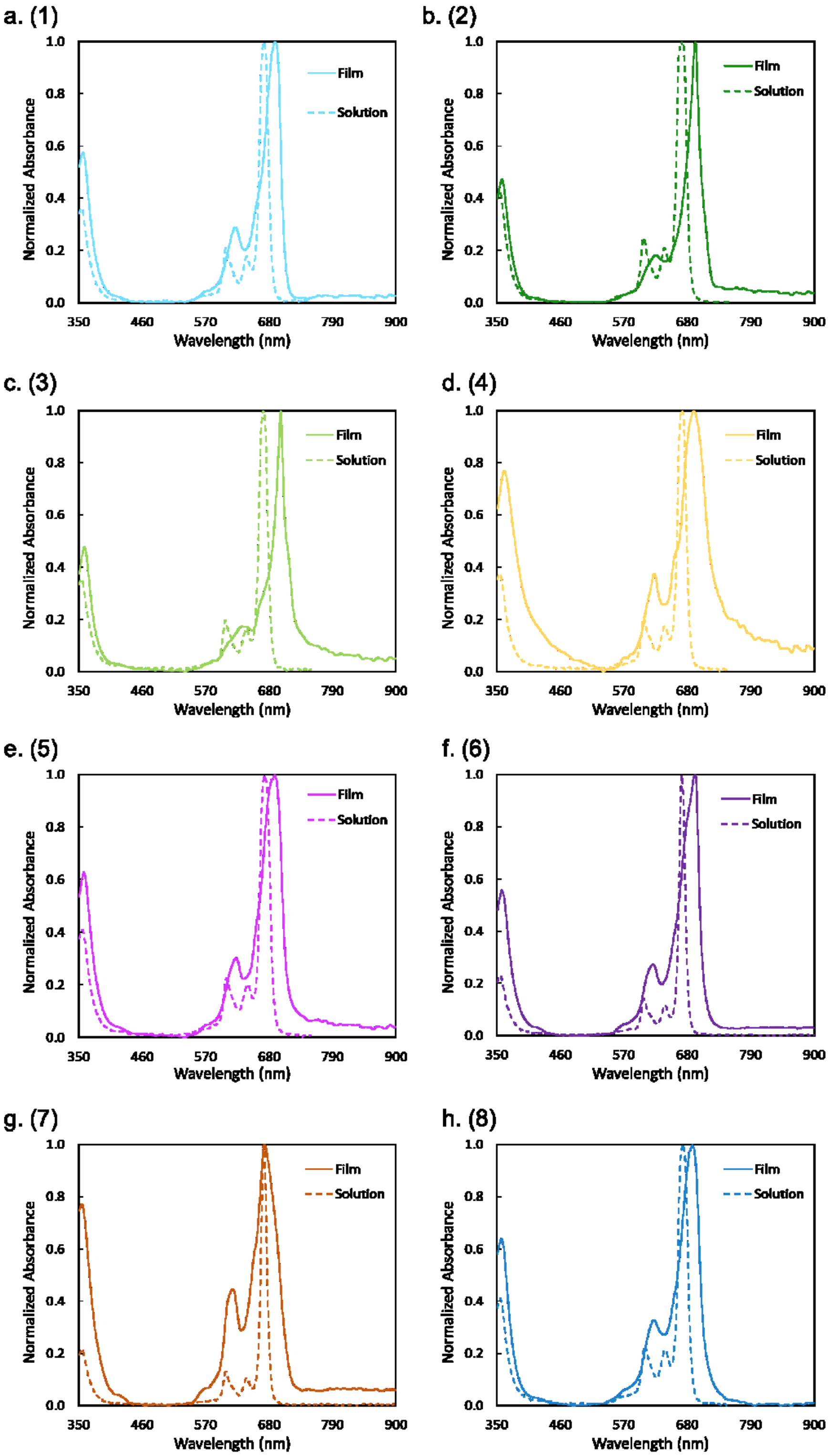

Figure S2.7. UV-vis absorption spectra of $(OR)_2$-SiPcs films, materials **1-8** (a-h), spin coated onto OTS treated glass slides, and $(OR)_2$-SiPcs in toluene solution. Reproduced with permission from reference 32 and reference 43. Copyright 2019 ACS Applied Electronic Materials. Copyright 2020 Langmuir.

Table S2.3. Max peak location, full-width at half-max (FWHM), and peak shift between $(OR)_2$-SiPc films spin coated onto OTS treated glass slides, and $(OR)_2$-SiPcs in toluene solution determined by UV-vis absorption.

Material	State	Max (nm)	FWHM (nm)	Peak Shift (nm)
1	Liquid	671.53	17.7	19.0
	Thin-film	690.56	33.5	
2	Liquid	671.53	19.6	22.5
	Thin-film	694.06	26.4	
3	Liquid	669.88	17.2	30.5
	Thin-film	700.37	23.1	
4	Liquid	671.77	17.4	19.5
	Thin-film	691.26	50.3	
5	Liquid	672.71	19.5	17.4
	Thin-film	690.09	31.0	
6	Liquid	670.83	12.3	23.2
	Thin-film	694.06	36.4	
7	Liquid	671.06	11.8	1.6
	Thin-film	672.71	48.7	
8	Liquid	671.77	18.8	16.9
	Thin-film	688.68	39.7	

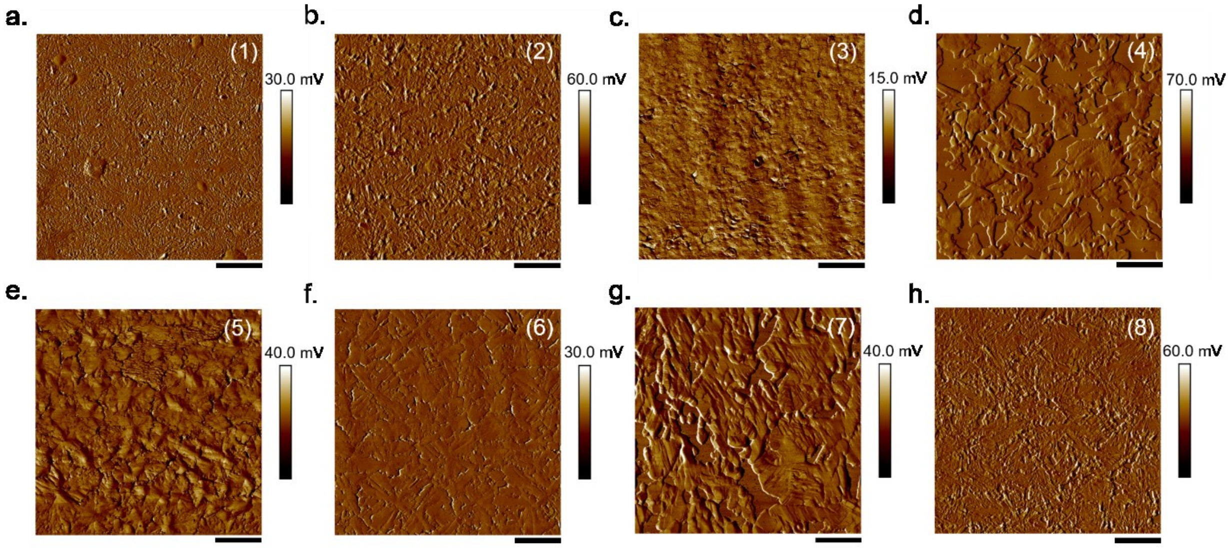

Figure S2.8. Inphase AFM images (10 µm x 10 µm) of materials **1-8** (a-h) with a scale bar of 2.0 µm. All films were spun from chloroform at 1500 RPM for 90 sec and annealed at 100°C for 1 hr.

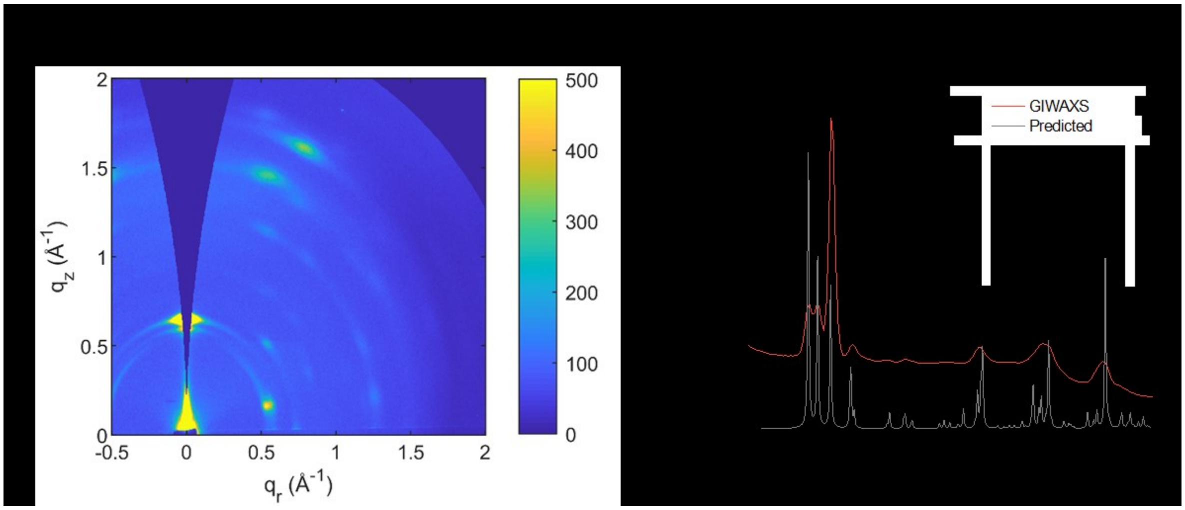

Figure S2.9. (a) 2D scattering pattern α = 0.03°, and (b) diffraction pattern predicted from single crystal and GIWAXS for material **6** films spun from chloroform at 1500 RPM for 90 sec and annealed at 25°C.

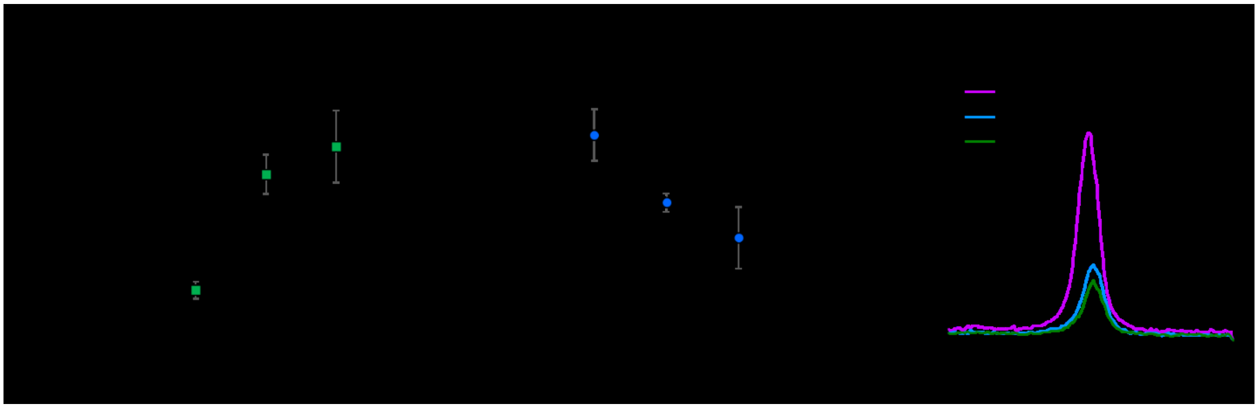

Figure S2.10. Change in (a) electron field-effect mobility (μ_e), (b) threshold voltage (V_T) for **6** OTFTs spun at 30 sec, 60 sec, and 90 sec, and (c) X-ray diffraction pattern of thin-films. All films were spun from chloroform at 1500 RPM for the indicated time and annealed at 100°C for 1 hr.

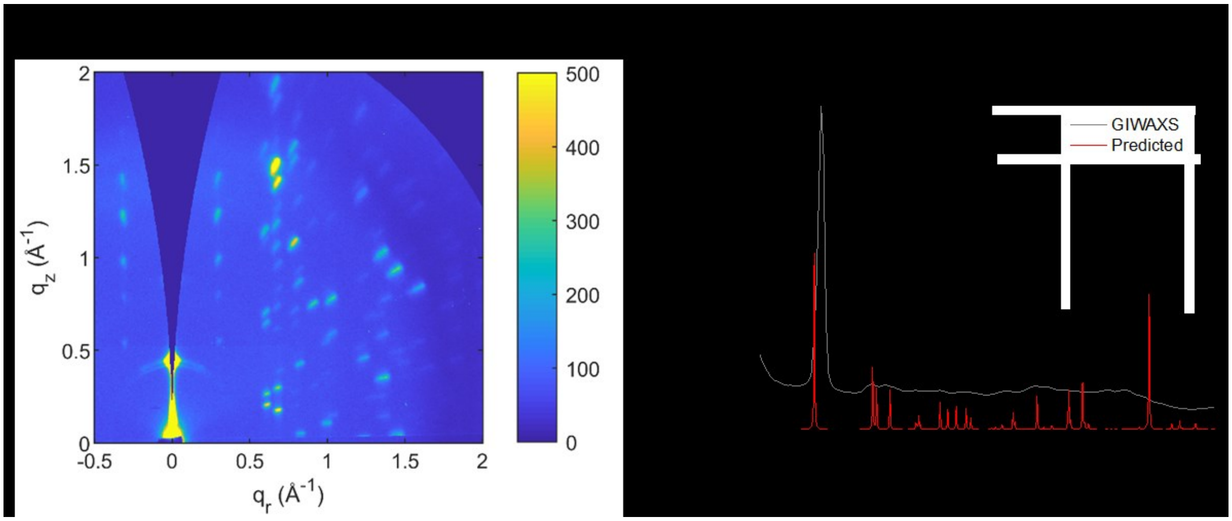

Figure S2.11. (a) 2D scattering pattern α = 0.07°, and (b) diffraction pattern predicted from single crystal and GIWAXS for material **3** films spun from chloroform at 1500 RPM for 90 sec and annealed at 25°C.

Table S2.4. Solubility of **6** in common organic solvents.

Solvent	**Solubility (mg ml^{-1})**
Acetone	1
Heptanes	1.4
Ethyl Acetate	2
NMP	10
Xylenes (mix)	20
Dichlorobenzene	31
Toluene	47
THF	115

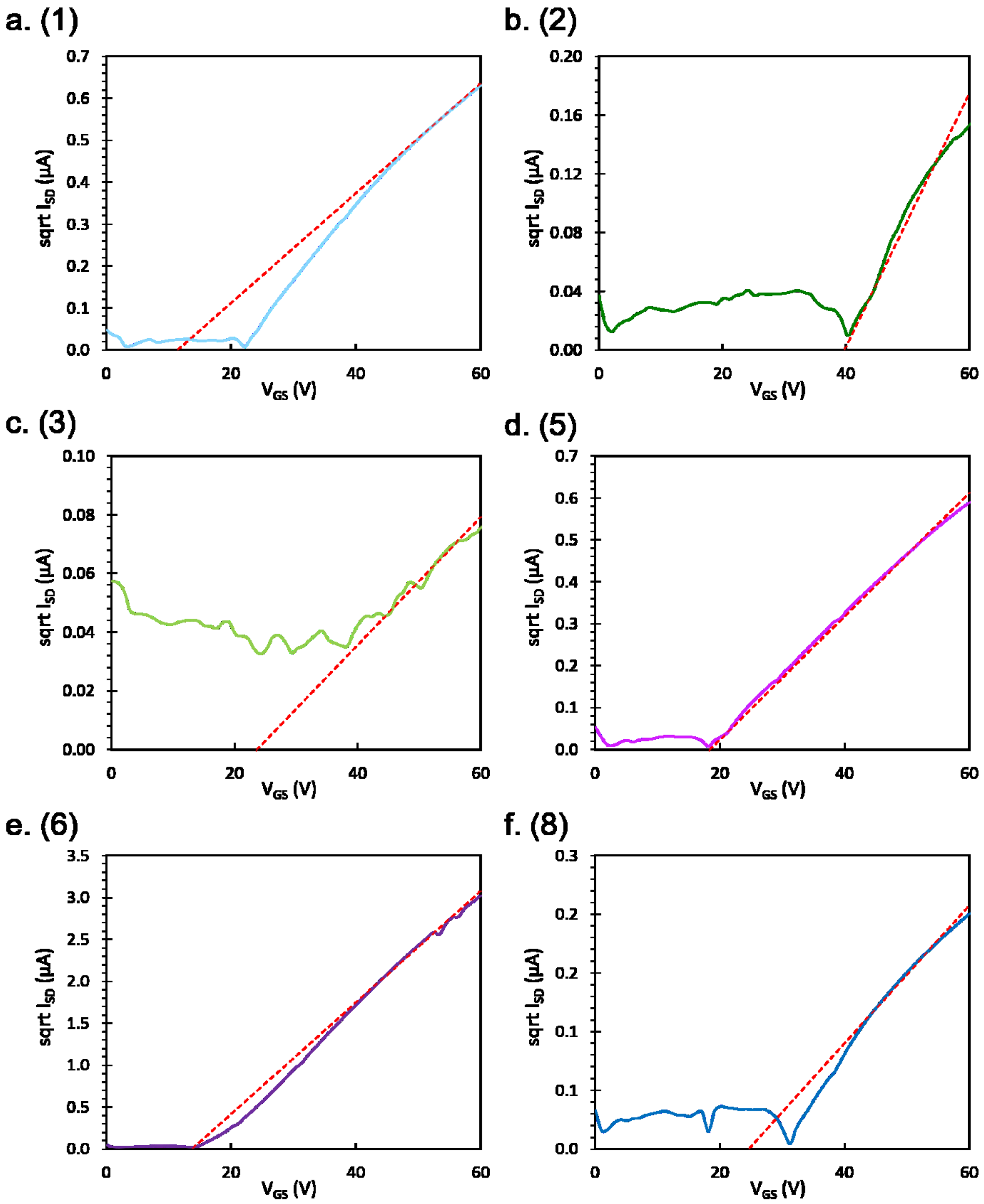

Figure S2.12. Sample $\sqrt{I_{SD}}$ vs. V_{GS} curves for materials (a) **1**, (b) **2**, (c) **3**, (d) **5**, (e) **6**, and (f) **8**, characterized at room temperature in nitrogen. (OR)$_2$-SiPc films were spun from chloroform at 1500 RPM for 90 sec and annealed at 100°C under vacuum for 1 hr. The red dashed line represents the tangent used to calculate μ_e and V_T.

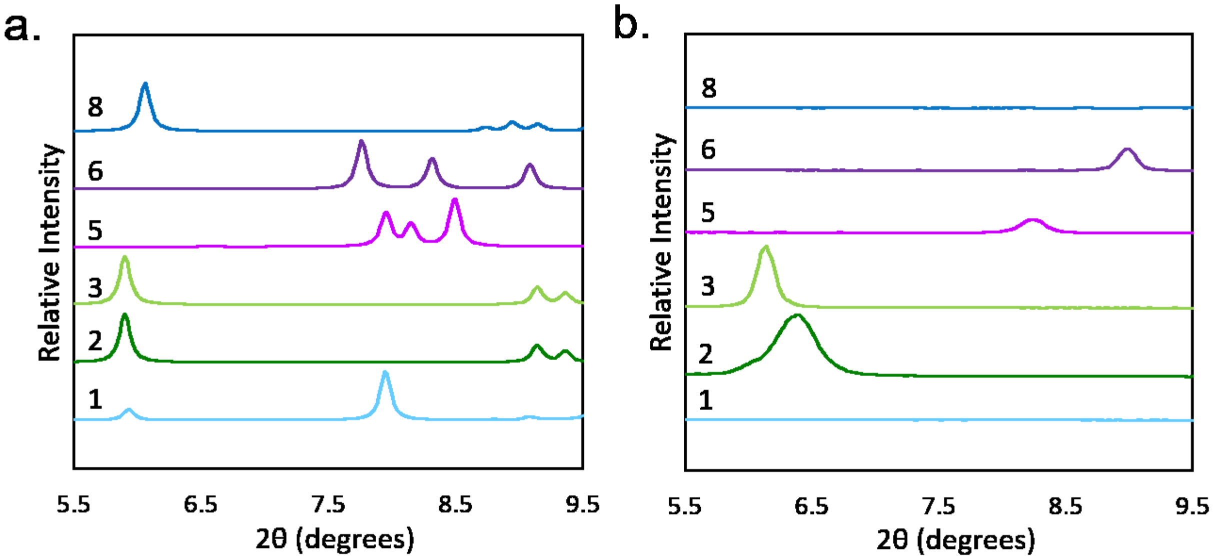

Figure S2.13. XRD pattern of functional materials (a) predicted from single crystal, and (b) measured from thin films.

References

1 Comeau, Z. J. et al. On-the-Spot Detection and Speciation of Cannabinoids Using Organic Thin-Film Transistors. ACS Sensors 4, 2706–2715 (2019).

2 Boileau, N. T., Melville, O. A., Mirka, B., Cranston, R. & Lessard, B. H. P and N type copper phthalocyanines as effective semiconductors in organic thin-film transistor based DNA biosensors at elevated temperatures. RSC Adv. 9, 2133–2142 (2019).

3 Someya, T. et al. A large-area, flexible pressure sensor matrix with organic field-effect transistors for artificial skin applications. Proc. Natl. Acad. Sci. 101, 9966–9970 (2004).

4 Zhou, L. et al. All-organic active matrix flexible display. Appl. Phys. Lett. 88, 2004–2007 (2006).

5 Gelinck, G. H. et al. Flexible active-matrix displays and shift registers based on solution-processed organic transistors. Nat. Mater. 3, 106–110 (2004).

6 Zhang, F. et al. Critical Role of Alkyl Chain Branching of Organic Semiconductors in Enabling Solution-Processed N-Channel Organic Thin-Film Transistors with Mobility of up to 3.50 cm2 V–1 s–1. J. Am. Chem. Soc. 135, 2338–2349 (2013).

7 Lee, S. S. et al. Controlling Nucleation and Crystallization in Solution-Processed Organic Semiconductors for Thin-Film Transistors. Adv. Mater. 21, 3605–3609 (2009).

8 Minemawari, H. et al. Inkjet printing of single-crystal films. Nature 475, 364–367 (2011).

9 Forrest, S. R. Electronic Appliances on Plastic. Nature 428, 911–918 (2004).

10 Li, J. et al. A stable solution-processed polymer semiconductor with record high-mobility for printed transistors. Sci. Rep. 2, 754 (2012).

11 Paterson, A. F. et al. Addition of the Lewis Acid Zn(C6F5)2 Enables Organic Transistors with a Maximum Hole Mobility in Excess of 20 cm2 V−1 s−1. Adv. Mater. 31, 1–8 (2019).

12 Mitsui, C. et al. High-performance solution-processable N-shaped organic semiconducting materials with stabilized crystal phase. Adv. Mater. 26, 4546–4551 (2014).

13 Quinn, J. T. E., Zhu, J., Li, X., Wang, J. & Li, Y. Recent progress in the development of n-type organic semiconductors for organic field effect transistors. J. Mater. Chem. C 5, 8654–8681 (2017).

14 Mei, J., Kim, D. H., Ayzner, A. L., Toney, M. F. & Bao, Z. Siloxane-Terminated Solubilizing Side Chains: Bringing Conjugated Polymer Backbones Closer and Boosting Hole Mobilities in Thin-Film Transistors. J. Am. Chem. Soc. 133, 20130–20133 (2011).

15 Tsao, H. N. et al. Ultrahigh mobility in polymer field-effect transistors by design. J. Am. Chem. Soc. 133, 2605–2612 (2011).

16 Lei, T., Wang, J.-Y. & Pei, J. Roles of Flexible Chains in Organic Semiconducting Materials. Chem. Mater. 26, 594–603 (2014).

17 Sung, A., Ling, M. M., Tang, M. L., Bao, Z. & Locklin, J. Correlating Molecular Structure to Field-Effect

Mobility: The Investigation of Side-Chain Functionality in Phenylene−Thiophene Oligomers and Their Application in Field Effect Transistors. Chem. Mater. 19, 2342–2351 (2007).

18 Osaka, I. et al. High-Lamellar Ordering and Amorphous-Like π-Network in Short-Chain Thiazolothiazole−Thiophene Copolymers Lead to High Mobilities. J. Am. Chem. Soc. 131, 2521–2529 (2009).

19 Zhang, C. et al. Pursuing High-Mobility n-Type Organic Semiconductors by Combination of "Molecule-Framework" and "Side-Chain" Engineering. Adv. Mater. 28, 8456–8462 (2016).

20 Gao, X. et al. Core-Expanded Naphthalene Diimides Fused with 2-(1,3-Dithiol-2-Ylidene)Malonitrile Groups for High-Performance, Ambient-Stable, Solution-Processed n-Channel Organic Thin Film Transistors. J. Am. Chem. Soc. 132, 3697–3699 (2010).

21 Melville, O. A., Lessard, B. H. & Bender, T. P. Phthalocyanine-Based Organic Thin-Film Transistors: A Review of Recent Advances. ACS Appl. Mater. Interfaces 7, 13105–13118 (2015).

22 Pearson, A. J. et al. Silicon phthalocyanines as dopant red emitters for efficient solution processed OLEDs. J. Mater. Chem. C 5, 12688–12698 (2017).

23 Zysman-Colman, E. et al. Solution-Processable Silicon Phthalocyanines in Electroluminescent and Photovoltaic Devices. ACS Appl. Mater. Interfaces 8, 9247–9253 (2016).

24 Dang, M. T. et al. Bis(tri-n-alkylsilyl oxide) silicon phthalocyanines: A start to establishing a structure property relationship as both ternary additives and non-fullerene electron acceptors in bulk heterojunction organic photovoltaic devices. J. Mater. Chem. A 5, 12168–12182 (2017).

25 Zhang, Y., Ng, D. K. P. & Fong, W. P. Antitumor immunity induced by the photodynamic action of BAM-SiPc, a silicon (IV) phthalocyanine photosensitizer. Cell. Mol. Immunol. 16, 676–678 (2019).

26 Ma, D. et al. Benzyl ester dendrimer silicon phthalocyanine based polymeric nanoparticle for in vitro photodynamic therapy of glioma. J. Lumin. 207, 597–601 (2019).

27 Bonardi, A.-H. et al. Photoinduced Thermal Polymerization Reactions. Macromolecules 51, 8808–8820 (2018).

28 H. Bonardi, A. et al. High Performance Near-Infrared (NIR) Photoinitiating Systems Operating under Low Light Intensity and in the Presence of Oxygen. Macromolecules 51, 1314–1324 (2018).

29 Melville, O. A., Grant, T. M. & Lessard, B. H. Silicon phthalocyanines as N-type semiconductors in organic thin film transistors. J. Mater. Chem. C 6, 5482–5488 (2018).

30 Yutronkie, N. J., Grant, T. M., Melville, O. A., Lessard, B. H. & Brusso, J. L. Old molecule, new chemistry: Exploring silicon phthalocyanines as emerging N-type materials in organic electronics. Materials (Basel). 12, 5–10 (2019).

31 Melville, O. A. et al. Ambipolarity and Air Stability of Silicon Phthalocyanine Organic Thin-Film Transistors. Adv. Electron. Mater. 5, 1–7 (2019).

32 Grant, T. M., Rice, N. A., Muccioli, L., Castet, F. & Lessard, B. H. Solution-Processable n-Type Tin Phthalocyanines in Organic Thin Film Transistors and as

Ternary Additives in Organic Photovoltaics. ACS Appl. Electron. Mater. 1, 494–504 (2019).

33 Wei Chou, K. et al. Late stage crystallization and healing during spin-coating enhance carrier transport in small-molecule organic semiconductors. J. Mater. Chem. C 2, 5681–5689 (2014).

34 Li, R. et al. Heterogeneous nucleation promotes carrier transport in solution-processed organic field-effect transistors. Adv. Funct. Mater. 23, 291–297 (2013).

35 Hölzl, J. & Schulte, F. K. Work function of metals. in Solid Surface Physics 1–150 (Springer, 1979). doi:10.1007/BFb0048919.

36 D'Avino, G. et al. Electrostatic Phenomena in Organic Semiconductors: Fundamentals and Implications for Photovoltaics. J. Phys. Condens. Matter 28, 1–21 (2016).

37 Marom, N., Hod, O., Scuseria, G. E. & Kronik, L. Electronic structure of copper phthalocyanine: A comparative density functional theory study. J. Chem. Phys. 128, 164107 (2008).

38 Swick, S. M. et al. Closely packed, low reorganization energy π-extended postfullerene acceptors for efficient polymer solar cells. Proc. Natl. Acad. Sci. 115, E8341–E8348 (2018).

39 Gali, S. M., Matta, M., Lessard, B. H., Castet, F. & Muccioli, L. Ambipolarity and Dimensionality of Charge Transport in Crystalline Group 14 Phthalocyanines: A Computational Study. J. Phys. Chem. C 122, 2554–2563 (2018).

40 Shi, Y. & Li, X. Solution-processable ambipolar organic field-effect transistor based on Co-planar bisphthalocyaninato copper. Org. Electron. 15, 286–293 (2014).

41 Chang, P. C. et al. Film Morphology and Thin Film Transistor Performance of Solution-Processed Oligothiophenes. Chem. Mater. 16, 4783–4789 (2004).

42 Oh, J. H., Liu, S., Bao, Z., Schmidt, R. & Würthner, F. Air-stable n -channel organic thin-film transistors with high field-effect mobility based on N, N′ -bis(heptafluorobutyl)-3,4:9,10-perylene diimide. Appl. Phys. Lett. 91, (2007).

43 C. Vebber, M., M. Grant, T., L. Brusso, J. & H. Lessard, B. Bis (tri-alkylsilyl oxide) silicon phthalocyanines: understanding the role of solubility on device performance as ternary additives in organic photovoltaics. Langmuir 0, (2020).

44 Rivnay, J., Mannsfeld, S. C. B., Miller, C. E., Salleo, A. & Toney, M. F. Quantitative Determination of Organic Semiconductor Microstructure from the Molecular to Device Scale. Chem. Rev. 112, 5488–5519 (2012).

45 Li, L., Tang, Q., Li, H. & Hu, W. Molecular Orientation and Interface Compatibility for High Performance Organic Thin Film Transistor Based on Vanadyl Phthalocyanine. J. Phys. Chem. B 112, 10405–10410 (2008).

46 Giri, G. et al. Tuning charge transport in solution-sheared organic semiconductors using lattice strain. Nature 480, 504–508 (2011).

47 Tantiwiwat, M., Tamayo, A., Luu, N., Dang, X.-D. & Nguyen, T.-Q. Oligothiophene Derivatives Functionalized with a Diketopyrrolopyrrolo Core for Solution-Processed Field Effect Transistors: Effect of Alkyl Substituents and Thermal Annealing. J. Phys. Chem. C 112, 17402–17407 (2008).

48 Sung, C. F. et al. Flexible fullerene field-Effect transistors fabricated through solution processing. Adv. Mater. 21, 4845–4849 (2009).

49 Mityashin, A. et al. Multiscale Modeling of the Electrostatic Impact of Self-Assembled Monolayers used as Gate Dielectric Treatment in Organic Thin-Film Transistors. ACS Appl. Mater. Interfaces 6, 15372–15378 (2014).

50 Youn, J. et al. Fused thiophene semiconductors: Crystal structure-film microstructure transistor performance correlations. Adv. Funct. Mater. 23, 3850–3865 (2013).

51 Hutchison, G. R., Ratner, M. A. & Marks, T. J. Intermolecular charge transfer between heterocyclic oligomers. Effects of heteroatom and molecular packing on hopping transport in organic semiconductors. J. Am. Chem. Soc. 127, 16866–16881 (2005).

52 Liman, C. D. et al. Two-dimensional GIWAXS reveals a transient crystal phase in solution-processed thermally converted tetrabenzoporphyrin. J. Phys. Chem. B 117, 14557–14567 (2013).

53 Melville, O. A. et al. Contact Engineering Using Manganese, Chromium, and Bathocuproine in Group 14 Phthalocyanine Organic Thin-Film Transistors. ACS Appl. Electron. Mater. 2, 1313–1322 (2020).

54 Valeev, E. F., Coropceanu, V., da Silva Filho, D. A., Salman, S. & Brédas, J.-L. Effect of Electronic Polarization on Charge-Transport Parameters in Molecular Organic Semiconductors. J. Am. Chem. Soc. 128, 9882–9886 (2006).

55 Stehr, V., Pfister, J., Fink, R. F., Engels, B. & Deibel, C. First-principles calculations of anisotropic charge-carrier mobilities in organic semiconductor crystals. Phys. Rev. B 83, 155208 (2011).

56 Neese, F. The ORCA program system. WIREs Comput. Mol. Sci. 2, 73–78 (2012).

57 Frisch, M. J. et al. Gaussian 16. (2016).

58 Jiang, Z. GIXSGUI : a MATLAB toolbox for grazing-incidence X-ray scattering data visualization and reduction, and indexing of buried three-dimensional periodic nanostructured films. J. Appl. Crystallogr. 48, 917–926 (2015).

Chapter 3. Highlighting the Processing Versatility of a Silicon Phthalocyanine Derivative for OTFTs

This chapter is adapted from: ***Cranston, R. R.****, King, B., Dindault, C., Grant, T. M., Rice, N. A., Tonnelé, C., Muccioli, L., Castet, F., Swaraj, S., Lessard, B. H. Highlighting the Processing Versatility of a Silicon Phthalocyanine Derivative for Organic Thin-Film Transistors. J. Mater. Chem. C (2022).*

Context

Learning from the structure-property-performance relationship established in **Chapter 2**, a SiPc derivative with axially substituted short linear alkyl chains was developed and synthesized. This molecule possessed unique properties allowing it to be processed by both sublimation and solution fabrication processes. Using this SiPc derivative I fabricated OTFTs by spin-coating with my colleague Dr. Benjamin King fabricating OTFTs by physical vapour deposition. For this work, I wanted to investigate the difference in SiPc thin-film formation and OTFT electrical characteristics between the two fabrication techniques to better understand the nucleation, crystallization, and thin-film formation processes of SiPcs deposited from solution. OTFTs using this SiPc derivative achieved higher mobility transistors compared to the longer alkyl chain SiPcs used in **Chapter 2**, and demonstrated consistent device performance despite the considerable differences in film formation achieved by PVD and solution fabrication.

Contributions of Authors

This work was completed through contributions of all authors. For this work, I fabricated and characterized solution deposited OTFTs, conducted data analysis and wrote the manuscript. B.K. fabricated and characterized PVD deposited OTFTs. C.D. conducted STXM experiments with analysis. T.M.G synthesised the SiPc derivate used for this work. C.T and L.M. conducted DFT calculations with analysis. N.A.R conducted AFM imaging. F.C., S.S., and B.H.L., provided supervision for the project.

Abstract

Silicon phthalocyanine (SiPc) derivatives have recently emerged as promising materials for n-type organic thin-film transistors (OTFTs) with the ability to be fabricated either by solid state or solution processes through axial functionalization. Among those, bis(tri-*n*-propylsilyl oxide) SiPc ((3PS)$_2$-SiPc) is unique as it can be processed by sublimation, while being soluble enough for solution processing. In this work, the charge transport properties of (3PS)$_2$-SiPc and its polymorphic forms were studied through Kinetic Monte Carlo (KMC) simulations and density functional theory (DFT) calculations along with the characterization of (3PS)$_2$-SiPc in n-type OTFTs fabricated by physical vapour deposition (PVD) and spin coating. Post-deposition thin-film characterization by X-ray diffraction (XRD), atomic force microscopy (AFM), and scanning transmission X-ray microscopy (STXM) was used to assess film morphology and microstructure in relation to the electrical performance of OTFTs. The differences in film formation by PVD and solution fabrication had little effect on OTFT performance with comparable field-effect mobility and threshold voltage ranging between 0.01-0.04 cm^2 V^{-1} s^{-1} and 18-36 V respectively. Consistent charge transport properties of (3PS)$_2$-SiPc OTFTs achieved at different fabrication conditions highlights the processing versatility of this material.

Introduction

Since the 1980s organic thin-film transistors (OTFTs) using conjugated polymer and small molecule materials have been envisioned as an improved technology to traditional inorganic silicon and germanium transistors.[1,2] The low switching speed and charge carrier mobility of many organic semiconducting materials contribute to the fact that OTFTs are meant to supplement inorganic technologies, and advance novel applications requiring large areas, high flexibility, less energy intensive processing conditions, and low cost. Most notably, OTFTs serve as the main component of inexpensive flexible electronic circuits facilitating the design of state-of-the-art biological sensors[3–5], wearable electronics[6–8], and flexible displays[9–11]. An applied positive or negative voltage can yield either an accumulation of holes or electrons in the intrinsically semiconducting materials used in OTFTs, resulting in n- or p-type transistor behaviour. For many organic small molecules p-type transistor operation is dominant, however through the synthesis of materials with high electron affinities significant advances have been made in the development of n-type OTFTs. Unfortunately, many n-type behaving materials demonstrate lower mobilities, worse environmental/chemical stability, and lower solubility compared to materials for p-type OTFTs, making them impractical for many applications.[12,13]

Metal or metalloid phthalocyanines (MPcs) are a vast group of semiconducting organic small molecules comprised of a conjugated aromatic structure with a central chelated metal ion. For over 90 years MPcs have been used extensively as dyes, pigments, and more recently as commercial photoreceptors owing to their brilliant colour, ease of synthesis, favourable opto-electric properties, and high thermal, mechanical, and environmental stability.[14] Compared to divalent MPcs, silicon phthalocyanine (SiPc) derivatives offer two additional axial positions for added molecular tunability. Additionally, SiPcs possess n-type semiconducting behaviour rather than the more common p-type behaviour demonstrated by most MPc based OTFTs. The high thermal stability of phenoxy substituted SiPcs have enabled the fabrication of n-type OTFTs by physical vapour deposition (PVD) with a maximum mobility of 0.54 $cm^2\ V^{-1}\ s^{-1}$ achieved by bis(pentafluorophenoxy) SiPc (F10-SiPc).[15–18] Phenoxy substituted SiPcs have also demonstrated promising results in mixed PVD and solution fabricated organic photovoltaic devices (OPVs) exhibiting an open-circuit voltage (V_{oc}) of 0.88 V.[19] The highly soluble alkyl substituted SiPc derivatives have been used for solution fabricated n-type OTFTs[20,21] and OPVs[22,23], with bis(tri-*n*-butylsilyl oxide) SiPc ($(3BS)_2$-SiPc) demonstrating the highest performance in both types of devices. Bis(tri-*n*-propylsilyl oxide) SiPc ($(3PS)_2$-SiPc) is a unique derivative as its synthetic simplicity, scalable synthesis, n-type behaviour, high solubility, and high thermal stability makes it an exceedingly versatile material (**Figure 3.1**).[24] Unlike previously reported SiPcs,[25] $(3PS)_2$-SiPc possesses unique processing duality facilitating fabrication by both PVD and solution processing, owing to its ability to sublime without decomposing and its high solubility in chlorinated solvents (15 mg ml^{-1}).[24] These features of $(3PS)_2$-SiPc allow for easy purification and a multitude of choice for device fabrication processing methods and conditions.

Herein, the fabrication and characterization of PVD and solution fabricated bottom-gate top-contact $(3PS)_2$-SiPc OTFTs are reported. The performance of PVD and solution fabricated devices was compared through post-deposition characterization by thin-film X-ray diffraction (XRD) and atomic force microscopy (AFM). Additionally, scanning transmission X-ray microscopy (STXM) was used to elucidate the distribution of $(3PS)_2$-SiPc molecules in films fabricated from solution. Kinetic Monte Carlo (KMC) simulations and density functional theory (DFT) calculations were performed to evaluate the crystal structure and access the charge transport dimensionality of each polymorphic form of $(3PS)_2$-SiPc and related to OTFT characterization. This work aims to highlight the fabrication versatility and exceptional performance of $(3PS)_2$-SiPc in OTFTs with hopes to further the advancement of high performing n-type MPc based organic electronic devices.

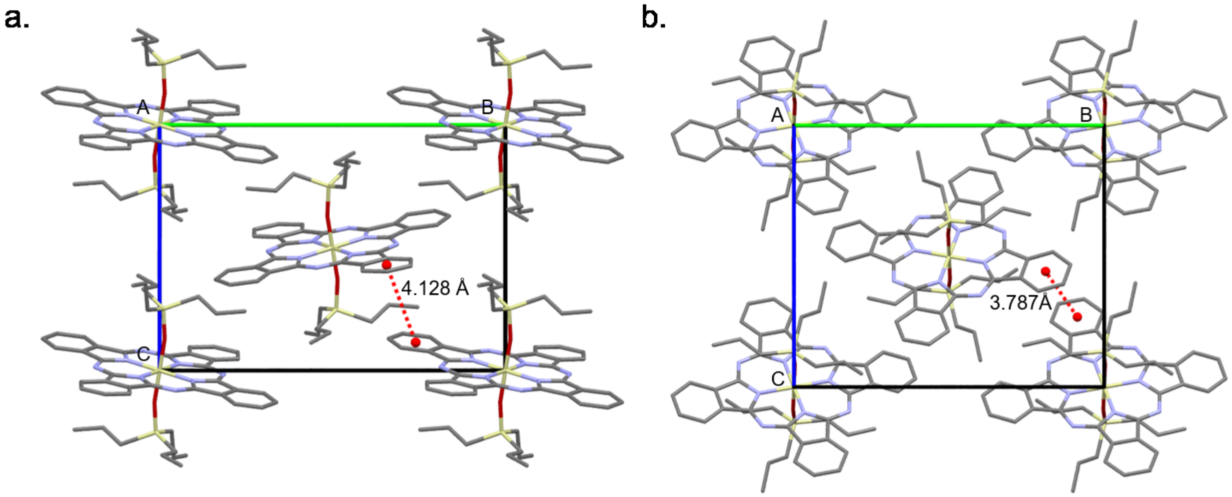

Figure 3.1. Stick representation of the crystal packing of (a) polymorph 1 (CCDC# 2091746) with unit cell (a 11.26, b 17.32, c 12.52, α 90, β 101.5, γ 90) and (b) polymorph 2 (CCDC# 2067659) with unit cell (a 10.23, b 16.43, c 14.62, α 90, β 108.9, γ 90) of $(3PS)_2$-SiPc viewed along the a axis.

Results and Discussion

Quantum Chemical Calculations

Transport levels, optical properties and charge transport parameters of the $(3PS)_2$-SiPc molecule were first studied with DFT and time-dependent (TD) DFT calculations. The highest occupied molecular orbital (HOMO), lowest unoccupied molecular orbital (LUMO), and LUMO+1 energies, equaling -5.11 eV, -2.92 eV, and -2.91 eV respectively, are close to those of similar alkylsiloxy-substituted SiPcs[21] and rather appropriate for ambipolar transport. Vertical transition energies (ΔE) and oscillator strengths (f) from the ground state S_0 towards the nearly degenerate singlet states S_1 and S_2 of $(3PS)_2$-SiPc were calculated to be ΔE_{01} (f_{01}) = 2.057 eV (0.33) and ΔE_{02} (f_{02}) = 2.061 eV (0.34). The electron affinity (EA) of $(3PS)_2$-SiPc, equal to 1.99 eV, is again very similar to EA values calculated for previously reported MPcs.[21] However, the internal charge transfer reorganization energy (λ = 210 meV), which characterizes the amplitude of geometric relaxation effects occurring upon electron transfer, is slightly lower than those previously reported for other alkylsiloxy-substituted SiPcs (213-266 meV).[21] Compared to these materials, electron delocalization in the frame of an activated hopping-like transport is thus expected to be slightly more favoured in $(3PS)_2$-SiPc (**Equation 3.1**).

The largest electronic couplings (transfer integrals) calculated between molecular neighbours in polymorphs 1 and 2 are shown in **Figure 3.2**, while the complete set of non-negligible J_e values are reported in **Table S3.1** and **Table S3.2**. The largest coupling in polymorph 1 amounts to 7.6 meV and occurs between molecules stacked parallel to the (0; ±0.5; ±0.5) directions. In polymorph 2, the highest J_e value is found along the (±1; 0; 0) direction, i.e. parallel to the *a* crystal axis, with a larger magnitude of 11.4 meV. As reported in **Table S3.1** and **Table S3.2**, rather large electronic couplings (10.1 eV) also exist in polymorph 2 along the (±0.5; ±0.5; ±0.5) directions. On the contrary, these secondary transfer integrals are much lower in polymorph 1 (1.6 meV, along the *a* axis), which makes polymorph 2 more prone to display efficient and multidimensional charge transport. This is confirmed by the calculated electron mobilities reported in **Table S3.3** and **Figure 3.3**: besides having mobilities approximately three times lower, polymorph 1 is almost not conducing along the a axis, as a consequence of the above mentioned small transfer integrals. These results suggest that charge transport through $(3PS)_2$-SiPc should be highly dependent on the amount and nature of the polymorphs which are present in the device.

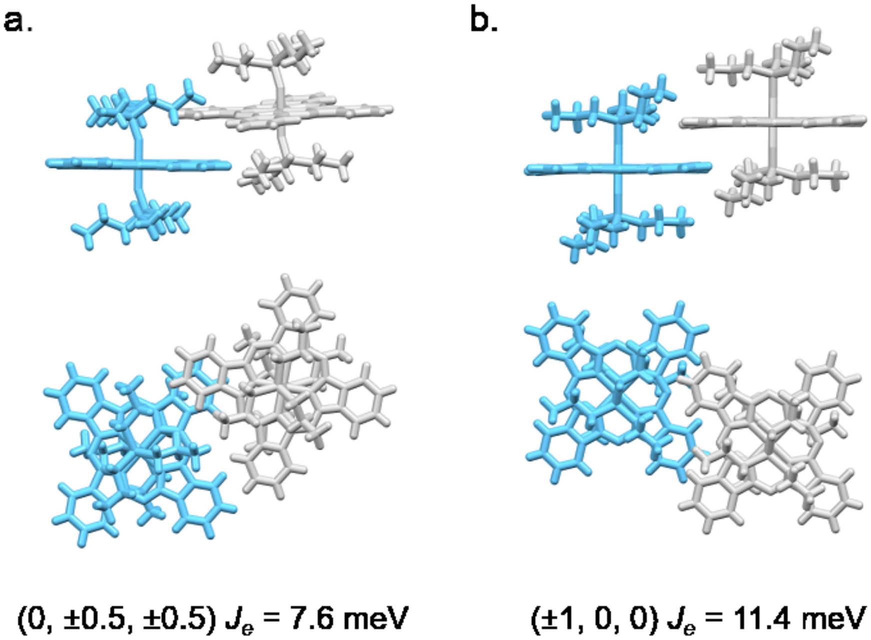

Figure 3.2. Top and side views of molecular dimers giving rise to the largest electronic couplings (J_e) of (a) polymorph 1 and (b) polymorph 2 of $(3PS)_2$-SiPc.

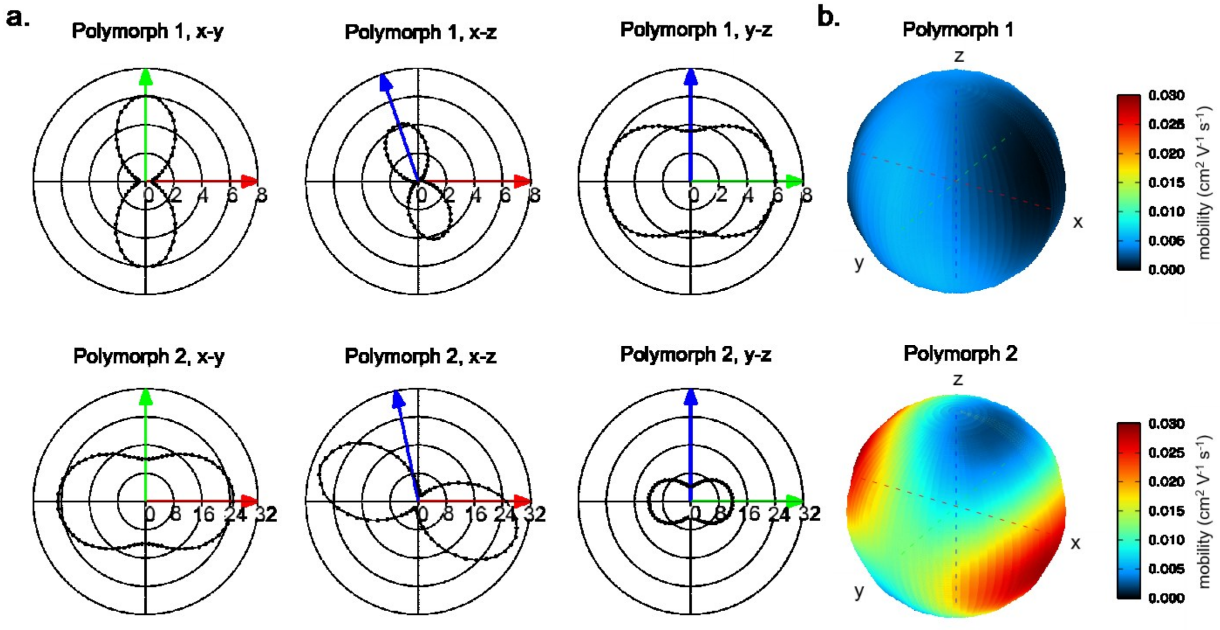

Figure 3.3. (a) Polar plots of electron mobility (x 10^{-3} cm^2 V^{-1} s^{-1}) as a function of the direction of the applied electric field in the x-y, x-z and y-z planes. Red, green and blue arrows represent the projection in those planes of *a*, *b*, and *c* crystal axes, respectively. (b) 3D map of electron mobility as a function of the direction of the applied electric field. The position on the spherical surface represents the direction of the applied electric field, and the color the magnitude of mobility. Mobilities were calculated by Kinetic Monte Carlo simulations, using the Marcus model ($E = 1000$ V cm^{-1}, $\lambda = 0.41$ eV, $T = 300$ K, $\sigma = 0.052$ eV).

Organic Thin-Film Transistors

Bottom-gate top-contact OTFTs were fabricated on silicon substrates with a dielectric layer comprised of thermally grown silicon oxide. (3PS)$_2$-SiPc thin-films were deposited by either PVD or spin coating and annealed to create the semiconducting active layer. All OTFT electrical characterization was performed in a nitrogen environment at room temperature to obtain the saturation regime electron field-effect mobility (μ_e), threshold voltage (V_T) and on/off current ratio ($I_{on/off}$) of each transistor with results displayed in **Table 3.1**. Characteristic output curves, as well as forward and reverse transfer curves of PVD and solution fabricated OTFTs are displayed in **Figures S3.4** and **Figure S3.5** respectively. OTFTs made by both fabrication methods resulted in remarkably similar electrical performance with average mobilities in the range of 1.0-3.9 x 10^{-2} cm^2 V^{-1} s^{-1} for PVD devices and 2.3-4.1 x 10^{-2} cm^2 V^{-1} s^{-1} for solution, with threshold voltages between 18 V and 32 V for both methods. In comparison to other bottom-gate top-contact bis(tri-alkylsilyl oxide) SiPc OTFTs which exhibit average mobilities ranging from 10^{-4}-10^{-2} cm^2 V^{-1} s^{-1}

and threshold voltages between 20-40 V,[21] $(3PS)_2$-SiPc OTFTs displayed comparable or superior electrical performance. All OTFTs exhibited consistently high $I_{on/off}$, between 10^4-10^5, suitable for device operation and comparable to that of other SiPc OTFTs fabricated by both solution and evaporative processing.[17,21] To date, the highest performing solution fabricated SiPc OTFT was reported with $(3BS)_2$-SiPc exhibiting a $\mu_{e,\ max}$ of 4.3 x 10^{-2} cm^2 V^{-1} s^{-1}, $\mu_{e,\ avg}$ of 2.8 x 10^{-2} cm^2 V^{-1} s^{-1} and V_T of 17.6 V.[21] However, the $(3PS)_2$-SiPc OTFTs reported herein surpasses these results with a $\mu_{e,\ max}$ of 4.9 x 10^{-2} cm^2 V^{-1} s^{-1}, and $\mu_{e,\ avg}$ of 4.1 x 10^{-2} cm^2 V^{-1} s^{-1}, despite a notably greater V_T of 27.6 V. Axially substituted phenoxy SiPc OTFTs with a bottom-gate top-contact architecture fabricated by PVD have demonstrated similar electrical performance to alkyl substituted SiPcs with mobilities in the range of 10^{-3}-10^{-2} cm^2 V^{-1} s^{-1} and threshold voltages between 20-40 V.[17] PVD fabricated $(3PS)_2$-SiPc OTFTs display similar or greater electrical performance compared to phenoxy substituted SiPcs, with the exception of F10-SiPc, which to our knowledge reports the greatest $\mu_{e,\ avg}$ of 0.27 cm^2 V^{-1} s^{-1} with a V_T of 23.5 V for PVD fabricated bottom-gate top-contact SiPc OTFTs.[16]

Owing to the difference in crystallite nucleation and film growth between PVD and solution fabrication methods, one would expect differences in the electrical performance between OTFTs fabricated by these different processes. While crystallite growth by PVD relies on a carefully controlled deposition rate and substrate temperature, crystallite growth from solution is characterized by the rate of solvent evaporation, which is hardly controllable and typically occurs orders of magnitude faster than PVD.[26–29] The variable crystallization rate achieved by solution fabrication can lead to large crystallite formation which can negatively impact charge transport due to wider grain boundaries and a high degree of molecular disorder.[21,30] However, it is well known that charge transport is dependent not only on crystallite size but also on several other factors including grain boundary effects, surface roughness, crystallite packing, and molecular orientation, with the interplay between these parameters is crucial for achieving high mobility OTFTs.[31–34] For $(3PS)_2$-SiPc, the effects of these factors are mitigated by the efficient charge transport in the material, resulting in OTFTs with similar electrical performance irrespective of fabrication method and thin-film characteristics.

Table 3.1. Summary of PVD and solution fabricated bottom-gate top-contact $(3PS)_2$-SiPc transistor characteristics, measured at room temperature in nitrogen environment. Averages were calculated from *n* unique transistors.

Deposition Method	Annealing Temp (°C)	$\mu_{e,\,max}$ (10^{-2} cm^2 V^{-1}s^{-1})	$\mu_{e,\,avg}$ (10^{-2} cm^2 V^{-1} s^{-1})	V_T (V)	$I_{on/off}$	*n*
PVD	25	6.4	3.9 ± 0.91	26.8 ± 3.5	10^5	39
	50	2.0	1.5 ± 0.26	31.5 ± 1.7	10^5	27
	100	6.5	2.6 ± 0.66	26.6 ± 2.7	10^5	30
	150	1.6	1.0 ± 0.11	18.4 ± 2.1	10^5	36
Solution	25	2.9	2.3 ± 0.40	34.0 ± 3.3	10^5	17
	50	4.8	3.4 ± 0.97	32.3 ± 4.0	10^5	12
	100	4.9	4.1 ± 0.41	27.6 ± 1.6	10^4	13
	150	3.5	2.8 ± 0.48	19.6 ± 3.2	10^4	12

To further assess $(3PS)_2$-SiPc thin-film formation by PVD and solution fabrication, the effects of post-deposition thermal annealing were studied through OTFT electrical performance and XRD. Characteristic transfer curves of PVD (**Figure 3.4a**) and solution (**Figure 3.4b**) fabricated OTFTs annealed from 25-150°C displayed little change in μ_e. However, at an annealing temperature of 150°C a reduction in V_T was observed in all OTFTs, with PVD devices exhibiting a 7.2 V decrease from an average V_T of 26.8 V to 18.4 V, and solution devices exhibiting a greater reduction of 14.4 V from an average V_T of 34.0 V to 19.6 V. Thermogravimetric analysis (TGA) and differential scanning calorimetry (DSC) measurements of $(3PS)_2$-SiPc powder show no significant thermal events before the decomposition temperature at approximately 340°C and no phase transitions between 25-240°C.[24] The high thermal stability of $(3PS)_2$-SiPc, together with the three dimensional character of charge transport of polymorph 2, as revealed by DFT and KMC calculations, may be the reasons for the consistently high μ_e observed in OTFTs fabricated by different methods, suggesting that thermal annealing can be used on $(3PS)_2$-SiPc devices to further improve V_T without affecting μ_e.

To investigate in detail the effect of annealing on crystalline order, XRD patterns of PVD and solution fabricated $(3PS)_2$-SiPc thin-films annealed at increasing temperatures are shown in **Figure 3.4c** and **Figure 3.4d**. PVD films exhibit a primary peak at approximately $2\theta = 9.00°$ corresponding to a d-spacing of 9.85 Å, and a secondary lower intensity peak at $2\theta = 7.80°$ corresponding to a d-spacing of 11.35 Å. At higher annealing temperatures the intensity of the secondary peak decreases, while an increase in intensity is observed for the primary peak. In contrast, solution fabricated films exhibit a single high intensity peak at 2θ = 8.90° corresponding to a d-spacing of 9.96 Å when annealed at 25°C, which shifts to 2θ = 9.02° (d-spacing of 9.83 Å), decreases in width, and increases in intensity when annealed at 150°C. With both fabrication methods, thermal annealing at 150°C results in an increase in peak intensity and shift in peak position to 2θ = 9.02°, indicating the conversion to a different crystallite packing structure. As PVD fabricated thin-films exhibit an XRD signal around 2θ = 9.00-9.02°, it is suggested that this fabrication method initially produces this packing structure; with post deposition thermal annealing the packing of additional crystallites are converted resulting in the greater peak intensity. Conversely, solution fabrication does not initially produce thin-films with this packing structure and requires thermal annealing for conversion as evidenced by the large peak shift from 2θ = 8.90° to 2θ = 9.02°.

XRD peak intensity is related to grain texture, crystallite orientation and degree of crystallinity with a higher intensity indicating a more consistently oriented thin-film.[35] Peak position is attributed to the intermolecular d-spacing and peak width to grain size, such that an increase in peak position along the 2θ axis represents a decrease in d-spacing, with a narrower peak indicating larger crystallite formation.[35] Therefore, the increase in peak intensity and shift in peak position that occurs at higher annealing temperatures indicates the formation of more highly ordered, densely packed, crystalline thin-films as evident by the reduction in intermolecular d-spacing and increase in peak intensity. Additionally, the narrower and higher intensity peaks exhibited by solution fabricated films suggest the films are comprised of larger crystallites compared to PVD films, which is corroborated by AFM images of PVD (**Figure 3.4e**) and solution fabricated (**Figure 3.4f**) $(3PS)_2$-SiPc thin-films. PVD films annealed at 25°C show a densely packed network of small circular crystallites, with many grain boundaries and a surface roughness of 4.33 nm. In contrast, the morphology of solution fabricated films exhibits large plate like crystallites, with fewer boundaries and a surface roughness of 1.65 nm. Although there are significant differences in thin-film morphology between PVD and solution fabricated $(3PS)_2$-SiPc films, both morphologies exhibit interconnected, and largely homogenous features that promote efficient charge transport.

The predicted XRD patterns (**Figure S3.6**) of polymorph 1 and 2 calculated from single crystal data shows two peaks at 2θ = 8.82° and 9.50° for polymorph 1 and 2θ = 8.36° and 9.14°

for polymorph 2. As neither of the thin-film XRD data of PVD and solution fabricated films aligns with these peaks, we surmise that a new polymorphic form is present in films compared to powder samples. As discussed, the polymorphic nature of $(3PS)_2$-SiPc dictates the degree of charge transport with a high dimensional dependence. Both PVD and solution fabrication methods resulted in $(3PS)_2$-SiPc thin-films with high mobilities and favourable charge transport, suggesting that the new polymorph present in films may have a similar structure to that of polymorph 2.

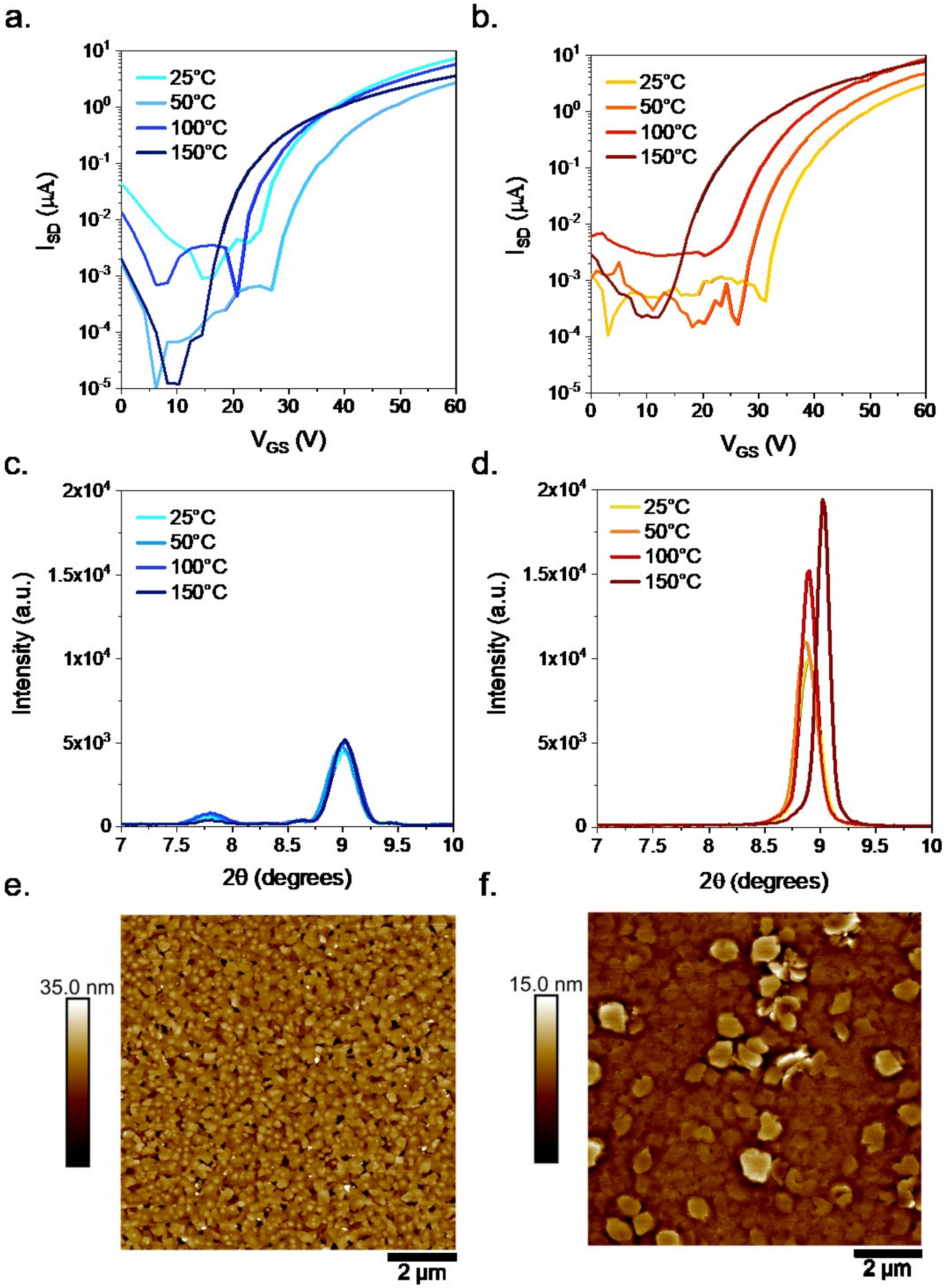

Figure 3.4. Characteristic transfer curves of (a) PVD and (b) solution fabricated transistors annealed at various temperatures. XRD patterns of annealed $(3PS)_2$-SiPc thin-films fabricated by (c) PVD and (d) solution fabrication. AFM image (10 μm x 10 μm) of $(3PS)_2$-SiPc thin-films annealed at 25°C fabricated by (e) PVD and (f) solution fabrication.

STXM Characterization

STXM measurements at the carbon K-edge were carried out on a solution fabricated thin-film of $(3PS)_2$-SiPc with X-rays irradiated in normal incidence to the sample and measurements executed by altering the polarization of the beam between linear horizontal (LH) and linear vertical (LV) (**Figure 3.5a**). Planar MPcs, such as SiPcs, commonly form a herringbone packing structure with alternating face-to-edge and face-to-face molecular packing oriented either or both edge-on and face-on to the substrate surface.[36–38] For the OTFT architecture used herein, edge-on orientation of the $(3PS)_2$-SiPc molecules is desired as the increased π-π stacking along this direction results in greater charge transport between the source-drain electrodes, ultimately resulting in higher mobility OTFTs.[17,21,39,40] The highly anisotropic nature and directional dependent charge transport of MPcs, in particular $(3PS)_2$-SiPc as evident by polymorph 1 and polymorph 2 in **Figure 3.3**, further justifies additional thin-film characterization.

Figure 3.5b shows the carbon (C) 1s near edge X-ray absorption fine structure (NEXAFS) spectra of $(3PS)_2$ SiPc, which exhibits a sharp peak at 285 eV corresponding to the C 1s $\rightarrow \pi^*$ transition of the C=C bonds, a small shoulder at approximately 288 eV corresponding to the C 1s $\rightarrow \sigma^*$ transition of the C-H bonds, and two broad contributions at 293 eV and 304 eV corresponding to the C 1s $\rightarrow \sigma^*$ transition of the C-C bonds.[41] In NEXAFS spectroscopy, the intensity of a transition is proportional to the square of the cosine of the angle between the transition vector ($\overrightarrow{\pi^*}$ in our case at 285 eV) and the electric field vector of the beam ($\overrightarrow{E_{LV}}$ or $\overrightarrow{E_{LH}}$ in our case).[42] Monitoring the resonance intensity as a function of the polarization can thus provide information about the local molecular orientation. The NEXAFS spectra of a $(3PS)_2$ SiPc film shows a strong dichroic behaviour with an increase in resonance from 0.28 to 0.40 of the 285 eV peak when the polarization is switched from LH to LV. This partial increase, corresponding to a C 1s $\rightarrow \pi^*$ transition perpendicular to the SiPc plane, indicates that the molecules are not orientated purely face-on nor purely edge-on to the substrate but rather aligned in pseudo edge-on configuration. Optical density images were taken at 285 eV for both LV and LH polarizations with a LH-LV difference image generated from these (**Figure 3.5c** and **Figure 3.5d** respectively). The dichroic behaviour can be clearly seen from these images as shown by the highlighted cluster of pixels which turns on from LH to LV, with an averaged difference in optical density of -0.1. From the LH-LV difference image, the domains of various intensity correspond to different SiPc molecular orientations, indicating the films are comprised of molecules orientated in many angles to the substrate surface. Given the small amplitude in the π* resonance intensity differences, these variations in molecular orientation are relatively small, therefore the film remains relatively homogenous throughout with $(3PS)_2$ SiPc domains on the order of 1-4 µm. This analysis demonstrates that STXM is a powerful technique that can be used to characterize MPcs thin-films and provide insight into the molecular orientation through the entire film.

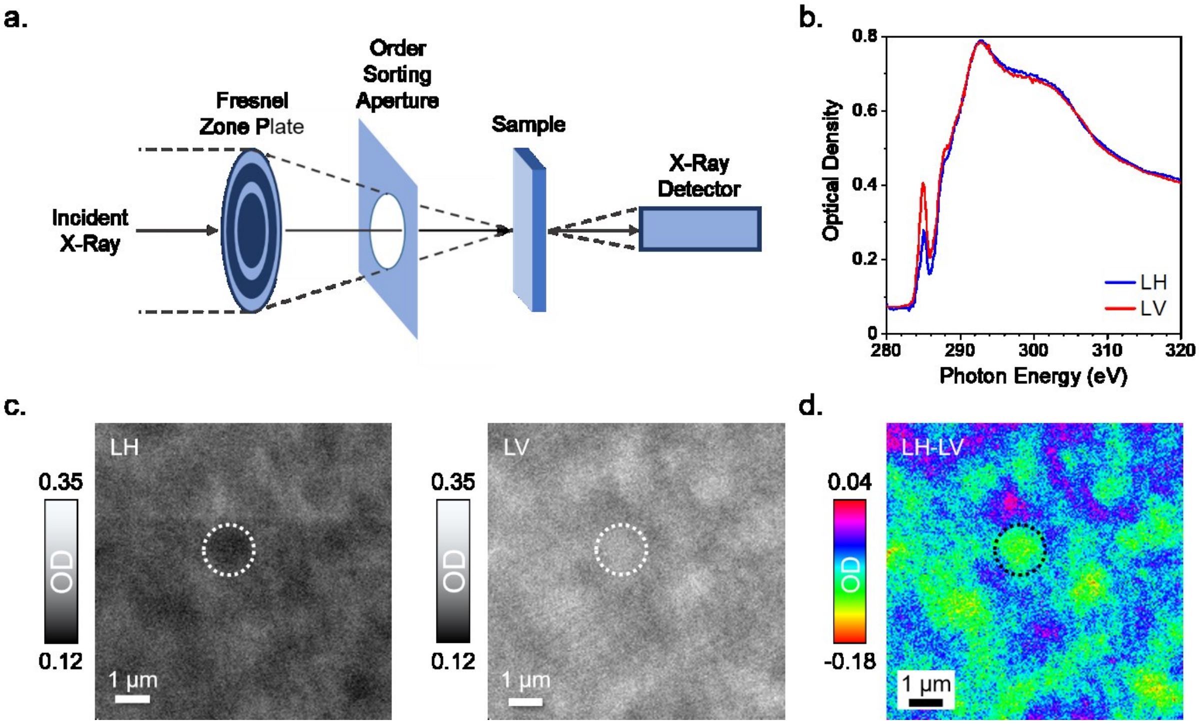

Figure 3.5. (a) Schematic diagram of STXM equipment. (b) NEXAFS spectra at the carbon K-edge, (c) optical density images (10 µm x 10 µm) at 285 eV of solution fabricated $(3PS)_2$-SiPc thin-films determined by STXM and (c) LH-LV difference image generated from the optical density images.

Conclusion

In this work the charge transport properties of the polymorphic forms of the $(3PS)_2$-SiPc crystal were determined by KMC simulations and DFT calculations, and the differences between $(3PS)_2$-SiPc OTFTs fabricated by PVD and solution processing were accessed through electrical characterization, topographical imaging, and the determination of thin-film microstructure. OTFTs fabricated from solid state and solution methods resulted in similar performance metrics with average mobilities in the range of 1.0-3.9 x 10^{-2} cm^2 V^{-1} s^{-1} for PVD devices and 2.3-4.1 x 10^{-2} cm^2 V^{-1} s^{-1} for solution. Post-deposition thermal annealing was shown to have little effect on the μ_e of OTFTs although a noticeable decrease in V_T at greater annealing temperature was observed across all devices, suggesting that thermal annealing can be used as a method to reduce V_T without negatively impacting μ_e. Synchrotron based STXM measurements demonstrated that the films are constituted by domains of 1-4 µm where the $(3PS)_2$-SiPc are primarily oriented in the same pseudo edge-on direction. This study demonstrates the unique ability to integrate $(3PS)_2$-SiPc into n-type OTFTs through solution and vapour fabrication techniques, providing opportunity for hybrid manufacturing.

Experimental

Materials

Bis(tri-*n*-propylsilyl oxide) silicon phthalocyanine was synthesized as described in literature.[24] All solvents were purchased from commercial suppliers and used as received.

Computational

Quantum chemical calculations were performed using the same levels of approximation as in our previous works.[17,20,21,30,43] Energies of the highest occupied and lowest unoccupied molecular orbitals (HOMO and LUMO) were obtained after optimizing the molecular geometry using density functional theory (DFT) at the B3LYP/6-31G(d) level. Vertical transition energies and oscillator strengths towards the first optically allowed excited states were computed by means of time-dependent DFT with the same level of approximation. The electron affinity (EA) was obtained using the differences in the total energies of the charged and neutral molecules in their optimized geometries.

The charge transfer rates between adjacent molecules i and j were calculated according to the semi classical rate equation due to Marcus (**Equation 3.1**), which displays a dependence on the square of the electronic coupling J_{ij}:[44]

$$k_{ij} = \frac{2\pi}{\hbar}\frac{J_{ij}^2}{\sqrt{4\pi\lambda k_B T}}\exp\left[-\frac{\left(\Delta G_{ij}+\lambda\right)^2}{4\lambda k_B T}\right] \tag{3.1}$$

where $\hbar$ and k_B are the reduced Planck and Boltzmann constants respectively, and $T = 300$ K. The reorganization energy, $\lambda = \lambda_i + \lambda_s$, includes both the fast fluctuations of the energy of the molecules and their surroundings, and $\Delta G_{ij} = -EA_j + EA_i - e\mathbf{E}\cdot\mathbf{r_{ij}}$ comprises the spatial (static) variations of electron affinities and the contribution of an external electric field $\boldsymbol{E}$, which in turn depends on the intermolecular vector $\boldsymbol{r_{ij}}$. The intramolecular fraction of reorganization energy (λ_i) for electron transport was obtained with the four points method[45] and B3LYP/6-31G(d) calculations. The external fraction λ_s was set to 0.2 eV, a value predicted for a low dielectric constant medium by continuum model calculations.[46] The electronic couplings J_{ij} were obtained by employing the projection method involving the LUMOs of monomers,[47] and assuming the degeneracy of the LUMO and LUMO+1 levels.[43] Since simulations were performed on a defect-free crystal structure, another important parameter affecting charge mobility, the standard deviation σ of the transport levels (i.e. the site energies EA_i and EA_j), was also empirically adjusted, with the actual EA values drawn from a Gaussian distribution.

Electron mobilities were evaluated by means of Kinetic Monte Carlo (KMC) simulations based on the first reactions algorithm, performed in supercells in which the experimental X-ray crystal lattice was replicated to have roughly cubic boxes with sides of about 200 Å (polymorph 1, 6720 molecules, 20 x 12 x 14 supercell; polymorph 2, 6912 molecules, 18 x 12 x 16 supercell). Simulated mobilities were obtained by measuring the distance travelled by a single charge in the direction of the applied electric field **E**, divided by the elapsed time t and the field itself:

$$\mu = \boldsymbol{r}(t) \cdot \frac{\boldsymbol{E}}{E} \frac{1}{Et} \tag{3.2}$$

In practice, the distance was fixed to 5 x 10^6 Å, while the time t necessary to travel that distance is the actual simulation result. For each value and direction of the electric field, reported mobilities are the average of 100 KMC simulations, in which both the starting site for the charge and the site energies were randomly generated. Test calculations showing the influence of the internal reorganization energy and energetic disorder on the mobilities are reported in **Figures S3.1-S3.3**. We also demonstrated the consistency between zero-field mobilities extracted from KMC simulations with $\sigma = 0$ with those calculated, in previous works[17,20,21,30] using a simpler computational scheme that combines Einstein's electrical mobility equation and Marcus formula for the hopping rates (**Table S3.3**). Electronic structure calculations were performed using the ORCA[48] and Gaussian[49] programs. Transfer integrals were calculated using homemade codes.

PVD Fabricated OTFTs

Bottom-gate top-contact OTFTs with $(3PS)_2$-SiPc deposited by PVD were fabricated on n-doped silicon substrates (15 mm x 20 mm) with a 300 nm thermally grown silicon oxide dielectric layer purchased from Ossila. Substrates were first rinsed with acetone and isopropanol to remove the protective photoresist, followed by drying with nitrogen gas. Substrates were then cleaned by sonication in sequential baths of acetone and methanol for 5 min, each followed by drying with nitrogen before treatment with oxygen plasma for 15 min to clean and hydrolyze the surface. Plasma-treated substrates were then rinsed with water and isopropanol and dried with nitrogen before submersion in a solution of 1% v/v octyltrichlorosilane (OTS)-toluene solution. Surface treatment with OTS was carried out for 72 hrs at 70°C. OTS-treated substrates were then rinsed with toluene and isopropanol and dried under vacuum at 70°C for 1 hr. Bottom-gate top-contact OTFTs were fabricated by first thermally depositing a 300 Å film of $(3PS)_2$-SiPc by PVD through a square shadow mask as the active semiconducting layer at a target rate of 0.2 Å s^{-1} on room-temperature substrates using an Angstrom EvoVac thermal evaporator ($P < 2 \times 10^{-6}$ torr). Top contact source-drain electrodes were fabricated using shadow masks purchased from Ossila (channel length of 30 µm, channel width of 1000 µm) by depositing a 100 Å layer of manganese at a rate of 0.5 Å s^{-1} followed by depositing a 500 Å layer of silver at a rate of 1 Å s^{-1}.

Solution Fabricated OTFTs

Solution processed bottom-gate top-contact OTFTs were fabricated on the same n-doped silicon substrates purchased from Ossila as those used for PVD fabricated OTFTs. Substrates were cleaned by sequential 5 min long sonication baths of soapy water, distilled water, acetone and methanol, then dried with nitrogen. Substrates were then treated with air plasma for 15 min, before being rinsed with distilled water and isopropanol, and treated with a surface treatment of 1% v/v OTS in toluene by submersion in solution for 24 hrs at 70°C. After removal from the OTS solution, substrates were rinsed with toluene and isopropanol and dried in a vacuum oven at 70˚C for 1 hr. A 10 mg ml^{-1} $(3PS)_2$-SiPc solution in chloroform ($CHCl_3$) was prepared by heating at 50˚C for 1 hr in a nitrogen filled glovebox. The solution was then filtered through 0.2 µm pore size PTFE membrane, and deposited onto the OTS-treated substrates by spin-coating 60 µl of solution at 1500 RPM for 90 sec. The $(3PS)_2$-SiPc films were then either thermally annealed under vacuum for 1 hr or left to dry at room temperature in nitrogen. Electrodes were deposited by PVD using an Angstrom EvoVac thermal evaporator ($P < 2 \times 10^{-6}$ torr) using the same procedure as PVD fabricated OTFTs.

OTFT Characterization

Electrical characterization of OTFTs was performed as described in our previous works.[17,21] All characterization was done in a nitrogen filled glove box at room temperature using a multi tester consisting of 48 gold plated nickel probe tips that contact the source-drain and gate electrodes. A Keithley 2614B and a MCC USB DAQ was used to control the source-drain voltage (V_{SD} = 50 V) and gate voltage (0 V < V_{GS} < 60 V) to obtain source-drain current (I_{SD}) measurements in order to determine the μ_e, V_T, and $I_{on/off}$.

AFM

AFM images were collected using a Bruker Dimension Icon AFM with ScanAsyst-Air tips and analyzed with NanoScope Analysis v.1.8 software.

XRD

XRD data was collected using a Rigaku Ultima IV diffractometer with Cu Kα source (λ = 1.5418 Å), a scan range of 3° < 2θ < 20° and a rate of 0.5° min^{-1} with no spin. The interplanar spacing (d-spacing) between lattice plans was calculated using Bragg's Law shown by the following equation:

$$n\lambda = 2d\sin\theta \tag{3.3}$$

where λ is the wavelength of the incident wave equal to 1.54056 Å, d is the spacing between planes, θ is the angle of incidence in degrees, and n is a positive integer equal to 1 for this study.

STXM

Thin-films of $(3PS)_2$-SiPc (100 nm) were spin-coated onto a layer of poly(3,4-ethylenedioxythiophene) polystyrene sulfonate (PEDOT:PSS), floated in water and transferred onto a transmission electron microscopy (TEM) grid. STXM was performed on the HERMES beamline at the SOLEIL Synchrotron facility in Saint-Aubin, France to investigate the thin-film properties. The STXM equipment consisted of a Fresnel zone plate with 50 nm outer zone width, an order sorting aperture, the sample mounted onto a raster scanning piezo stage, and a photomultiplier tube to record the transmitted intensity. X-rays were irradiated in normal incidence to the sample surface and the linear polarization of the beam switched between linear horizontal (LH) and linear vertical (LV) using an undulator. Measurements were recorded in the energy range of 280-320 eV corresponding to the carbon K-edge to obtain 172 5 µm x 5 µm images with a step size of 50 nm and a dwell time of 3 ms. A photon energy of 285 eV with a 50 nm step size and a 3 ms dwell time was used to obtain 10 μm x 10 μm images. Analysis software aXis2000 was used to process all data.[50]

Associated Content

Acknowledgments

Benoît H. Lessard would like to acknowledge the Natural Sciences and Engineering Research Council of Canada (NSERC, RGPIN/2015-509 03987), the University of Ottawa, and the Canada Research Chair program for financial support. C. T. thank the Ministerio de Economía y Competitividad of Spain (projects PID2019-109555GB-I00 and RED2018-102815-T) and is thankful for the technical and human support provided by DIPC Computer Center. Computer time was provided by the Mésocentre de Calcul Intensif Aquitain (MCIA) of the University of Bordeaux, financed by the Conseil Régional d'Aquitaine and the French Ministry of Research and Technology. We acknowledge the Centre for Research in Photonics at the University of Ottawa (CRPuO) for access to the AFM and Dr. Jeffery Ovens for performing single crystal X-ray diffraction. The authors would like to thank the SOLEIL Synchrotron facility for providing beam time at the HERMES beamline. SOLEIL is supported by the National Center for Scientific Research (CNRS), the French Alternative Energies and Atomic Energy Commission (CEA), the Île-de-France Regional Council, the Essonne Department Council and the Centre Regional Council.

Supporting Information

Table S3.1. Relevant transfer integrals (J_e) and intermolecular vectors expressed in Cartesian (r_x, r_y, r_z) and cell coordinates (a, b, c) for polymorph 1.

#	J_e (eV)	r_x (Å)	r_y (Å)	r_z (Å)	$\|r\|$ (Å)	*a*	*b*	*c*
1	1.6	-10.23	0	0	10.23	-1	0	0
2	1.6	+10.23	0	0	10.23	+1	0	0
3	7.6	+2.38	-8.21	-6.92	11.00	0	-1/2	-1/2
4	7.6	+2.38	8.21	-6.92	11.00	0	+1/2	-1/2
5	7.6	-2.38	-8.21	+6.92	11.00	0	+1/2	-1/2
6	7.6	+2.38	8.21	+6.92	11.00	0	+1/2	+1/2

Table S3.2. Relevant transfer integrals (J_e) and intermolecular vectors expressed in Cartesian (r_x, r_y, r_z) and cell coordinates (a, b, c) for polymorph 2.

#	J_e (eV)	r_x (Å)	r_y (Å)	r_z (Å)	$\|r\|$ (Å)	*a*	*b*	*c*
1	11.4	-11.27	0	0	11.27	-1	0	0
2	11.4	+11.27	0	0	11.27	+1	0	0
3	0.7	-4.39	+8.66	-6.13	11.48	-1/2	+1/2	-1/2
4	0.7	+4.39	+8.66	+6.13	11.48	+1/2	+1/2	+1/2
5	0.7	-4.39	-8.66	-6.13	11.48	-1/2	-1/2	-1/2
6	0.7	4.39	-8.66	+6.13	11.48	+1/2	-1/2	1/2
7	10.1	+6.88	+8.66	-6.31	12.65	1/2	+1/2	-1/2
8	10.1	-6.88	+8.66	+6.31	12.65	-1/2	+1/2	+1/2
9	10.1	+6.88	-8.66	-6.31	12.65	+1/2	-1/2	-1/2
10	10.1	-6.88	-8.66	+6.31	12.65	-1/2	-1/2	+1/2

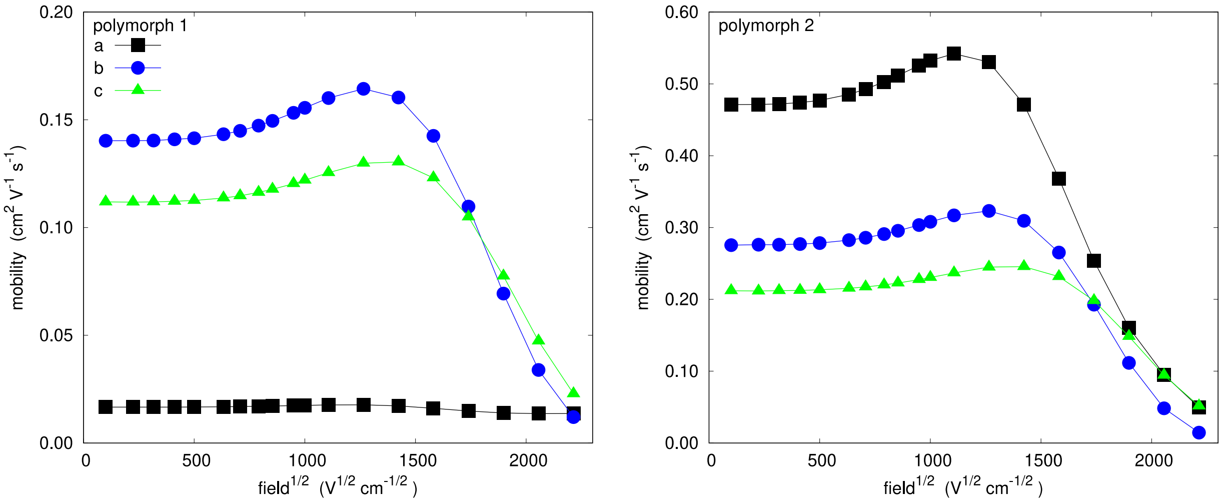

Figure S3.1. Electron mobility as a function of the magnitude of the electric field, set to be parallel to one of the crystallographic axes a, b, c, calculated in absence of external reorganization energy and of diagonal disorder ($E = 1000$ V cm^{-1}, $\lambda = 0.21$ eV, $T = 300$ K, $\sigma = 0$ eV).

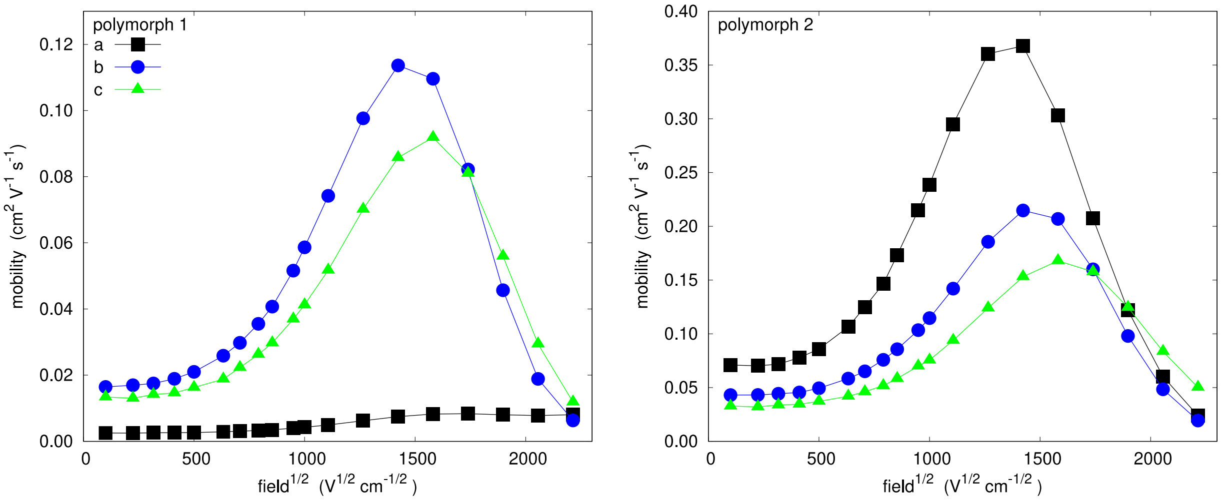

Figure S3.2. Electron mobility as a function of the magnitude of the electric field, set to be parallel to one of the crystallographic axes *a*, *b*, *c*, calculated without external reorganization energy and with diagonal disorder (E = 1000 V cm^{-1}, λ = 0.21 eV, T = 300 K, σ = 0.052 eV).

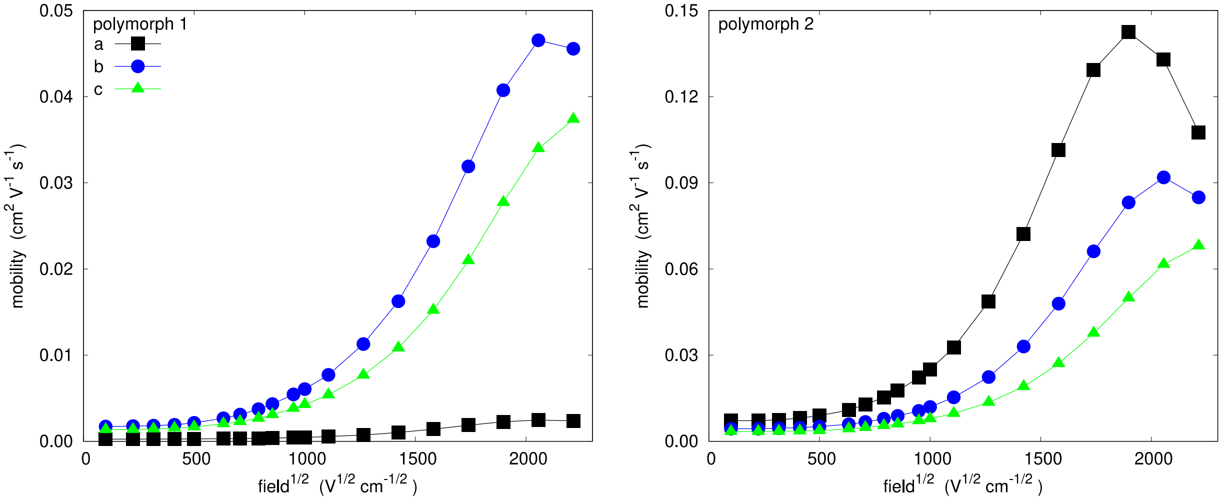

Figure S3.3. Electron mobility as a function of the magnitude of the electric field, set to be parallel to one of the crystallographic axes *a*, *b*, *c*, calculated assuming an external reorganization energy of 0.2 eV and diagonal disorder (E = 1000 V cm^{-1}, λ = 0.41 eV, T = 300 K, σ = 0.052 eV).

Table S3.3. Computed electron mobilities at zero field along the crystal axes and average mobility ($\mu_{e,\,avg} = (\mu_a + \mu_b + \mu_c) / 3$) of polymorph 1 and polymorph 2 determined by at zero field, using the expression:

$$\mu_i = \frac{q}{h}\left(\frac{\pi}{kT}\right)^{3/2} \frac{1}{\sqrt{\lambda_i}} \exp\left(-\frac{\lambda_i}{4kT}\right) \sum_m J_m^2 \left(\vec{r}_m \cdot \vec{e}_i\right)^2 \tag{3.4}$$

Where the sum runs over all pairs of molecular neighbours separated by the distance vector $\vec{r}_m$, $\vec{e}_i$ is a unit vector representing the direction. Variables q, h and k are respectively the elementary charge, the Planck and Boltzmann constants, and $T = 300$ K. These mobilities are compared with Kinetic Monte Carlo mobilities extrapolated at zero field and without energetic disorder (**Figure S3.1**).

Polymorph	μ_a (x 10^{-2} cm^2 V^{-1} s^{-1})	μ_b (x 10^{-2} cm^2 V^{-1} s^{-1})	μ_c (x 10^{-2} cm^2 V^{-1} s^{-1})	$\mu_{e,\,avg}$ (x 10^{-2} cm^2 V^{-1} s^{-1})
1-Equation	1.7	14.2	11.6	8.9
2-Equation	50.8	14.3	33.9	33.0
1-KMC	1.7	14.0	11.1	8.9
2-KMC	47.1	27.6	21.2	32.0

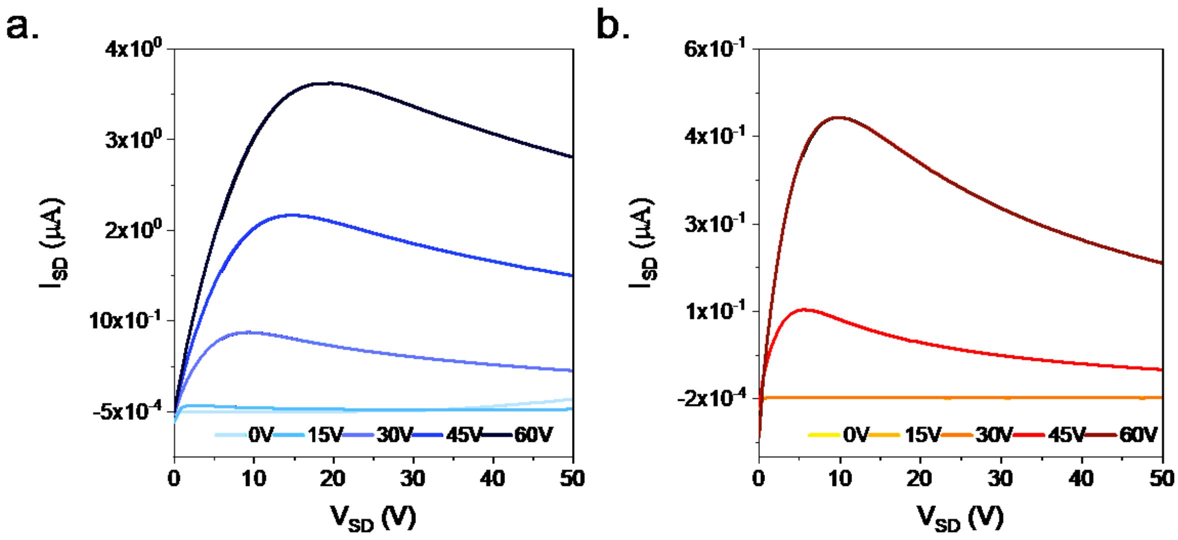

Figure S3.4. Characteristic output curves of (a) PVD and (b) solution fabricated (3PS)$_2$-SiPc OTFTs annealed at 25°C for 1 hr and characterized at room temperature in a nitrogen environment.

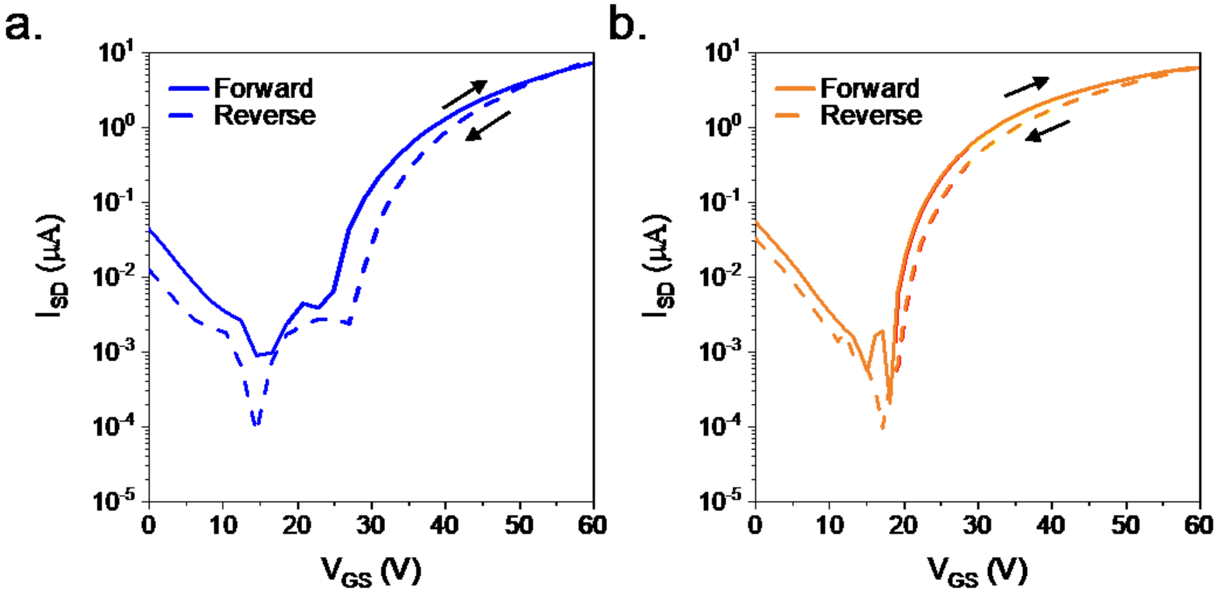

Figure S3.5. Characteristic forward and reverse transfer curves of (a) PVD and (b) solution fabricated $(3PS)_2$-SiPc OTFTs annealed at 25°C for 1 hr and characterized at room temperature in a nitrogen environment.

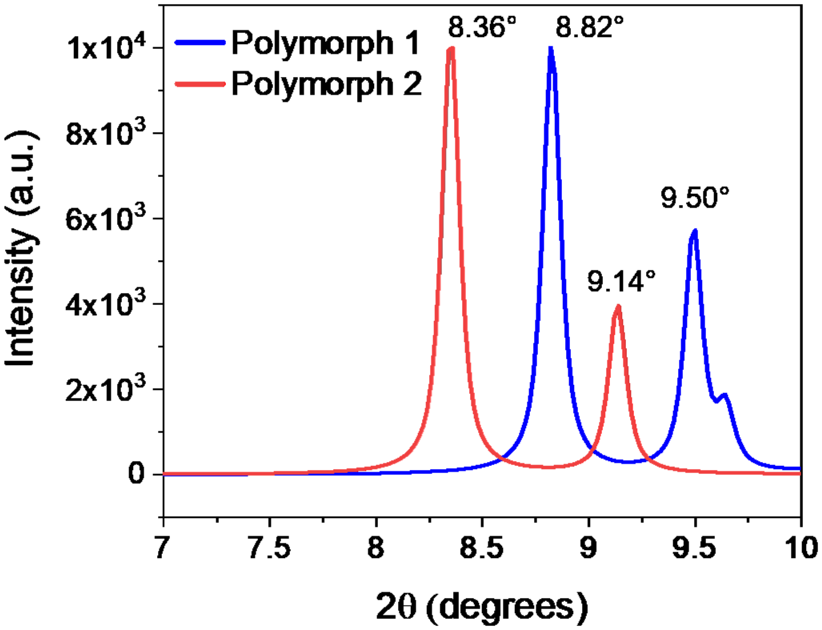

Figure S3.6. XRD pattern of polymorph 1 and polymorph 2 predicated from single crystal data using Mercury: visualization and analysis of crystal structures, from the Cambridge Crystallographic Data Centre.

References

1 Kudo, K., Yamashina, M. & Moriizumi, T. Field Effect Measurement of Organic Dye Films. Jpn. J. Appl. Phys. 23, 130–130 (1984).

2 Ebisawa, F., Kurokawa, T. & Nara, S. Electrical properties of polyacetylene/polysiloxane interface. J. Appl. Phys. 54, 3255–3259 (1983).

3 Roberts, M. E. et al. Water-stable organic transistors and their application in chemical and biological sensors. Proc. Natl. Acad. Sci. 105, 12134–12139 (2008).

4 Sun, C., Wang, X., Auwalu, M. A., Cheng, S. & Hu, W. Organic thin film transistors-based biosensors. EcoMat 3, (2021).

5 Mabeck, J. T. & Malliaras, G. G. Chemical and biological sensors based on organic thin-film transistors. Anal. Bioanal. Chem. 384, 343–353 (2005).

6 Baeg, K. & Lee, J. Flexible Electronic Systems on Plastic Substrates and Textiles for Smart Wearable Technologies. Adv. Mater. Technol. 5, 2000071 (2020).

7 Cosseddu, P., Lai, S. & Bonfiglio, A. Highly flexible and low voltage Organic Thin Film Transistors for wearable electronics and e-skin applications. in 2015 IEEE 15th International Conference on Nanotechnology (IEEE-NANO) 1317–1319 (IEEE, 2015). doi:10.1109/NANO.2015.7388876.

8 Huang, W., Feng, L., Wang, G. & Reichmanis, E. Wearable Organic Nano-sensors. in Flexible and Wearable Electronics for Smart Clothing 1–27 (Wiley, 2020). doi:10.1002/9783527818556.ch1.

9 Zhou, L. et al. All-organic active matrix flexible display. Appl. Phys. Lett. 88, 2004–2007 (2006).

10 Mizukami, M. et al. Flexible AM OLED panel driven by bottom-contact OTFTs. IEEE Electron Device Lett. 27, 249–251 (2006).

11 Fujisaki, Y. et al. Transparent Nanopaper-Based Flexible Organic Thin-Film Transistor Array. Adv. Funct. Mater. 24, 1657–1663 (2014).

12 Meng, Q. & Hu, W. Recent progress of n-type organic semiconducting small molecules for organic field-effect transistors. Phys. Chem. Chem. Phys. 14, 14152 (2012).

13 Yan, C. et al. Non-fullerene acceptors for organic solar cells. Nat. Rev. Mater. 3, 18003 (2018).

14 Claessens, C. G., Hahn, U. & Torres, T. Phthalocyanines: From outstanding electronic properties to emerging applications. Chem. Rec. 8, 75–97 (2008).

15 Melville, O. A. et al. Ambipolarity and Air Stability of Silicon Phthalocyanine Organic Thin-Film Transistors. Adv. Electron. Mater. 5, 1900087 (2019).

16 Melville, O. A. et al. Contact Engineering Using Manganese, Chromium, and Bathocuproine in Group 14 Phthalocyanine Organic Thin-Film Transistors. ACS Appl. Electron. Mater. 2, 1313–1322 (2020).

17 King, B. et al. Silicon Phthalocyanines for n-Type Organic Thin-Film Transistors: Development of Structure-Property Relationships. ACS Appl. Electron. Mater. 3, 325–336 (2021).

18 King, B. et al. Cyanophenoxy-Substituted Silicon Phthalocyanines for Low Threshold Voltage n-Type Organic Thin-Film Transistors. ACS Appl. Electron. Mater. 3, 2212–2223 (2021).

19 Faure, M., Grant, T. & Lessard, B. Silicon Phthalocyanines as Acceptor Candidates in Mixed Solution/Evaporation Processed Planar Heterojunction Organic Photovoltaic Devices. Coatings 9, 203 (2019).

20 Grant, T. M., Rice, N. A., Muccioli, L., Castet, F. & Lessard, B. H. Solution-Processable n-Type Tin Phthalocyanines in Organic Thin Film Transistors and as Ternary Additives in Organic Photovoltaics. ACS Appl. Electron. Mater. 1, 494–504 (2019).

21 Cranston, R. R. et al. Thin-Film Engineering of Solution-Processable n-Type Silicon Phthalocyanines for Organic Thin-Film Transistors. ACS Appl. Mater. Interfaces 13, 1008–1020 (2021).

22 Grant, T. M. et al. High Voc solution-processed organic solar cells containing silicon phthalocyanine as a non-fullerene electron acceptor. Org. Electron. 87, 105976 (2020).

23 Vebber, M. C., Grant, T. M., Brusso, J. L. & Lessard, B. H. Bis(trialkylsilyl oxide) Silicon Phthalocyanines: Understanding the Role of Solubility in Device Performance as Ternary Additives in Organic Photovoltaics. Langmuir 36, 2612–2621 (2020).

24 Grant, T. M., Dindault, C., Rice, N. A., Swaraj, S. & Lessard, B. H. Synthetically facile organic solar cells with >4% efficiency using P3HT and a silicon phthalocyanine non-fullerene acceptor. Mater. Adv. 2, 2594–2599 (2021).

25 Lessard, B. H. The Rise of Silicon Phthalocyanine: From Organic Photovoltaics to Organic Thin Film Transistors. ACS Appl. Mater. Interfaces 13, 31321–31330 (2021).

26 Virkar, A. A., Mannsfeld, S., Bao, Z. & Stingelin, N. Organic Semiconductor Growth and Morphology Considerations for Organic Thin-Film Transistors. Adv. Mater. 22, 3857–3875 (2010).

27 Markov, V. I. Crystal Growth for Beginners: Fundamentals of Nucleation, Crystal Growth, and Epitaxy. (World Scientific, 2016).

28 Diao, Y., Shaw, L., Bao, Z. & Mannsfeld, S. C. B. Morphology control strategies for solution-processed organic semiconductor thin films. Energy Environ. Sci. 7, 2145–2159 (2014).

29 Lee, S. S. et al. Controlling Nucleation and Crystallization in Solution-Processed Organic Semiconductors for Thin-Film Transistors. Adv. Mater. 21, 3605–3609 (2009).

30 Cranston, R. R. et al. N-Type Solution-Processed Tin versus Silicon Phthalocyanines: A Comparison of Performance in Organic Thin-Film Transistors and in Organic Photovoltaics. ACS Appl. Electron. Mater. 3, 1873–1885 (2021).

31 Rivnay, J., Mannsfeld, S. C. B., Miller, C. E., Salleo, A. & Toney, M. F. Quantitative Determination of Organic Semiconductor Microstructure from the Molecular to Device Scale. Chem. Rev. 112, 5488–5519 (2012).

32 Don Park, Y., Lim, J. A., Lee, H. S. & Cho, K. Interface engineering in organic transistors. Mater. Today 10, 46–54 (2007).

33 Locklin, J., Roberts, M. E., Mannsfeld, S. C. B. & Bao, Z. Optimizing the Thin

Film Morphology of Organic Field-Effect Transistors: The Influence of Molecular Structure and Vacuum Deposition Parameters on Device Performance. J. Macromol. Sci. Part C Polym. Rev. 46, 79–101 (2006).

34 Katz, H. E. & Bao, Z. The Physical Chemistry of Organic Field-Effect Transistors. J. Phys. Chem. B 104, 671–678 (2000).

35 Holder, C. F. & Schaak, R. E. Tutorial on Powder X-ray Diffraction for Characterizing Nanoscale Materials. ACS Nano 13, 7359–7365 (2019).

36 Cranston, R. R. & Lessard, B. H. Metal phthalocyanines: thin-film formation, microstructure, and physical properties. RSC Adv. 11, 21716–21737 (2021).

37 Peisert, H. et al. Order on disorder: Copper phthalocyanine thin films on technical substrates. J. Appl. Phys. 90, 466–469 (2001).

38 Biswas, I. et al. Initial molecular orientation of phthalocyanines on oxide substrates. Phys. status solidi 206, 2524–2528 (2009).

39 Li, L., Hu, W., Fuchs, H. & Chi, L. Controlling Molecular Packing for Charge Transport in Organic Thin Films. Adv. Energy Mater. 1, 188–193 (2011).

40 Li, L., Tang, Q., Li, H. & Hu, W. Molecular Orientation and Interface Compatibility for High Performance Organic Thin Film Transistor Based on Vanadyl Phthalocyanine. J. Phys. Chem. B 112, 10405–10410 (2008).

41 McNeill, C. R. & Ade, H. Soft X-ray characterisation of organic semiconductor films. J. Mater. Chem. C 1, 187–201 (2013).

42 Stöhr, J. NEXAFS Spectroscopy. vol. 25 (Springer Berlin Heidelberg, 1992).

43 Gali, S. M., Matta, M., Lessard, B. H., Castet, F. & Muccioli, L. Ambipolarity and Dimensionality of Charge Transport in Crystalline Group 14 Phthalocyanines: A Computational Study. J. Phys. Chem. C 122, 2554–2563 (2018).

44 Marcus, R. A. Electron transfer reactions in chemistry. Theory and experiment. Rev. Mod. Phys. 65, 599–610 (1993).

45 Coropceanu, V. et al. Hole- and Electron-Vibrational Couplings in Oligoacene Crystals: Intramolecular Contributions. Phys. Rev. Lett. 89, 275503 (2002).

46 Lemaur, V., Steel, M., Beljonne, D., Brédas, J.-L. & Cornil, J. Photoinduced Charge Generation and Recombination Dynamics in Model Donor/Acceptor Pairs for Organic Solar Cell Applications: A Full Quantum-Chemical Treatment. J. Am. Chem. Soc. 127, 6077–6086 (2005).

47 Valeev, E. F., Coropceanu, V., da Silva Filho, D. A., Salman, S. & Brédas, J.-L. Effect of Electronic Polarization on Charge-Transport Parameters in Molecular Organic Semiconductors. J. Am. Chem. Soc. 128, 9882–9886 (2006).

48 Neese, F. The ORCA program system. WIREs Comput. Mol. Sci. 2, 73–78 (2012).

49 Frisch, M. J. et al. Gaussian 16. (2016).

50 Hitchcock, A. aXis 2000-Analysis of X-Ray Images and Spectra. (1997).

Chapter 4. Polarized Raman Microscopy to Image Microstructure Changes in Silicon Phthalocyanine Thin-Films

This chapter is adapted from: ***Cranston, R. R.****, Lanosky, T. D., Ewenike, R., Mckillop, S., King, B., Lessard, B. H. Polarized Raman Microscopy to Image Microstructure Changes in Silicon Phthalocyanine Thin-Films. Small Science. (2024).*

Context

Building from the thermal annealing studies presented in **Chapter 3**, this work examined the effects of annealing temperature on the formation of $(3PS)_2$-SiPc thin-films using polarized Raman microscopy. As a new characterization technique to our research group, I spent a considerable amount of time setting up and implementing the procedures to conduct polarized Raman microscopy experiments, specifically to determine the orientation of molecules in a sample through 2D surface maps. This method of characterization provides analysis similar to that of synchrotron X-ray diffraction methods, but is significantly more accessible as experimentation can be performed in house and with high-throughput. This work again examined differences in film formation and OTFT performance of solution and physical vapour deposited films with high temperature thermal annealing. Using polarized Raman microscopy and XRD, a new polymorph was identified in films fabricated by physical vapour deposition, while solution fabricated films did not undergo the same structural reorganization with thermal annealing.

Contributions of Authors

This work was completed through contributions of all authors. For this work, I fabricated and characterized OTFTs and thin-films, conducted data analysis and wrote the manuscript. T.D.L assisted in OTFT fabrication and characterization. R.E. assisted in XRD experiments. S.M conducted film thickness measurements by profilometry. B.K assisted in PVD fabrication and B.H.L. provided supervision for the project.

Abstract

The choice of deposition technique and post deposition treatment can significantly influence the performance of organic electronic devices by altering the complex relationship between film properties and charge transport. Herein, the influence of deposition method and post deposition thermal annealing on the thin-film properties of an emerging semiconductor, bis(tri-*n*-propylsilyl oxide) SiPc ($(3PS)_2$-SiPc), is examined by polarized Raman microscopy. Comparing physical vapor deposition (PVD) and spin-coating, the orientation of $(3PS)_2$-SiPc molecules in films is determined and further characterized by X-ray diffraction to assess variations in microstructure and morphology due to thermal annealing. Despite differences in film formation, non-annealed organic thin-film transistors (OTFTs) fabricated by PVD and spin-coating resulted in similar electron mobilities (μ_e) on the order of 10^{-2} cm^2 V^{-1} s^{-1} and threshold voltages (V_T) of 10-20 V. Films fabricated by PVD annealed at 175°C transition to a new polymorphic form with molecules aligned at a higher angle to the substrate and exhibiting reduced device performance. Conversely, spin-coated films do not undergo any new polymorph formation or structural reorganization with thermal annealing. PVD fabricated films are thus more readily able to undergo transformations to structure and morphology with post deposition processing, while the microstructure of spin-coated films is established at the time of deposition.

Introduction

The micro and nano scale features of organic thin-films have a significant impact on resulting device performance.[1-4] While topological imaging can be used to study film homogeneity and texture[5,6] and diffraction techniques can assay film crystallinity and molecular orientation,[7,8] Raman microscopy offers the unique ability to simultaneously characterize both film morphology and structural orientation while maintaining high spatial resolution. Material characterization by Raman microscopy involves the measurement and identification of distinct vibrational modes and the analysis of their relative intensities across a sample area, ultimately providing compositional maps. The intensity of a Raman band depends on the orientation of a materials' axes of symmetry with respect to the direction of excited laser and scattered light polarizations.[9,10] Thus, Raman microscopy enables the non-destructive characterization of a wide range of samples with no restrictions on substrate material, dimension, or specialized sample preparation. Additionally, unlike diffraction methods which require highly crystalline samples, Raman microscopy can be used to gather information on amorphous and crystalline phases while being faster, more accessible, and less energy intensive then synchrotron methods.

Polarized Raman microscopy can be used to quantify the orientation of an organic thin-film by either the external crystal modes, if the crystal structure of the material is known, or by the internal molecular vibration approach.[11-14] The internal molecular vibration approach has been extensively used to determine the molecular orientation, packing structure, and polymorph formation of planar and non-planar small molecule thin-films including copper, zinc, and aluminum chloride phthalocyanines (Pcs).[13,15-20] However, to the best of the authors knowledge, this method has yet to be used for the analysis of tetravalent metal and metalloid Pcs such as silicon phthalocyanines ((OR_2)-SiPcs). As promising semiconducting materials $(OR)_2$-SiPcs have well established syntheses with a customizable molecular design and a wide range of processing compatibilities,[21-23] enabling their use as the active material in organic photovoltaics (OPVs),[24,25] thin-film gas sensors,[26] and organic thin-film transistors (OTFTs).[27,28] In particular, bis(tri-*n*-propylsilyl oxide) SiPc ($(3PS)_2$-SiPc, **Figure 4.1a**) is a high performing n-type $(OR)_2$-SiPc derivative which is processable by both sublimation and solution deposition techniques.[29] As thin-film formation, morphology, packing, and trap density play critical roles in the effectiveness and utility of a material for device applications,[30-33] understanding the interplay between film fabrication and microstructural properties on device performance is paramount for the further development and advancement of n-type devices based on this family of organic semiconductors.

In this work, we report the first use of polarized Raman surface maps to estimate the molecular angle of $(3PS)_2$-SiPc films by the internal molecular vibration approach. From single crystal X-ray diffraction (SCXRD) and ultraviolet-visible spectroscopy (UV-vis), $(3PS)_2$-SiPc is determined to be a planar molecule with D_{4h} symmetry and a slip-stacked packing structure,[29,34] enabling characterization by the internal molecular vibration approach and polarized Raman microscopy. Thin-films of $(3PS)_2$-SiPc were fabricated by physical vapour deposition (PVD) and spin-coating, and characterized by thin-film XRD, and polarized Raman microscopy to assay film crystallinity, morphology, and molecular orientation. Differences in fabrication method were correlated to OTFT device performance by comparing electron field-effect mobilities (μ_e), hysteresis, and threshold voltages (V_T), while the influence of post deposition thermal annealing on film microstructure and polymorph formation was investigated by *in-situ* polarized Raman surface maps of films fabricated by PVD. Key annealing temperatures were identified ex-situ for $(3PS)_2$-SiPc thin-films fabricated by both sublimation and solution deposition methods, with considerable differences in the re-organization of PVD and spin-coated films observed at high temperature annealing. Here we find that the initial differences in film microstructure and morphology resulting from the choice of material deposition dictates the final film microstructure post thermal treatment. This is in opposition to the more intuitive use of high temperature annealing as a method to rectify film properties post deposition.

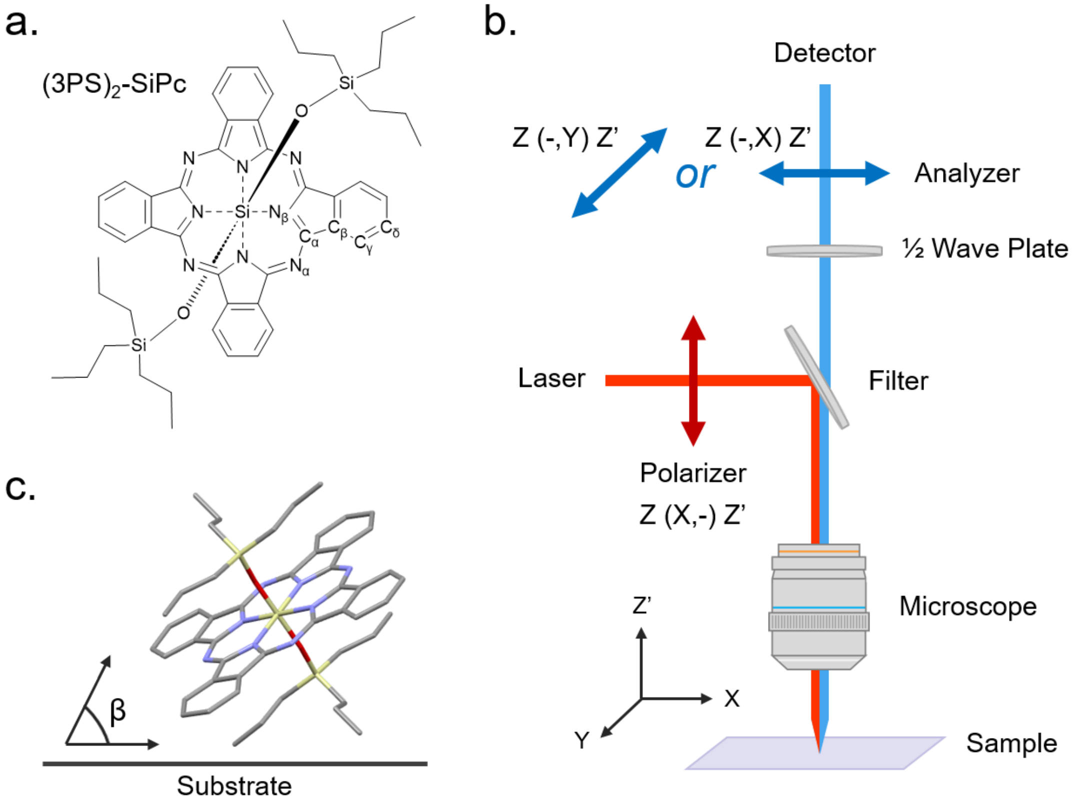

Figure 4.1. (a) Structure and atomic notation of the (3PS)$_2$-SiPc molecule. (b) Diagram of the polarized Raman microscope configuration and the orientation of polarization axes with respect to the sample and the corresponding Porto notation. (c) Diagram representing the β of a (3PS)$_2$-SiPc molecule to the substrate.

Results and Discussion

Thin-Film Fabrication

As the extent of Raman scattering for a given mode is described by its Raman tensor, the interaction between molecules and the polarization direction of light can be related to Raman intensity.[9,10] From the internal molecular vibration approach, information on the orientation and distribution of molecules in a film is obtained from the elements of the scattering tensor matrix for a selected vibration.[9,10] The components of a Raman tensor are probed by quantifying the intensity ratio of diagonal (parallel or Z(X,X)Z') and non-diagonal (cross or Z(X,Y)Z') polarization of incident and scattered light (**Figure 4.1b**). For Pcs with D_{4h} symmetry, the Raman active nondegenerate modes A_{1g} and B_{1g} are in-plane vibrations corresponding to molecular symmetry, and can therefore be used to determine film orientation by polarized Raman spectroscopy.[11,12,15,16] In the case of planar Pc thin-films, the intensity of a Raman band at Z(X,X)Z’ and Z(X,Y)Z’ polarizations can be described by **Equation 4.1** and **Equation 4.2** found in the ***Experimental***.[11,12,15,16] The orientation of a molecule in a film can then be estimated using **Equation 4.3** to calculate the angle of molecules relative to the substrate (β, **Figure 4.1c**) using the ratio of Raman band intensities at each polarization.

Through Raman surface maps taken with Z(X,X)Z’ and Z(X,Y)Z’ polarizations the integral intensity ratio of the B_{1g} pyrrole stretch mode was found, and the corresponding β of $(3PS)_2$-SiPc molecules to the substrate estimated for films fabricated by PVD (150 nm) and spin-coating (95 nm). For films fabricated by PVD, **Figure 4.2ai** shows a uniform surface with $(3PS)_2$-SiPc orientated predominantly pseudo edge-on, with an average β of approximately 52° to the substrate, which agrees with previous work by scanning transmission X-ray microscopy (STXM).[29] Conversely, spin-coated films show a more varied orientation (**Figure 4.2aii**) with much of the film aligned pseudo edge-on to the substrate with a β between 46-49°. However there exhibits areas with lower ($\beta_{min} = 44°$) and higher ($\beta_{max} = 57°$) angles to the substrate, compared to films fabricated by PVD ($\beta_{min} = 47°$ and $\beta_{max} = 55°$). The increased inhomogeneity of spin-coated films is reflected in the microscopy images where PVD yielded films with an effectively uniform surface morphology, spin-coated films were marked by large spherulites roughly 35 µm across (**Figure 4.2b**).

XRD patterns of PVD and spin-coated films shown in **Figure 4.2c** indicate a difference in film crystallinity between the two fabrication methods. Films deposited by PVD exhibit a narrow high intensity peak at $2\theta = 9.02°$ with a full width at half maximum (FWHM) of 0.13°, while spin-coated films exhibit a relatively broad peak with reduced intensity at $2\theta = 8.86°$ and a FWHM of 0.26°. The higher peak intensity of films fabricated by PVD may partly be due to a larger film thickness compared to spin-coated, however the narrower peak shape and shift in 2θ indicates a film with larger crystallite domains and a smaller intermolecular d-spacing. The broad low intensity XRD peak observed in spin-coated films agrees with the larger distribution and variation in β seen by polarized Raman surface maps. Additionally, analogous to previous work,[29] neither fabrication method results in an XRD pattern that matches the polymorphic forms of $(3PS)_2$-SiPc predicated from single crystal (**Figure S4.1**).

The impact of $(3PS)_2$-SiPc film deposition on the electrical characteristics of OTFTs was determined with characteristic transfer and output curves found in **Figure S4.2** and **Figure S4.3**. OTFTs fabricated by PVD and spin-coating exhibited notably similar metrics with PVD OTFTs having an average μ_e of 0.44 ± 0.05 x 10^{-2} cm^2 V^{-1} s^{-1} and V_T of 16.6 ± 1.7 V, and spin-coated OTFTs having an average μ_e of 0.74 ± 0.17 x 10^{-2} cm^2 V^{-1} s^{-1} and V_T of 21.0 ± 2.8 V (**Table S4.1**). Between the two fabrication methods, spin-coating resulted in a higher V_T and increased hysteresis between the forward and reverse transfer curves (**Figure 4.2d**). This could be a result of bias stress behaviour during device operation causing a shift in V_T over time, which is more prominent in solution processed films due to their increased defect density and trapping sites.[35-38] As the driving force, time scale, and controllability of crystallite nucleation and film growth for PVD and spin-coating are very different, it is expected that OTFTs fabricated by these two methods would exhibit large differences in device performance. However, our previous work demonstrated how the relationship between crystallinity, grain boundary effects, surface roughness, and molecular orientation have less of an effect on the performance of $(3PS)_2$-SiPc OTFTs due to its unique material properties.[29] This result is corroborated herein as despite differences in film microstructure and morphology between $(3PS)_2$-SiPc films fabricated from sublimation or solution, the electrical characteristics of OTFTs are comparable.

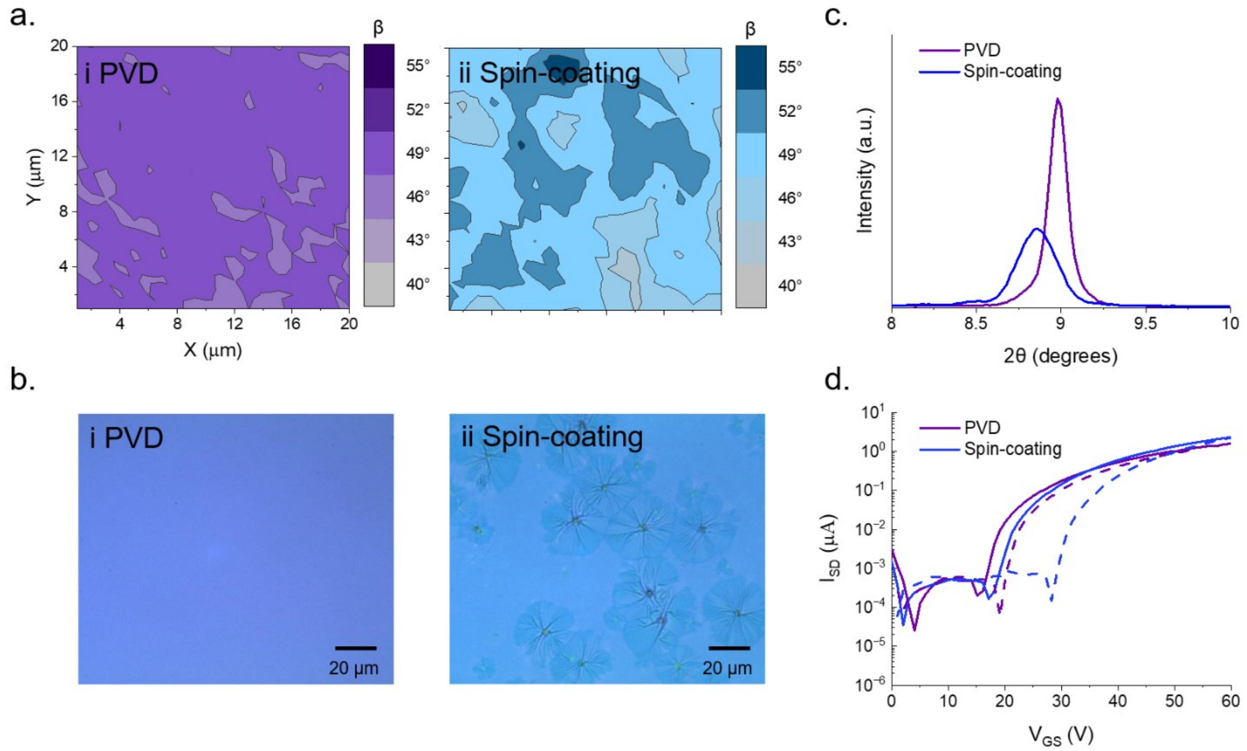

Figure 4.2. (a) Maps of *β* (20 μm x 20 μm) between $(3PS)_2$-SiPc and substrate estimated from polarized Raman spectra, (b) bright field real-colour microscopy images, (c) XRD patterns and (d) characteristic forward (solid line) and reverse (dashed line) transfer curves of $(3PS)_2$-SiPc OTFTs and thin-films fabricated by (i) PVD and (ii) spin-coating. No post deposition thermal annealing was performed on thin-films in this data set.

In-Situ Thermal Annealing

To ascertain the effects of film re-organization, *in-situ* thermal annealing characterized by Raman microscopy was conducted on thin-films fabricated by PVD such that pre-annealed polarized Raman surface maps were taken at a starting temperature of 25°C and used to estimate *β*. The temperature was then increased at a rate of 5°C min^{-1} until 180°C which was held for 30 min before cooling to 25°C where post-annealed polarized Raman surface maps were measured at the identical location on the film. **Figure 4.3a** and **Figure 4.3d** present the Raman spectra using Z(X,X)Z' and Z(X,Y)Z' polarizations pre- and post-annealing at the same location on the film. For Z(X,X)Z' polarization the A_{1g} band (591 cm^{-1}) associated with benzene ring deformation, the B_{1g} band (681 cm^{-1}) related to macrocycle breathing, and the B_{1g} band (1545 cm^{-1}) correlated to pyrrole stretch are clearly present.[39-41] By changing the polarization to Z(X,Y)Z' a loss in intensity is observed such that the B_{1g} pyrrole stretch band remains most prominent. Distinct changes in the fingerprint region of the spectral range (1350-1550 cm^{-1}), which correspond to isoindole stretching, vibrations of the N-Si and C-H bonds, and displacements of the C_α-N_β-C_α bridge bond of the $(3PS)_2$-SiPc molecule,[40,42,43] are noticeable with changing polarization. For directionally orientated films, the scattering intensity for a particular Raman mode depends on the alignment of the bond axes relative to the direction of polarization. Therefore, when the polarization is parallel or perpendicular to a bond axis, the intensity of Raman scattering will not be equal, and information regarding orientation can be determined. Greater C-C and C-N intensity with Z(X,X)Z’ (parallel) polarization compared to Z(X,Y)Z’ (perpendicular) polarization indicates the $(3PS)_2$-SiPc molecules are more closely aligned with these bond axes parallel to the substrate with a lower β. Conversely, more intense B_{1g} scattering with Z(X,Y)Z’ polarization relative to Z(X,X)Z’, suggests the $(3PS)_2$-SiPc molecules have a greater angle to the substrate. The pre- and post-annealed polarized Raman spectra in **Figure 4.3a** and **Figure 4.3d** reveal that after thermal annealing the intensity of the B_{1g} peak increases with Z(X,Y)Z’ polarization, whereas the pre-annealed film shows a decrease in peak intensity at this polarization. This polarization dependant change in B_{1g} peak intensity indicates a transition in the thin-film structure resulting from thermal annealing.

Figure 4.3b and **Figure 4.3e** display maps of β between $(3PS)_2$-SiPc and the substrate for pre- and post-annealed thin-films estimated from polarized Raman surface maps. The pre-annealed film shows a similar orientation to **Figure 4.2a** with a β around 48° to the substrate. After thermal annealing more areas with a β of 48° are present with additional regions of much lower and higher angle (β_{min} = 38° and β_{max} = 54°) that are not found in the pre-annealed map (**Figure 4.3e**). This can also be seen through the histograms presented in **Figure 4.3c** and **Figure 4.3f**, where the distribution of β for the post-annealed film is much wider than the pre-annealed film. As these measurements were conducted *in-situ* to ensure the same film location, the difference in β and film uniformity of pre- and post-annealed thin-films is therefore not a result of deposition or variation in measurement region, but rather a direct change caused by thermal annealing. Post deposition thermal annealing is a common method to alter the microstructure of Pc thin-films and induce a polymorphic change.[29,44,45] As PVD films undergo a microstructural change with thermal annealing, spin-coated films will likely have a similar orientation change. The film re-organization caused by thermal annealing suggests that a morphological change may also occur, which coupled with a change in β would imply a large difference in the electrical performance of OTFTs pre- and post-thermal annealing.

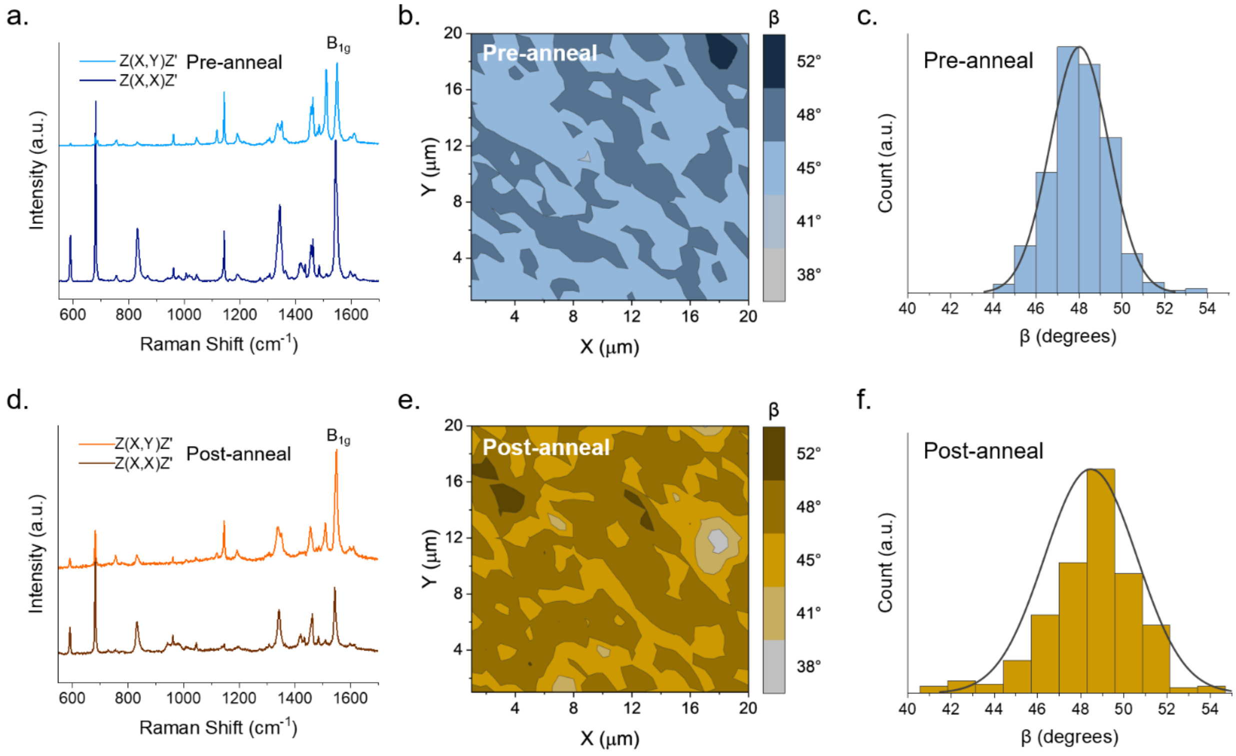

Figure 4.3. (a,d) Polarized Raman spectra, (b,e) in-situ maps of β (20 μm x 20 μm) between $(3PS)_2$-SiPc and substrate estimated from polarized Raman spectra, and (c,f) distribution histograms of β shown in Raman maps of $(3PS)_2$-SiPc thin-films fabricated by PVD pre- and post-annealing. All measurements are taken at the same location on the film.

Post Deposition Thermal Annealing Temperature

For PVD and spin-coated films the post deposition thermal annealing temperature was varied from 25°C (no thermal annealing) to 200°C to assay microstructural changes with increasing annealing temperature. A maximum annealing temperature of 200°C was selected as $(3PS)_2$-SiPc readily sublimes above 200°C under 100 mTorr pressure.[34] The XRD patterns of PVD films, displayed in **Figure 4.4a**, exhibit an increase in peak intensity at 2θ ≈ 9.0° with increasing annealing temperature, suggesting higher temperatures yield more crystalline films. After annealing at 175°C the films fabricated by PVD exhibit a drastic change in film structure, with a complete loss of the 2θ ≈ 9.0° peak and the emergence of two lower intensity peaks at 2θ ≈ 7.8° and 2θ ≈ 10.0°. The total change in XRD pattern indicates PVD films transition from one polymorphic form to another when annealed at 175°C and above. Notably spin-coated films do not undergo the same polymorphic change with annealing temperature as seen in **Figure 4.4d**. For spin-coated films an increase in peak intensity and a shift in peak location from 2θ = 8.86° to 9.00° is observed with increasing annealing temperature. However, no change in polymorphic form occurs after annealing at 175°C contrary to the transition observed in films fabricated by PVD. Microscope images of PVD fabricated films show a large difference in surface characteristics only at annealing temperatures of 175°C and 200°C, while spin-coated films show morphological changes throughout the temperature range (**Figure S4.4**). Although non-polarized Raman spectroscopy has previously been used to identify polymorph formation in Pc films,[46-48] no significant change in the non-polarized Raman spectra or location of key Raman bands (1341 cm^{-1}, 1458 cm^{-1}, and 1545 cm^{-1}) were observed with annealing temperature as seen by **Figure S4.5** and **Figure S4.6** respectively.

Similar to *in-situ* measurements, polarized Raman spectra of films fabricated by PVD and spin-coating exhibit a change in B_{1g} peak intensity ratio with post deposition thermal annealing (**Figure S4.7** and **Figure S4.8**). From **Figure 4.4c**, the β map of a film fabricated by PVD annealed at 150°C is comparable to that of a non-annealed film (**Figure 4.2a**), with the majority of $(3PS)_2$-SiPc molecules aligned approximately 49° to the substrate. Annealing at or above 175°C results in an increase in β to 56° and a much larger distribution in angle with a minimum and maximum of 30° and 74° when annealed at 200°C, compared to 47° and 51° when annealed at 150°C. In addition to the more varied film and less homogenous microstructure, the increase in β agrees with the formation of a new polymorph as identified by XRD. Conversely, spin-coated films annealed at 200°C have a comparable average β to films annealed at 150°C, however with more $(3PS)_2$-SiPc molecules aligned 52-55° to the substrate (**Figure 4.4f**). The minimum, maximum, and average β of $(3PS)_2$-SiPc films annealed at each temperature for both deposition methods can be found in **Table S4.2**. In addition to annealing temperature, annealing times of 15 min, 30 min, and 60 min were studied at a constant temperature, with no significant changes in PVD or spin-coated film microstructure observed by XRD and polarized Raman surface maps (**Figure S4.9**). The transition of PVD fabricated films to a new polymorph is therefore primarily brought on by thermal annealing temperature, while spin-coated films do not undergo polymorph formation with annealing temperature, but rather only exhibit changes in film crystallinity and homogeneity.

Characteristic transfer curves of PVD and spin-coated OTFTs non-thermally annealed, annealed before the polymorph transition temperature at 150°C, and annealed after the polymorph transition temperature at 200°C are shown in **Figure 4.4b** and **Figure 4.4e**. For OTFTs fabricated using PVD, thermal annealing at 150°C resulted in a higher μ_e compared to non-annealed transistors (**Table S4.1**). This can be attributed to the higher degree of crystallinity that is achieved with thermal annealing as determined by XRD. After the polymorph transition temperature, OTFTs annealed at 200°C experience a severe reduction in device performance, with three orders of magnitude decrease in average μ_e from $1.13 \pm 0.13 \times 10^{-2}$ cm^2 V^{-1} s^{-1} to $7.93 \pm 5.7 \times 10^{-5}$ cm^2 V^{-1} s^{-1}. The worse electrical performance of devices annealed at 200°C can be due in part to the more irregular films that occur with high temperature annealing, or a result of the second polymorph of $(3PS)_2$-SiPc which may be less effective at charge transport. The effectiveness of different polymorphs of a material at charge transport depends on the tilt angle between molecular planes and the degree of π-electron overlap, with higher conductivity observed by polymorphs with increased π-electron overlap and multidimensional electronic coupling.[29,49,50] Therefore, the secondary polymorph of $(3PS)_2$-SiPc likely results in reduced device performance due to decreased π-electron overlap as a result of the solid state arrangement of molecules in thin-films fabricated by PVD. Spin-coated films experience a similar reduction in device performance with average μ_e decreasing from $0.55 \pm 0.15 \times 10^{-2}$ cm^2 V^{-1} s^{-1} to $2.09 \pm 2.0 \times 10^{-4}$ cm^2 V^{-1} s^{-1} when annealed at 150°C versus 200°C. However, spin-coated OTFTs exhibit less of a decrease in device performance compared to OTFTs fabricated by PVD, likely due to film inhomogeneity rather than microstructural re-organization such as polymorph formation.

All thin-films and OTFTs were fabricated using the same substrate, surface modification, active material, and device architecture, with the only difference in fabrication being deposition method. As the driving force of crystallite nucleation and thin-film growth for PVD and spin-coating are quite different, it is expected that films fabricated by these methods will have different properties and characteristics. Pc molecules can be considerably mobile within a film and have been shown to re-orientate into more energetically favourable positions with annealing temperature,[51,52] solvent exposure,[53,54] and even strong magnetic and gravitational fields[55-57]. For the films fabricated herein, after applying sufficient thermal energy to induce re-organization the resultant microstructures of films deposited by PVD and spin-coating remain unalike, undergoing different processes with high temperature annealing. These results suggest that the initial differences in film microstructure and morphology obtained by sublimation or solution processing are too great to overcome by post deposition processes despite the restructuring ability of Pcs. PVD fabricated films can therefore more easily undergo transformations to structure and morphology after deposition, while the molecular arrangement of spin-coated films is largely determined by the initial deposition process. The greater re-organizational abilities of PVD films, may be due in part to the inherent process of a material going from a vapour phase to a solid film. The beginning stages of film formation involves the diffusion of the initial low-density distribution of molecules across the substrate to thermodynamically stable locations.[58-60] Meanwhile, for solution processing the rapid evaporation of solvent leaves little time for surface mobility or diffusion resulting in molecules locked in place on the substrate.[61-64] This key difference in the initial stages of film formation between sublimation and solution fabrication may make films deposited by PVD more susceptible to re-organization by post deposition processes.

a. PVD

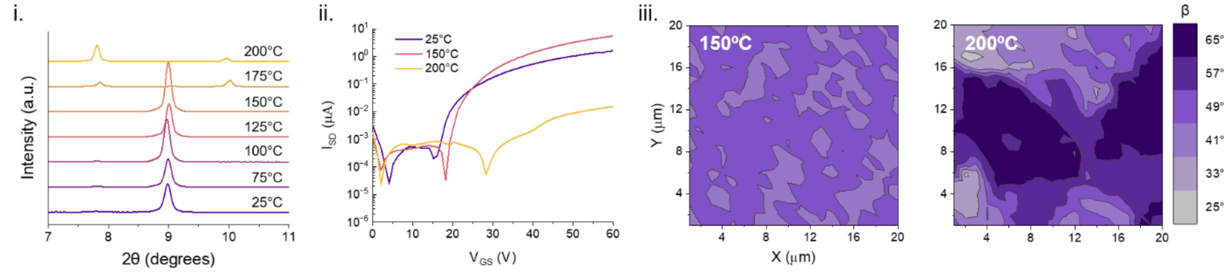

b. Spin-coating

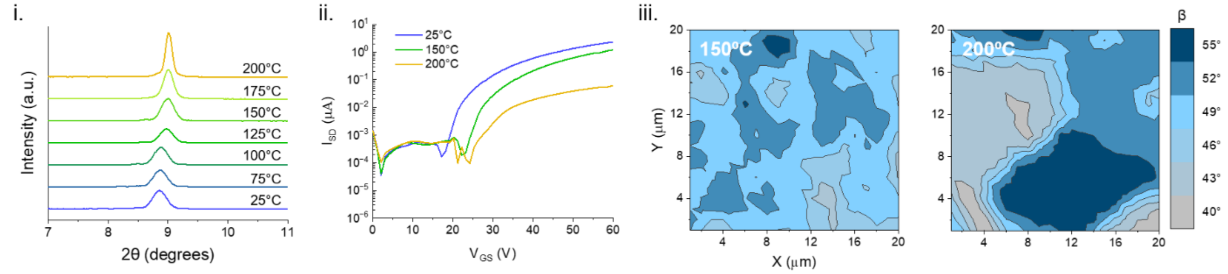

Figure 4.4. (i) XRD patterns, (ii) characteristic transfer curves, and (iii) maps of β (20 μm x 20 μm) between $(3PS)_2$-SiPc and substrate estimated from polarized Raman spectra of $(3PS)_2$-SiPc thin-films fabricated by (a) PVD and (b) spin-coating thermally annealed at indicated temperatures.

Conclusion

Polarized Raman microscopy was used to estimate the molecular orientation of $(3PS)_2$-SiPc thin-films fabricated by PVD and spin-coating to determine differences in film microstructure as a result of deposition method and post deposition thermal annealing. Films fabricated by PVD yielded highly uniform, well-oriented thin-films while spin-coating resulted in inhomogeneous films with large variations in morphology and molecular orientation. Although both deposition methods resulted in different film formations, OTFTs fabricated by PVD and spin-coating exhibited similar μ_e and V_T, with the only significant difference being improved hysteresis for OTFTs processed by sublimation. Through XRD and Raman microscopy, thermal annealing was found to have a distinct effect on films fabricated by PVD which was markedly different from spin-coated films. Films deposited by PVD annealed at 175°C underwent a polymorphic change in packing structure, characterized by a different diffraction pattern, an increase in β, and a reduction in OTFT performance. Conversely, films deposited by spin-coating exhibited increased crystallinity and β, however to a lesser extent than PVD fabricated films, with no observed change in molecular packing or polymorph formation after annealing at or above 175°C. This work demonstrates the importance of material deposition on thin-film properties and the impact on device application despite the use of post deposition processing that is primarily used to enhances film formation and device performance

Experimental

Materials

Bis(tri-*n*-propylsilyl oxide) silicon phthalocyanine ($(3PS)_2$-SiPc) was synthesized as described in literature and purified by train sublimation before use.[29,34] Hexamethyldisilane (HMDS, 98+%) was purchased from Thermo Fischer Scientific. Solvents were purchased from commercial suppliers and used as received.

OTFT and Thin-Film Fabrication

Bottom-gate top-contact OTFTs were fabricated on 15 mm x 20 mm n-doped silicon substrates purchased from Ossila with a 300 nm thick thermally grown SiO_2 dielectric layer. Substrates were cleaned by sequential sonication baths of soapy water, distilled water, acetone and methanol, then dried with nitrogen and treated with air plasma for 15 min. HMDS surface treatment was carried out in a nitrogen filled glovebox by spin-coating 50 µl of HMDS onto cleaned substrates at 3000 RPM for 30 sec, then drying at 150°C for 1 hr under vacuum. A solution of $(3PS)_2$-SiPc at a concentration of 10 mg ml^{-1} in toluene was prepared by heating at 50°C for 45 min, then filtering through a PTFE membrane with a pore size of 0.45 µm. Solution fabricated thin-films were fabricated by spin-coating 60 µl of solution at 1500 RPM for 90 sec. PVD fabricated thin-films were deposited using an Angstrom EvoVac thermal evaporator ($P < 2 \times 10^{-6}$ torr) at a rate of 0.2 Å s^{-1} until a final thickness of 150 nm was reached. All films were then thermally annealed at indicated temperatures for 30 min. Source-drain electrodes were fabricated by PVD using shadow masks purchased from Ossila (channel length of 30 µm, channel width of

1000 μm) by depositing 10 nm of manganese at a rate of 0.5 Å s^-1 followed by 50 nm of silver at a rate of 1 Å s^{-1}.

OTFT Characterization

OTFT characterization was performed using the same procedure outlined in our previous works.[65] Characterization occurred in a nitrogen filled glove box at room temperature. A Keithley 2614B and a MCC USB DAQ was used to control the source-drain voltage (V_{SD} = 50 V) and gate voltage (0 V < V_{GS} < 60 V) to obtain source-drain current (I_{SD}) measurements. The electron field effect mobility (μ_e), and threshold voltage (V_T) were calculated by the MOSFET model.[66]

XRD

XRD measurements were obtained using a Rigaku Ultima IV powder diffractometer with a Cu Kα (λ = 1.5418 Å) source, a scan range of 3° < 2θ < 12°, and rate of 0.5° min^{-1}.

Raman Microscopy

Non-polarized and two types of polarized, Z(X,X)Z' and Z(X,Y)Z', Raman spectra were recorded in the backscattering geometry using a Renishaw inVia InSpec confocal Raman microscope with a custom Linkam stage for *in-situ* temperature control. The Raman microscope uses a Leica Microsystems bright field microscope with a DM2700 light source. A 500 mW 532 nm wavelength laser with a 2400 l mm^{-1} grating was used to obtain measurements in the spectral range of 550-1700 cm^{-1}, focused on the sample by an X50L objective with a numerical aperture of 0.5. With the objective and laser combination used herein, the Raman microscope has a spectral resolution of 0.3 cm^{-1} (FWHM), a theoretical spatial resolution of approximately 640 nm, and a theoretical depth of focus of approximately 3.0 μm. Calibration was performed prior to all measurements against the 520 cm^{-1} silicon reference peak within 0.5 cm^{-1}.

Each polarized Raman spectra were taken at the same location on the sample. Single Raman spectra were taken with 5% laser power (25 mW) and an exposure time of 10 sec. The Raman spectra of a clean SiO_2 substrate can be found in **Figure S4.10** for reference. Raman maps (20 μm x 20 μm) were generated from 400 individual spectra using a 1.0 μm step size with a 5% laser (25 mW) power and a 2 sec exposure time. Each spectrum was fitted to the theoretical Lorentz curve using Wire 5.6 inVia software to obtain integral intensity (I_{XX} and I_{XY}) of the B_{1g} pyrrole stretch Raman mode. For planar Pc thin-films, the intensity of a Raman band at Z(X,X)Z' and

Z(X,Y)Z’ polarizations is described by **Equation 4.1** and **Equation 4.2**.[11,12,15,16] **Equation 4.3** can then be used to estimate the angle of $(3PS)_2$-SiPc molecules to the substrate (*β*).

$$I_{XX} = k^2 cos^4\beta \tag{4.1}$$

$$I_{XY} = \frac{k^2}{2} cos^2\beta sin^2\beta \tag{4.2}$$

$$\frac{I_{XX}}{I_{XY}} = 2cot^2\beta \tag{4.3}$$

In-situ Raman maps were obtained by heating the sample at a rate of 5°C min^{-1} to a starting temperature of 25°C which was held for 30 min before the spectra was measured with Z(X,X)Z’ and Z(X,Y)Z’ polarization. The sample was then heated at the same rate to 150°C and held at temperature for 30 min before cooling at a rate of 5°C min^{-1} to 25°C which was held for 10 min before measuring the spectra using both polarizations. This procedure was repeated for a high temperature anneal at 180°C before final cooling to room temperature.

To guarantee no degradation occurred during repeated polarized measurements and mapping experiments the exposure time, scan repetitions, and mapping step size was carefully controlled. **Figure S4.11** shows no damage to the sample when the exposure time to the laser was increased from 1 sec to 10 sec for either polarization directions. To generate maps of *β* it is necessary to measure the mapping area twice, one for each polarization, for a total of 800 scans per *β* map over the same 20 µm x 20 µm sample area. To ensure that this does not cause any damage or unwanted changes to the film, the spectra and B_{1g} peak intensity at the start and end of the scan was compared for three sequential mapping measurements at each polarization totalling 2400 scans over the same sample area (**Figure S4.12** and **Figure S4.13**). For each polarization minimal changes in peak intensity and signal-to-noise ratio was observed between the start and end of each map, and between map repetitions indicating no substantial changes to the film caused by repeated exposure to the laser. Additionally, the mapping step size was decreased from 1.0 µm to 0.5 µm resulting in each map consisting of 1600 scans and greatly increasing the amount of time the laser is open to the sample. **Figure S4.14** displays the effects of lower step size on B_{1g} peak intensity and spectra at the start and end of the map scan. A complete lose in B_{1g} peak intensity and a large increase in the signal-to-noise ratio was observed as the scan progressed indicating film damage over time. Resultantly, all mapping experiments were conducted with a scan step size of 1.0 µm to reduce damage to the sample.

Associated Content

Acknowledgments

B.H.L and R.R.C are financially supported by the Natural Sciences and Engineering Research Council of Canada (RGPIN-04079-2020 to B.H.L, CGSD-569930-2022 to R.R.C) and the University of Ottawa. B.H.L. is a Canada Research Chair which helped contribute funding for this work.

Supporting Information

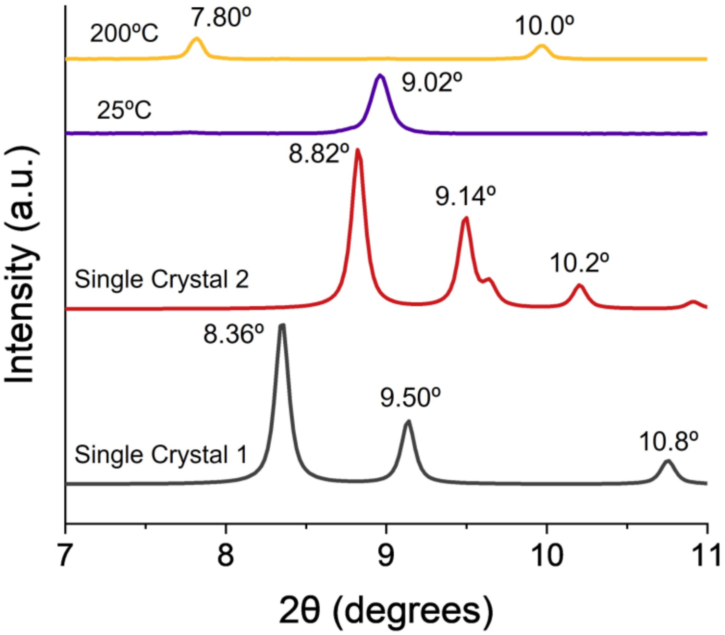

Figure S4.1. XRD patterns of $(3PS)_2$-SiPc thin-films fabricated by PVD thermally annealed at 25ºC and 200ºC, and XRD pattern of polymorph 1 and polymorph 2 predicated from single crystal data using Mercury: visualization and analysis of crystal structures, from the Cambridge Crystallographic Data Centre (CCDC# 2091746 and CCDC# 2067659).

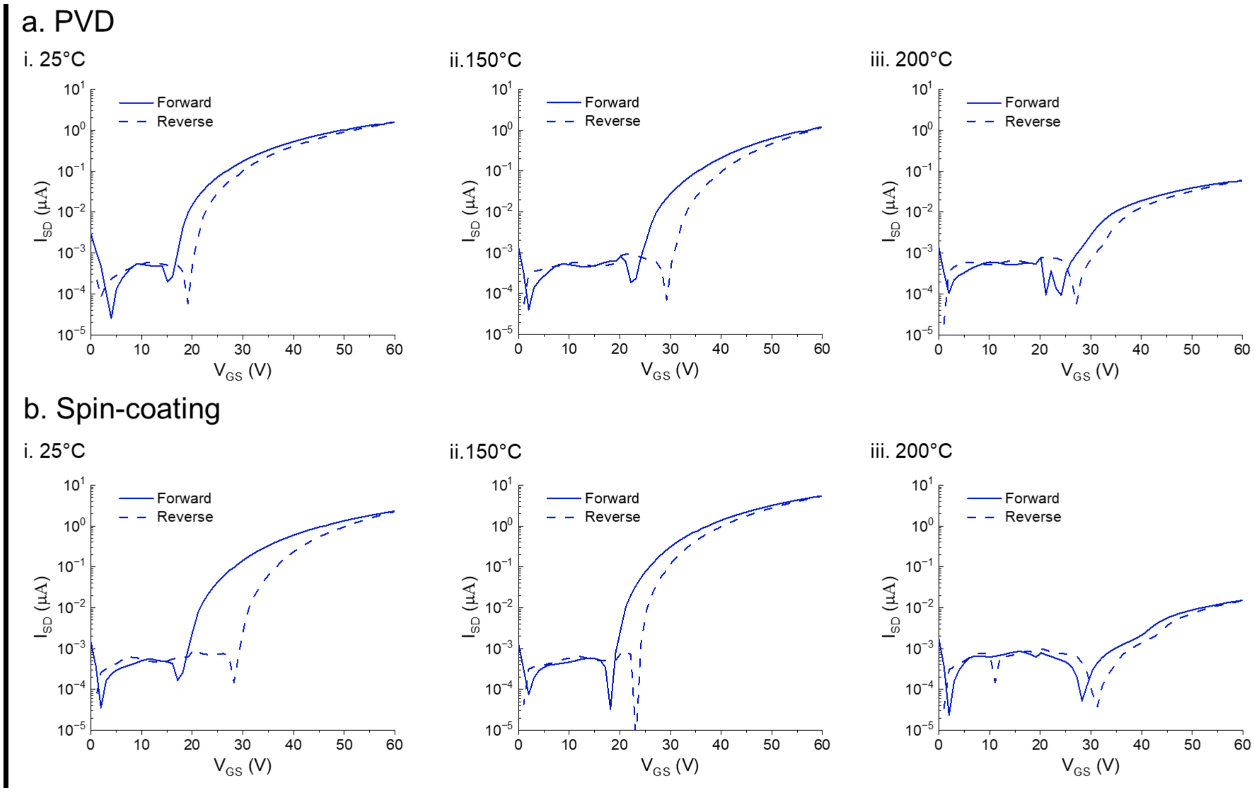

Figure S4.2. Characteristic forward and reverse transfer curves of (a) PVD and (b) spin-coating fabricated $(3PS)_2$-SiPc OTFTs annealed at (i) 25°C, (ii) 150°C and (iii) 200°C characterized at room temperature in a nitrogen environment.

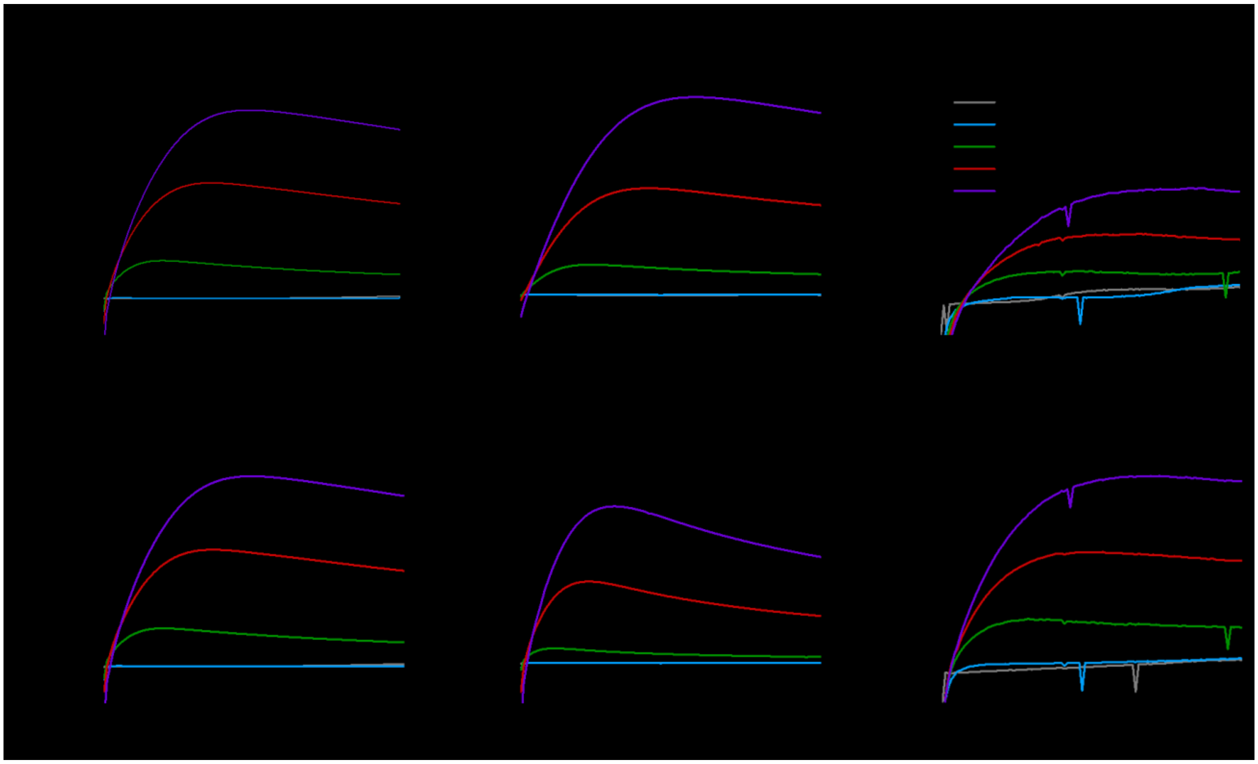

Figure S4.3. Characteristic output curves of (a) PVD and (b) spin-coating fabricated $(3PS)_2$-SiPc OTFTs annealed at (i) 25°C, (ii) 150°C and (iii) 200°C characterized at room temperature in a nitrogen environment. All OTFTs characterized at gate voltages of 0 V (grey), 15 V (blue), 30 V (green), 45 V (red), and 60 V (purple).

Table S4.1. Average electrical characteristics of OTFTs calculated from *n* transistors.

Deposition	**Temp.**	**$\mu_{e,avg}$ (x 10^{-2} cm^2 V^{-1} s^{-1})**	**V_T (V)**	**$I_{on/off}$**	***n***
PVD	25°C	0.44 ± 0.05	16.6 ± 1.7	10^5	37
	150°C	1.13 ± 0.13	21.5 ± 1.2	10^5	40
	200°C	7.93 ± 5.7 x 10^{-3}	24.4 ± 2.1	10^3	30
Spin Coat	25°C	0.74 ± 0.17	21.0 ± 2.8	10^5	39
	150°C	0.55 ± 0.15	25.9 ± 3.1	10^4	33
	200°C	2.09 ± 2.0 x 10^{-2}	23.6 ± 4.2	10^3	8

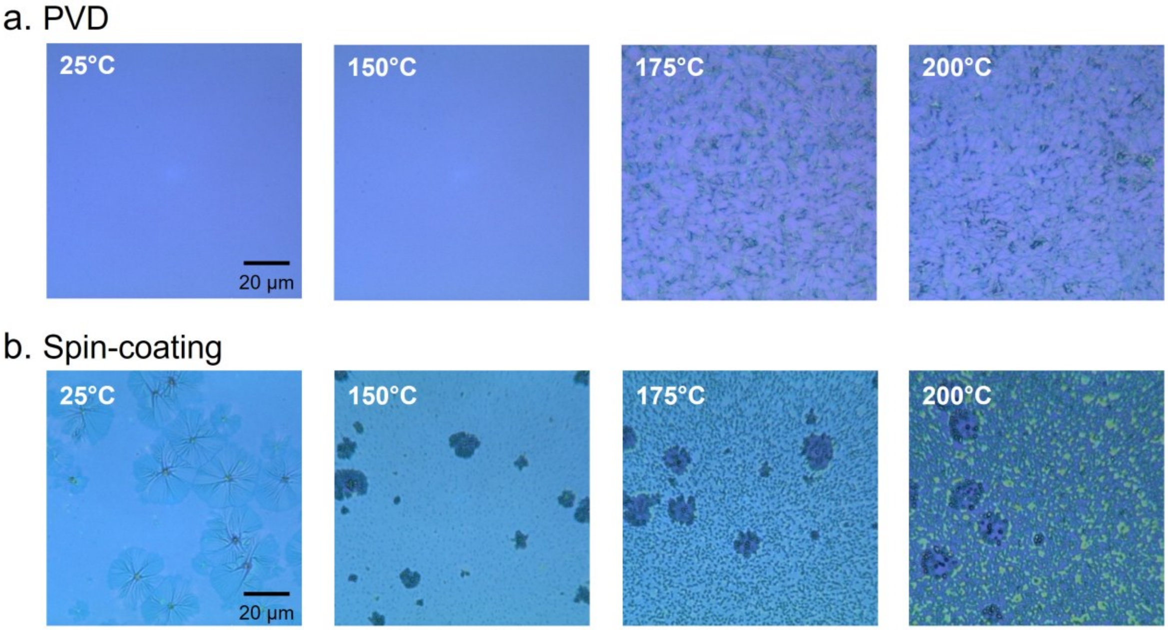

Figure S4.4. Bright field real-colour microscopy images of $(3PS)_2$-SiPc thin-films fabricated by (a) PVD and (b) spin-coating thermally annealed 25ºC, 150ºC, 175ºC, and 200ºC.

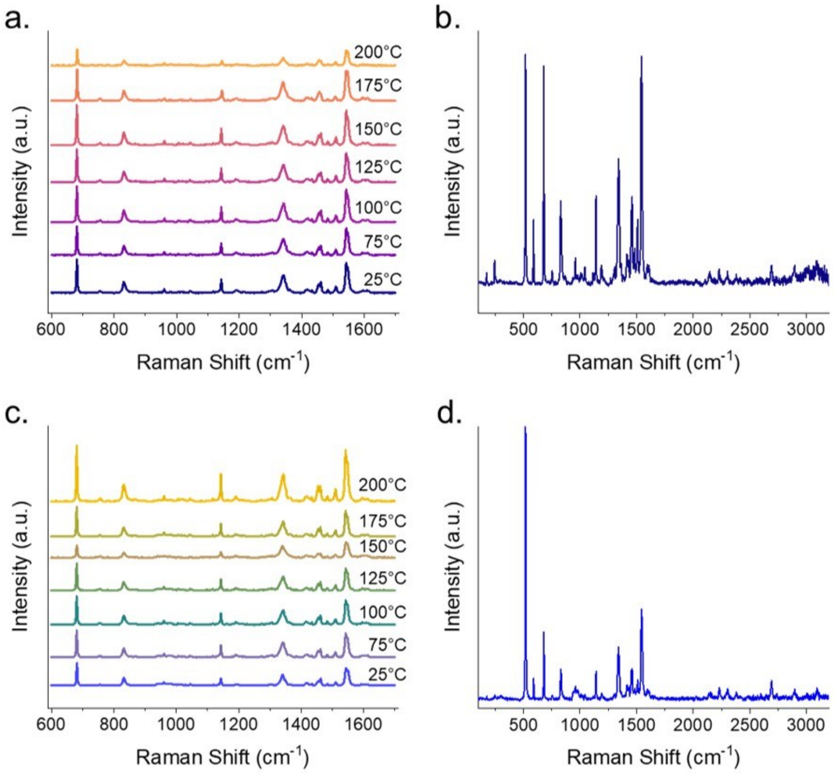

Figure S4.5. Raman spectra of thermally annealed $(3PS)_2$-SiPc thin-films fabricated by (a) PVD and (c) spin-coating. Extended Raman spectra of $(3PS)_2$-SiPc thin-films annealed at 25°C fabricated by (b) PVD and (d) spin-coating.

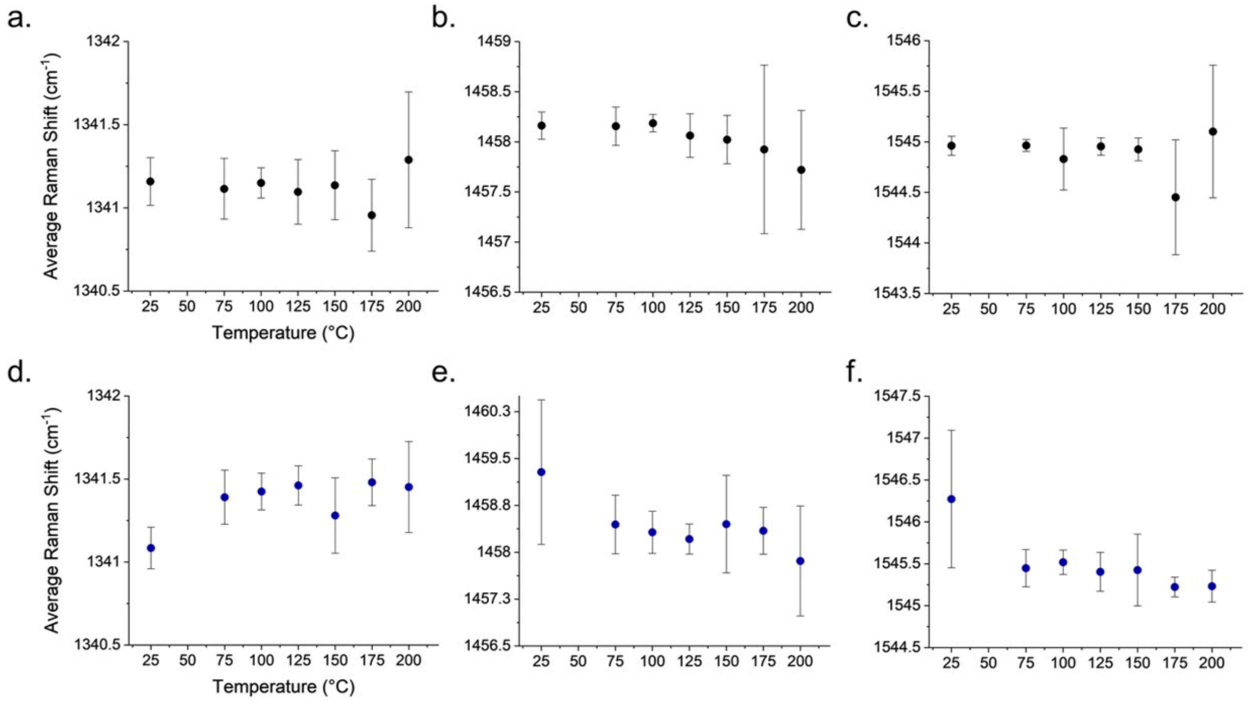

Figure S4.6. Average shift in (a,d) 1341 cm^{-1}, (b,e) 1458 cm^{-1}, and (c,f) 1545 cm^{-1} peak location with increasing annealing temperature observed in the Raman spectra of (a-c) PVD and (d-f) spin-coating fabricated $(3PS)_2$-SiPc thin-films. Averages taken from 10 individual measurements at each annealing temperature.

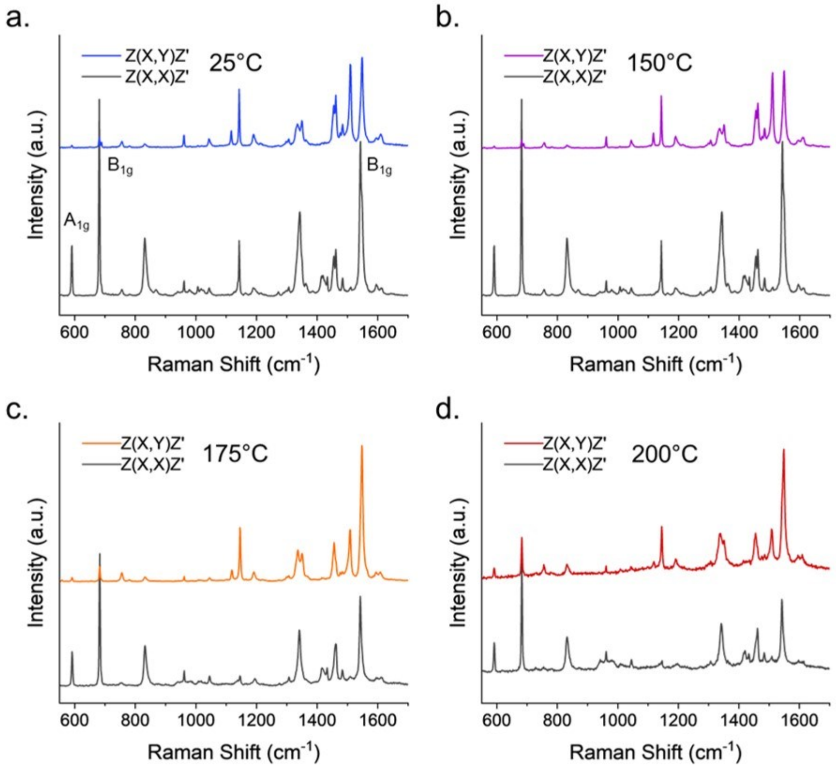

Figure S4.7. Polarized Raman spectra of $(3PS)_2$-SiPc thin-films fabricated by PVD thermally annealed at (a) 25°C, (b) 150°C, (c) 175°C, and (d) 200°C.

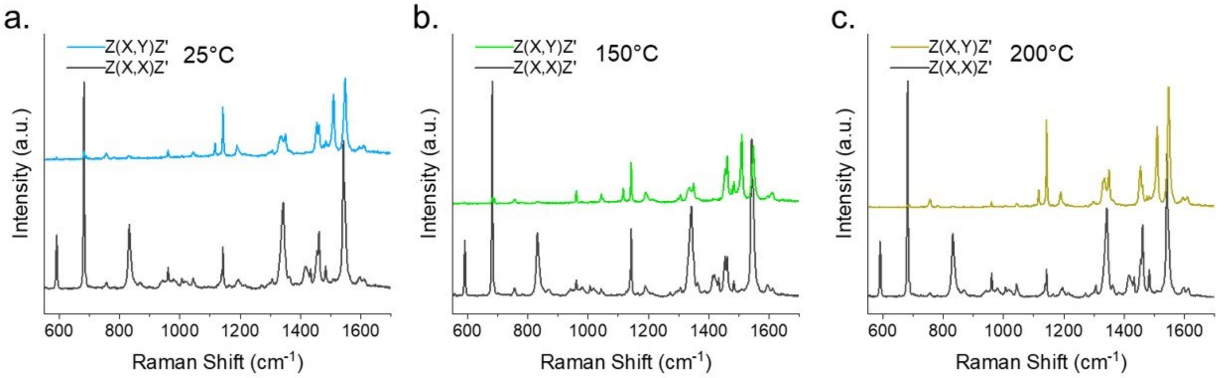

Figure S4.8. Polarized Raman spectra of $(3PS)_2$-SiPc thin-films fabricated by spin-coating thermally annealed at (a) 25°C, (b) 150°C, and (c) 200°C.

Table S4.2. Minimum, maximum and average molecular angle of $(3PS)_2$-SiPc to the substrate of PVD and spin-coated thin-films annealed at indicated temperatures, estimated from polarized Raman surface maps. Standard deviation (σ) calculated from the entire data set.

Deposition	Temp.	β_{min} (degrees)	β_{max} (degrees)	β_{avg} (degrees)	σ (degrees)
PVD	25°C	47.8	55.1	51.9	1.9
	150°C	47.0	51.3	49.2	0.7
	175°C	25.0	65.0	41.4	7.7
	200°C	30.6	73.6	56.6	10.4
Spin Coat	25°C	44.1	56.6	50.7	2.1
	150°C	43.3	55.4	50.4	2.1
	200°C	39.9	57.8	50.7	5.0

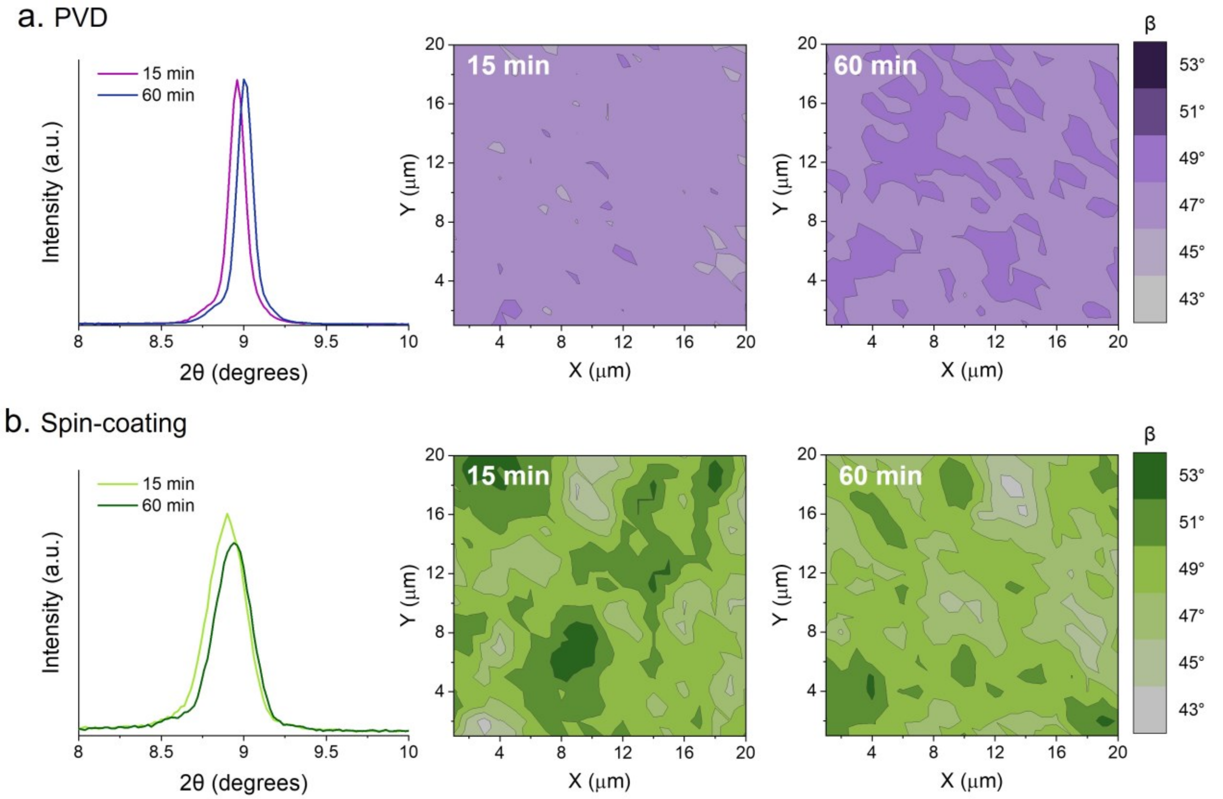

Figure S4.9. XRD patterns and maps (20 μm x 20 μm) of the molecular angle between $(3PS)_2$-SiPc and substrate estimated from polarized Raman spectra of $(3PS)_2$-SiPc thin-films fabricated by (a) PVD and (b) spin-coating thermally annealed at 100°C for 15 min and 60 min.

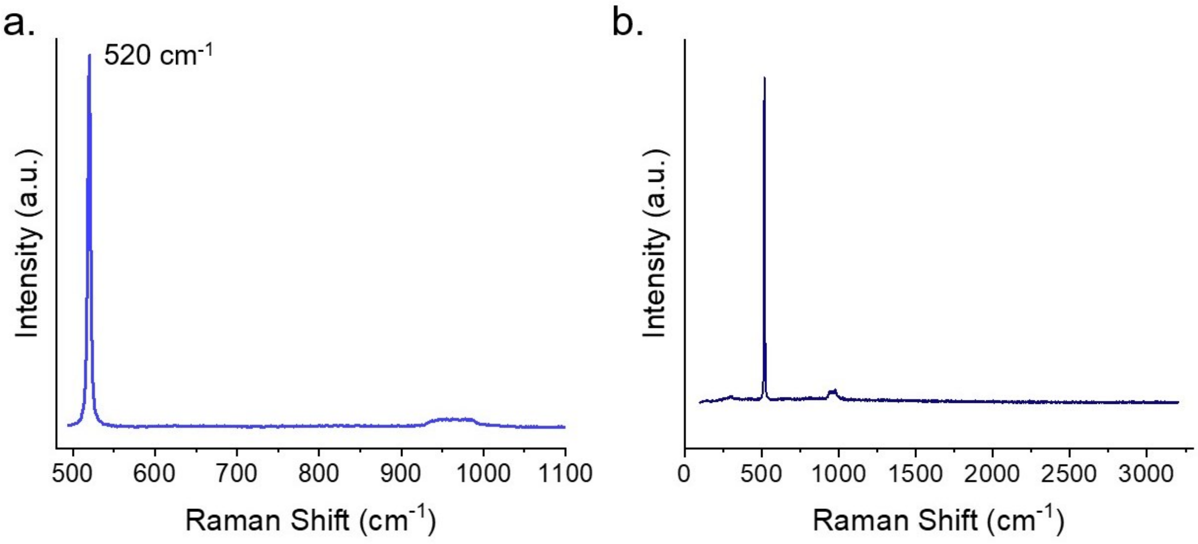

Figure S4.10. Raman spectra of a clean SiO_2 substrate from (a) 495-1685 cm^{-1} and (b) 100-3200 cm^{-1}.

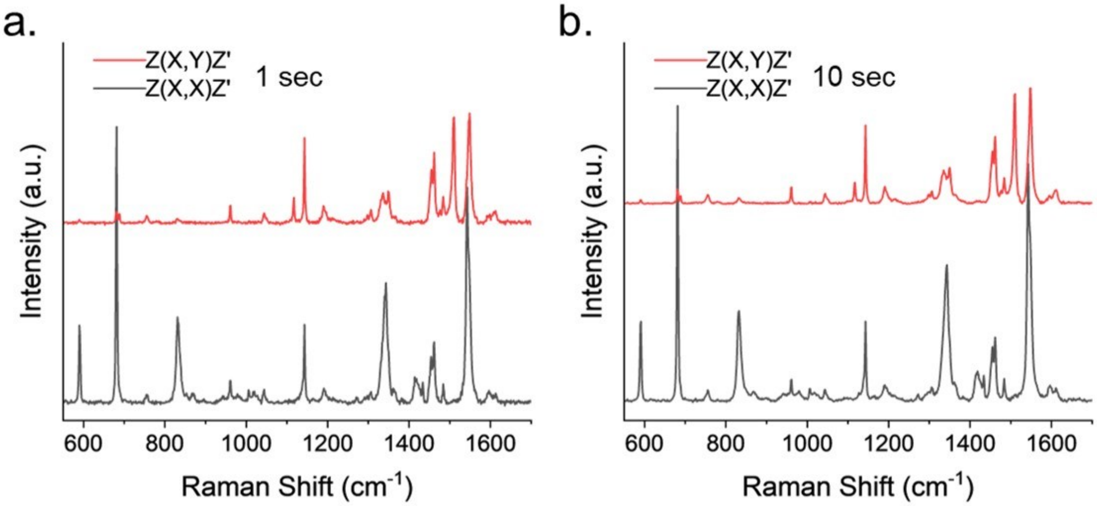

Figure S4.11. Polarized Raman spectra of $(3PS)_2$-SiPc thin-films fabricated by PVD thermally annealed at 25°C, with (a) 1 sec and (b) 10 sec exposures to the laser during measurement.

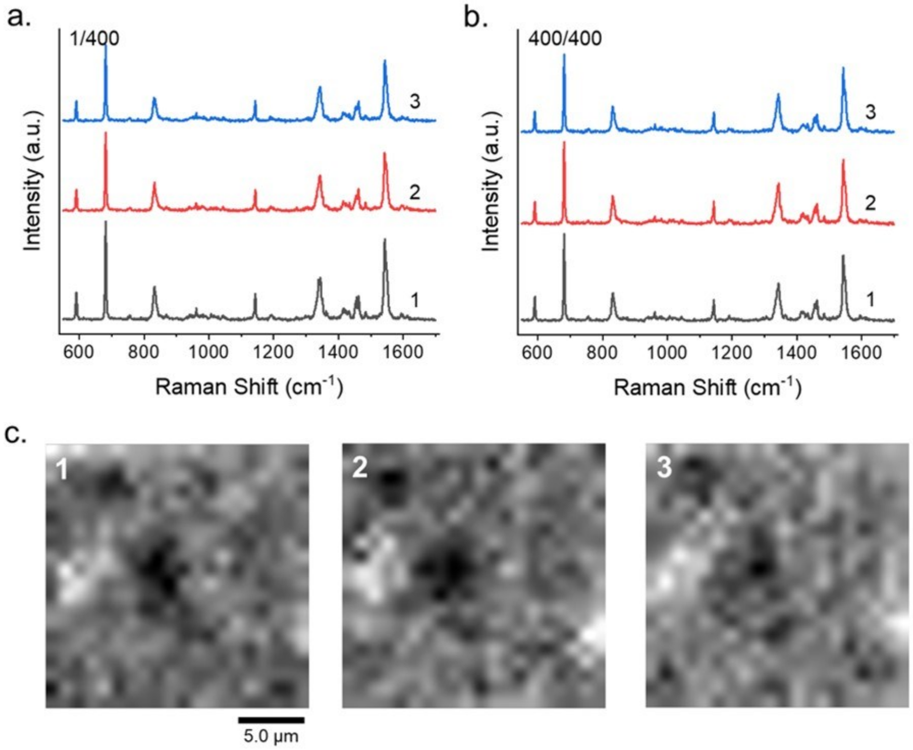

Figure S4.12. Z(X,X)Z' polarized Raman spectra taken from three sequential Raman maps of $(3PS)_2$-SiPc thin-films fabricated by PVD thermally annealed at 25°C, at (a) the start of scan (1/400 measurements) and (b) end of scan (400/400 measurements). (c) Sequential intensity at B_{1g} 1545 cm^{-1} maps (20 µm x 20 µm) of films

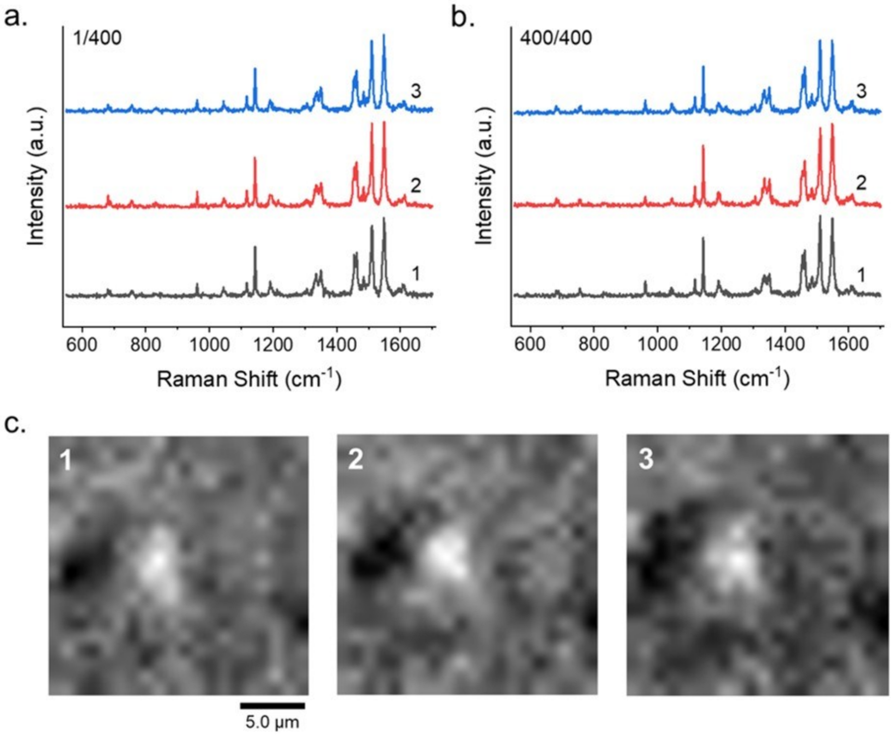

Figure S4.13. Z(X,Y)Z’ polarized Raman spectra taken from three sequential Raman maps of $(3PS)_2$-SiPc thin-films fabricated by PVD thermally annealed at 25°C, at (a) the start of scan (1/400 measurements) and (b) end of scan (400/400 measurements). (c) Sequential intensity at B_{1g} 1545 cm^{-1} maps (20 μm x 20 μm) of films.

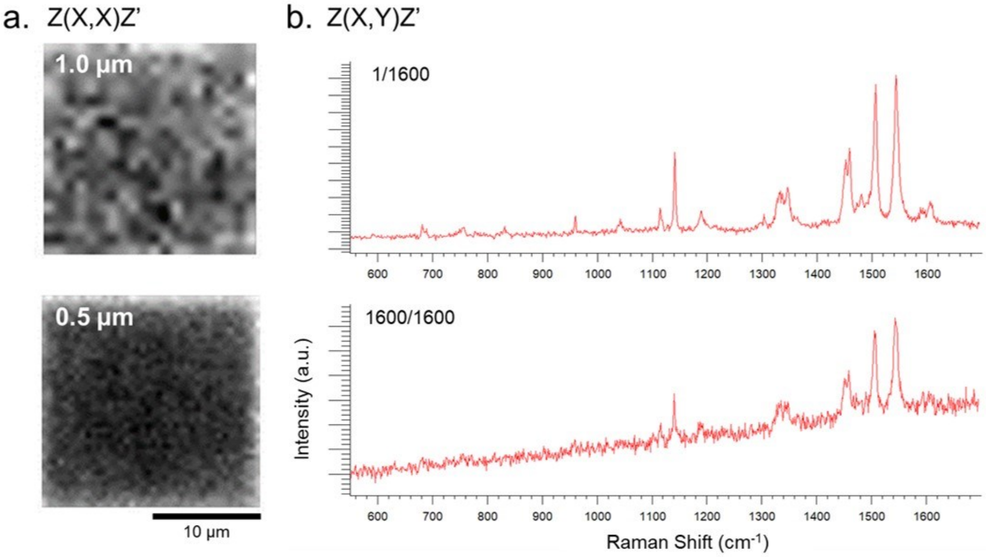

Figure S4.14. (a) Comparison of intensity at B_{1g} 1545 cm^{-1} maps (20 μm x 20 μm) of $(3PS)_2$-SiPc films using a step size of 1.0 μm and 0.5 μm with Z(X,X)Z’ polarization. (b) Z(X,Y)Z’ polarized Raman spectra taken from intensity at B_{1g} 1548 cm^{-1} Raman maps using a step size of 0.5 μm, at the start of scan (1/1600 measurements) and end of scan (1600/1600 measurements).

References

1 Virkar, A. A., Mannsfeld, S., Bao, Z. & Stingelin, N. Organic Semiconductor Growth and Morphology Considerations for Organic Thin-Film Transistors. Advanced Materials 22, 3857–3875 (2010).

2 Liu, F. et al. Characterization of the morphology of solution-processed bulk heterojunction organic photovoltaics. Prog Polym Sci 38, 1990–2052 (2013).

3 Tadayyon, S. M. et al. CuPc buffer layer role in OLED performance: A study of the interfacial band energies. Org Electron 5, 157–166 (2004).

4 Lai, S. et al. Morphology Influence on the Mechanical Stress Response in Bendable Organic Field-Effect Transistors with Solution-Processed Semiconductors. Adv Electron Mater 4, 1–9 (2018).

5 McNeill, C. R. Imaging the domain structure of organic semiconductor films. J Polym Sci B Polym Phys 49, 909–919 (2011).

6 Wen, Y., Liu, Y., Guo, Y., Yu, G. & Hu, W. Experimental Techniques for the Fabrication and Characterization of Organic Thin Films for Field-Effect Transistors. Chem Rev 111, 3358–3406 (2011).

7 DeLongchamp, D. M., Kline, R. J., Fischer, D. A., Richter, L. J. & Toney, M. F. Molecular Characterization of Organic Electronic Films. Advanced Materials 23, 319–337 (2011).

8 Rivnay, J., Mannsfeld, S. C. B., Miller, C. E., Salleo, A. & Toney, M. F. Quantitative Determination of Organic Semiconductor Microstructure from the Molecular to Device Scale. Chem Rev 112, 5488–5519 (2012).

9 Xu, B., Mao, N., Zhao, Y., Tong, L. & Zhang, J. Polarized Raman Spectroscopy for Determining Crystallographic Orientation of Low-Dimensional Materials. J Phys Chem Lett 12, 7442–7452 (2021).

10 Tanaka, M. & Young, R. J. Review Polarised Raman spectroscopy for the study of molecular orientation distributions in polymers. J Mater Sci 41, 963–991 (2006).

11 Basova, T. V. & Kolesov, B. A. Raman polarization studies of the orientation of molecular thin films. Thin Solid Films 325, 140–144 (1998).

12 Szybowicz, M. et al. High temperature study of FT-IR and Raman scattering spectra of vacuum deposited CuPc thin films. J Mol Struct 704, 107–113 (2004).

13 Kolesov, B. A., Basova, T. V. & Igumenov, I. K. Determination of the orientation of CuPc film by raman spectroscopy. Thin Solid Films 304, 166–169 (1997).

14 Huang, C.-W. et al. Micro-Raman imaging of isomeric segregation in small-molecule organic semiconductors. Commun Chem 2, 22 (2019).

15 Szybowicz, M., Bała, W., Fabisiak, K., Paprocki, K. & Drozdowski, M. The molecular structure ordering and orientation of the metallophthalocyanine CoPc, ZnPc, CuPc, and MgPc thin layers deposited on silicon substrate, as studied by micro-Raman spectroscopy. J Mater Sci 46, 6589–6595 (2011).

16 Szybowicz, M., Bała, W., Fabisiak, K., Paprocki, K. & Drozdowski, M. Micro-Raman spectroscopic investigations of cobalt phthalocyanine thin films

deposited on quartz and diamond substrates. Crystal Research and Technology 45, 1265–1271 (2010).

17 Szybowicz, M. et al. Temperature and orientation study of cobalt phthalocyanine CoPc thin films deposited on silicon substrate as studied by micro-Raman scattering spectroscopy. Thin Solid Films 520, 623–627 (2011).

18 Szybowicz, M. & Makowiecki, J. Orientation study of iron phthalocyanine (FePc) thin films deposited on silicon substrate investigated by atomic force microscopy and micro-Raman spectroscopy. J Mater Sci 47, 1522–1530 (2012).

19 Latteyer, F. et al. Laterally Resolved Orientation and Film Thickness of Polar Metal Chlorine Phthalocyanines on Au and ITO. The Journal of Physical Chemistry C 115, 11657–11665 (2011).

20 Basova, T. V., Kiselev, V. G., Sheludyakova, L. A. & Yushina, I. V. Molecular organization in the thin films of chloroaluminium hexadecafluorophthalocyanine revealed by polarized Raman spectroscopy. Thin Solid Films 548, 650–656 (2013).

21 Mitra, K. & Hartman, M. C. T. Silicon phthalocyanines: synthesis and resurgent applications. Org Biomol Chem 19, 1168–1190 (2021).

22 Yutronkie, N. J., Grant, T. M., Melville, O. A., Lessard, B. H. & Brusso, J. L. Old Molecule, New Chemistry: Exploring Silicon Phthalocyanines as Emerging N-Type Materials in Organic Electronics. Materials 12, 1334 (2019).

23 King, B. et al. Silicon Phthalocyanines for n-Type Organic Thin-Film Transistors: Development of Structure-Property Relationships. ACS Appl Electron Mater 3, 325–336 (2021).

24 Vebber, M. C., Rice, N. A., Brusso, J. L. & Lessard, B. H. Thermodynamic Property-Performance Relationships in Silicon Phthalocyanine-Based Organic Photovoltaics. ACS Appl Energy Mater 5, 3426–3435 (2022).

25 Vebber, M. C., Grant, T. M., Brusso, J. L. & Lessard, B. H. Bis(trialkylsilyl oxide) Silicon Phthalocyanines: Understanding the Role of Solubility in Device Performance as Ternary Additives in Organic Photovoltaics. Langmuir 36, 2612–2621 (2020).

26 Ganesh Moorthy, S. et al. Molecular Engineering of Silicon Phthalocyanine to Improve the Charge Transport and Ammonia Sensing Properties of Organic Heterojunction Gas Sensors. Advanced Sensor Research 2, (2023).

27 King, B., Radford, C. L., Vebber, M. C., Ronnasi, B. & Lessard, B. H. Not Just Surface Energy: The Role of Bis(pentafluorophenoxy) Silicon Phthalocyanine Axial Functionalization and Molecular Orientation on Organic Thin-Film Transistor Performance. ACS Appl Mater Interfaces (2023) doi:10.1021/acsami.2c22789.

28 King, B. et al. Peripherally Fluorinated Silicon Phthalocyanines: How Many Fluorine Groups Are Necessary for Air-Stable Electron Transport in Organic Thin-Film Transistors? Chemistry of Materials 35, 8517–8528 (2023).

29 Cranston, R. R. et al. Highlighting the processing versatility of a silicon phthalocyanine derivative for organic thin-film transistors. J Mater Chem C Mater 10, 485–495 (2022).

30 Anand, S., Goetz, K. P., Lamport, Z. A., Zeidell, A. M. & Jurchescu, O. D. Field-dependent charge transport in organic thin-film transistors: Impact of device structure and organic semiconductor

microstructure. Appl Phys Lett 115, (2019).

31 Chung, H. & Diao, Y. Polymorphism as an emerging design strategy for high performance organic electronics. J Mater Chem C Mater 4, 3915–3933 (2016).

32 Diao, Y. et al. Understanding Polymorphism in Organic Semiconductor Thin Films through Nanoconfinement. J Am Chem Soc 136, 17046–17057 (2014).

33 Pandolfi, L. et al. Precursor polymorph determines the organic semiconductor structure formed upon annealing. J Mater Chem C Mater 9, 10865–10874 (2021).

34 Grant, T. M., Dindault, C., Rice, N. A., Swaraj, S. & Lessard, B. H. Synthetically facile organic solar cells with >4% efficiency using P3HT and a silicon phthalocyanine non-fullerene acceptor. Mater Adv 2, 2594–2599 (2021).

35 Singh, S. & Mohapatra, Y. N. Bias stress effect in solution-processed organic thin-film transistors: Evidence of field-induced emission from interfacial ions. Org Electron 51, 128–136 (2017).

36 Jia, X., Fuentes-Hernandez, C., Wang, C.-Y., Park, Y. & Kippelen, B. Stable organic thin-film transistors. Sci Adv 4, (2018).

37 Park, J. H. et al. Origin of Bias-Stress Induced Instability in Organic Thin-Film Transistors with Semiconducting Small-Molecule/Insulating Polymer Blend Channel. ACS Appl Mater Interfaces 5, 1625–1629 (2013).

38 Wo, S., Headrick, R. L. & Anthony, J. E. Fabrication and characterization of controllable grain boundary arrays in solution-processed small molecule organic semiconductor films. J Appl Phys 111, (2012).

39 Basova, T. V. & Kolesov, B. A. Raman Spectra of Copper Phthalocyanin: Experiment and Calculation. Journal of Structural Chemistry 41, 770–777 (2000).

40 Zhang, Y., Zhang, X., Liu, Z., Xu, H. & Jiang, J. Comparative density functional theory study of the structures and properties of metallophthalocyanines of group IV B. Vib Spectrosc 40, 289–298 (2006).

41 Liu, Z., Zhang, X., Zhang, Y. & Jiang, J. Theoretical investigation of the molecular, electronic structures and vibrational spectra of a series of first transition metal phthalocyanines. Spectrochim Acta A Mol Biomol Spectrosc 67, 1232–1246 (2007).

42 Zhang, X., Lin, W., Zhao, H. & Wang, R. Raman spectra study of p -tert-butylphenoxy-substituted phthalocyanines with different central metal and substitution positions. Vib Spectrosc 96, 26–31 (2018).

43 Tackley, D. R., Dent, G. & Ewen Smith, W. Phthalocyanines: structure and vibrations. Physical Chemistry Chemical Physics 3, 1419–1426 (2001).

44 Heutz, S., Bayliss, S. M., Middleton, R. L., Rumbles, G. & Jones, T. S. Polymorphism in Phthalocyanine Thin Films: Mechanism of the α → β Transition. J Phys Chem B 104, 7124–7129 (2000).

45 Basova, T. V. et al. Optical Spectroscopy and XRD Study of Molecular Orientation, Polymorphism, and Phase Transitions in Fluorinated Vanadyl Phthalocyanine Thin Films. The Journal of Physical Chemistry C 117, 7097–7106 (2013).

46 Zou, T. et al. Controllable Molecular Packing Motif and Overlap Type in Organic Nanomaterials for Advanced Optical Properties. Crystals (Basel) 8, 22 (2018).

47 Coppedè, N. et al. Controlled Polymorphism in Titanyl Phthalocyanine on Mica by Hyperthermal Beams: A Micro-Raman Analysis. The Journal of Physical Chemistry C 114, 7038–7044 (2010).

48 Kumar, A. et al. Influence of substrate on molecular order for self-assembled adlayers of CoPc and FePc. Journal of Raman Spectroscopy 49, 1015–1022 (2018).

49 Iwatsu, F. Size effects on the alpha-beta transformation of phthalocyanine crystals. J Phys Chem 92, 1678–1681 (1988).

50 Ai, X. et al. Phase modification of copper phthalocyanine semiconductor by converting powder to thin film. Appl Surf Sci 428, 788–792 (2018).

51 Gonzalez Arellano, D. L. et al. Phase Transition of Graphene-Templated Vertical Zinc Phthalocyanine Nanopillars. J Am Chem Soc 140, 8185–8191 (2018).

52 Zawadzka, A. et al. Structural and nonlinear optical properties of as-grown and annealed metallophthalocyanine thin films. Thin Solid Films 545, 429–437 (2013).

53 Xu, J. et al. Effect of solvent–vapour annealing on morphology, structure of copper(II) phthalocyanine thin films and device performance. Bulletin of Materials Science 41, 111 (2018).

54 Yang, J. L., Schumann, S. & Jones, T. S. Tuning the morphology and molecular orientation of copper hexadecafluorophthalocyanine thin films by solvent annealing. Thin Solid Films 519, 3709–3715 (2011).

55 Debe, M. K. & Kam, K. K. Effect of gravity on copper phthalocyanine thin films II: Spectroscopic evidence for a new oriented thin film polymorph of copper phthalocyanine grown in a microgravity environment. Thin Solid Films 186, 289–325 (1990).

56 Fatima, N., Karimov, Kh. S., Abid, M., Farooq, A. & Khan, M. U. Effect of humidity and temperature on organic semiconductor CuPc films deposited at different gravity conditions. in 2015 International Conference on Industrial Engineering and Operations Management (IEOM) 1–5 (IEEE, 2015). doi:10.1109/IEOM.2015.7228099.

57 Comeau, Z. J., Cranston, R. R., Lamontagne, H. R., Shuhendler, A. J. & Lessard, B. H. Strong Magnetic Field Annealing for Improved Phthalocyanine Organic Thin-Film Transistors. Small 19, (2023).

58 Venables, J. A. Atomic processes in crystal growth. Surf Sci 299, 798–817 (1994).

59 Reichelt, K. Nucleation and growth of thin films. Vacuum 38, 1083–1099 (1988).

60 Verlaak, S. et al. Nucleation of organic semiconductors on inert substrates. Phys Rev B Condens Matter Mater Phys 68, 1–11 (2003).

61 Lee, J.-H., Kim, S., Kim, H. & Lee, J. Solvent-dependent performance of solution-processed small-molecule organic field-effect transistors. Org Electron 52, 184–189 (2018).

62 Diao, Y., Shaw, L., Bao, Z. & Mannsfeld, S. C. B. Morphology control strategies for solution-processed organic

semiconductor thin films. Energy Environ Sci 7, 2145–2159 (2014).

63 Chen, S., Li, Z., Qiao, Y. & Song, Y. Solution-processed organic semiconductor crystals for field-effect transistors: from crystallization mechanism towards morphology control. J Mater Chem C Mater 9, 1126–1149 (2021).

64 Khasbaatar, A. et al. From Solution to Thin Film: Molecular Assembly of π-Conjugated Systems and Impact on (Opto)electronic Properties. Chem Rev 123, 8395–8487 (2023).

65 Cranston, R. R. et al. Thin-Film Engineering of Solution-Processable n-Type Silicon Phthalocyanines for Organic Thin-Film Transistors. ACS Appl Mater Interfaces 13, 1008–1020 (2021).

66 Zaumseil, J. & Sirringhaus, H. Electron and Ambipolar Transport in Organic Field-Effect Transistors. Chem Rev 107, 1296–1323 (2007).

Chapter 5. High Performance Solution Processed N-Type OTFTs Through Surface Engineered F-F Interactions Using Asymmetric Silicon Phthalocyanines

This chapter is adapted from: ***Cranston, R. R.****, Vebber, M. C., Faleiro Berbigier, J., Brusso, J., Kelly, T. L., Lessard, B. High Performance Solution Processed n-Type OTFTs through Surface Engineered F–F Interactions Using Asymmetric Silicon Phthalocyanines. Advanced Electronic Materials (2022).*

Context

To improve the performance of OTFTs, I sought to use interactions at the dielectric-semiconductor interface to enhance the order of the semiconducting film via controlled self-assembly. To this end, two novel asymmetric SiPc derivatives, each with an axially substituted fluorine and an alkyl group, were synthesized for this work. A self-assembled monolayer of fluorinated silane was used to fluorinate the surface of SiO_2 substrates where the fluorinated SiPc derivatives were then deposited. Through the selective fluorination of the SiPc molecule, coupled with the fluorinated surface treatment, I achieved the highest mobility solution processed n-type SiPc OTFTs at the time of publication. In addition to fluorine-fluorine interactions between the dielectric and semiconductor layers, I also explored the effects of dielectric surface energy and solvent evaporation rate on SiPc deposition to yield films comprised of large area crystalline domains that favour charge transport.

Contributions of Authors

This work was completed through contributions of all authors. For this work, I fabricated and characterized all OTFTs and thin-films, conducted data analysis and wrote the manuscript. M.C.V. synthesized all SiPc derivatives, and collected UV-vis, CV, TGA, and DSC data. J.F.B conducted GIWAXS experiments with analysis. J.B, T.L.K., and B.H.L. provided supervision for the project.

Abstract

Two novel asymmetric silicon phthalocyanine (SiPc) derivatives consisting of one axially substituted fluorine and one tri-alkyl silane group were synthesized and characterized in n-type

solution processed bottom-gate top-contact organic thin-film transistors (OTFTs). The effect of surface energy and fluorination were investigated at the dielectric-semiconductor interface by thin-film X-ray diffraction (XRD), atomic force microscopy (AFM), dark field real-colour microscopy, and grazing-incidence wide-angle X-ray scattering (GIWAXS) to assess alterations in film conformation, microstructure, and morphology. Low surface energy dielectric modification and the presence of fluorine interactions produced films with large area crystalline domains that promoted charge carrier transport resulting in high performing OTFTs, with a clear relationship determined between surface energy, fluorination, and OTFT operation. Through modifying deposition solvent and the exploitation of fluorine-fluorine interactions, the asymmetric SiPc derivative, (tri-*n*-hexylsilyl oxide) fluorosilicon phthalocyanine (F-3HS-SiPc), led to high performing n-type OTFTs with an average field-effect mobility of 0.13 cm^2 V^{-1} s^{-1} and a threshold voltage of 26.3 V. These results successfully demonstrate the use of asymmetric axial fluorination as a rout to high performance n-type OTFT devices through controlled self-assembly by fluorine-fluorine interactions.

Introduction

Organic thin-film transistors (OTFTs) have attracted significant interest due to their low-cost high-throughput solution processability and the potential for flexible integration enabling next generation electronic applications including displays,[1,2] sensors,[3–6] and wearable electronics[7,8]. Improving transistor operation focuses on the synthesis of new organic semiconductors, optimizing device architecture, and the engineering of key interfaces such as the dielectric-semiconductor and semiconductor-electrodes.[9–12] Currently, few OTFTs have demonstrated high charge carrier mobilities while maintaining a feasible operating voltage,[13–15] with even fewer exhibiting n-type, or electron dominate, charge transfer characteristics[16–19]. High performance n-type organic semiconductors are crucial for the development of more complex electronic devices like integrated circuits,[20,21] and such their scarcity is one of the prevailing factors hindering the proliferation of OTFT applications.

Post-deposition thin-film modification and rearrangement is a common strategy used to increase charge carrier mobilities and the overall performance of OTFTs. Methods of improving thin-film microstructure, such as annealing, increases the expense and manufacturing time required and thus is generally less applicable to large scale manufacturing. Instead, by the careful design of both the organic semiconductor and OTFT architecture, thin-film formation can be controlled during the deposition process to produce the desired microstructure and morphology that enables high performance OTFTs. Modifications of the dielectric-semiconductor interface by surface treatment can be employed to increased semiconductor crystallinity, improved grain interconnectivity, and influence molecular orientation, resulting in greater charge carrier mobilities.[22–24] In literature, fluorinated self-assembled monolayers (SAMs) have been used to selectively control and self-pattern the microstructure of fluorinated organic semiconductors by creating crystalline domains of molecules in the regions where fluorine-fluorine interactions are present, while surrounding regions exhibit a mixture of crystalline textures.[25,26] The regions of highly ordered molecules create favourable π-stacking and promote charge transport at the dielectric-semiconductor interface, while mixed phase regions inhibit charge transport. The ability to control the film formation of organic semiconductors during deposition offers simple fabrication by eliminating common, yet industrially impractical, post processing steps such as solvent and temperature annealing.

Metal and metalloid phthalocyanines (MPcs) are a family of organic small molecules with highly customizable structures through variations in metal center, and the inclusion of peripheral, bay, or axial functional groups which influence both physical and chemical properties. In particular, axially substituted silicon phthalocyanines (SiPcs) employing flexible non-conjugated alkyl chains as solubilizing groups have demonstrated promising results in n-type OTFTs[27,28] and as acceptors in organic photovoltaic (OPV) devices[29–32]. Substituted alkyl chains contribute to the dissolution of small molecules in solution through increased van der Waals interactions, hindering interactions between the π-conjugated systems of the semiconductor, and thus enabling increased solubility and solution processability.[33] Additionally, SiPcs offer two chemical handles in the axial position enabling the potential for asymmetric substitutions and the incorporation of fluorine atoms for self-patterning potential and as electron withdrawing groups for enhanced stability[34,35].

In this work, we report the synthesis of two novel asymmetric SiPc derivatives and characterized their structural, thermal, physical, optical, and electronic properties by single crystal X-ray diffraction (XRD), thermal gravimetric analysis (TGA), differential scanning calorimetry (DSC), and ultraviolet-visible spectroscopy (UV-vis). Typically in literature asymmetric phthalocyanines are synthesized using different phthalonitriles leading to asymmetry in the periphery[36,37] of the phthalocyanine while in this study the asymmetry is in the axial direction. The asymmetric SiPc derivatives consist of one axial fluorine and one axial tri-alkyl group with chains of either four or six carbons in length, denoted as F-3BS-SiPc and F-3HS-SiPc respectively (**Figure 5.1a**). The previously characterized symmetric analogs of these derivatives designated (3BS)$_2$-SiPc and (3HS)$_2$-SiPc are shown in **Figure 5.1b** for ease of comparison.[27] OTFTs with a bottom-gate top-contact architecture, shown in **Figure 5.1c**, were fabricated by solution processing using F-3BS-SiPc and F-3HS-SiPc as the organic semiconductor. The average electron field-effect mobility (μ_e), threshold voltage (V_T), and on/off current ratio ($I_{on/off}$) of OTFTs were determined and compared to their symmetric non-fluorinated counterparts. The influence of surface energy and fluorine-fluorine interaction at the dielectric-semiconductor interface was investigated by silane surface treatment. Changes in thin-film microstructure, and morphology were determined by thin-film XRD, atomic force microscopy (AFM), dark field real-colour microscopy, and grazing-incidence wide-angle X-ray scattering (GIWAXS) and related to OTFT performance. By the careful selection of deposition solvent, we obtained the highest reported performing, solution fabricated, n-type SiPc-based OTFTs, without the need for post deposition processes.

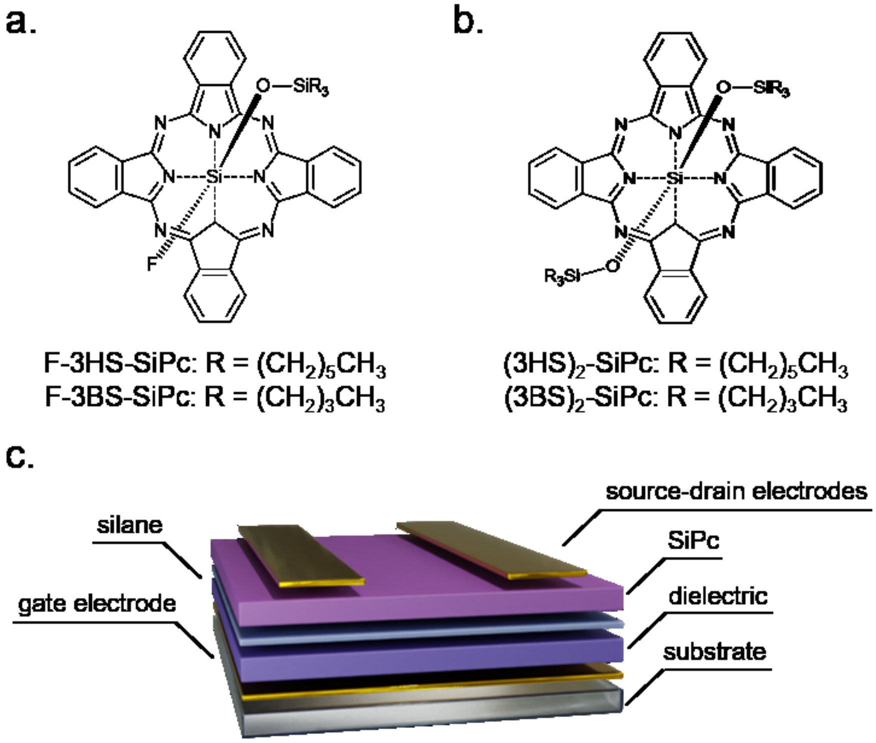

Figure 5.1. Structure of (a) asymmetrically fluorinated F-3BS-SiPc and F-3HS-SiPc and (b) symmetrical non-fluorinated, (3BS)$_2$-SiPc and (3HS)$_2$-SiPc. (c) Diagram of bottom-gate top-contact OTFT architecture.

Results and Discussion

Synthesis and Material Characterization

Herein we report the synthesis and characterization of two novel asymmetric SiPcs, F-3BS-SiPc and F-3HS-SiPc, alongside well-studied symmetric derivatives, $(3BS)_2$-SiPc and $(3HS)_2$-SiPc.[27,29,38] **Figure 5.2** illustrates the synthetic pathway used in the production of the novel asymmetric SiPcs. This pathway is a combination of adapted procedures reported by Li and Lieberman (i),[39] Gessner at al. (ii),[40] Xu et al.(iii),[41] and Grant et al.(iv).[42] Reaction (i) is used to make a SiPc with one protected axial position, preventing double functionalization when carrying out step (ii). The photoreaction (iii) is used to deprotect the axial position. Step (iv), which in the original reference pertained the fluorination of Cl_2-SiPc, was the most drastically altered procedure. The acidification of the medium was necessary in order to effectively remove axial hydroxyl groups, which forms a stronger bond with silicon when compared to chlorine, likely by creating a more viable leaving group via the protonating the axial substituent. The fluorination of the asymmetric SiPcs (**Figure 5.2 iv**) is a necessary step to remove hydroxyl groups from the SiPc core, which is reported to act as a charge trap.[43] The overall yield of the synthesis is approximately 10 % (compounding the yield of all steps), which is reasonable considering the additional steps required and harsh fluorination conditions.

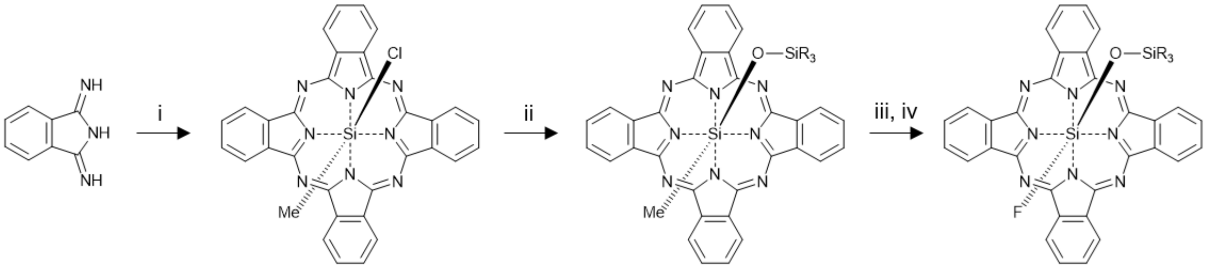

Figure 5.2. Synthetic pathway to produce asymmetric SiPcs. (i) $SiMeCl_3$, quinoline, 220°C, 3 hr; (ii) chlorotrialkylsilane, NaOH, aliquat HTA, Cl-benzene, 130°C, 6 hr; (iii) H_2O, triethylamine, THF, RT, 48 hr, hν and (iv) CsF, DMF, H_2SO_4, 120°C, 1 hr.

A comparison of the optical (**Figure S5.1**), electrochemical (**Figure S5.2**) and thermal properties (**Figure S5.3**) of symmetric and asymmetric SiPcs is found in **Table 5.1**. Only small changes of < 0.1 eV in highest occupied molecular orbitals (HOMO) and lowest unoccupied molecular orbitals (LUMO) energy levels were observed when comparing $(3BS)_2$-SiPc and $(3HS)_2$-SiP to F-3BS-SiPc and F-3HS-SiPc, respectively, likely due to the introduction of the more electronegative fluorine when compared to the bulky oxytrialkylsilane groups substituent. Thermal analysis shows that F-3HS-SiPc and $(3HS)_2$-SiPc have virtually identical melting points (T_m). Alternatively, F-3BS-SiPc did not show any events in the DSC spectrum up to 250°C, which compared to $(3BS)_2$-SiPc (T_m = 232°C) indicates that the reduction from two to a single bulky group increased the melting point of the compound. Overall, the optical, electrochemical, and thermal properties of the asymmetric SiPc compounds are similar to corresponding symmetric derivatives.

Table 5.1. Optical (UV-vis), electrochemical (CV) and thermal (DSC) characterization of SiPcs.

Material	λ_{max}^a (nm)	$E_g{}^a$ (eV)	$E_{Ox}{}^b$ (V)	$E_{HOMO}{}^c$ (eV)	$E_{LUMO}{}^c$ (eV)	$T_m{}^d$ (°C)
$(3BS)_2$-SiPc*	669	1.82	0.98	-5.3	-3.5	232
$(3HS)_2$-SiPc*	669	1.82	0.98	-5.3	-3.5	173
F-3BS-SiPc	672	1.80	1.06	-5.4	-3.6	NA
F-3HS-SiPc	674	1.80	1.06	-5.4	-3.6	172

* data taken from ref. 27

a. peak absorbance determined in DCM, E_g = energy bandgap determined from the onset of UV-vis absorption spectrum

b. half wave potential of oxidation

c. highest occupied molecular orbital energy level and lowest unoccupied molecular orbital energy level

d. endothermic peak from solid-state DSC in N_2

OTFT Characterization

For ease of comparison, initial electrical characterization of F-3BS-SiPc and F-3HS-SiPc was carried out in the same manner as our previous works on symmetrical SiPc derivatives.[27,28] F-3BS-SiPc and F-3HS-SiPc were deposited as the semiconductor layer in bottom-gate top-contact OTFTs by spin-coating the SiPc solutions onto OTS treated silicon substrates with a SiO_2 dielectric layer. Electrical characterization of OTFTs was performed in the saturation operating regime to determine the average μ_e, V_T, and $I_{on/off}$ as detailed in the ***Experimental*** section. **Table 5.2** summarizes these transistor characteristics in addition to the previously studied symmetric $(3BS)_2$-SiPc and $(3HS)_2$-SiPc, with **Figure S5.4** and **Figure S5.5** providing example transfer and output curves. Idealistic transistor operating is defined by a high μ_e, V_T close to 0 V, and a high $I_{on/off}$, generally as a result of highly-ordered low-defect crystalline thin-films that provide efficient charge transport pathways between electrodes.

Table 5.2. Average electrical characteristics of SiPc OTFTs calculated from *n* unique transistors.

Material	Solvent	Surface	μ_e (x 10^{-2} cm^2 V^{-1} s^{-1})	V_T (V)	$I_{on/off}$	*n*
$(3BS)_2$-SiPc*	chloroform	OTS	2.80 ± 0.53	17.6 ± 2.3	10^5	40
$(3HS)_2$-SiPc*	chloroform	OTS	not functional			
F-3BS-SiPc	chloroform	OTS	0.50 ± 0.02	39.0 ± 1.5	10^4	11
F-3HS-SiPc	chloroform	OTS	1.64 ± 0.91	34.8 ± 3.6	10^5	36
F-3HS-SiPc	chloroform	PFTS	0.13 ± 0.37	41.0 ± 1.9	10^4	15
F-3HS-SiPc	chloroform	PTS	0.016 ± 0.05	31.3 ± 2.2	10^3	13
F-3HS-SiPc	chloroform	MPTS	0.015 ± 0.05	33.6 ± 1.6	10^3	15
F-3HS-SiPc	chloroform	SiO_2	0.003 ± 0.008	44.4 ± 6.7	10^2	9
F-3HS-SiPc	toluene	PFTS	12.6 ± 6.68	26.3 ± 3.5	10^5	17

* data taken from ref. 27

OTFTs using F-3HS-SiPc as the semiconductor exhibited the highest μ_e equal to 1.64 x 10^{-2} cm^2 V^{-1} s^{-1} with a V_T of 34.8 V. $(3HS)_2$-SiPc, the symmetric counterpart to F-3HS-SiPc, was found to be non-functional in OTFTs with the same architecture and fabrication conditions as this study.[27] F-3BS-SiPc OTFTs exhibited the lowest μ_e of 0.50 x 10^{-2} cm^2 V^{-1} s^{-1} and highest V_T of 39.0 V. The high V_T displayed by F-3HS-SiPc and F-3BS-SiPc OTFTs may be due to a difference in the LUMO of the asymmetric SiPcs (-3.6 eV) and the low work function manganese (-4.1 eV) that was used as a source-drain electrode interlayer. This dissimilarity in energy levels, and the potential presence of charge traps resulting from non-ideal thin-film morphologies, can increase contact resistance causing a high V_T.[44] It has been previously established that alkyl chain length and symmetry of the axial groups play an important role in the molecular packing and structure of SiPc thin-films, where long highly asymmetric alkyl chains disrupt the packing structure and hinder charge transport resulting in poor semiconducting properties.[27] Following the trend between chain length and OTFT performance observed with symmetric SiPc OTFTs, F-3BS-SiPc should display more favourable OTFT operation due to the shorter alkyl chains of its axial group. The addition of the asymmetric axial fluorine to F-3BS-SiPc increases the overall asymmetry of the molecule likely reducing the number of efficient charge transport pathways in a similar manner to asymmetric alkyl chains.[27] Conversely, the addition of an axial fluorine and asymmetric structure of F-3HS-SiPc enhanced OTFT performance, potentially as a result of preventing the long alkyl chains from obstructing one another and hindering molecular packing.

From single crystal XRD of $(3BS)_2$-SiPc (CCDC #1522758)[45] and F-3BS-SiPc (CCDC #2165855) an increase in intermolecular spacing and a herringbone packing structure is observed with axial fluorination (**Figure S5.6**). Larger atomic distances between SiPc molecules and the alternating face-to-edge and face-to-face molecular orientation of herringbone packing can result in decreased π-electron overlap reducing charge transfer and subsequent OTFT performance. **Figure S5.7** shows that unlike F-3BS-SiPc, F-3HS-SiPc (CCDC #2165547) has a π-stacked, also known as slip stacked, packing structure which may provide a greater π-electron overlap and thus the order of magnitude increase in μ_e between the two materials.[46] It has been observed that the semiconducting properties of axially substituted SiPcs in OTFTs depends largely on the size and symmetry of the axial groups, where OTFT performance has been demonstrated to decrease with increasing chain length and asymmetry.[27] For F-3BS-SiPc, an overall increase in molecular asymmetry led to a herringbone packing structure and increased intermolecular spacing contributing to a decrease in device performance compared to the symmetric derivative $(3BS)_2$-SiPc. Asymmetric fluorination of the longer alkyl chain derivative $(3HS)_2$-SiPc improved transistor operation and produced films of a π-stacked structure, demonstrating how asymmetric axial fluorination can significantly alter the crystal structure and subsequent charge transfer properties of different materials.

Thin-Film and F-F Surface Characterization

To study the influence between fluorinated dielectric modifications and fluorinated SiPc semiconductors on OTFT operation and thin-film microstructure, a number on silane surface treatments were examined for OTFT fabrication using F-3HS-SiPc as the semiconductor. In OTFTs, charge transport occurs in the conductive channel that forms at the dielectric-semiconductor interface, making this region one of the most important in terms of operation. Dielectric modification by silane surface treatment is a common strategy employed to improve charge transfer in bottom gate SiO_2 OTFTs by altering surface energy, roughness, and charge trap density.[47,48] The various silane surfaces, displayed in **Figure 5.3a**, have a broad range of chemical structures with short and long chain lengths, non-fluorinated and fluorinated chains, trichloro and trimethoxysilyl end groups, and phenyl and alkyl groups. Additionally, the surface energy varies for each silane as indicated by their water contact angle (θ_w), with a higher θ_w corresponding to a more hydrophobic and lower energy surface. Characteristic transfer curves of functional OTFTs made with the silane treated substrates are displayed in **Figure 5.3b** with average μ_e, V_T, and $I_{on/off}$

values reported in **Table 5.2**. Transfer curves and characteristic output curves of OTFTs fabricated using silane surface treatments are provided in **Figure S5.8** and **Figure S5.9**. Due to the highly hydrophobic nature of FOTS and ODTS significant de-wetting of F-3HS-SiPc was observed making functional OTFTs unattainable. Additionally, OTFTs made with MODTS were found to be non-functional; likely as a result of its long alkyl chain which has been previously determined to reduce ideal transistor behaviour in evaporated SiPc OTFTs.[47]

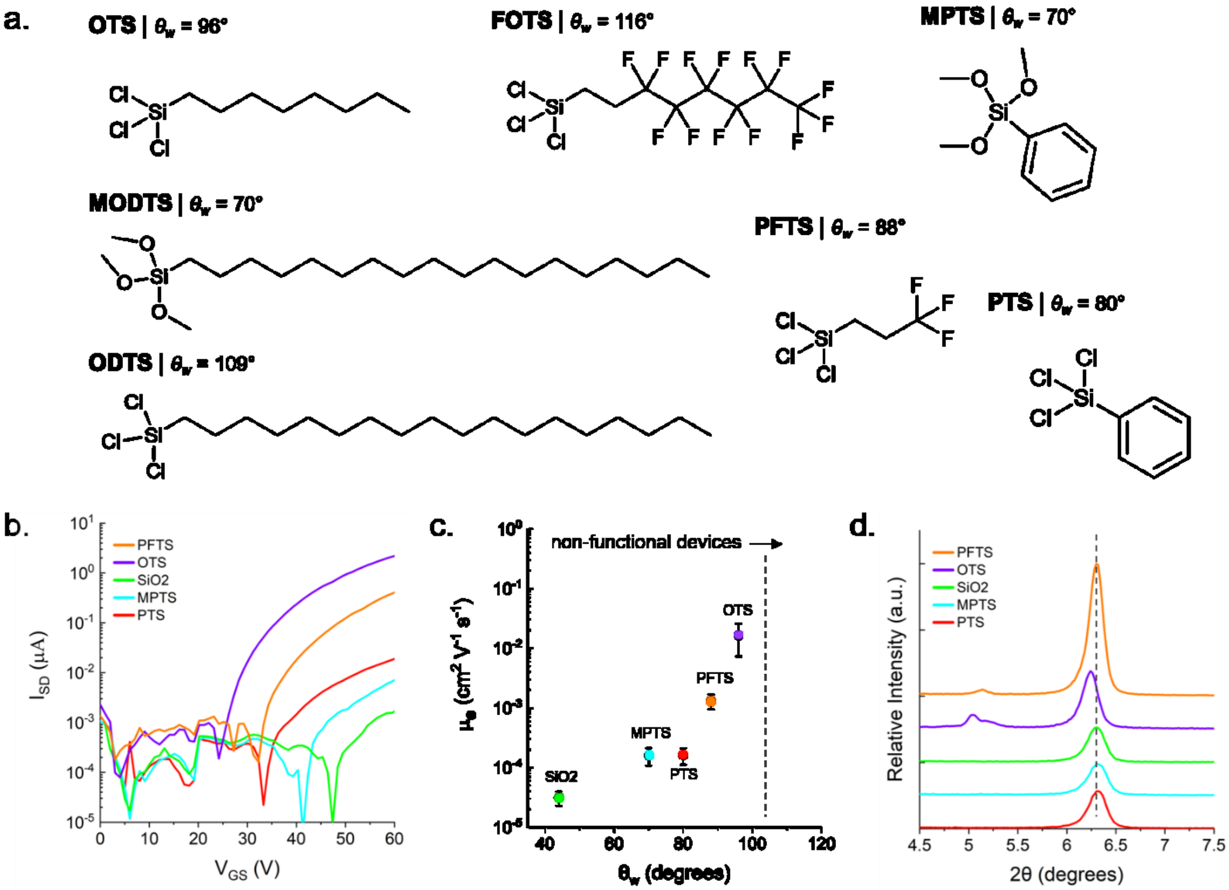

Figure 5.3. (a) Structure of silane surface treatments with θ_w measured on SiO_2 ($\theta_w = 44°$). (b) Characteristic transfer curves, (c) average μ_e versus θ_w and (d) XRD pattern of F-3HS-SiPc OTFTs deposited from chloroform on silane surface treated substrates.

The best performing OTFTs were obtained using OTS as the surface treatment, exhibiting an average μ_e of 1.64 x 10^{-2} cm^2 V^{-1} s^{-1} and a V_T of 34.8 V, with PFTS exhibiting the second highest μ_e of 0.13 x 10^{-2} cm^2 V^{-1} s^{-1} and V_T of 41.0 V. **Figure 5.3c**, demonstrates a relationship between hydrophobicity and μ_e, where more hydrophobic low energy surfaces leads to greater device μ_e. This result is in agreement with the relationship between surface energy and organic thin-film formation for other conjugated semiconductors.[48–50] Inorganic metal oxides such as SiO_2 typically have hydrophilic high energy states, while organic small molecules like SiPcs have hydrophobic low energy states. This incompatibility in surface energy yields poor quality films as a result of insufficient crystal formation and aggregation. If the dielectric and organic semiconductor possess similar surface energies, crystalline, large grain film formation is promoted, favouring efficient charge transport.[48–50] Thin-film formation by solution processes complicates this relationship as there exists a trade-off between hydrophobic dielectric modifications and de-wetting of the organic semiconductor solution as demonstrated by the high θ_w silanes ODTS and FOTS studied herein.

Dielectric surface treatment is also proven to modify thin-film microstructure evident by the XRD patterns of F-3HS-SiPc OTFTs in **Figure 5.3d**. MPTS and PTS modified substrates, as well as bare SiO_2, display a single low intensity peak at 2θ = 6.34° corresponding to a d-spacing of 13.9 Å. The low diffraction intensity displayed by F-3HS-SiPc on these silane treatments indicate low crystallinity films which likely contribute to their low μ_e and high V_T device performance. The fluorinated silane treatment, PFTS, displays an intense peak at 2θ = 6.34° and a small peak at 2θ = 5.16° corresponding to a d-spacing of 17.1 Å. Similarly, OTS led to multiple peaks by XRD with a high intensity peak at 2θ = 6.26° (d-spacing of 14.2 Å), and a low intensity peak with shoulder at 2θ = 5.06° (d-spacing of 17.5 Å) and 2θ = 5.22° (d-spacing of 16.9 Å). The peak shift from 2θ = 6.34° to 2θ = 6.26° and the additional low angle peak at 2θ = 5.06° indicate a different film structure and polymorph formation which could contribute to the improved device μ_e.

The nucleation and growth of small molecule thin-films by solution processing is dictated by the rate of solvent evaporation which directly corresponds to the rate of material crystallization. High evaporation rate solvents can lead to the formation of large uneven clusters as molecules have little time to move on the substrate to more favourable configurations. This often results in rough films with a non-uniform morphology. Conversely, solvents with low evaporation rates facilitate the formation of highly ordered homogenous films typically favourable for charge transport in electronic devices such as OTFTs. To improve the performance of OTFTs fabricated with a fluorinated dielectric treatment and a fluorinated semiconductor, a slow evaporating solvent was used for deposition to increase nucleation time and slow the rate of crystallization. OTFTs were fabricated using F-3HS-SiPc deposited from either chloroform or toluene onto PFTS treated substrates, with **Table 5.2** summarizing the OTFT performance metrics and **Figure S5.10a** displaying the forward transfer curves of these devices. Using toluene as the deposition solvent increased the average μ_e by two orders of magnitude to 0.13 cm^2 V^{-1} s^{-1} with an average V_T reduction from 41.0 V to 26.3 V. The XRD patterns of chloroform and toluene fabricated F-3HS-SiPc thin-films on PFTS treated substrates, displayed in **Figure S5.10b**, both exhibit a high intensity peak at approximately 2θ = 6.34°, however films fabricated from toluene display a secondary peak at 2θ = 4.44° corresponding to d-spacing of 19.9 Å. This second low angle peak is similar to that of the F-3HS-SiPc films fabricated from chloroform on OTS treated substrates shown in **Figure 5.3d**. F-3HS-SiPc thin-films deposited from toluene on PFTS treated substrates led to improved OTFT performance compared to F-3HS-SiPc deposited from chloroform on OTS. By using a slower evaporating solvent to decrease the rate of crystallization, films with a similar microstructure to using a low surface energy dielectric treatment, such as OTS, are produced.

F-3HS-SiPc films deposited on PFTS, PTS, MPTS and bare SiO_2 were characterized by dark field microscopy and AFM imaging to further highlight how surface energy and dielectric modification dictates thin-film morphology (**Figure 5.4**). The low θ_w hydrophilic surfaces, PTS, MPTS and SiO_2, display non-uniform films with minimal defined grains and large areas of poorly distributed material. In contrast, F-3HS-SiPc on PFTS treated substrates exhibit highly crystalline films with large elongated interconnected features and distinct grains. As discussed, the lower surface energy of PFTS provides better material aggregation and crystallization corresponding well with thin-film morphology, OTFT performance, and the XRD pattern displayed in **Figure 5.3d**. The morphology and microstructure of F-3HS-SiPc on PFTS is likely not only a result of surface energy effects but that additional interactions between the fluorinated dielectric surface and fluorinated semiconducting material are likely inducing a significant change in structure.

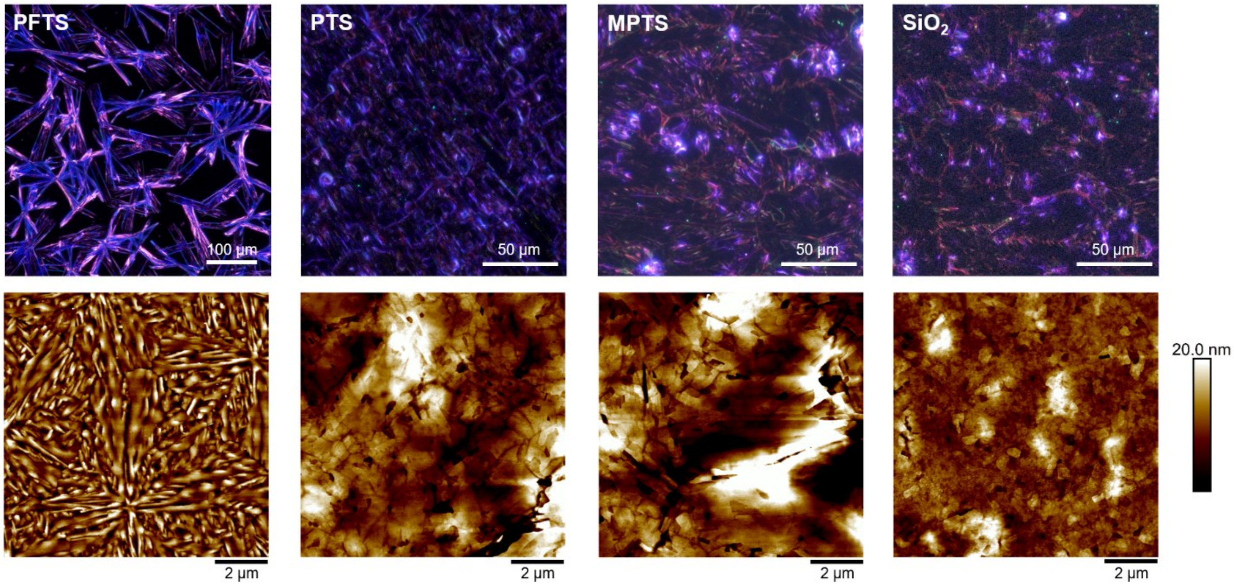

Figure 5.4. Dark field real-colour microscopy images of F-3HS-SiPc drop-casted on PFTS (x500), PTS (x1500), MPTS (x1500) and SiO_2 (x1500) with AFM images (10 µm x 10 µm) of F-3HS-SiPc spin-coated on PFTS, PTS, MPTS and SiO_2.

Through GIWAXS the interaction between fluorinated dielectric surface treatment and fluorinated semiconducting materials is explored using thin-films of $(3HS)_2$-SiPc and F-3HS-SiPc deposited on PFTS treated substrates, with **Figure 5.5a** displaying the 2D scattering patterns of each material. The azimuthally-integrated GIWAXS pattern of $(3HS)_2$-SiPc is in good agreement with the pattern predicted by single crystal XRD (**Figure S5.11a**). The arched scattering pattern indicates a distribution of crystallite orientations; however, the (001) reflection at q = 0.49 Å^{-1} is predominantly out-of-plane (along q_z), while the (010) reflection at q = 0.51 Å^{-1} is predominantly in-plane, indicating an orientational preference. This preferred orientation has the SiPc ring oriented 53° relative to the substrate surface (**Figure 5.5b**). Additionally, the (100) reflection at q = 0.67 Å^{-1} appears to have a slight preference for out-of-plane scattering along q_z, which would be consistent with a second preferred orientation, where the SiPc ring is oriented 24° relative to the substrate surface. Multiple orientation preferences have been observed previously for SiPc films on OTS treated substrates.[27] The 2D scattering pattern of F-3HS-SiPc on PFTS treated substrates exhibits significant differences in molecular order and structure, evident by the highly speckled scattering pattern in **Figure 5.5a** which indicates a crystalline film with a distinct orientation. The azimuthally-integrated GIWAXS pattern matches poorly with that predicated by single crystal XRD (**Figure S5.11b**). The large difference between the GIWAXS diffraction pattern and the powder pattern predicted from single crystal XRD data suggests that the interaction between the fluorinated dielectric and semiconducting materials induces the formation of a new polymorph with a distinct crystallite orientation. The 2D scattering and diffraction pattern of toluene fabricated F-3HS-SiPc films, determined by GIWAXS (**Figure S5.12**), shows no significant difference in crystal structure compared to chloroform, with both solvents resulting in the same polymorph and the same preferred orientation. These results suggest fluorine-fluorine interactions between asymmetric F-3HS-SiPc and PFTS leads to unique molecular self-assembly and thin-film organization which provides favourable charge transport properties and ultimately improved OTFT performance.

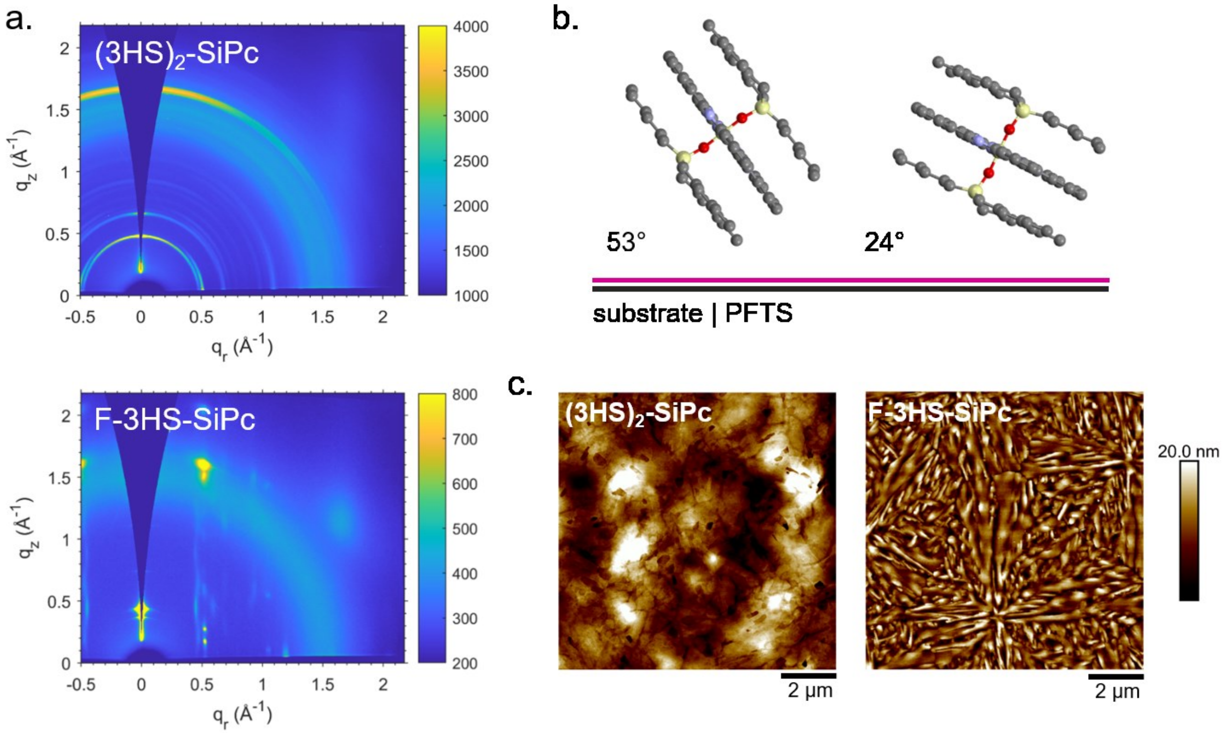

Figure 5.5. (a) 2D scattering patterns of $(3HS)_2$-SiPc and F-3HS-SiPc deposited from chloroform on PFTS treated substrates, (b) schematic diagram representing the preferred orientations of $(3HS)_2$-SiPc molecules relative to a PFTS treated substrate determined by GIWAXS, and (c) AFM images (10 μm x 10 μm) of $(3HS)_2$-SiPc and F-3HS-SiPc deposited from chloroform on PFTS treated substrates.

Conclusion

Herein, the synthesis and characterization of the structural, thermal, physical, optical and electrical properties of two novel asymmetric axially substituted SiPcs, F-3BS-SiPc and F-3HS-SiPc, is presented. Fluorinated SiPc derivatives were successfully employed as the semiconducting layer in OTFTs fabricated by solution processing, with transistor performance assessed with respect to their previously studied symmetric analogs in terms of μ_e, V_T, and $I_{on/off}$. The effect of surface energy and fluorination on F-3HS-SiPc thin-film formation and OTFT performance was investigated through dielectric modification by silane treatment where a direct relationship between surface energy and OTFT performance was observed. Decreasing the surface energy of the dielectric layer, such that it more closely matches F-3HS-SiPc provided more favourable conditions for the formation of large area crystalline domains, which promoted efficient charge transport and resulted in high μ_e OTFTs. Using both the fluorinated surface, PFTS, and the asymmetric fluorinated semiconductor, F-3HS-SiPc, highly ordered crystalline film formation was observed. By reducing the rate of crystallization during deposition the OTFT performance of F-3HS-SiPc on PFTS was significantly improved without the use of post deposition processes. To our knowledge, we report the highest μ_e achieved by solution processed n-type SiPc OTFTs with an average μ_e of 0.13 cm^2 V^{-1} s^{-1}. This work demonstrates that high performance, solution processed n-type OTFTs, can be achieved through engineering interactions between the dielectric and semiconductor layers using an asymmetric axially fluorinated SiPc paired with fluorinated surface treatment without auxiliary post deposition processes.

Experimental

Materials

1,3-Diiminoisoindoline (DI3, 96%) was purchased from Abacipharma and used as received. Trichloro(octyl)silane (OTS, 97%), trichloro(3,3,3-trifluoropropyl)silane (PFTS, 97%), trimethoxy(octadecyl)silane (MODTS, 95%), trichloro(octadecyl)silane (ODTS, 90%), trimethoxy(phenyl)silane (MPTS, 97%), trichloro(phenyl)silane (PTS, 97%), trichloro(1H, 1H, 2H, 2H-perfluorooctyl)silane (FOTS, 97%), quinoline (98%), trichloromethylsilane (MeSiCl3, 99%), chlorotrihexylsilane (95%), chlorotributylsilane (95%), Aliquat HTA-1 (30-35% in water) were purchased from Sigma-Aldrich and used without further purification. Solvents were purchased from commercial suppliers and used as received, unless otherwise specified.

Synthesis of Axially Asymmetric Silicon Phthalocyanines

Synthesis of methylchlorosilicon phthalocyanine (Cl-MeSiPc)

The procedure used in the preparation of MeCl-SiPc has been adapted from the literature.[39] In a typical synthesis, DI3 (6 g, 45.3 mmol) and quinoline (70 ml) were charged in a 250 ml round-bottom flask and stirred (400-600 RPM) to form a slurry. The mixture was then heated to 50°C and purged by N_2 bubbling. After 30 min, flask was maintained under a N_2 atmosphere and $MeSiCl_3$ (4.5 ml, 26.3 mmol) was added with a syringe through a rubber septum. The mixture was then heated to 220°C under vigorous stirring (900 RPM), forming a deep dark green solution overtime. After 2 hr, the heat was turned off and, once the mixture had cooled below 100°C, the solids were precipitated in 500 ml of isopropanol. Solids were filtered using a medium porosity fritted glass filter, with the aid of a vacuum pump. Solids were then washed with toluene (100 ml), acetone (200 ml) and methanol (500-1000 ml) until the filtrate was mostly clear (faint green colour may persist). Drying was carried out in a vacuum oven to afford 2.8 g of purple solids. Yield 56%.

Synthesis of (tri-*n*-hexylsilyl oxide) methylsilicon phthalocyanine (3HS-MeSiPc)

The axial substitution of the silicon SiPc core has been carried with an adapted method from literature.[40] Cl-MeSiPc (2 g, 2.4 mmol), NaOH (340 mg, 8.4 mmol), chlorotrihexylsilane (2.2 ml, 6 mmol), chlorobenzene (20 ml) and Aliquat HTA-1 (0.1 ml, 0.030 mmol) were charged into a 100 ml round bottom flask, which was covered with aluminum foil to protect it from light, and heated to 130°C. After reacting for 1 hr, another fraction of chlorotrihexylsilane (0.8 ml, 1.9 mmol) was added to the mixture with a syringe. At the 2 hr mark, additional NaOH (170 mg, 4.2 mmol) and chlorotrihexylsilane (2.2 ml, 6 mmol) were introduced in the mixture, and reacted for further 4 hr. Heating was then turned off and once the flask had cooled to room temperature, the mixture was filtered by gravity and solids washed with DCM until filtrate was clear (~200 ml). Filtrate solvents were removed under reduced pressure, followed by the addition of 100-200 ml of methanol to precipitate and wash the solids. Product was collected by gravity filtration, yielding 1.8 g of purple solids. Yield: 62%

Synthesis of (tri-*n*-hexylsilyl oxide) hydroxysilicon phthalocyanine (3HS-OHSiPc)

Procedure adapted from literature[39,41]: 3HS-MeSiPc (1 g, 1.2 mmol), THF (800 ml), triethylamine (5 ml, 36 mmol) and distilled water (1 ml, 55 mmol) were added to a 1 L glass beaker and stirred gently (300 RPM) at room temperature. A 10 W white LED spotlight lamp (no UV) was placed next to the beaker, making sure all the light was going through the solution. The photoreaction was maintained until the solution changed colour, from green to blue (~48 hr). Solution was filtered by gravity, through an $MgSO_4$ bed to remove water, and the filtrate solvents removed under reduced pressure. The blue/purple solids were washed with Methanol (200 ml), affording 0.7 g of product. Yield 70%.

Synthesis of (tri-*n*-hexylsilyl oxide) fluorosilicon phthalocyanine (F-3HS-SiPc)

A solvent mixture of DMF and 0.5% v/v H_2SO_4 was prepared prior to this reaction. 3HS-OHSiPc (500 mg, 0.6 mmol), CsF (250 mg, 1.65 mmol) and the acidified DMF (10 ml) were charged in a 100 ml round bottom flask and stirred gently (300 ml). N_2 was bubbled through the solution during the entirety of the reaction. After 30 min of N_2 purging, the mixture was heated to 125°C and maintained at that temperature for 1 hr. Then, mixture was cooled to room temperature and precipitated in 100 ml of MeOH. Solids were collected and dried under reduced pressure. Purification was carried out by train sublimation at 230°C and 130 mtorr. Yield after sublimation: 40%.

^{1}HNMR: 9.63 ppm (m, 8H); 8.31 ppm (m, 8H); 0.81 ppm (m, 6H); 0.69 ppm (t, 9H); 0.34 ppm (m, 6H); 0.00 ppm (m, 6H); -1.30 (m, 6H). ^{19}FNMR: -100.52 (s). HR-MS: expected mass 858.40, obtained mass 858.40.

Synthesis of (tri-*n*-butylsilyl oxide) fluorosilicon phthalocyanine (F-3BS-SiPc)

Synthesis of 3BS-FSiPc was carried out by repeating steps 1-5 and replacing the appropriate silane in step 2, with the same molar quantity. Yield after sublimation: 31%.

^{1}HNMR: 9.63 ppm (m, 8H); 8.34 ppm (m, 8H); -0.06 ppm (m, 15H); -1.28 (m, 6H). ^{19}FNMR: -100.58 (s). HR-MS: expected mass 774.31, obtained mass 775.31.

Compound Characterization

Solution UV-vis spectra of the novel axially asymmetric SiPcs were recorded in a Cary 5000 spectrometer in dual-beam mode, from 300 nm to 800 nm, using a quartz cuvette and DCM as solvent. For cyclic voltammograms, the compounds were dissolved in DCM, containing tetrabutylammonium permanganate as auxiliary electrolyte. Voltammograms were obtained in DCM solutions containing 0.1 M of tetrabutylammonium perchlorate as auxiliary electrolyte. A coiled platinum wire was utilised as working electrode, a coiled platinum wire as counter electrode and an Ag/AgCl standard as reference electrode. Ferrocene voltammograms were recorded as standards to estimate HOMO and LUMO levels, using the empirical correlation E_{HOMO} (eV) = -($E_{ox,onset}$ - $E_{oxFc/Fc+,onset}$) - 4.80. Differential scanning calorimetry (DSC) were carried out in a TA instruments Q2000 DSC equipment, under N_2 atmosphere and with a heating rate of 10°C min^{-1}. Single crystals were grown from solution, by dissolving each compound in chloroform and let the solvent slowly evaporate at room temperature over 24-48 hr.

OTFT Fabrication

OTFTs were fabricated on 15 mm x 20 mm n-doped silicon substrates purchased from Ossila with a 300 nm thermally grown SiO_2 dielectric layer. Substrates were cleaned by sequential sonication baths of soapy water, distilled water, acetone and methanol, then dried with nitrogen gas and treated with air plasma for 15 min. Solutions of non-fluorinated silanes (OTS, MODTS, ODTS, MPTS, PTS) were prepared at 1% v/v while fluorinated silanes (PFTS, FOTS) were prepared at 0.1% v/v in anhydrous toluene in a controlled nitrogen filled glove box to avoid exposure to moisture. All substrates were rinsed with distilled water and isopropanol then submerged in silane solutions for 1 hr at 70°C. Treated substrates were then rinsed with toluene and isopropanol and dried in a vacuum oven at 70°C for 1 hr. SiPc solutions were made at a concentration of 10 mg ml^{-1} in chloroform or toluene by heating at 50˚C for 1 hr. The solutions were deposited onto the treated substrates by spin-coating 60 μl of solution at 1500 RPM for 90 sec. All films were then thermally annealed at 100°C for 1 hr under vacuum. Top contact source-drain electrodes were fabricated using shadow masks purchased from Ossila (channel length of 30 μm, channel width of 1000 μm) by depositing 10 nm of manganese at a rate of 0.5 Å s^{-1} followed by 50 nm of silver at a rate of 1 Å s^{-1} using an Angstrom EvoVac thermal evaporator (P < 2 x 10-6 torr).

OTFT Characterization

OTFT characterization was performed using the same procedure outlined in our previous works.[27,28,51] Characterization occurred in a nitrogen filled glove box at room temperature using a custom made testing apparatus that simultaneously made contact with the source-drain and gate electrodes of each transistor. A Keithley 2614B and a MCC USB DAQ was used to control the source-drain voltage (V_{SD} = 50 V) and gate voltage (0 V < V_{GS} < 60 V) to obtain source-drain current (I_{SD}) measurements in order to determine the saturation regime μ_e, V_T, and $I_{on/off}$.

XRD

XRD measurements were obtained using a Rigaku Ultima IV powder diffractometer with a Cu Kα ($\lambda = 1.5418$ Å) source, a scan range of $3° < 2\theta < 15°$, and rate of 0.5° min^{-1}. The d-spacing between successive parallel diffraction planes was calculated using Bragg's Law (**Equation 5.1**):

$$n\lambda = 2d\sin\theta \qquad (5.1)$$

where λ is the incident wavelength equal to 1.54056 Å, d is the spacing between planes, θ is the angle of incidence, and n is a positive integer equal to 1.

AFM

AFM images were taken using a Bruker Dimension Icon AFM with ScanAsyst-Air tips at a rate of 0.815 Hz and analyzed using NanoScope Analysis v.1.8 software.

GIWAXS

GIWAXS experiments were performed at the Brockhouse X-ray Diffraction and Scattering Beamlines - Low Energy Wiggler (BXDS-WLE) beamline at the Canadian Light Source (CLS) with a photon energy of 15.1 keV. All samples were collected using a Rayonix MX300 CCD detector (73.242 μm x 73.242 μm pixel size), with an angle of incidence of $\theta = 0.2°$. Silver behenate (AgBeh) standards were used to calibrate all data using the GIXSGUI software package in MATLAB.[52]

Associated Content

Acknowledgments

B.H.L is financially supported by the Natural Sciences and Engineering Research Council of Canada (NSERC, RGPIN-2020-04079) and the University of Ottawa. B.H.L. is a Canada Research Chair. The research was undertaken, in part, thanks to funding from the Canada Research Chair program. The Canadian Light Source (CLS) is supported by CFI, NSERC, the University of Saskatchewan, the Government of Saskatchewan, Western Economic Diversification Canada, and the Canadian Institutes of Health Research. The authors would also like to acknowledge the Centre for Research in Photonics at the University of Ottawa for access to the AFM and Dr. Jeffery Ovens for performing single crystal XRD.

Supporting Information

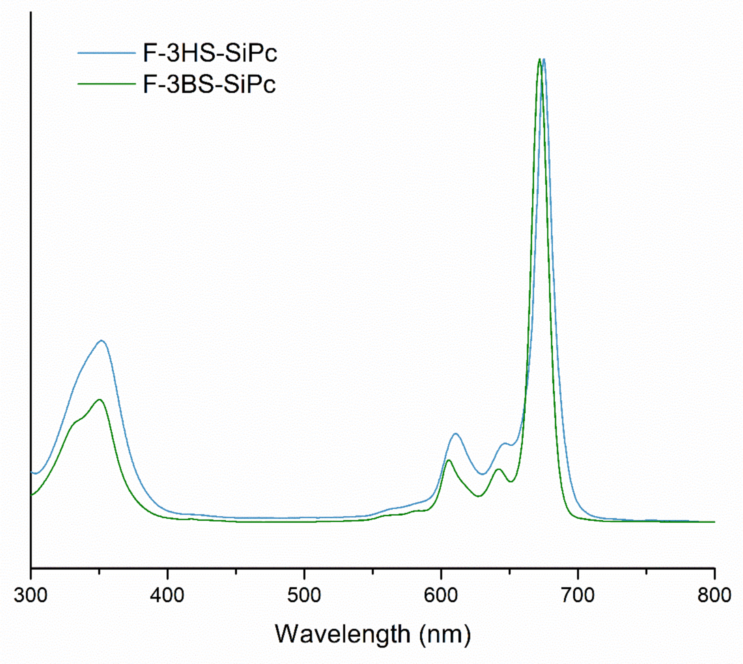

Figure S5.1. UV-Vis spectra of F-3HS-SiPc and F-3BS-SiPc in dichloromethane (DCM).

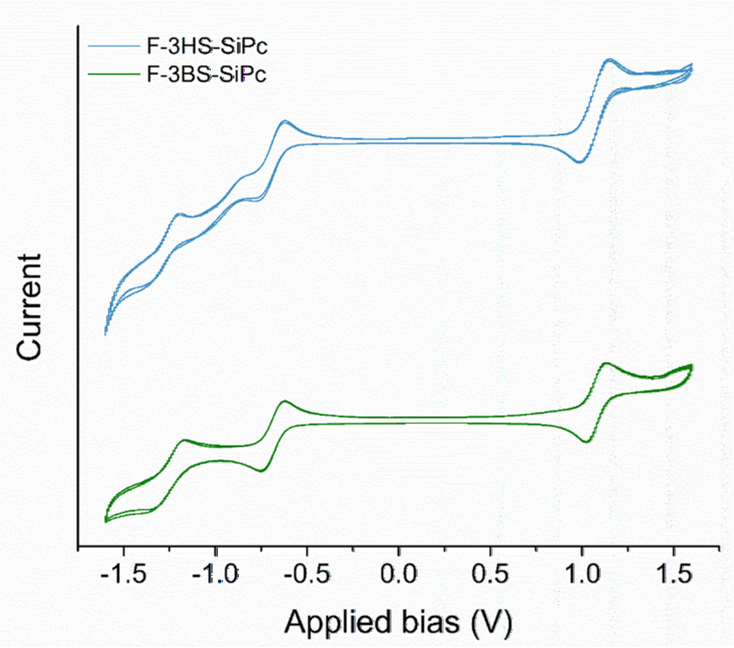

Figure S5.2. CV spectra of F-3HS-SiPc and F-3BS-SiPc.

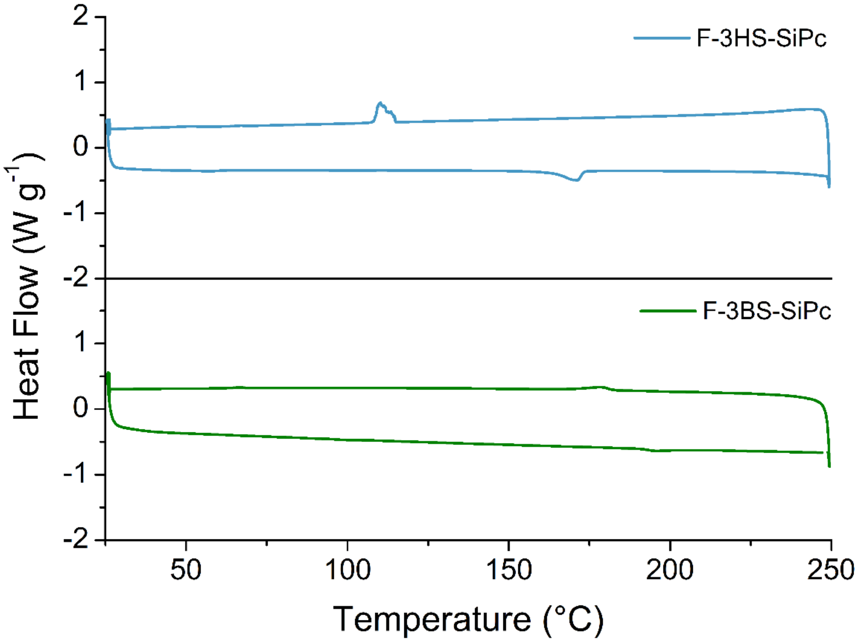

Figure S5.3. DSC thermogram and (a) F-3BS-SiPc and (b) F-3HS-SiPc.

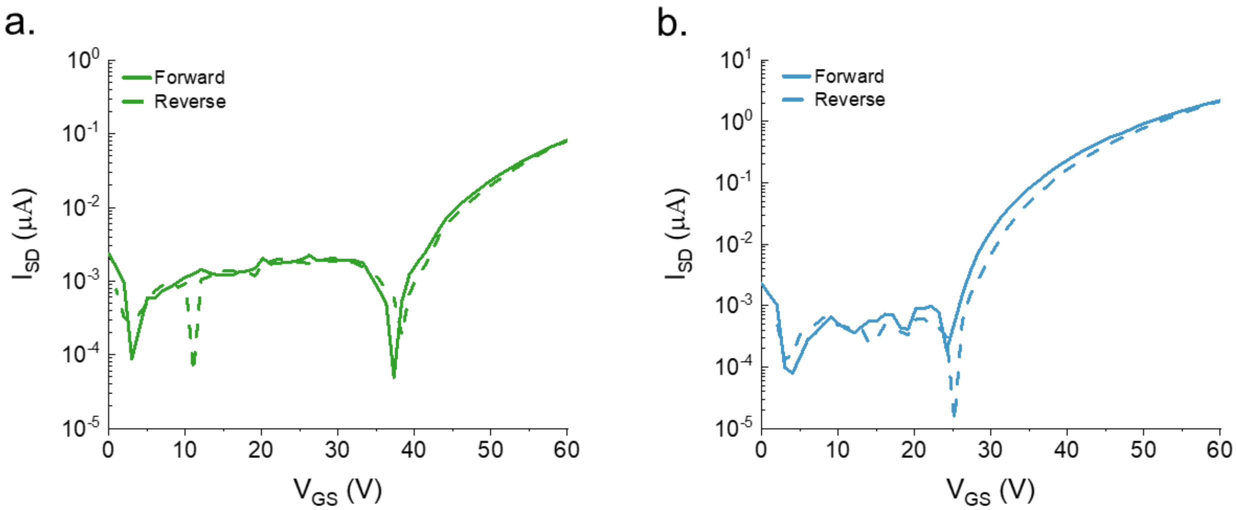

Figure S5.4. Characteristic transfer curves of (a) F-3BS-SiPc, and (b) F-3HS-SiPc on OTS treated substrates. SiPcs were spun from 10 mg ml^{-1} chloroform solutions at a rate of 1500 RPM for 90 sec and annealed at 100°C under vacuum for 1 hr.

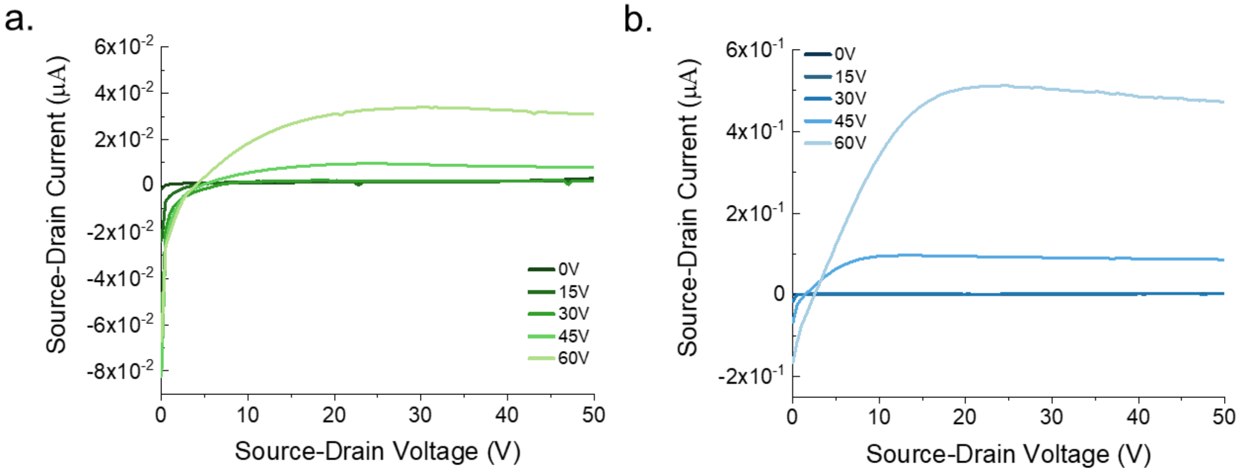

Figure S5.5. Characteristic output curves of (a) F-3BS-SiPc, and (b) F-3HS-SiPc on OTS treated substrates. SiPcs were spun from 10 mg ml^{-1} chloroform solutions at a rate of 1500 RPM for 90 sec and annealed at 100°C under vacuum for 1 hr.

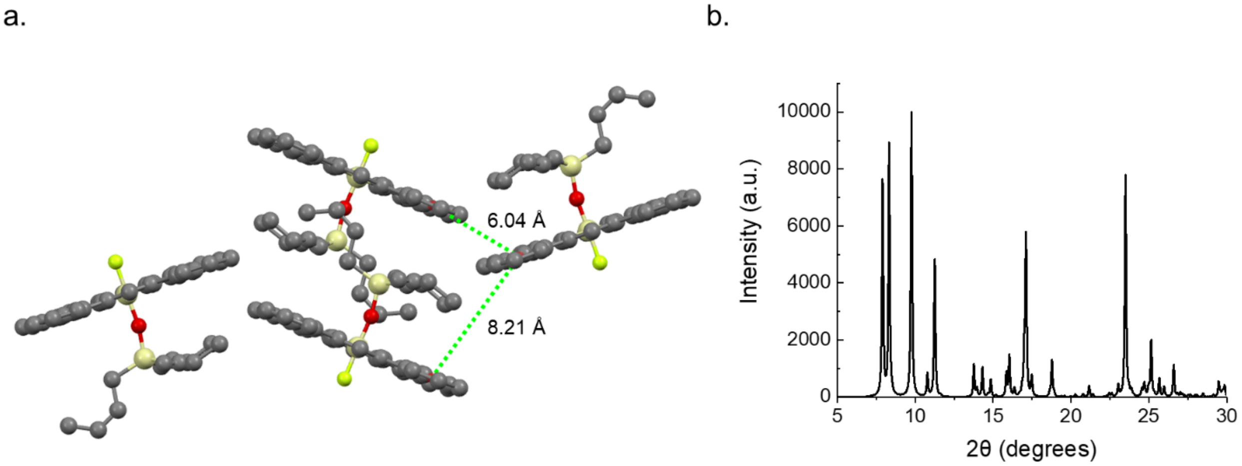

Figure S5.6. (a) Crystal structure (CCDC #2165855) and (b) predicated powder diffraction pattern of F-3BS-SiPc determined by single crystal XRD.

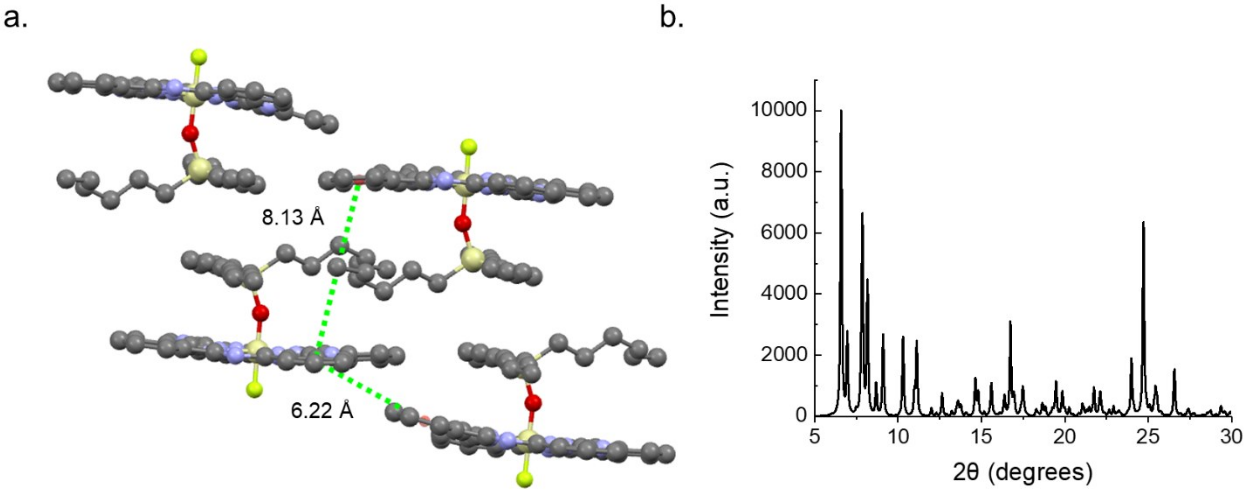

Figure S5.7. (a) Crystal structure (CCDC #2165547) and (b) predicated powder diffraction pattern of F-3HS-SiPc determined by single crystal XRD.

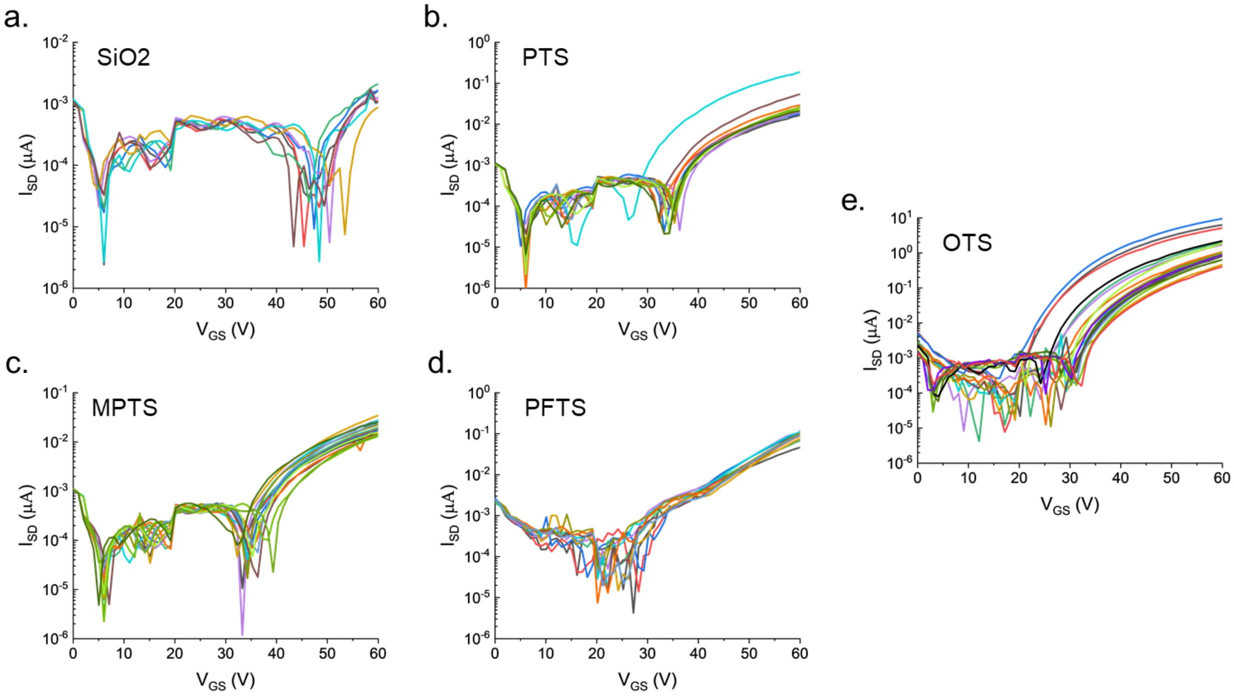

Figure S5.8. Transfer curves of F-3HS-SiPc on (a) bare SiO_2, (b) PTS, (c) MPTS, (d) PFTS, and (e) OTS treated substrates. SiPcs were spun from 10 mg ml^{-1} chloroform solutions at a rate of 1500 RPM for 90 sec and annealed at 100°C under vacuum for 1 hr.

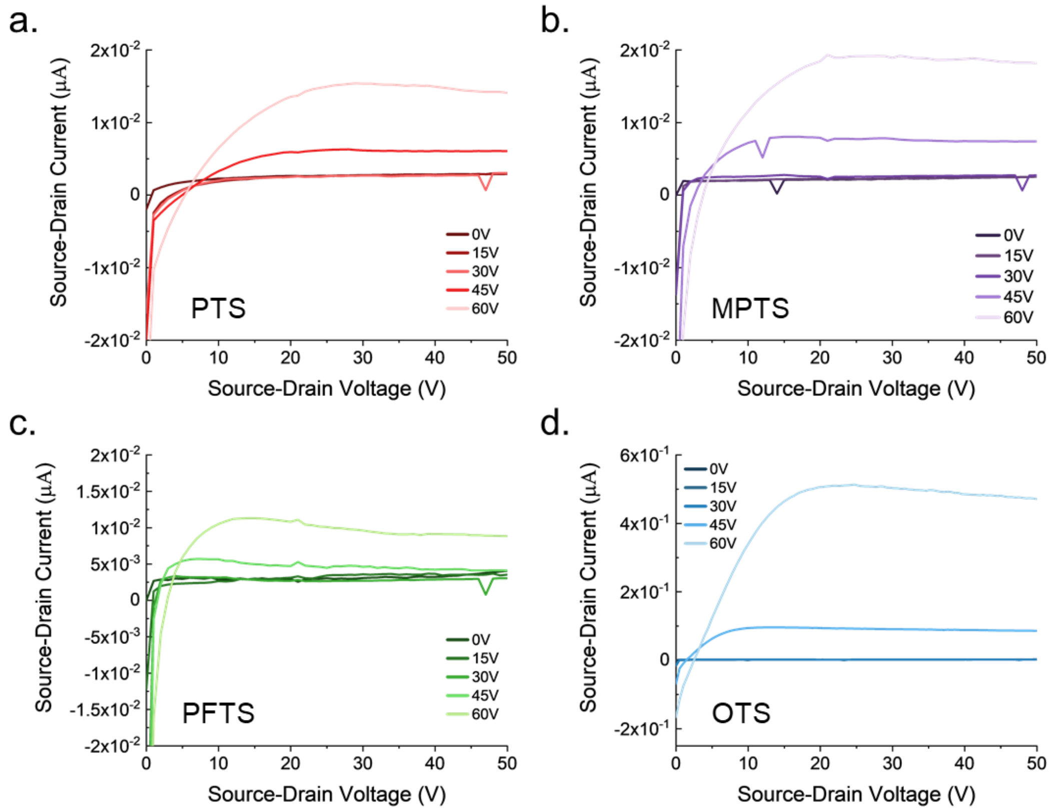

Figure S5.9. Characteristic output curves of F-3HS-SiPc on (a) PTS, (b) MPTS, (c) PFTS, and (d) OTS treated substrates. SiPcs were spun from 10 mg ml^{-1} chloroform solutions at a rate of 1500 RPM for 90 sec and annealed at 100°C under vacuum for 1 hr.

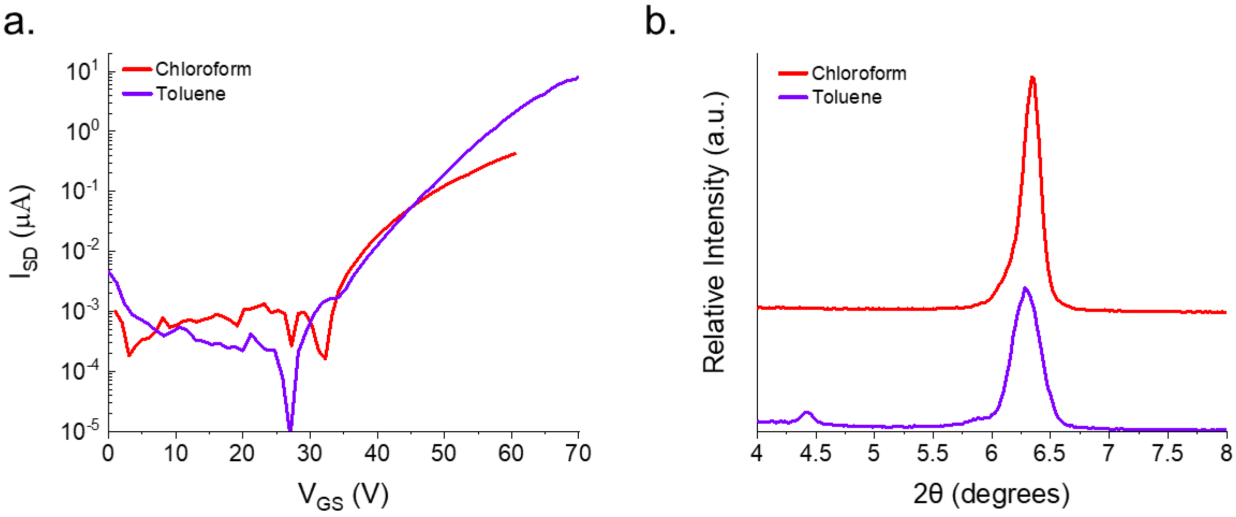

Figure S5.10. (a) Characteristic transfer curves, and (b) XRD patterns of F-3HS-SiPc OTFTs fabricated from chloroform and toluene solutions on PFTS treated substrates.

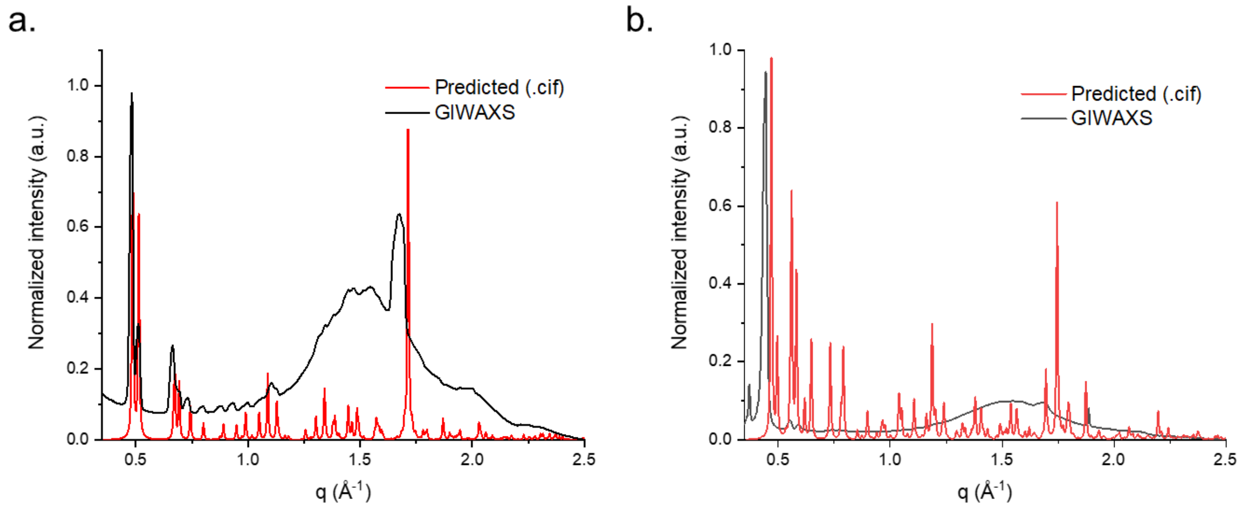

Figure S5.11. Diffraction patterns of (a) (3HS)$_2$-SiPc and (b) F-3HS-SiPc deposited from chloroform on PFTS treated substrates determined by GIWAXS and predicated by single crystal XRD.

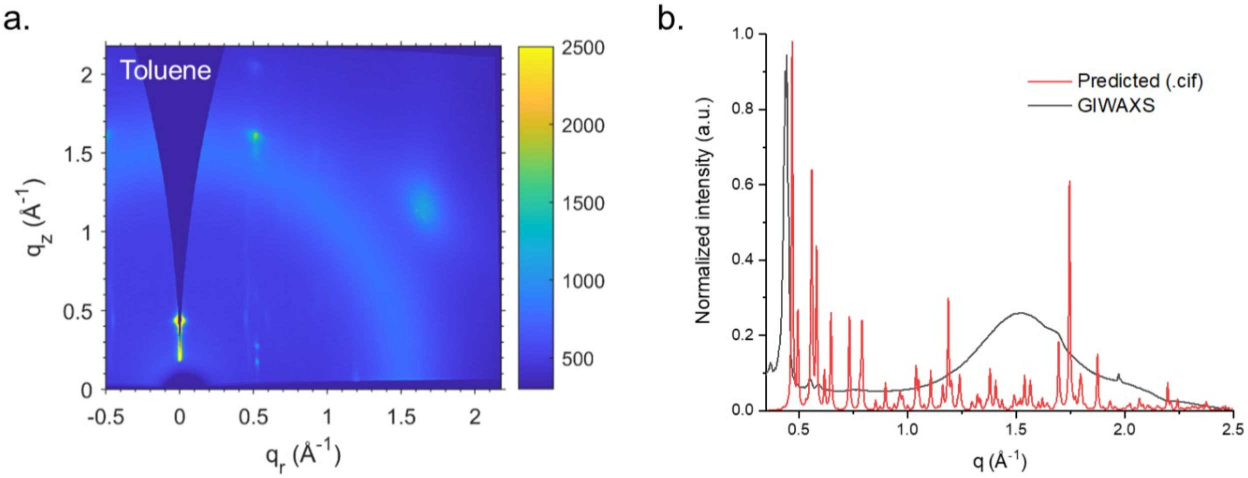

Figure S5.12. (a) 2D scattering pattern and (b) diffraction patterns of F-3HS-SiPc deposited from toluene on PFTS treated substrates determined by GIWAXS and predicated by single crystal XRD.

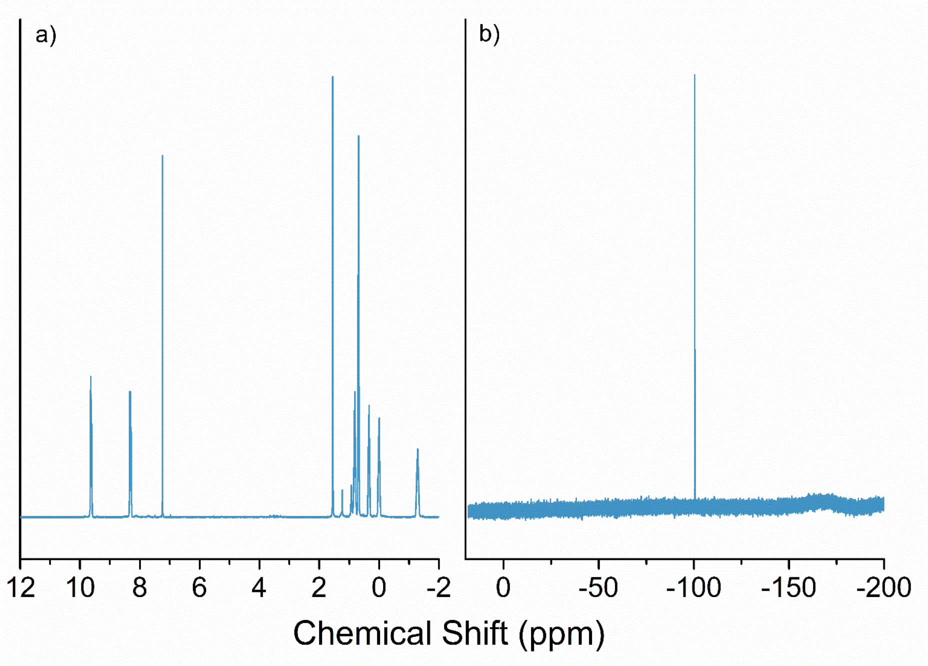

Figure S5.13. (a) ^{1}H NMR and (b) ^{19}F NMR spectra of purified F-3HS-SiPc.

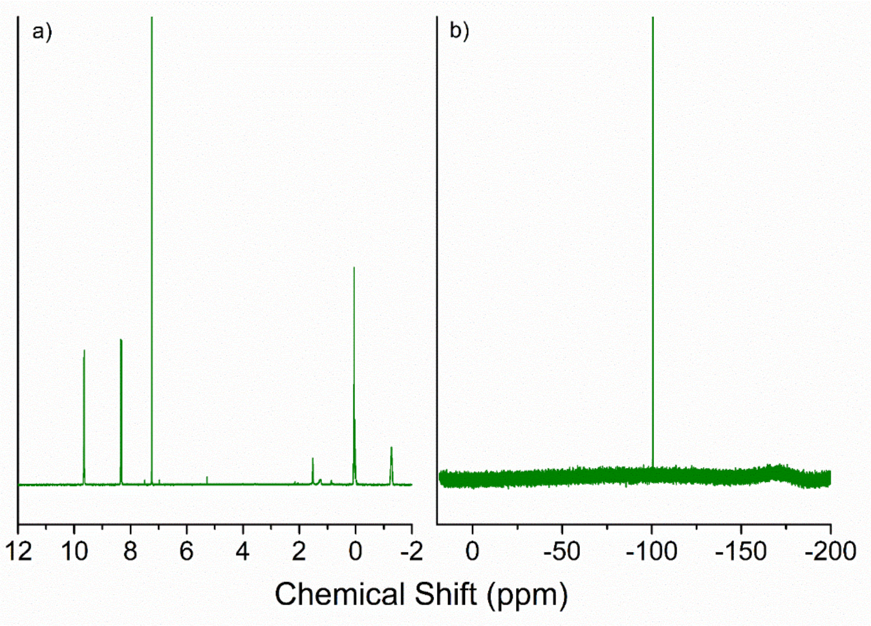

Figure S5.14. (a) ^{1}H NMR and (b) ^{19}F NMR spectra of purified F-3BS-SiPc.

References

1 Zhou, L. et al. All-organic active matrix flexible display. Appl. Phys. Lett. 88, 2004–2007 (2006).

2 Gelinck, G. H. et al. Flexible active-matrix displays and shift registers based on solution-processed organic transistors. Nat. Mater. 3, 106–110 (2004).

3 Comeau, Z. J. et al. On-the-Spot Detection and Speciation of Cannabinoids Using Organic Thin-Film Transistors. ACS Sensors 4, 2706–2715 (2019).

4 Boileau, N. T., Melville, O. A., Mirka, B., Cranston, R. & Lessard, B. H. P and N type copper phthalocyanines as effective semiconductors in organic thin-film transistor based DNA biosensors at elevated temperatures. RSC Adv. 9, 2133–2142 (2019).

5 Bouvet, M. Phthalocyanine-based field-effect transistors as gas sensors. Anal. Bioanal. Chem. 384, 366–373 (2005).

6 Bouvet, M. et al. Phthalocyanine-based field-effect transistor as ozone sensor. Sensors Actuators B Chem. 73, 63–70 (2001).

7 Wang, N., Yang, A., Fu, Y., Li, Y. & Yan, F. Functionalized Organic Thin Film Transistors for Biosensing. Acc. Chem. Res. 52, 277–287 (2019).

8 Ren, H. et al. High-Performance, Ultrathin, Ultraflexible Organic Thin-Film Transistor Array Via Solution Process. Small 14, 1801020 (2018).

9 Sirringhaus, H. 25th Anniversary Article: Organic Field-Effect Transistors: The Path Beyond Amorphous Silicon. Adv. Mater. 26, 1319–1335 (2014).

10 Mei, J., Diao, Y., Appleton, A. L., Fang, L. & Bao, Z. Integrated Materials Design of Organic Semiconductors for Field-Effect Transistors. J. Am. Chem. Soc. 135, 6724–6746 (2013).

11 Guo, X., Han, L. & Hou, X. Insights into the device structure, processing and material design for an organic thin-film transistor towards functional circuit integration. Mater. Chem. Front. 5, 6760–6778 (2021).

12 Kumar, B., Kaushik, B. K. & Negi, Y. S. Organic Thin Film Transistors: Structures, Models, Materials, Fabrication, and Applications: A Review. Polym. Rev. 54, 33–111 (2014).

13 Paterson, A. F. et al. Small Molecule/Polymer Blend Organic Transistors with Hole Mobility Exceeding 13 cm 2 V −1 s −1. Adv. Mater. 28, 7791–7798 (2016).

14 Yuan, Y. et al. Ultra-high mobility transparent organic thin film transistors grown by an off-centre spin-coating method. Nat. Commun. 5, 3005 (2014).

15 Lamport, Z. A. et al. A simple and robust approach to reducing contact resistance in organic transistors. Nat. Commun. 9, 5130 (2018).

16 Gao, X. & Hu, Y. Development of n-type organic semiconductors for thin film transistors: a viewpoint of molecular design. J. Mater. Chem. C 2, 3099–3117 (2014).

17 Zhao, X. & Zhan, X. Electron transporting semiconducting polymers in organic electronics. Chem. Soc. Rev. 40, 3728 (2011).

18 Anthony, J. E., Facchetti, A., Heeney, M., Marder, S. R. & Zhan, X. n-Type Organic Semiconductors in Organic Electronics. Adv. Mater. 22, 3876–3892 (2010).

19 Zaumseil, J. & Sirringhaus, H. Electron and Ambipolar Transport in Organic Field-Effect Transistors. Chem. Rev. 107, 1296–1323 (2007).

20 Quinn, J. T. E., Zhu, J., Li, X., Wang, J. & Li, Y. Recent progress in the development of n-type organic semiconductors for organic field effect transistors. J. Mater. Chem. C 5, 8654–8681 (2017).

21 Baeg, K.-J., Caironi, M. & Noh, Y.-Y. Toward Printed Integrated Circuits based on Unipolar or Ambipolar Polymer Semiconductors. Adv. Mater. 25, 4210–4244 (2013).

22 Melville, O. A., Lessard, B. H. & Bender, T. P. Phthalocyanine-Based Organic Thin-Film Transistors: A Review of Recent Advances. ACS Appl. Mater. Interfaces 7, 13105–13118 (2015).

23 Dong, H., Fu, X., Liu, J., Wang, Z. & Hu, W. 25th Anniversary Article: Key Points for High-Mobility Organic Field-Effect Transistors. Adv. Mater. 25, 6158–6183 (2013).

24 Liu, D. & Miao, Q. Recent progress in interface engineering of organic thin film transistors with self-assembled monolayers. Mater. Chem. Front. 2, 11–21 (2018).

25 Ward, J. W. et al. Rational design of organic semiconductors for texture control and self-patterning on halogenated surfaces. Adv. Funct. Mater. 24, 5052–5058 (2014).

26 Joseph Kline, R. et al. Controlling the Microstructure of Solution-Processable Small Molecules in Thin-Film Transistors through Substrate Chemistry. Chem. Mater. 23, 1194–1203 (2011).

27 Cranston, R. R. et al. Thin-Film Engineering of Solution-Processable n-Type Silicon Phthalocyanines for Organic Thin-Film Transistors. ACS Appl. Mater. Interfaces 13, 1008–1020 (2021).

28 Cranston, R. et al. Highlighting the processing versatility of a silicon phthalocyanine derivative for organic thin-film transistors. J. Mater. Chem. C (2022).

29 Vebber, M. C., Grant, T. M., Brusso, J. L. & Lessard, B. H. Bis(trialkylsilyl oxide) Silicon Phthalocyanines: Understanding the Role of Solubility in Device Performance as Ternary Additives in Organic Photovoltaics. Langmuir 36, 2612–2621 (2020).

30 Grant, T. M., Dindault, C., Rice, N. A., Swaraj, S. & Lessard, B. H. Synthetically facile organic solar cells with 4% efficiency using P3HT and a silicon phthalocyanine non-fullerene acceptor. Mater. Adv. 2, 2594–2599 (2021).

31 Grant, T. M. et al. High Voc solution-processed organic solar cells containing silicon phthalocyanine as a non-fullerene electron acceptor. Org. Electron. 87, 105976 (2020).

32 Vebber, M. C., Rice, N. A., Brusso, J. L. & Lessard, B. H. Thermodynamic Property–Performance Relationships in Silicon Phthalocyanine-Based Organic Photovoltaics. ACS Appl. Energy Mater. 5, 3426–3435 (2022).

33 Lei, T., Wang, J.-Y. & Pei, J. Roles of Flexible Chains in Organic Semiconducting Materials. Chem. Mater. 26, 594–603 (2014).

34 Schmidt, R. et al. Core-fluorinated perylene bisimide dyes: Air stable n-channel organic semiconductors for thin film transistors with exceptionally high on-to-off current ratios. Adv. Mater. 19, 3692–3695 (2007).

35 Chen, H. Z. et al. Air Stable n -Channel Organic Semiconductors for Thin Film

Transistors Based on Fluorinated Derivatives of Perylene Diimides. Chem. Mater. 19, 816–824 (2007).

36 Polaske, N. W. et al. Phosphonic Acid Functionalized Asymmetric Phthalocyanines: Synthesis, Modification of Indium Tin Oxide, and Charge Transfer. Langmuir 27, 14900–14909 (2011).

37 Nemykin, V. N. et al. Synthetic approaches to asymmetric phthalocyanines and their analogues. Arkivoc 2014, 142–204 (2014).

38 Yutronkie, N. J., Grant, T. M., Melville, O. A., Lessard, B. H. & Brusso, J. L. Old molecule, new chemistry: Exploring silicon phthalocyanines as emerging N-type materials in organic electronics. Materials (Basel). 12, 5–10 (2019).

39 Li, Z. & Lieberman, M. Axial reactivity of soluble silicon(IV) phthalocyanines. Inorg. Chem. 40, 932–939 (2001).

40 Gessner, T., Sens, R., Ahlers, W. & Vamvakaris, C. Preparation of silicon phthalocyanines and germanium phthalocyanines and related substances. US 2010/0113767 (2010).

41 Xu, H., Ohkita, J., Tamai, Y., Benten, H. & Ito, S. Interface Engineering for Ternary Blend Polymer Solar Cells with a Heterostructured Near-IR Dye. Adv. Mater. 27, 5868–5874 (2015).

42 Grant, T. M. et al. Straightforward and Relatively Safe Process for the Fluoride Exchange of Trivalent and Tetravalent Group 13 and 14 Phthalocyanines. ACS Omega 4, 5317–5326 (2019).

43 Bisoyi, S. et al. A comprehensive study of charge trapping in organic field-effect devices with promising semiconductors and different contact metals by displacement current measurements. Semicond. Sci. Technol. 31, 25011 (2015).

44 Melville, O. A. et al. Contact Engineering Using Manganese, Chromium, and Bathocuproine in Group 14 Phthalocyanine Organic Thin-Film Transistors. ACS Appl. Electron. Mater. 2, 1313–1322 (2020).

45 Grant, T. M., Rice, N. A., Muccioli, L., Castet, F. & Lessard, B. H. Solution-Processable n-Type Tin Phthalocyanines in Organic Thin Film Transistors and as Ternary Additives in Organic Photovoltaics. ACS Appl. Electron. Mater. 1, 494–504 (2019).

46 Li, L. et al. Organic thin-film transistors of phthalocyanines. Pure Appl. Chem. 80, 2231–2240 (2008).

47 Melville, O. A., Grant, T. M. & Lessard, B. H. Silicon phthalocyanines as N-type semiconductors in organic thin film transistors. J. Mater. Chem. C 6, 5482–5488 (2018).

48 Di, C., Liu, Y., Yu, G. & Zhu, D. Interface Engineering: An Effective Approach toward High-Performance Organic Field-Effect Transistors. Acc. Chem. Res. 42, 1573–1583 (2009).

49 Yang, S. Y., Shin, K. & Park, C. E. The Effect of Gate-Dielectric Surface Energy on Pentacene Morphology and Organic Field-Effect Transistor Characteristics. Adv. Funct. Mater. 15, 1806–1814 (2005).

50 Lim, S. C. et al. Surface-treatment effects on organic thin-film transistors. Synth. Met. 148, 75–79 (2005).

51 Cranston, R. R. et al. N-Type Solution-Processed Tin versus Silicon Phthalocyanines: A Comparison of Performance in OTFTs and OPVs. ACS Appl. Electron. Mater. 3, 1873–1885 (2021).

52 Jiang, Z. GIXSGUI : a MATLAB toolbox for GIXS data visualization and reduction. J. Appl. Crystallogr. 48, 917–926 (2015).

Chapter 6. Rapid Prototyping for Accelerated Establishment of Property-Performance Relationships in Silicon Phthalocyanine OFETs

This chapter is adapted from: ***Cranston, R. R.****, Mauthe, J., Wang, T., Thapa, G. J., Amassian, A., and Lessard, B. H. Rapid Prototyping for Accelerated Establishment of Property-Performance Relationships in Silicon Phthalocyanine OFETs. Submitted to Advanced Electronic Materials (2024).*

Context

For all previous chapters, SiPc OTFTs were fabricated by spin-coating, a common small area lab scale deposition method. Although spin-coating is a simple and accessible fabrication technique it is very different from the large area and high throughput manufacturing methods used for commercial applications. To more closely match these processes, high throughput printing and meniscus guided deposition methods can be used to better understand the thin-film formation of materials fabricated at large scales. For this work I collaborated with researchers from the Organic and Carbon Electronics Laboratories at North Carolina State University to use ultrasonic printing for SiPc deposition and OTFT fabrication. Ultrasonic printing allowed for rapid characterization of fabrication parameters such as print speed, solvent composition, substrate temperature, and SiPc molecule and thus accelerated the establishment of property-performance relationships. The results of this work highlight the necessity of high throughput printing techniques and their use in achieving the large-scale data sets that are needed to fully understand the complex relationships in organic electronic devices.

Contributions of Authors

This work was completed through contributions of all authors. For this work, I fabricated and characterized all OTFTs and films, performed GIWAXS and Raman microscopy experiments, conducted data analysis, and wrote the manuscript. J.M. and G.J.T assisted in GIWAXS experiments and set-up of laboratory equipment. T.W. assisted in set-up of laboratory equipment. A.A and B.H.L. provided supervision for the project.

Abstract

Understanding the complex relationships underlying the performance of organic electronic devices, such as organic field-effect transistors (OFETs), typically requires researchers to navigate a multi-dimensional parameter space that includes material design, solution formulation, fabrication parameters, and device geometry. This can be time, resource, and labour intensive, limiting scientific exploration and device optimization. Herein, we demonstrate a recently developed materials acceleration platform, named the RoboMapper, to perform direct on-chip fabrication of OFETs by ultrasonic meniscus printing of silicon phthalocyanine (SiPc) derivatives as the organic semiconductor. OFETs using bis(tri-*n*-butylsilyl oxide) SiPc ((3BS)$_2$-SiPc) exhibited the best device performance characterized by the highest electron field-effect mobility (μ_e) and lowest threshold voltage (V_T). Through optical microscopy and grazing-incidence wide-angle X-ray scattering (GIWAXS), the favourable performance of (3BS)$_2$-SiPc was attributed to the specific film morphology and molecular packing achieved by printing this material. Investigating the impact of deposition parameters using a variety of print conditions, solution formulations, and substrate temperatures unveils the crucial role of solvent evaporation rate and print speed in achieving high-quality film formation. Optimal fabrication conditions for (3BS)$_2$-SiPc devices include slow print speeds and fast evaporating solutions achieved by using a mixture of fast and slow evaporating co-solvents and an elevated substrate temperature. The results of this work reveal distinct relationships between deposition conditions, film properties, and device performance for each individual SiPc derivative and emphasize the necessity of high throughput experimentation to comprehensively understand property-performance relationships in organic semiconductors.

Introduction

Over the past two decades organic field-effect transistors (OFETs) have rapidly developed into promising components for inexpensive light-weight organic electronic devices and as research tools for the identification of novel materials, device structures, and fabrication methods. OFETs offer the ability to use organic semiconductor materials that are compatible with solution-based scalable manufacturing processes and have demonstrated utility in flexible displays[1–4] and specialized sensors[5–8], with some successfully commercialized applications.[9,10] Facilitating the transition of OFETs from research and development to commercialization, requires high-throughput, large-scale, and low-cost manufacturing while maintaining product uniformity and stability. The intricate relationship between molecular structure, deposition conditions, and film formation is critical to achieving optimal OFET performance. Computer driven experimentation, from predictive modeling to smart data visualization and machine learning, is a necessary and useful step to understanding these complex systems. In particular, device properties depend on the molecular structure of a material, the microscopic arrangement of molecules in a film, and the mesoscale film formation, with the latter two depending on both processing conditions as well as molecular design. Thus, truly understanding process-property-performance relationships in OFETs can currently only be achieved by comprehensively evaluating materials through the characterization of films and devices, often requiring large datasets and considerable resources.[11–15]

Materials and device acceleration platforms have recently emerged as a promising technology for reducing the time, cost, and waste generation of comprehensive material evaluation by employing a combination of automated synthesis, film processing, device characterization, and smart data analysis.[16–19] This is especially valuable for the study of organic active materials for device applications, as currently the development of high performing devices poses a multi-objective optimization problem which is predominantly done through manual experimentation. However, to address these issues, the design and use of materials and device acceleration platforms for solution processed thin-film photovoltaic devices has grown considerably,[17,19–21] cementing their place as critical infrastructure for materials science research. Although there are significant similarities between the materials, solution formulations, and deposition methods used for OFET and photovoltaic devices, these devices are considerably different in terms of device physics, architecture, and scale which place unique constraints on their manufacturing. Adapting materials and device acceleration platforms designed for photovoltaics towards OFET fabrication would significantly accelerate OFET research while reducing the materials and resources used.

The RoboMapper is a benchtop workstation that combines liquid handling for the rapid formulation of solutions with high resolution meniscus printing (**Figure 6.1a**).[20] Using picoliter volume ultrasonic dispensing, the RoboMapper can print diverse materials and formulations which are otherwise not feasible with automated spin-coating or blade-coating systems.[20] Computer-controlled self-cleaning of the print capillary allows the RoboMapper to perform continuous material deposition while the ultrasonic meniscus printing system can dispense solutions with a wide range of viscosities. A well plate is used to hold solutions of different compositions along with solvent washes to clean the capillary after leftover solution is withdrawn via vacuum. Additionally, substrates can be placed on top of a thermoelectric heating element to control the substrate temperature during deposition. This dispensing method has been previously demonstrated for the fabrication of liquid crystal, small molecule, and carbon nanotube transistors,[22–24] highlighting the utility of this scalable deposition method, and compatibility with commercial manufacturing processes. However, while the RoboMapper has been used as a platform for materials evaluation and data generation,[20] it has yet to be used for the direct fabrication and prototyping of OFET devices.

Herein, the capabilities of the RoboMapper platform are used to demonstrate direct on-chip prototyping of phthalocyanine (Pc) based OFETs using different molecular designs, solution formulations, and print conditions. Pcs are a family of π-conjugated organic small molecules most commonly used as commercial pigments and photoreceptors.[25,26] The ease of synthesis, molecular tunability, delocalized π-electron system, and ability to form highly crystalline microstructures has enabled the use of Pcs in optoelectronic devices.[27,2]8 Silicon Pcs (SiPcs) are a promising subset of this family as their tetravalent metal center allows for the incorporation of axial substituents such as solubilizing alkyl chains making them compatible with solution deposition processes. SiPcs have realized some of the highest performing n-type Pc based OFETs fabricated from solution,[29] proving their compatibility with organic electronic devices and their manufacturing processes.

In this work, three SiPc derivatives, bis(tri-*n*-propylsilyl oxide) SiPc ($(3PS)_2$-SiPc), bis(tri-*n*-butylsilyl oxide) SiPc ($(3BS)_2$-SiPc), and bis(tri-*n*-hexylsilyl oxide) SiPc ($(3HS)_2$-SiPc) with respective axially substituted alkyl groups of three, four, and six carbon chain lengths (Figure 1b) were employed as the organic semiconducting layer in OFETs. Bright-field optical microscopy and grazing-incidence wide-angle X-ray scattering (GIWAXS) were used to determine the effect of alkyl chain length on film microstructure and morphology in relation to device performance. Using a small-scale data set of transistor characteristics and microscopy images, the relationship between fabrication parameters, deposition solvent and print speed, were established. A larger scale data set, incorporating high-throughput microstructural characterization via polarized Raman microscopy, investigated this relationship further and was used to establish correlations between SiPc derivative, OFET performance characteristics, and film properties. The results of this work highlight the necessity of multidimensional characterization of processing parameters and the value of materials acceleration platforms for OFET fabrication.

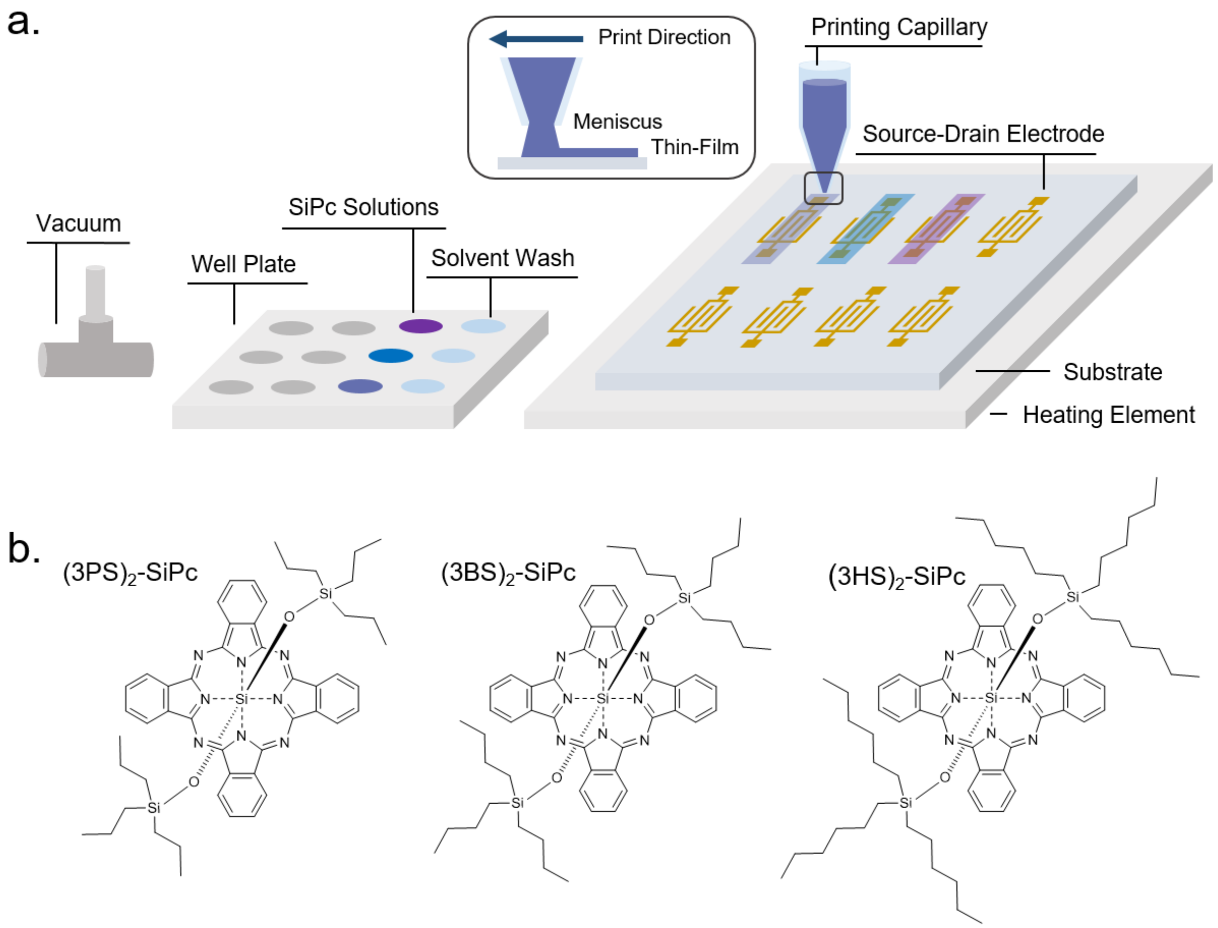

Figure 6.1. (a) Schematic diagram of the RoboMapper platform including well plate, cleaning mechanism, ultrasonic meniscus printing process, and pre-patterned OFET substrate placed on a heating element. (b) Structure of $(3PS)_2$-SiPc, $(3BS)_2$-SiPc and $(3HS)_2$-SiPc molecules.

Results and Discussion

As illustrated in **Figure 6.1a**, ultrasonic meniscus printing was used to deposit SiPc derivatives, $(3PS)_2$-, $(3BS)_2$- and $(3HS)_2$-SiPc, as the active layer in bottom-gate bottom-contact OFETs through the RoboMapper platform (**Figure 6.2a**). Ultrasonic meniscus printing uses a hollow capillary which contacts the substrate where solution dispensing is then initiated by piezoelectric action. As the capillary moves across the substrate surface at a set speed a meniscus front is formed and surface tension draws the solution resulting in a meniscus-guided deposition process as solvent evaporates. Electrical characterization of OFETs was performed in the saturation operating regime to determine the average μ_e and V_T of devices, with **Figure S6.1** and

Figure S6.2 providing example transfer and output curves. Ideal transistor operation is defined by a high μ_e and a V_T close to 0 V, typically resulting from a highly-ordered low-defect crystalline film which promotes efficient charge transport pathways between source-drain electrodes.[30] **Figure 6.2c** displays the forward and reverse transfer curves of $(3PS)_2$-, $(3BS)_2$- and $(3HS)_2$-SiPc OFETs fabricated and characterized using the same conditions. Transistors using $(3BS)_2$-SiPc as the semiconductor resulted in the best performing devices with the highest μ_e and lowest V_T. From previous works on spin-coated $(3PS)_2$-SiPc OFETs, the short symmetric linear alkyl chains of $(3PS)_2$-SiPc have shown to improve OFET performance compared to longer alkyl chain SiPc derivatives such as $(3BS)_2$- and $(3HS)_2$-SiPc.[31,32] However herein OFETs using $(3PS)_2$-SiPc deposited by printing exhibited lower μ_e and V_T compared to $(3BS)_2$-SiPc devices. Additionally, printed $(3HS)_2$-SiPc OFETs were functional, although with low μ_e and high V_T, whereas the long chains of $(3HS)_2$-SiPc, when deposited by spin-coating, have historically resulted in poor film formation and non-functional devices.[33]

To understand the higher μ_e observed by $(3BS)_2$-SiPc OFETs, a series of microscopic and structural characterization was performed. Optical microscopy images of printed SiPc films reveal distinct surface morphologies resulting from the different alkyl chain length derivatives (**Figure 6.2b**). $(3PS)_2$-SiPc films display an uneven film morphology with an interconnected feather-like texture, whereas $(3BS)_2$-SiPc films display a morphology with broader, smoother linear striations and fewer domain boundaries. Similar to $(3PS)_2$-SiPc, $(3HS)_2$-SiPc films have a more uneven surface morphology with many domain boundaries although more disconnected and spherical in texture. These inhomogeneous morphologies are common for solution fabricated thin films where the rapid and poorly controlled rate of crystallite formation is dictated by interactions between the deposit material, solvent evaporation, and substrate surface.[34–37] Domain and grain boundaries can act as charge carrier traps or localized barriers for charge transport, hindering the electrical performance of devices, suggesting that film morphologies with fewer boundaries will have improved charge transport and device performance.[38,39] The higher μ_e observed in $(3BS)_2$-SiPc OFETs is therefore likely due to the more favourable film morphology achieved by printing this material.

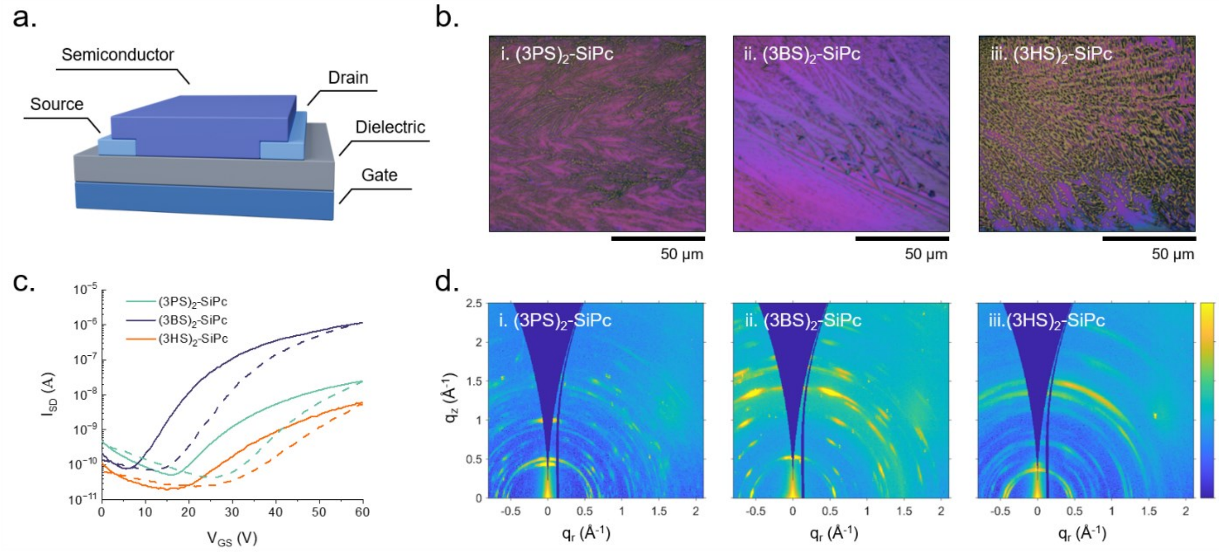

Figure 6.2. (a) Diagram of bottom-gate bottom-contact OTFT architecture. (b) Bright-field optical microscopy images, (c) forward (solid line) and reverse (dashed line) transfer curves of OFETs, and (d) 2D scattering patterns of (i) $(3PS)_2$-SiPc, (ii) $(3BS)_2$-SiPc and (iii) $(3HS)_2$-SiPc thin-films fabricated at a print speed of 1000 μm s^{-1} using a solution composition of 40% v/v toluene and 60% v/v DCB.

Figure 6.2d displays the 2D scattering patterns of $(3PS)_2$-, $(3BS)_2$- and $(3HS)_2$-SiPc films determined by GIWAXS with the azimuthally-integrated and single crystal diffraction patterns found in **Figure S6.3**. All films are highly crystalline with the arced scattering patterns indicating a distribution of face-on and edge-on crystallite orientations within the films which agrees with previously reported GIWAXS patterns of these materials.[29,33] $(3PS)_2$-SiPc films exhibit the most ordered microstructure with the (011) and (100) reflections at $q = 0.59$ Å^{-1} and $q = 0.66$ Å^{-1} aligned in-plane along the q_z axis. $(3BS)_2$-SiPc films exhibit a slightly less ordered film structure with the (100) reflection at $q = 0.65$ Å^{-1} aligned in-plane while the (010) reflection at $q = 0.59$ Å^{-1} is aligned out-of-plane along q_z. $(3HS)_2$-SiPc results in the most disordered films, evident by the highly arched diffraction pattern with the (001) reflection at $q = 0.49$ Å^{-1} predominantly out-of-plane along q_z, with the (010) reflection at $q = 0.51$ Å^{-1} in-plane along q_z, consistent with the microscopy images showing a more uneven surface morphology and with increased domain boundaries. Additionally, $(3HS)_2$-SiPc films exhibit a larger intermolecular d-spacing (16.5 Å) compared to $(3PS)_2$- and $(3BS)_2$-SiPc films (14.6 Å and 11.4 Å respectively) due to the longer alkyl chains of this material. Therefore, the poor device performance of $(3HS)_2$-SiPc OFETs is likely a result of the more disordered microstructure, larger intermolecular d-spacing, and disconnected, uneven morphology contributing to a reduction in quality charge transport pathways.

Fabricating devices using a range of parameters typically requires individual substrates per fabrication condition, greatly increasing the amount of resources and in-lab human hours required for large-scale experimentation. Unlike common lab scale deposition methods such as spin-coating and blade-coating, a printing platform such as the RoboMapper, allows for the quick and easy examination of fabrication parameters with reduced material consumption as multiple solutions and printing conditions can be tested in quick succession using a single substrate. Using the best performing material, $(3BS)_2$-SiPc, OFETs were made at print speeds ranging from 100 µm s^{-1} to 1200 µm s^{-1} deposited from a slow evaporating solution using 1,2-dichlorobeneze (DCB) as the solvent, and a faster evaporating solution using a solvent mixture of 60% v/v toluene and 40% v/v DCB (**Figure 6.3**). Transistors deposited from the slower evaporating pure DCB solution were highly susceptible to changes in print speed, with **Figure 6.3a** displaying the variation in OFET performance. Increasing the rate of solvent evaporation by adding toluene as a co-solvent reduced the impact of print speed and yielded consistent device performance throughout the tested range (**Figure 6.3b**). The difference in OFET performance with print speed when using solutions of different solvent composition demonstrates how small changes in formulation and processing can influence OFET behaviour and that a small data set representing a subset of the parameter space can present an incomplete picture of the relationship between fabrication parameters. Thus, mapping the larger parameter space is crucial to understanding the interplay between parameters which is often necessary for integrating new materials to deposition platforms more aligned with high throughput manufacturing and for developing process-property-performance relationships.

Optical microscopy images of the printed SiPc films demonstrate how, at the same print speed, similar film morphologies are obtained regardless of solution composition (**Figure 6.3c** and **Figure 6.3d**). The relationship between print speed and organic small molecule thin film formation is well established for meniscus guided coating methods.[40–44] With slow deposition speeds, solvent evaporation is dominant and film formation is dictated by the rate of solution evaporation at the meniscus front rather than the forces imposed by printing.[45] As a result, large thick crystallite formation occurs, creating films with an incohesive morphology. By increasing the deposition speed, the meniscus is dragged out creating a liquid film at the meniscus front where continuous steady crystallite growth occurs, leading to the formation of highly orientated domains.[45–47] Further increasing deposition speed leads to solvent evaporation that is separate from the meniscus and is solely a function of print speed.[45–47] This regime is characterized by unguided crystallite growth often resulting in anisotropic or spherulitic morphologies. Additionally, print speed had no large impact on the orientation of $(3BS)_2$-SiPc molecules in films determined by the 2D GIWAXS patterns found in **Figure S6.4**.

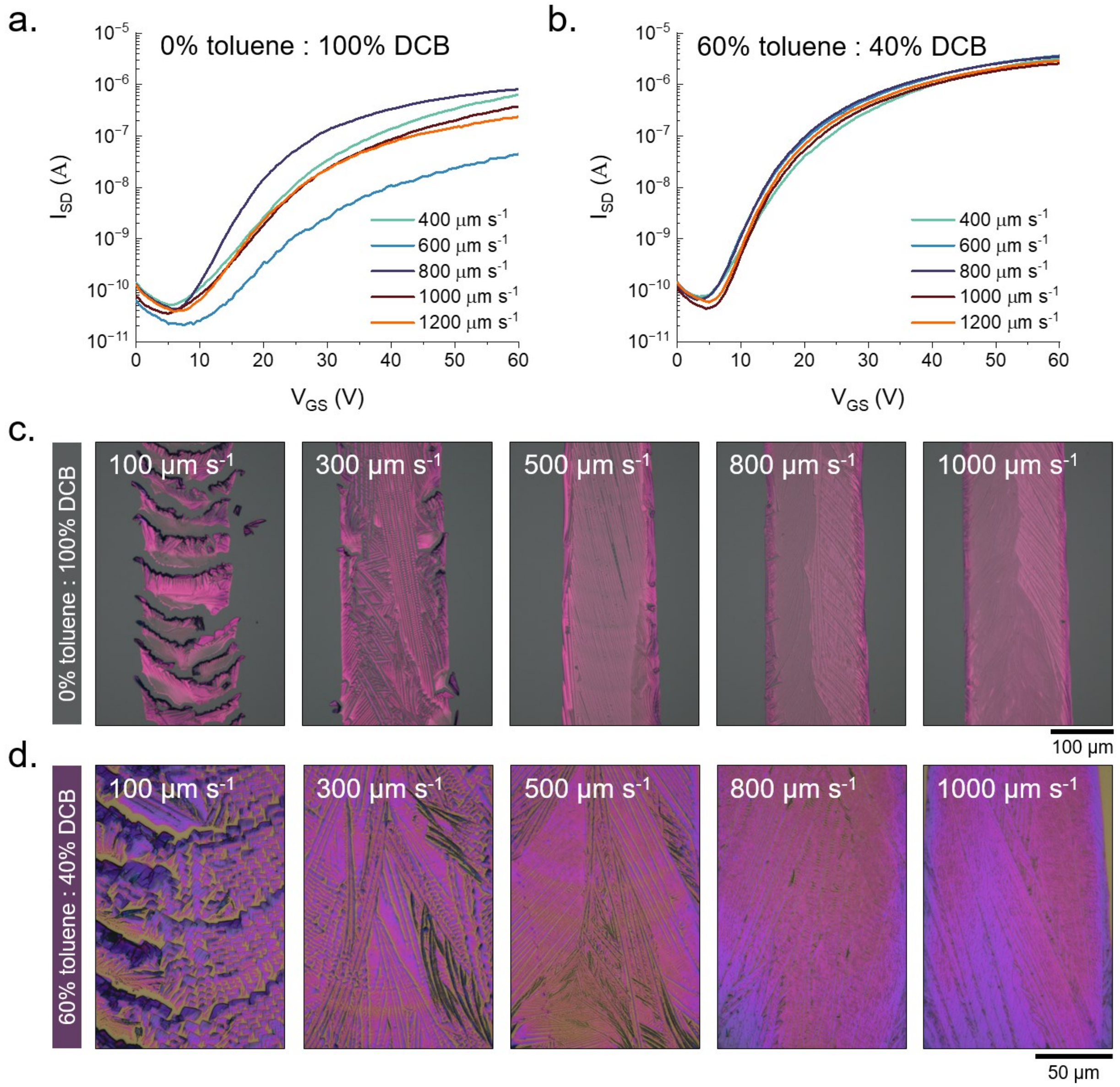

Figure 6.3. Transfer curves of $(3BS)_2$-SiPc OFETs fabricated at indicated print speeds using solution compositions of (a) 100% DCB and (b) 60% v/v toluene and 40% v/v DCB. Bright-field optical microscopy images of $(3BS)_2$-SiPc thin-films fabricated at indicated print speeds using solution compositions of (c) 100% v/v DCB and (d) 60% v/v toluene and 40% v/v DCB.

Using the RoboMapper, a more comprehensive data set with a wide range of print speeds and solution compositions was completed for all three SiPc derivatives. **Figure 6.4** summarizes the OFET performance, film morphology, and film microstructure characteristics using $(3BS)_2$-SiPc as the organic semiconductor. The performance of $(3BS)_2$-SiPc OFETs in terms of μ_e and V_T are displayed by the heat maps presented in **Figure 6.4a** with labels (1), (2), and (3), indicating the worst, average, and best performing devices respectively. A complete summary of all transistor characteristics in this data set can be found in **Table S6.1**. In general, OFETs exhibited higher μ_e and lower V_T when deposited at lower print speeds from faster evaporating solutions, with the best performing device (3) achieved with a solution of 60% v/v toluene and 40% v/v DCB and a print speed of 600 $\mu m\ s^{-1}$. OFET performance was shown to decrease with higher amounts of DCB in solution and faster print speeds, with the worst performing device (1) resulting from a solution of 20% v/v toluene and 80% v/v DCB with a print speed of 1000 $\mu m\ s^{-1}$. The approximate size of surface features (f_{size}) for films were estimated using the microscopy images found in **Figure S6.5** and correlated to device performance. Slower print speeds and higher % v/v toluene in deposition solution increased f_{size} and corresponded to higher μ_e transistors (**Figure 6.4a** and **Figure 6.4b**). This is similar to the results shown in **Figure 6.2**, where larger domains with fewer domain boundaries improved charge transport and overall device performance.

To evaluate the molecular scale structure within the printed films, polarized Raman microscopy was used to determine the integral intensity ratio of the B_{1g} pyrrole stretch mode using diagonal and non-diagonal polarizations in order to estimate the orientation (β) of $(3BS)_2$-SiPc molecules relative to the substrate. The Raman surface maps in **Figure 6.4b** illustrate the change in $(3BS)_2$-SiPc orientation with respect to the substrate plane of devices labeled (1), (2), and (3), and demonstrate a clear trend between molecular orientation and device performance. The best performing device, labeled (3), exhibited the most uniform film microstructure with molecules aligned on average 46° to the substrate in a pseudo face-on orientation (**Table S6.2**). The worst performing device (1) shows evidence of considerable heterogeneity with a broader distribution of molecular angle (**Figure 6.4c**) corresponding to a less uniform and ordered film with a higher average angle to the substrate of 56°. Increased edge-on alignment is typically favoured for small molecule semiconductors as the direction of π-π stacking is aligned with the direction of charge transport within the semiconducting channel.[48–52] However, for axially substituted molecules it has been demonstrated that a more edge-on orientation can hinder device performance as the axial groups can interfere with the intermolecular packing within films and increase the distance between molecules.[32,53] The Raman maps presented in **Figure S6.6** display the difference in

$(3BS)_2$-SiPc orientation using solutions of 60% v/v toluene with 40% v/v DCB and 100% v/v DCB, the best and worst solution compositions for device fabrication respectively. Although using 100% v/v DCB yielded films with a predominately face-on orientation which should favour efficient charge transport, these films have a very broad distribution of molecular orientations indicating more disordered film structures (**Figure S6.6b**). The disordered nature and feather-like features of these films are likely the cause of the lower μ_e observed in devices.

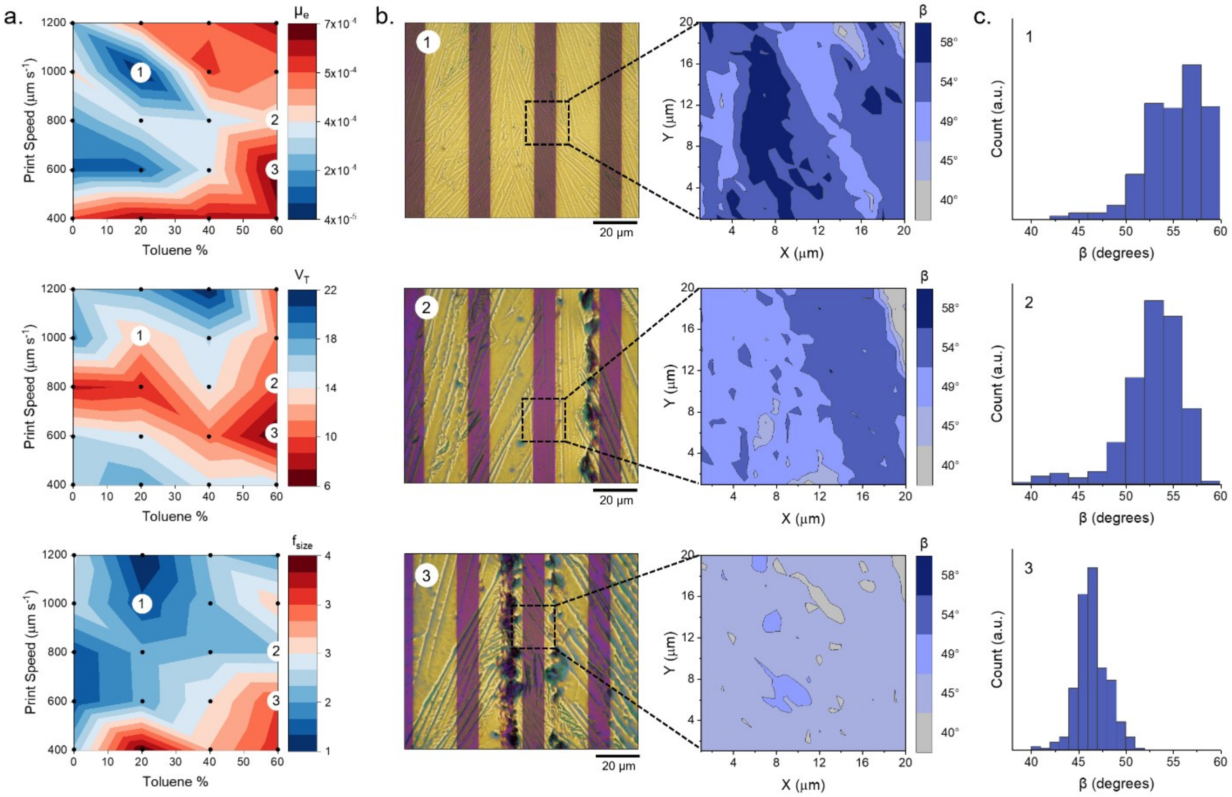

Figure 6.4. (a) Heat maps displaying the change in μ_e ($cm^2\ V^{-1}\ s^{-1}$), V_T (V), and f_{size} (μm) of $(3BS)_2$-SiPc OFETs with films deposited at indicated print speeds and solution compositions. (b) Molecular orientation (β) maps (20 μm x 20 μm) between $(3BS)_2$-SiPc molecules and substrate estimated from polarized Raman spectra of the (1) worst, (2) average, and (3) best performing OFETs with corresponding bright-field microscopy images of films and location of mapped area. (c) Distribution histograms of β shown in Raman maps of (1), (2), and (3).

In addition to print speed and solution composition, the substrate temperature during deposition and print direction were investigated to determine their impact on OFET performance with results summarised in **Figure S6.7-9** and **Table S6.3-5**. In order to improve crystallite nucleation and film formation substrates were heated to temperatures of 40°C, 50°C, and 60°C during deposition. Modulating the substrate temperature during deposition is a method used to precisely control the rate of solvent evaporation and crystallite nucleation without changing the deposition solvent. Increasing the rate of solvent evaporation through elevated substrate temperatures enables better solution wettability to the substrate, increasing the film thickness and promoting well-oriented crystalline structures.[54–56] Substrate temperatures of 60°C consistently yielded higher μ_e devices for all SiPc materials, demonstrating more uniform molecular orientations throughout the films. Similarly, using a print direction perpendicular to the width of the source-drain channel, rather than along the channel width, improved device performance. For $(3PS)_2$- and $(3HS)_2$-SiPc OFET μ_e increased by an order of magnitude when deposited across the source-drain channel with $(3BS)_2$-SiPc OFETs exhibiting an increase in μ_e from 5.4×10^{-4} cm^2 V^{-1} s^{-1} to 8.7×10^{-4} cm^2 V^{-1} s^{-1} (**Table S6.5**). A print direction perpendicular to the channel enabled the growth of crystallite domains orientated parallel to the direction of charge transport with few boundaries crossing the semiconducting path, therefore resulting in improved transistor operation.[57–59]

The trends between solution composition and print speed on $(3BS)_2$-SiPc film formation and device performance shown in **Figure 6.4** were found to be different for $(3PS)_2$- and $(3HS)_2$-SiPcs. **Figure 6.5** illustrates these differences through the correlation between fabrication parameters and OFET and film properties including μ_e, V_T, on-off current ratio ($I_{on/off}$), device hysteresis (H), film thickness (t) and f_{size}. For each material, changing the rate of solvent evaporation through the amount of toluene in solution had a varying effect, with $(3PS)_2$-SiPc largely unaffected by this parameter while $(3BS)_2$- and $(3HS)_2$-SiPc had a predominantly positive correlation with % v/v toluene. Similarly, print speed effected the properties of OFETs and films of each material drastically differently while only film properties (t and f_{size}) exhibited the same correlation between all three materials. OFET characteristics and microscope images of $(3PS)_2$- and $(3HS)_2$-SiPc devices fabricated using varying print speeds and solution compositions are found in **Table S6.6** and **Figure S6.10**, and **Table S6.7** and **Figure S6.11** respectively. These results further highlight how trends determined from a large data set for one material are not always the same for different materials, even similar materials such as the SiPc derivatives used herein.

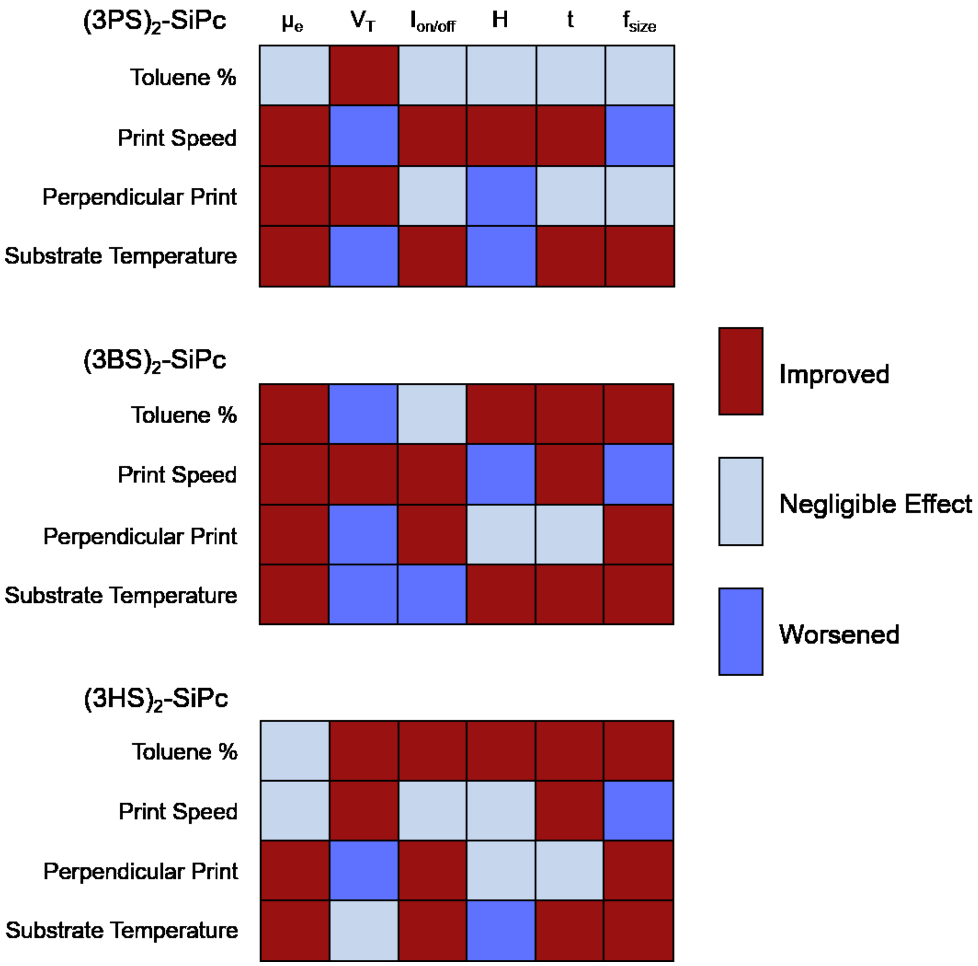

$(3PS)_2$-SiPc	μ_e	V_T	$I_{on/off}$	H	t	f_{size}
Toluene %	⬜	🟥	⬜	⬜	⬜	⬜
Print Speed	🟥	🟦	🟥	🟥	🟥	🟦
Perpendicular Print	🟥	🟥	⬜	🟦	⬜	⬜
Substrate Temperature	🟥	🟦	🟥	🟦	🟥	🟥

$(3BS)_2$-SiPc	μ_e	V_T	$I_{on/off}$	H	t	f_{size}
Toluene %	🟥	🟦	⬜	🟥	🟥	🟥
Print Speed	🟥	🟥	🟥	🟦	🟥	🟦
Perpendicular Print	🟥	🟦	🟥	⬜	⬜	🟥
Substrate Temperature	🟥	🟦	🟦	🟥	🟥	🟥

$(3HS)_2$-SiPc	μ_e	V_T	$I_{on/off}$	H	t	f_{size}
Toluene %	⬜	🟥	🟥	🟥	🟥	🟥
Print Speed	⬜	🟥	⬜	⬜	🟥	🟦
Perpendicular Print	🟥	🟦	🟥	⬜	⬜	🟥
Substrate Temperature	🟥	⬜	🟥	🟦	🟥	🟥

🟥 Improved
⬜ Negligible Effect
🟦 Worsened

Figure 6.5. Diagram representing the correlation between % v/v toluene in deposition solution, print speed, print direction, and substrate temperature on properties including μ_e, V_T, $I_{on/off}$, H, t and f_{size} of $(3PS)_2$-, $(3BS)_2$-, and $(3HS)_2$-SiPc OFETs and films, illustrating if the respective fabrication parameters improved, worsened, or had a negligible effect on each property.

Conclusion

For the first time, the RoboMapper materials acceleration platform is demonstrated for the rapid prototyping of the semiconductor layer in OFETs using three soluble SiPc derivatives, each featuring distinct alkyl chain length axial groups. $(3BS)_2$-SiPc, with the median length alkyl groups, proved to be the best performing organic semiconducting material yielding the highest μ_e and lowest V_T devices. The enhanced device performance of $(3BS)_2$-SiPc OFETs was attributed to the specific film morphology and microstructure achieved by printing this material. Onboarding these SiPc materials to the meniscus printing method highlighted the impact of deposition parameters on film formation and device performance. Solvent evaporation rate controlled by solution composition and substrate temperature during processing proved critically important to achieving high quality film formation. For $(3BS)_2$-SiPc devices, faster solvent evaporation by using solutions comprised of 60% v/v toluene and 40% v/v DCB and a substrate temperature of 60°C resulted in more favourable film morphologies which promoted charge transport and yielded higher μ_e transistors. Additionally, print speed was shown to have a larger impact on OFET performance when using slower evaporating solvent compositions compared to fast evaporating solutions. In general, slow print speeds of 400-600 $\mu m\ s^{-1}$ resulted in a film morphology of large crystalline domains and a uniform well-orientated microstructure leading to higher performing OFETs. For the three SiPc derivatives used for OFET fabrication, solvent evaporation rate and print speed had a varying effect on film formation and transistor characteristics. The trends in deposition conditions determined for $(3BS)_2$-SiPc OFETs were found to be different than that of $(3PS)_2$- and $(3HS)_2$-SiPc OFETs, with each material displaying a unique relationship between processing parameters, film properties, and device performance. The results of this work highlight the necessity of high throughput printing techniques and their use in achieving the large-scale data sets that are needed to fully understand process-property-performance relationships in organic semiconductors. Understanding these relationships is paramount for the further development, utility, and commercialization of organic electronic devices.

Experimental

Materials

Bis(tri-*n*-propylsilyl oxide) silicon phthalocyanine ($(3PS)_2$-SiPc), bis(tri-*n*-butylsilyl oxide) silicon phthalocyanine ($(3BS)_2$-SiPc), and bis(tri-*n*-hexylsilyl oxide) silicon phthalocyanine ($(3HS)_2$-SiPc) were synthesized and purified as described in literature.[52,53] Hexamethyldisilane (HMDS, 98+%) was purchased from Thermo Fischer Scientific. Solvents were purchased from commercial suppliers and used as received.

OFET Fabrication

Bottom-gate bottom-contact OFETs were fabricated using substrates purchased from Fraunhofer IPMS consisting of a 230 nm thick thermally grown SiO_2 dielectric layer with pre-patterned interdigitated gold source-drain electrodes with a channel width of 10,000 μm and length of 10 μm. All substrates were first rinsed with acetone and isopropanol to remove the protective photoresist layer then dried with nitrogen gas. Vapour treatment of HMDS was carried out in a nitrogen filled glovebox where substrates were first heated at 90°C on a hotplate for 20 min to dehydrate the surface. Substrates were then sealed in a glass container with a 1 dram vial of HMDS and heated at 90°C for 1 hr. After which the substrates were remove from the container and baked under vacuum at 150°C for 20 min. SiPc solutions were made at a concentration of 8 mg ml^{-1} in the indicated solvent ratios (% v/v) of toluene and 1,2-dichlorobenzene by heating at 50°C for 45 min, then filtering through a PTFE membrane with a pore size of 0.45 μm. SiPc deposition by ultrasonic printing was carried out using a Microplotter Proto dispensing platform from Sonoplot, as sub-system of the RoboMapper platform, with a 50 μm diameter capillary tip and a substrate temperature of 60°C unless otherwise stated. Printing speed was varied from 100-1200 μm s^{-1} as indicated. All films were then thermally annealed at 100°C for 1 hr under vacuum. A detailed description of the full RoboMapper system including hardware and software components can be found in literature.[20]

OFET Characterization

OTFT characterization was performed under vacuum (P = 10^{-5} MPa) at room temperature using a probe station purchased from American Linear Manufactures equipped with tungsten probe tips which contacted the source, drain and gate electrodes. A Keithley 4200A-SCS was used to control the source-drain voltage (V_{SD} = 50 V) and gate voltage (0 V < V_{GS} < 60 V) to obtain source-drain current (I_{SD}) measurements. The average saturation regime electron field effect mobility (μ_e) and threshold voltage (V_T) were calculated from two replicate transistors per stated condition using the MOSFET model.[62]

GIWAXS

GIWAXS experiments were performed at the Complex Materials Scattering (CMS) beamline at the National Synchrotron Light Source II (NSLS-II) with a photon energy of 13.5 keV. 2D scattering patterns were collected in vacuum (P = 10^{-4} MPa) using a 2M Pilatus 3S detector (172 μm x 172 μm pixel size) from Dectris, with an angle of incidence of $\theta = 0.1°$, and a sample to detector distance of 258 mm. All data was analyzed using the GIXSGUI software package in MATLAB[63] where both polarization and solid-angle corrections were applied. Intermolecular d-spacing was calculated using Bragg's Law.

Microscopy

Bright field optical microscope images of films were taken using a Nikon Eclipse LV100N POL microscope with X50 and X100 magnifications. ImageJ software was used for image analysis. Microscope images were first converted from RGB format to 8-bit format. Feature size (f_{size}) was calculated using the profile of a 10 µm line cut taken in the source-drain channel as outlined in **Figure S6.12**. All reported f_{size} values are an average from 10 line cuts taken at different locations along the source-drain channel.

Raman Microscopy

A Renishaw inVia Qontor confocal Raman microscope was used to record the Z(X,X)Z' and Z(X,Y)Z' polarized Raman spectra of films in the backscattering geometry to acquire Raman surface maps (20 µm x 20 µm) of molecular orientation as outlined in literature.[32] The Raman microscope uses a Leica Microsystems bright field microscope with a DM2700 light source. A 500 mW 532 nm wavelength laser with a 2400 l mm^{-1} grating was used to obtain measurements in the spectral range of 550-1700 cm^{-1}, focused on the sample by an X50L objective with a numerical aperture of 0.5. The spectral resolution of the Raman microscope is 0.3 cm^{-1} (full-width half-maximum), with a theoretical spatial resolution of approximately 640 nm, and a theoretical depth of focus of approximately 3.0 µm. Calibration was performed prior to all measurements using the 520 cm^{-1} silicon reference peak.

Associated Content

Acknowledgments

The authors would like to acknowledge the University of Ottawa and the Natural Sciences and Engineering Research Council of Canada (RGPIN-04079-2020 to B.H.L, CGSD-569930-2022 and CGSD-MSFSS-2023 to R.R.C) for their financial support. Additionally, B.H.L. is a Canada Research Chair with the Canada Research Chair program contributing funding for this work. J.M, A.A., and G.J.T. acknowledge the support of the Office of Naval Research under award number N00014-23-1-2001. T.W. and A.A. acknowledge support of the National Science Foundation ECCS-1936527. OFET measurements were performed in Prof. Daniel B. Dougherty's laboratory, a part of the ORaCEL cluster facility at North Carolina State University.

Supporting Information

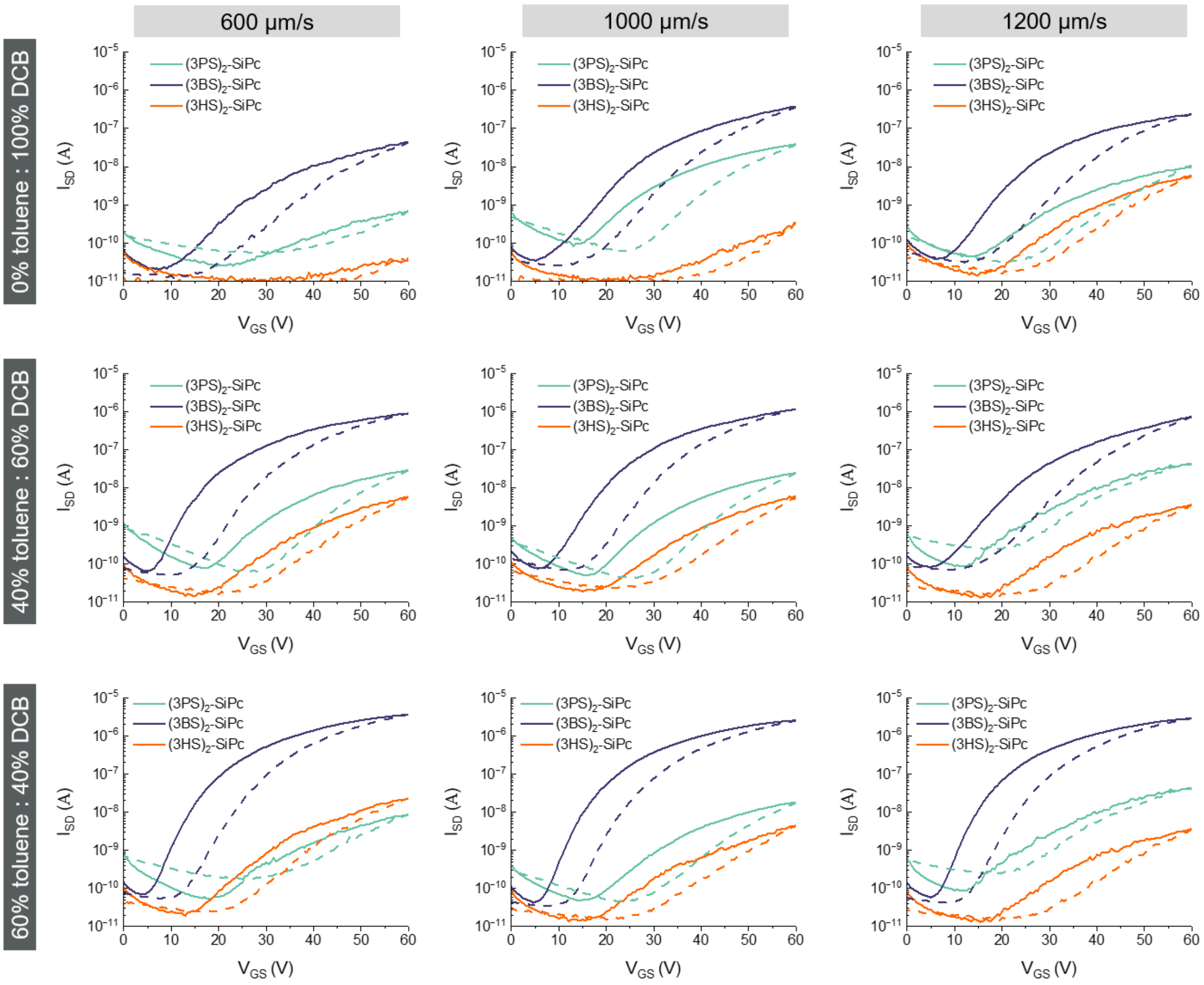

Figure S6.1. Characteristic forward (solid line) and reverse (dashed line) transfer curves of $(3PS)_2$-SiPc, $(3BS)_2$-SiPc, and $(3HS)_2$-SiPc OFETs fabricated at indicated print speeds and solution compositions.

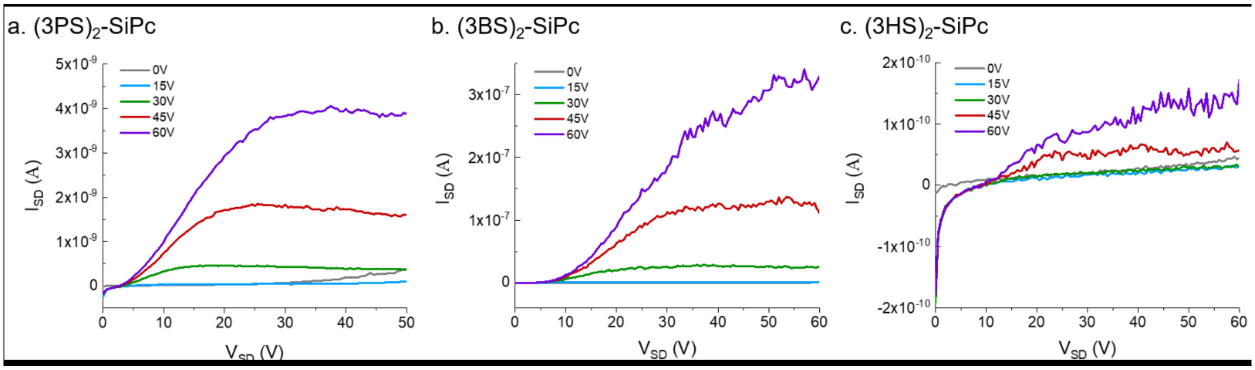

Figure S6.2. Characteristic output curves of (a) (3PS)$_2$-SiPc, (b) (3BS)$_2$-SiPc, and (c) (3HS)$_2$-SiPc OFETs fabricated at a print speed of 1000 µm s^{-1} using a solution composition of 40% toluene and 60% DCB.

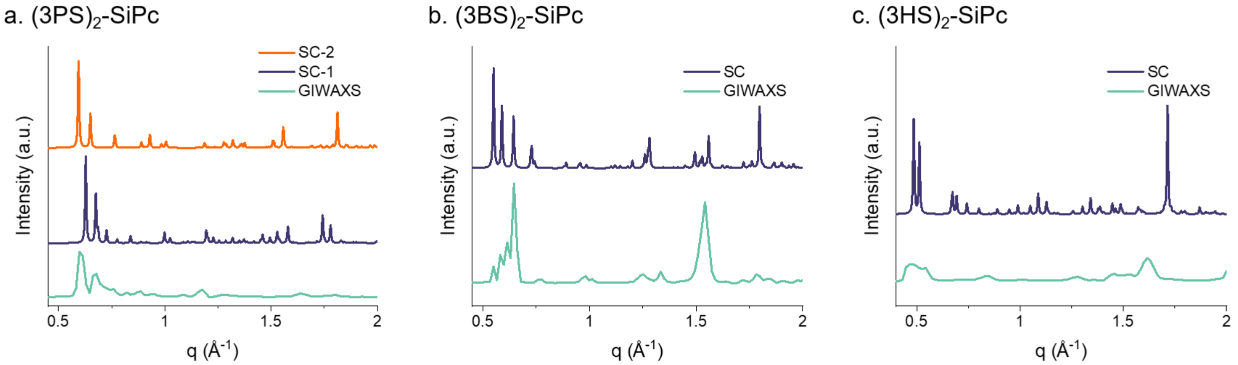

Figure S6.3. Diffraction patterns of (a) (3PS)$_2$-SiPc (CCDC #2091746, CCDC #2067659), (b) (3BS)$_2$-SiPc (CCDC #1522758), and (c) (3HS)$_2$-SiPc (CCDC #988974) determined by GIWAXS and predicated by single crystal (SC) XRD.

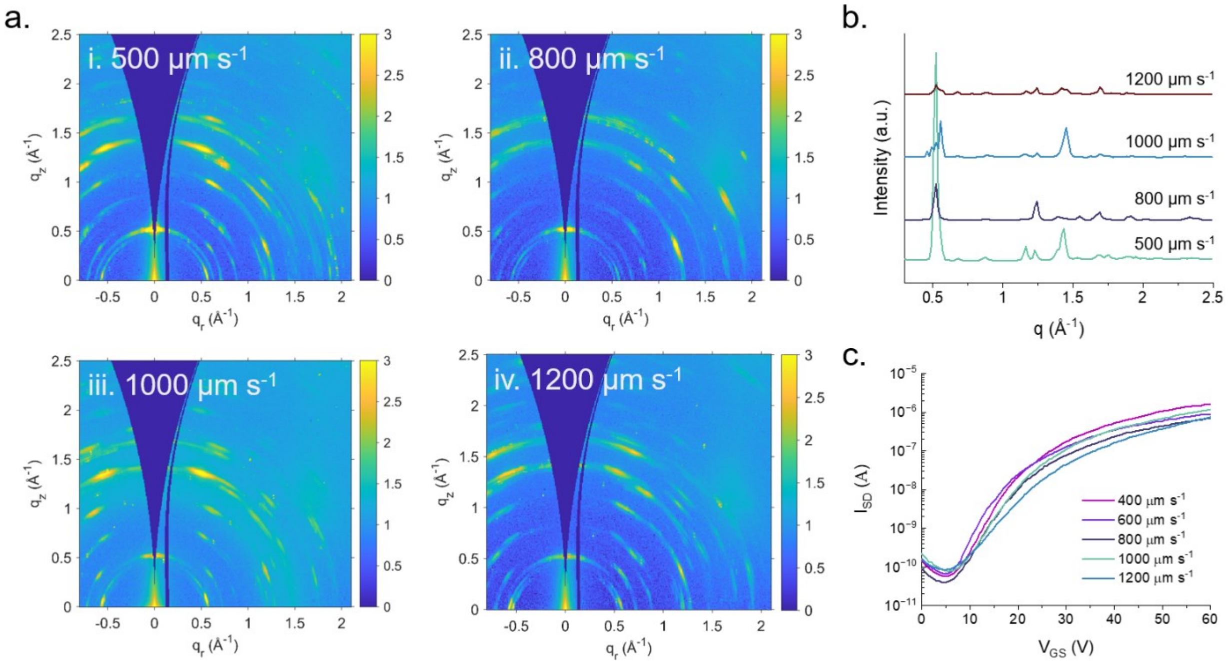

Figure S6.4. (a) 2D scattering patterns, (b) diffraction patterns determined by GIWAXS and (c) forward transfer curves of $(3BS)_2$-SiPc OFETs fabricated at indicated print speeds using a solution composition of 40% toluene and 60% DCB.

Table S6.1. Summary of $(3BS)_2$-SiPc transistor characteristics with data taken from two OFETs per condition.

Toluene %	Print Speed (μm s^{-1})	μ_e (cm^2 V^{-1} s^{-1})	V_T (V)	$I_{on/off}$
0	400	5.46×10^{-4}	15.8	10^4
	600	1.32×10^{-4}	15.2	10^3
	800	2.03×10^{-4}	7.90	10^4
	1000	3.82×10^{-4}	18.3	10^4
	1200	2.45×10^{-4}	16.4	10^4
20	400	6.54×10^{-4}	17.6	10^4
	600	1.31×10^{-4}	14.2	10^4
	800	3.46×10^{-4}	8.50	10^4
	1000	3.92×10^{-5}	12.1	10^2
	1200	5.04×10^{-4}	17.3	10^3
40	400	6.23×10^{-4}	14.2	10^4
	600	3.43×10^{-4}	10.5	10^4
	800	3.14×10^{-4}	14.1	10^4
	1000	5.44×10^{-4}	15.3	10^3
	1200	5.28×10^{-4}	21.9	10^4
60	400	6.15×10^{-4}	14.5	10^4
	600	6.97×10^{-4}	5.50	10^4
	800	3.91×10^{-4}	9.30	10^4
	1000	4.81×10^{-4}	10.8	10^4
	1200	6.24×10^{-4}	9.30	10^4

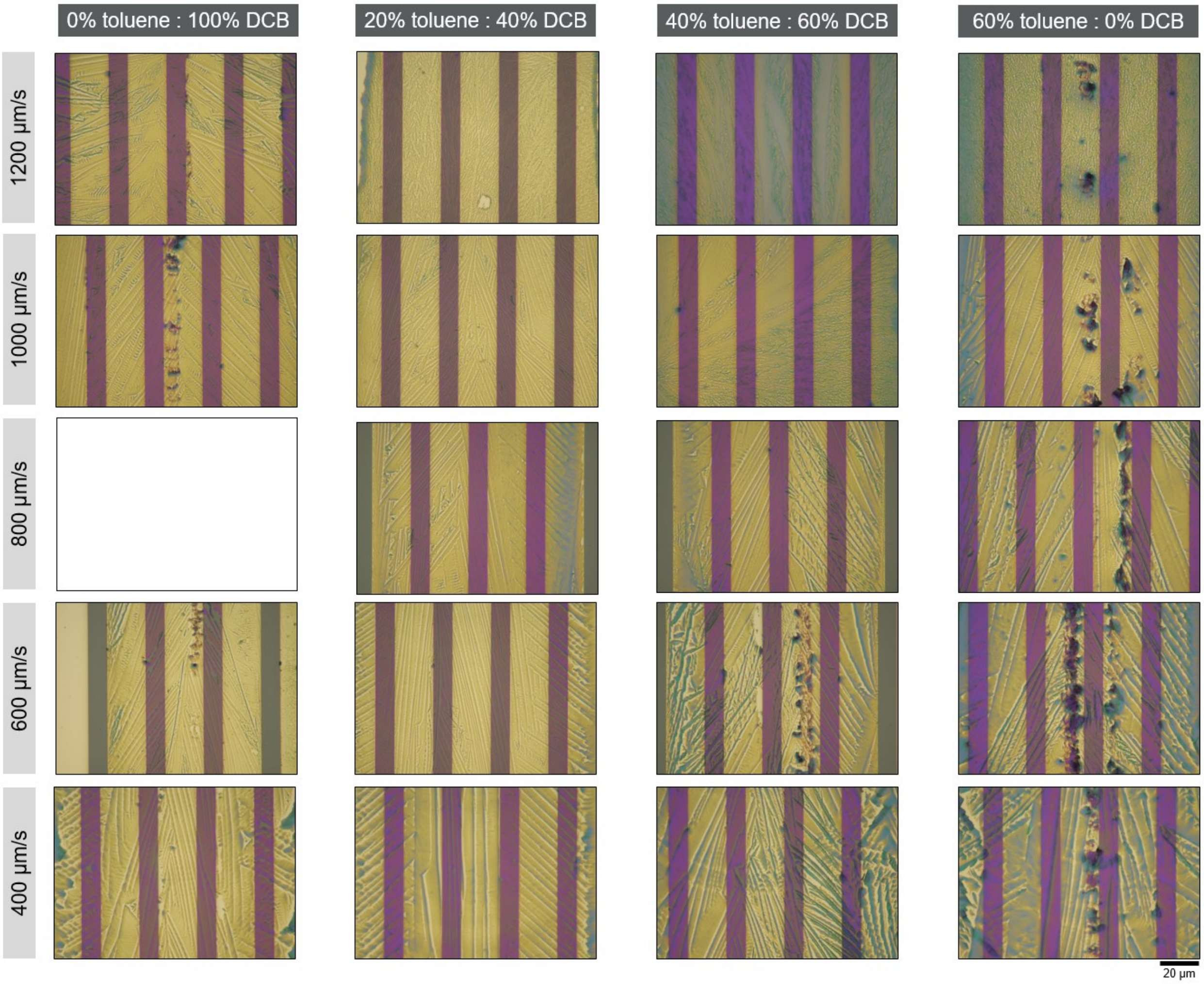

Figure S6.5. Bright field real-colour microscopy images of $(3BS)_2$-SiPc thin-films fabricated at indicated print speeds and solution compositions.

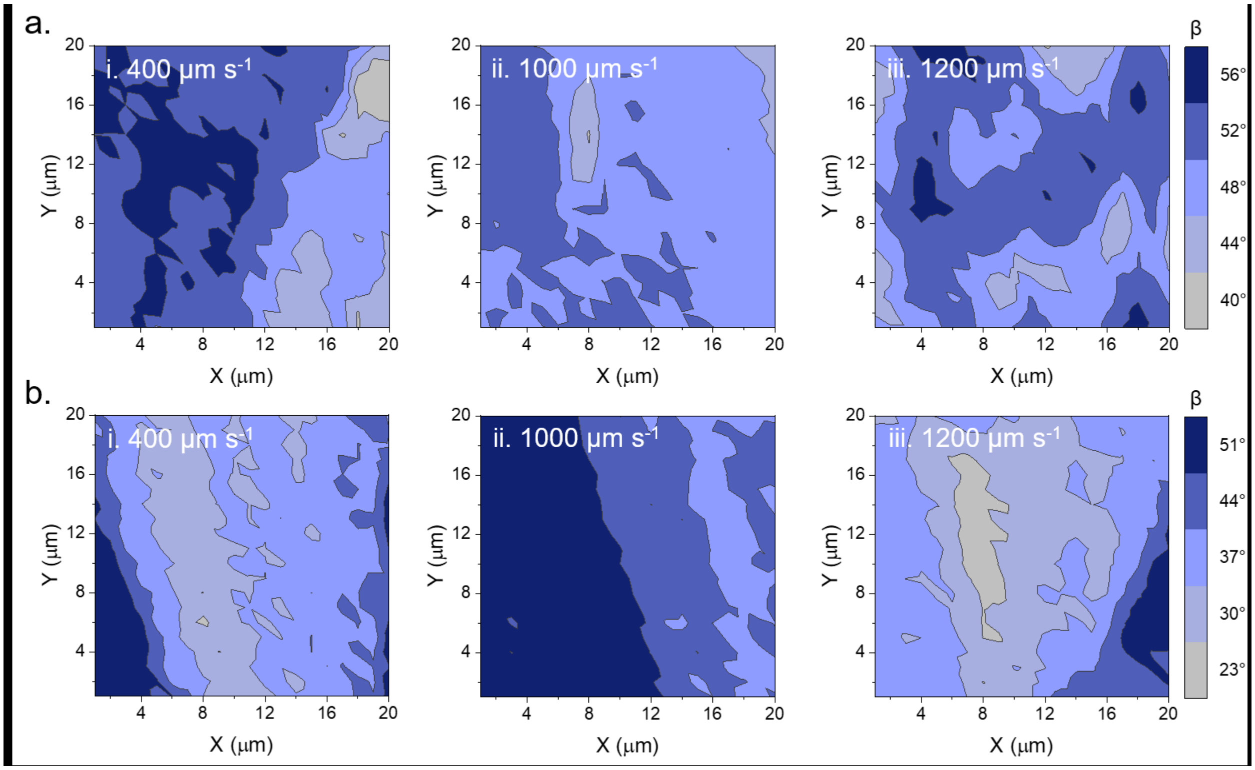

Figure S6.6. Maps (20 μm x 20 μm) of the molecular angle between $(3BS)_2$-SiPc and substrate estimated from polarized Raman spectra of thin-films fabricated at print speeds of (i) 400 μm s^{-1}, (ii) 1000 μm s^{-1}, and (iii) 1200 μm s^{-1} using a solution composition of (a) 60% v/v toluene and 40% v/v DCB and (b) 100% v/v DCB.

Table S6.2. Minimum, maximum and average molecular angle of $(3BS)_2$-SiPc to the substrate of films fabricated at indicated print speeds using a solution composition of 60% toluene and 40% DCB, estimated from polarized Raman surface maps. Standard deviation (σ) calculated from the entire data set.

Toluene %	Print Speed (μm s^{-1})	β_{min} (deg)	β_{max} (deg)	β_{avg} (deg)	σ (deg)
60	400	40.3	60.0	52.9	9.8
	600	40.7	51.4	46.5	5.3
	800	39.9	58.8	52.9	9.4
	1000	43.6	54.4	51.1	5.4
	1200	43.5	57.9	52.0	7.2
0	400	28.8	56.4	41.1	13.8
	1000	39.2	58.0	49.4	9.4
	1200	23.1	57.0	38.4	16.9

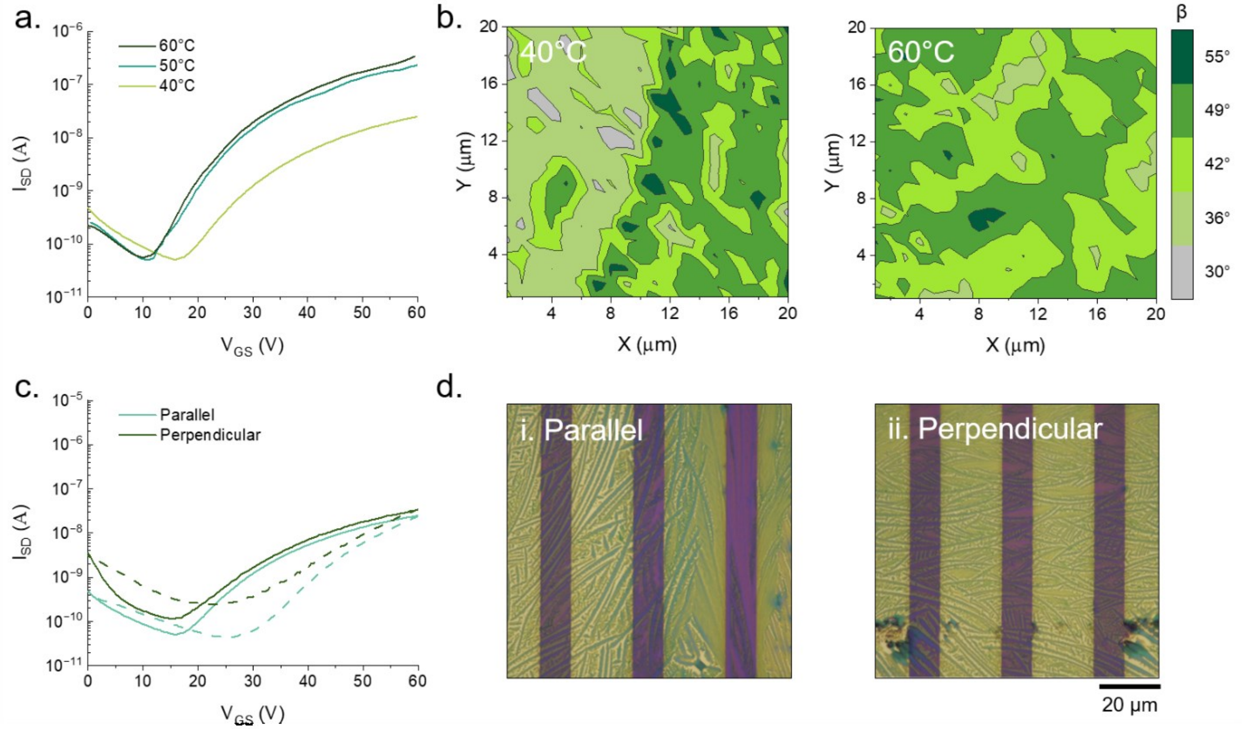

Figure S6.7. (a) Transfer curves and (b) maps (20 µm x 20 µm) of the molecular angle between $(3PS)_2$-SiPc and substrate estimated from polarized Raman spectra, and (c) transfer curves and (d) bright field real-colour microscopy images of $(3PS)_2$-SiPc OFETs fabricated at a print speed of 1000 µm s^{-1} using a solution composition of 40% toluene and 60% DCB, and (a,b) substrate temperatures of 40°C, 50°C and 60°C, and (c,d) a print direction along (parallel) or across (perpendicular) the source-drain electrodes.

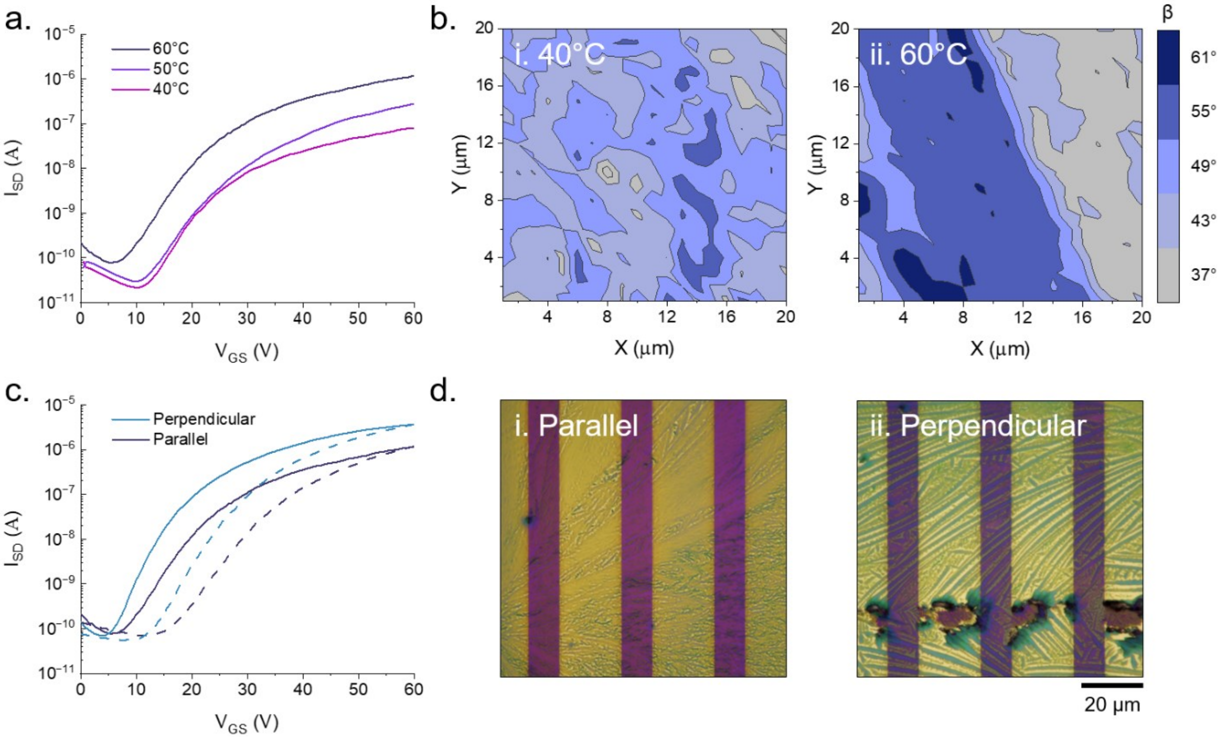

Figure S6.8. (a) Transfer curves and (b) maps (20 μm x 20 μm) of the molecular angle between (3BS)$_2$-SiPc and substrate estimated from polarized Raman spectra, and (c) transfer curves and (d) bright field real-colour microscopy images of (3BS)$_2$-SiPc OFETs fabricated at a print speed of 1000 μm s^{-1} using a solution composition of 40% toluene and 60% DCB, and (a,b) substrate temperatures of 40°C, 50°C and 60°C, and (c,d) a print direction along (parallel) or across (perpendicular) the source-drain electrodes.

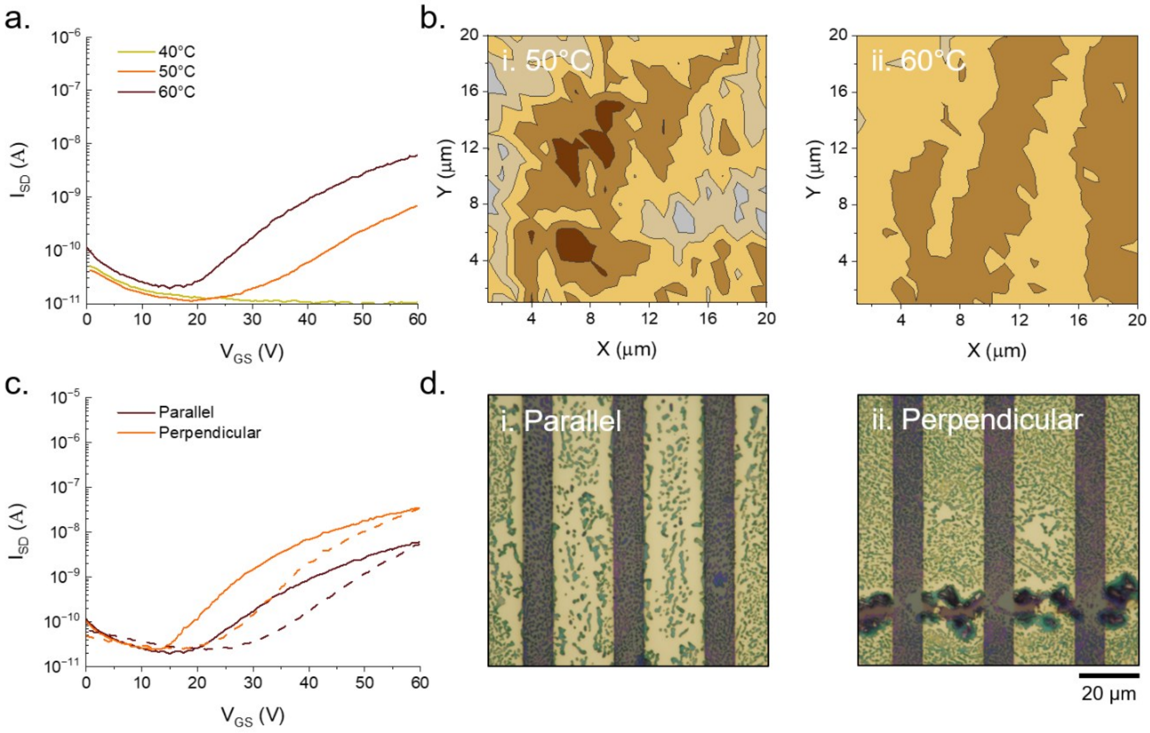

Figure S6.9. (a) Transfer curves and (b) maps (20 µm x 20 µm) of the molecular angle between (3HS)$_2$-SiPc and substrate estimated from polarized Raman spectra, and (c) transfer curves and (d) bright field real-colour microscopy images of (3HS)$_2$-SiPc OFETs fabricated at a print speed of 1000 µm s^{-1} using a solution composition of 40% toluene and 60% DCB, and (a,b) substrate temperatures of 40°C, 50°C and 60°C, and (c,d) a print direction along (parallel) or across (perpendicular) the source-drain electrodes.

Table S6.3. Minimum, maximum and average molecular angle to the substrate of $(3PS)_2$-SiPc and $(3BS)_2$-SiPc films fabricated at a print speed of 1000 µm s^{-1} using a solution composition of 40% toluene and 60% DCB, and substrate temperatures of 40°C, 50°C and 60°C. Values estimated from polarized Raman surface maps. Standard deviation (σ) calculated from the entire data set.

Material	Temp. (°C)	β_{min} (deg)	β_{max} (deg)	β_{avg} (deg)	σ (deg)
$(3PS)_2$-SiPc	40	37.4	63.1	49.5	12.8
	50	33.0	48.5	39.6	7.7
	60	37.2	56.6	48.0	9.7
$(3BS)_2$-SiPc	40	32.2	59.6	49.0	13.7
	50	36.0	63.8	51.4	13.9
	60	36.5	67.1	51.4	15.3
$(3HS)_2$-SiPc	40	-	-	-	-
	50	27.3	66.1	47.3	19.4
	60	38.1	57.2	50.0	9.6

Table S6.4. Summary of $(3PS)_2$-SiPc, $(3BS)_2$-SiPc, and $(3HS)_2$-SiPc transistor characteristics fabricated at a print speed of 1000 µm s^{-1} using a solution composition of 40% toluene and 60% DCB, and substrate temperatures of 40°C, 50°C and 60°C. Data taken from two OFETs per condition.

Material	Temp. (°C)	μ_e ($cm^2 V^{-1} s^{-1}$)	V_T (V)	$I_{on/off}$
$(3PS)_2$-SiPc	40	3.3×10^{-5}	20.1	10^2
	50	7.3×10^{-4}	18.1	10^4
	60	1.5×10^{-3}	21.1	10^4
$(3BS)_2$-SiPc	40	4.0×10^{-4}	18.2	10^4
	50	2.0×10^{-4}	11.7	10^3
	60	5.4×10^{-4}	15.3	10^3
$(3HS)_2$-SiPc	40	-	-	-
	50	2.7×10^{-6}	25.6	10
	60	6.3×10^{-6}	25.4	10^2

Table S6.5. Summary of $(3PS)_2$-SiPc, $(3BS)_2$-SiPc, and $(3HS)_2$-SiPc transistor characteristics fabricated at a print speed of 1000 µm s^{-1} using a solution composition of 40% toluene and 60% DCB, and a print direction along (parallel) or across (perpendicular) the source-drain electrodes. Data taken from two OTFTs per condition.

Material	**Direction**	**μ_e (cm^2 V^{-1} s^{-1})**	**V_T (V)**	**$I_{on/off}$**
$(3PS)_2$-SiPc	Along	3.3×10^{-5}	20.1	10^2
	Across	3.2×10^{-4}	22.0	10^2
$(3BS)_2$-SiPc	Along	5.4×10^{-4}	15.3	10^3
	Across	8.7×10^{-4}	9.8	10^4
$(3HS)_2$-SiPc	Along	6.3×10^{-6}	25.4	10^2
	Across	5.6×10^{-5}	22.9	10^3

Table S6.6. Summary of $(3PS)_2$-SiPc transistor characteristics with data taken from two OFETs per condition.

Toluene %	**Print Speed (µm s^{-1})**	**μ_e (cm^2 V^{-1} s^{-1})**	**V_T (V)**	**$I_{on/off}$**
0	600	1.26×10^{-6}	20.1	10^1
	1000	1.38×10^{-4}	20.3	10^2
	1200	9.16×10^{-5}	18.6	10^5
40	600	1.33×10^{-5}	21.7	10^2
	1000	3.27×10^{-5}	20.1	10^2
	1200	2.27×10^{-4}	21.6	10^3
60	600	1.25×10^{-5}	22.2	10^2
	1000	1.07×10^{-5}	22.0	10^2
	1200	6.50×10^{-5}	19.3	10^2

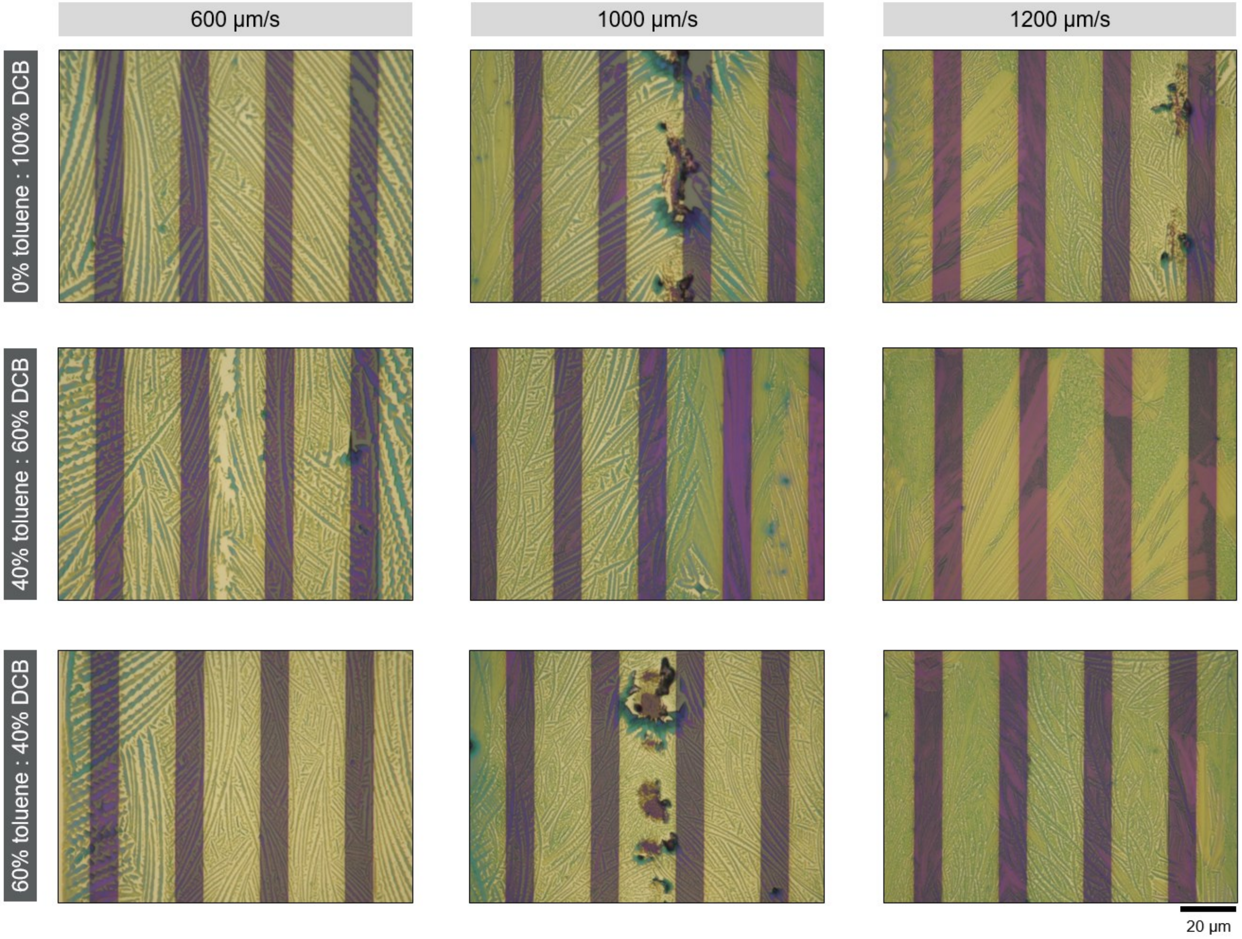

Figure S6.10. Bright field real-colour microscopy images of $(3PS)_2$-SiPc thin-films fabricated at indicated print speeds and solution compositions.

Table S6.7. Summary of $(3HS)_2$-SiPc transistor characteristics with data taken from two OFETs per condition.

Toluene %	Print Speed (μm s^{-1})	μ_e (cm^2 V^{-1} s^{-1})	V_T (V)	$I_{on/off}$
0	600	2.90×10^{-7}	7.00	10
	1000	2.07×10^{-6}	22.8	10^1
	1200	3.50×10^{-5}	25.6	10^2
40	600	1.10×10^{-5}	24.1	10^2
	1000	6.30×10^{-6}	25.4	10^2
	1200	1.74×10^{-5}	21.0	10^3
60	600	2.78×10^{-5}	23.7	10^3
	1000	9.96×10^{-6}	25.5	10^2
	1200	3.60×10^{-6}	22.0	10^2

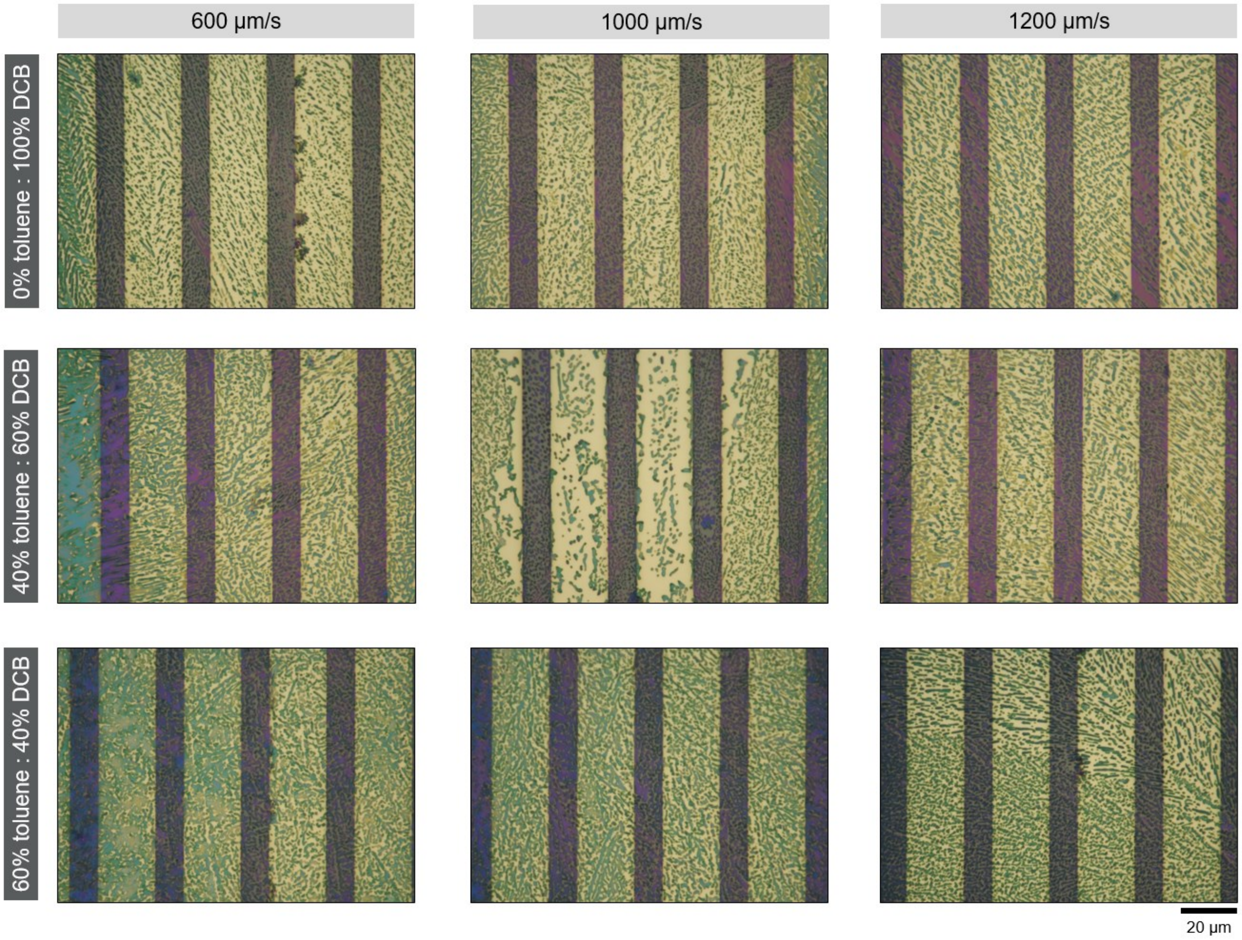

Figure S6.11. Bright field real-colour microscopy images of $(3HS)_2$-SiPc thin-films fabricated at indicated print speeds and solution compositions.

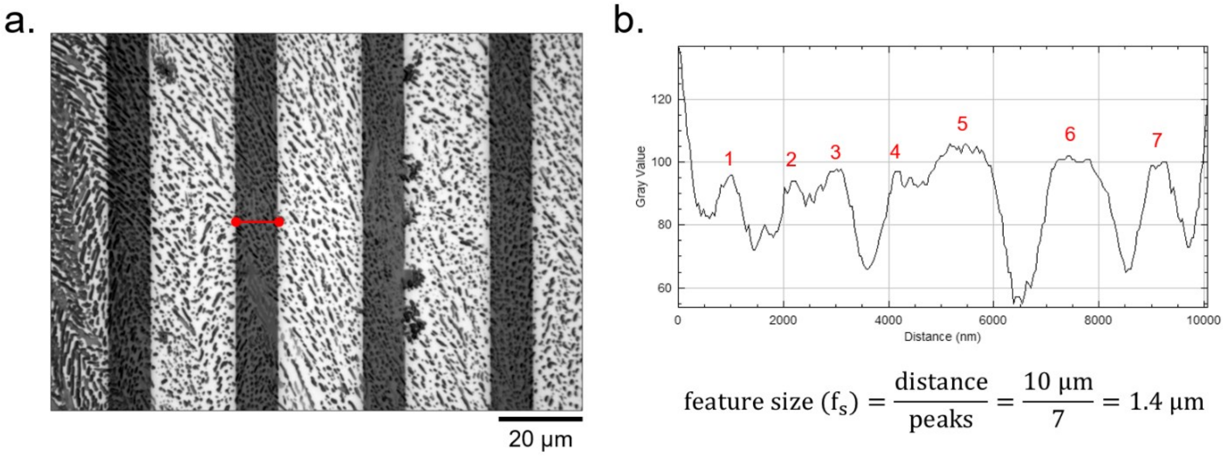

$$\text{feature size } (f_s) = \frac{\text{distance}}{\text{peaks}} = \frac{10\ \mu m}{7} = 1.4\ \mu m$$

Figure S6.12. (a) 8-bit grey scale microscope image processed using ImageJ for feature analysis with red line indicating a 10 μm line cut across the source-drain channel. (b) Example line cut profile and equation used to calculate feature size (f_{size}).

References

1 Mizukami, M. et al. Flexible Organic Light-Emitting Diode Displays Driven by Inkjet-Printed High-Mobility Organic Thin-Film Transistors. IEEE Electron Device Lett. 39, 39–42 (2018).

2 Nakajima, Y. et al. Improvement in image quality of a 5.8-in. OTFT-driven flexible AMOLED display. J. Soc. Inf. Disp. 19, 94–99 (2011).

3 Zhu, H. et al. Printable Semiconductors for Backplane TFTs of Flexible OLED Displays. Adv. Funct. Mater. 30, (2020).

4 Ryu, G. S., Kim, J. S., Jeong, S. H. & Song, C. K. A printed OTFT-backplane for AMOLED display. Org. Electron. 14, 1218–1224 (2013).

5 Lamport, Z. A. et al. Organic Thin Film Transistors in Mechanical Sensors. Adv. Funct. Mater. 30, (2020).

6 King, B. & Lessard, B. H. Review of recent advances and sensing mechanisms in solid-state organic thin-film transistor (OTFT) sensors. J. Mater. Chem. C 12, 5654–5683 (2024).

7 Takeda, Y. et al. Fabrication of Ultra-Thin Printed Organic TFT CMOS Logic Circuits Optimized for Low-Voltage Wearable Sensor Applications. Sci. Rep. 6, 25714 (2016).

8 Comeau, Z. J. et al. Surface engineering of zinc phthalocyanine organic thin-film transistors results in part-per-billion sensitivity towards cannabinoid vapor. Commun. Chem. 5, 178 (2022).

9 Burns, S. & Sirringhaus, H. TRANSISTOR-CONTROLLED DISPLAY DEVICES. 14 (2012).

10 Burns, S. E. et al. A scalable manufacturing process for flexible active-matrix e-paper displays. J. Soc. Inf. Disp. 13, 583 (2005).

11 Friederich, P. et al. Toward Design of Novel Materials for Organic Electronics. Adv. Mater. 31, (2019).

12 Kunkel, C., Schober, C., Oberhofer, H. & Reuter, K. Knowledge discovery through chemical space networks: the case of organic electronics. J. Mol. Model. 25, 87 (2019).

13 Omar, Ö. H., del Cueto, M., Nematiaram, T. & Troisi, A. High-throughput virtual screening for organic electronics: a comparative study of alternative strategies. J. Mater. Chem. C 9, 13557–13583 (2021).

14 Saeki, A. & Kranthiraja, K. A high throughput molecular screening for organic electronics via machine learning: present status and perspective. Jpn. J. Appl. Phys. 59, SD0801 (2020).

15 Yang, C.-H. et al. Multi-fidelity machine learning models for structure–property mapping of organic electronics. Comput. Mater. Sci. 213, 111599 (2022).

16 MacLeod, B. P. et al. Self-driving laboratory for accelerated discovery of thin-film materials. Sci. Adv. 6, (2020).

17 Wagner, J. et al. The evolution of Materials Acceleration Platforms: toward the laboratory of the future with AMANDA. J. Mater. Sci. 56, 16422–16446 (2021).

18 Flores-Leonar, M. M. et al. Materials Acceleration Platforms: On the way to autonomous experimentation. Curr. Opin. Green Sustain. Chem. 25, 100370 (2020).

19 Zhang, J., Hauch, J. A. & Brabec, C. J. Toward Self-Driven Autonomous Material and Device Acceleration Platforms (AMADAP) for Emerging

Photovoltaics Technologies. Acc. Chem. Res. 57, 1434–1445 (2024).

20 Wang, T. et al. Sustainable materials acceleration platform reveals stable and efficient wide-bandgap metal halide perovskite alloys. Matter 6, 2963–2986 (2023).

21 Rodríguez-Martínez, X., Pascual-San-José, E. & Campoy-Quiles, M. Accelerating organic solar cell material's discovery: high-throughput screening and big data. Energy Environ. Sci. 14, 3301–3322 (2021).

22 Fang, X. et al. Patterning Liquid Crystalline Organic Semiconductors via Inkjet Printing for High-Performance Transistor Arrays and Circuits. Adv. Funct. Mater. 31, (2021).

23 Liu, C. et al. Guided Formation of Large Crystals of Organic and Perovskite Semiconductors by an Ultrasonicated Dispenser and Their Application as the Active Matrix of Photodetectors. ACS Appl. Mater. Interfaces 10, 39921–39932 (2018).

24 Cai, L., Zhang, S., Miao, J., Yu, Z. & Wang, C. Fully Printed Stretchable Thin-Film Transistors and Integrated Logic Circuits. ACS Nano 10, 11459–11468 (2016).

25 de la Torre, G., Claessens, C. G. & Torres, T. Phthalocyanines: old dyes, new materials. Putting color in nanotechnology. Chem. Commun. 2000–2015 (2007) doi:10.1039/B614234F.

26 Gregory, P. Industrial applications of phthalocyanines. J. Porphyr. Phthalocyanines 4, 432–437 (2000).

27 Claessens, C. G., Hahn, U. & Torres, T. Phthalocyanines: From outstanding electronic properties to emerging applications. Chem. Rec. 8, 75–97 (2008).

28 Lessard, B. H. The Rise of Silicon Phthalocyanine: From Organic Photovoltaics to Organic Thin Film Transistors. ACS Appl. Mater. Interfaces 13, 31321–31330 (2021).

29 Cranston, R. R. et al. High Performance Solution Processed n-Type OTFTs through Surface Engineered F–F Interactions Using Asymmetric Silicon Phthalocyanines. Adv. Electron. Mater. 8, (2022).

30 Klauk, H. Organic thin-film transistors. Chem. Soc. Rev. 39, 2643 (2010).

31 Cranston, R. R. et al. Highlighting the processing versatility of a silicon phthalocyanine derivative for organic thin-film transistors. J. Mater. Chem. C 10, 485–495 (2022).

32 Cranston, R. R. et al. Polarized Raman Microscopy to Image Microstructure Changes in Silicon Phthalocyanine Thin-Films. Small Sci. (2024) doi:10.1002/smsc.202300350.

33 Cranston, R. R. et al. Thin-Film Engineering of Solution-Processable n-Type Silicon Phthalocyanines for Organic Thin-Film Transistors. ACS Appl. Mater. Interfaces 13, 1008–1020 (2021).

34 Galindo, S., Tamayo, A., Leonardi, F. & Mas-Torrent, M. Control of Polymorphism and Morphology in Solution Sheared Organic Field-Effect Transistors. Adv. Funct. Mater. 27, (2017).

35 Diao, Y., Shaw, L., Bao, Z. & Mannsfeld, S. C. B. Morphology control strategies for solution-processed organic semiconductor thin films. Energy Environ. Sci. 7, 2145–2159 (2014).

36 Richter, L. J., DeLongchamp, D. M. & Amassian, A. Morphology Development in Solution-Processed Functional Organic

Blend Films: An In Situ Viewpoint. Chem. Rev. 117, 6332–6366 (2017).

37 Virkar, A. A., Mannsfeld, S., Bao, Z. & Stingelin, N. Organic Semiconductor Growth and Morphology Considerations for Organic Thin-Film Transistors. Adv. Mater. 22, 3857–3875 (2010).

38 Wang, Y. et al. Grain boundary engineering of organic semiconductor films in organic transistors. Aggregate 4, (2023).

39 Rivnay, J., Mannsfeld, S. C. B., Miller, C. E., Salleo, A. & Toney, M. F. Quantitative Determination of Organic Semiconductor Microstructure from the Molecular to Device Scale. Chem. Rev. 112, 5488–5519 (2012).

40 Yang, S. et al. Employing Pneumatic Nozzle Printing for Controlling the Crystal Growth of Small Molecule Organic Semiconductor for Field-Effect Transistors. Adv. Electron. Mater. 4, (2018).

41 Guthrie, S. M., Gao, Y., Stone, K. H., Xu, B. & Giri, G. Probing Molecular Assembly of Small Organic Molecules during Meniscus-Guided Coating Using Experimental and Molecular Dynamics Approaches. J. Phys. Chem. C 125, 6269–6277 (2021).

42 Ren, C., Cao, L. & Wu, T. Meniscus-Guided Deposition of Organic Semiconductor Thin Films: Materials, Mechanism, and Application in Organic Field-Effect Transistors. Small 19, (2023).

43 Lu, Z. et al. Meniscus-guided coating of organic crystalline thin films for high-performance organic field-effect transistors. J. Mater. Chem. C 8, 9133–9146 (2020).

44 Riera-Galindo, S., Tamayo, A. & Mas-Torrent, M. Role of Polymorphism and Thin-Film Morphology in Organic Semiconductors Processed by Solution Shearing. ACS Omega 3, 2329–2339 (2018).

45 Janneck, R., Vercesi, F., Heremans, P., Genoe, J. & Rolin, C. Predictive Model for the Meniscus-Guided Coating of High-Quality Organic Single-Crystalline Thin Films. Adv. Mater. 28, 8007–8013 (2016).

46 Shaw, L. et al. Microstructural Evolution of the Thin Films of a Donor–Acceptor Semiconducting Polymer Deposited by Meniscus-Guided Coating. Macromolecules 51, 4325–4340 (2018).

47 Janneck, R., Karagiannis, D., Heremans, P., Genoe, J. & Rolin, C. Influence of Solute Concentration on Meniscus-Guided Coating of Highly Crystalline Organic Thin Films. Adv. Mater. Interfaces 6, 1900614 (2019).

48 Wang, H., Zhu, F., Yang, J., Geng, Y. & Yan, D. Weak Epitaxy Growth Affording High-Mobility Thin Films of Disk-Like Organic Semiconductors. Adv. Mater. 19, 2168–2171 (2007).

49 Zhang, C. et al. Insight into thin-film stacking modes of π-expanded quinoidal molecules on charge transport property via side-chain engineering. J. Mater. Chem. C 5, 1935–1943 (2017).

50 He, Z., Chen, J., Keum, J. K., Szulczewski, G. & Li, D. Improving performance of TIPS pentacene-based organic thin film transistors with small-molecule additives. Org. Electron. 15, 150–155 (2014).

51 Ward, J. W. et al. Rational Design of Organic Semiconductors for Texture Control and Self-Patterning on Halogenated Surfaces. Adv. Funct. Mater. 24, 5052–5058 (2014).

52 Li, P. & Lu, Z.-H. Interface Engineering

in Organic Electronics: Energy-Level Alignment and Charge Transport. Small Sci. 1, (2021).

53 Dindault, C. et al. Correlating Morphology, Molecular Orientation, and Transistor Performance of Bis(pentafluorophenoxy)silicon Phthalocyanine Using Scanning Transmission X-ray Microscopy. Chem. Mater. 34, 4496–4504 (2022).

54 Lim, J. A. et al. Self-Organization of Ink-jet-Printed Triisopropylsilylethynyl Pentacene via Evaporation-Induced Flows in a Drying Droplet. Adv. Funct. Mater. 18, 229–234 (2008).

55 Ryu, G. S., Lee, M. W., Jeong, S. H. & Song, C. K. Thermally Dried Ink-Jet Process for 6,13-Bis(triisopropylsilylethynyl)-Pentacene for High Mobility and High Uniformity on a Large Area Substrate. Jpn. J. Appl. Phys. 51, 051601 (2012).

56 Kang, B. J. & Oh, J. H. Influence of substrate temperature and overlap condition on the evaporation behavior of inkjet-printed semiconductor layers in organic thin film transistors. Thin Solid Films 598, 219–225 (2016).

57 Kim, D.-K. et al. Contact line curvature-induced molecular misorientation of a surface energy patterned organic semiconductor in meniscus-guided coating. Appl. Surf. Sci. 504, 144362 (2020).

58 Kim, K., Nam, K., Li, X., Lee, D. Y. & Kim, S. H. Programmed Design of Highly Crystalline Organic Semiconductor Patterns with Uniaxial Alignment via Blade Coating for High-Performance Organic Field-Effect Transistors. ACS Appl. Mater. Interfaces 11, 42403–42411 (2019).

59 Wu, D. et al. Blade Coating Aligned, High-Performance, Semiconducting-Polymer Transistors. Chem. Mater. 30, 1924–1936 (2018).

60 Vebber, M. C., Grant, T. M., Brusso, J. L. & Lessard, B. H. Bis(trialkylsilyl oxide) Silicon Phthalocyanines: Understanding the Role of Solubility in Device Performance as Ternary Additives in Organic Photovoltaics. Langmuir 36, 2612–2621 (2020).

61 Grant, T. M., Dindault, C., Rice, N. A., Swaraj, S. & Lessard, B. H. Synthetically facile organic solar cells with >4% efficiency using P3HT and a silicon phthalocyanine non-fullerene acceptor. Mater. Adv. 2, 2594–2599 (2021).

62 Zaumseil, J. & Sirringhaus, H. Electron and Ambipolar Transport in Organic Field-Effect Transistors. Chem. Rev. 107, 1296–1323 (2007).

63 Jiang, Z. GIXSGUI : a MATLAB toolbox for grazing-incidence X-ray scattering data visualization and reduction, and indexing of buried three-dimensional periodic nanostructured films. J. Appl. Crystallogr. 48, 917–926 (2015).

Chapter 7. Conclusions and Future Work

Summary of Main Findings

SiPc derivatives are well known for their brilliant colour and ease of synthesis making them useful in dyes and pigments. However, the stability, molecular tunability, and delocalized π electron system of SiPcs lends themselves well to more advanced applications in opto-electronic devices. In this thesis, axial substitution of solubilizing alkyl groups proves to be an effective strategy to control the crystal packing and charge transport properties of SiPcs in addition to making them compatible with the high-throughout, large-scale, and low-cost solution manufacturing methods which are required for commercialization. As the active semiconducting layer in OTFTs, axially substituted SiPcs demonstrate n-type charge transport whose performance can be optimized by exploiting the effects of molecular design and fabrication conditions. Studying how SiPc structure and solution fabrication parameters influence the solid-state properties of films and the electronic performance of OTFTs helps further our understanding of the complex processing-property-performance relationships in organic electronic devices. Fully understanding these relationships is paramount for the further development, utility, and commercialization of this area of research.

In **Chapter 2**, eight axially substituted SiPc derivatives were used as the semiconductor in OTFTs fabricated by spin coating, with six of the materials reported for the first time. Through AFM and the electrical characterization of OTFTs, a relationship between molecular structure and device performance was established with the length and symmetry of alkyl chains exhibiting a clear effect on film morphology and device performance. Symmetric trialkyl linear substituents with an optimum chain length of six carbons yielded the best performance in OTFTs with long asymmetric or highly branched groups hindering molecular packing, film formation, and charge transport. Additionally, post deposition thermal annealing was demonstrated as a method to control both film crystallinity and the orientation of SiPc molecules relative to the substrate to achieve higher μ_e devices with reduced V_T. Spin time was also shown to modify thin-film crystallinity without affecting the orientation of molecules in the film, making it a complimentary process to thermal annealing.

Using the structure property relationship established in **Chapter 2**, **Chapter 3** and **Chapter 4** highlighted the use of a symmetric short chain trialkyl linear SiPc derivative, $(3PS)_2$-

SiPc, in OTFTs. $(3PS)_2$-SiPc possess unique processing duality as it can be sublimed without melting, and is soluble enough to be used with solution deposition techniques. The differences between $(3PS)_2$-SiPc OTFTs fabricated by sublimation and solution processing were assessed through electrical characterization, topographical imaging, and the determination of thin-film microstructure. Films fabricated by sublimation yielded highly uniform, well-oriented thin-films while solution processing resulted in inhomogeneous films with large variations in morphology and molecular orientation. Although both deposition methods resulted in different film microstructural properties, OTFTs exhibited similar performance metrics. The influence of post deposition thermal annealing on film properties and polymorph formation was further studied, and was found to have a distinct effect on films fabricated by sublimation different from that of solution processed films. At high temperatures, sublimed films underwent a polymorphic change in packing structure while solution fabricated films did not, suggesting that sublimed films are more readily able to undergo transformations to structure and morphology with post deposition processing, while the microstructure of solution fabricated films is established at the time of deposition.

Chapter 5 reported the novel synthesis and characterization of two asymmetric axially substituted fluorinated SiPc derivatives, F-3BS-SiPc and F-3HS-SiPc, and incorporated these materials as the active layer in OTFTs. The effect of surface energy and fluorination on thin-film formation and OTFT performance was investigated through dielectric modification by silane treatment where a direct relationship between surface energy and OTFT performance was observed. Decreasing the surface energy of the dielectric layer, such that it more closely matched the fluorinated SiPc derivatives provided more favourable conditions for the formation of large area crystalline domains that promoted charge transport and improved device performance. Using fluorine-fluorine interactions between the dielectric surface and semiconductor, along with reducing the rate of crystallization during thin-film deposition, achieved the highest μ_e observed by solution processed n-type SiPc based OTFTs. The results of this study demonstrated how high performing, solution processed, n-type OTFTs can be achieved through engineering the dielectric-semiconductor interface without auxiliary post deposition processes.

Finally, **Chapter 6** on boarded three SiPc derivatives with different alkyl chain length axial groups, $(3PS)_2$-, $(3BS)_2$-, and $(3HS)_2$-SiPc, to a new thin-film deposition platform using ultrasonic meniscus guided printing. Previous chapters used spin coating for the solution deposition of SiPc materials, however this method is typically used only for small area devices at the lab-scale, and is not compatible with high-throughput solution manufacturing. Ultrasonic printing is a meniscus guided method that allows for the quick and easy examination of fabrication parameters with reduced material consumption that is analogous to large scale manufacturing processes. Using ultrasonic printing for SiPc thin-film fabrication highlighted the importance of deposition method and parameters on film formation and device performance. Solvent evaporation rate and print speed proved to be critically important in achieving the quality film morphology and microstructure needed for efficient charge transport and high μ_e OTFTs. For the three SiPc derivatives, solvent evaporation rate and print speed had a varying effect on film formation and transistor characteristics, with each material displaying a unique relationship between processing parameters, film properties, and device performance. The results of this study demonstrate the use of a high throughput printing technique and how it can be used for large data set experimentation that is typically unattainable at the academic research level.

Recommendations for Future Work

The promising results presented herein, along with the highly tunable nature of SiPc thin films through both molecular design and fabrication, demonstrate that SiPcs warrant further study of as organic semiconductors for various applications. I believe the next steps for research involving the use of SiPcs is to transition from SiO_2 as a substrate and dielectric material while improving the air and environmental stability of SiPc thin films. Two of the primary advantages of organic semiconductors is the ability to use low cost flexible materials as substrates, and their compatibility with low temperature ambient manufacturing processes. Prefabricated SiO_2 wafers that combine a Si gate with a thermally grown SiO_2 dielectric layer are commonly used for the research of new materials for organic electronic devices as they offer a highly uniform substrate surface alongside excellent gate and dielectric properties, ensuring consistency throughout experimentation. However, to fully capitalize on the advantages of organic semiconductors, a logical next step would be to use organic dielectric materials, such as conjugated polymers, and plastic or fiber-based substrates. This removes the cost and high temperature fabrication steps associated with SiO_2 substrates and enables flexible device designs. Flexible organic devices are complicated by the need for total material flexibility, limiting the possible materials for fabrication as each component must fulfill specific properties for not only optimum charge transfer but also to achieve high flexibility and mechanical stability. In addition to using flexible materials for the substrate, gate and dielectric layers, the flexibility of the organic semiconducting SiPc layer must also be improved if total device flexibility is to be achieved.

An additional concern which could be examined is further improvements to the air instability of the solution processable SiPc derivatives presented in this thesis. SiPcs are n-type charge transport materials with LUMO energy levels around -3.5 eV. The injection of electrons to the SiPc semiconducting film is similar to that of a reduction process in an electrochemical reaction, where the injected electron residing in the LUMO level is at a high-energy state, and is thus prone to react with oxygen and water causing the trapping or annihilation of electrons (**Figure 7.1**). Therefore, electron transport is typically severely limited when device operation occurs in ambient air. It has been theoretically proven, and empirically demonstrated, that a LUMO energy level of approximately -4.0 eV or lower is required to achieve air stable electron transport.[1–4] Therefore, one method of improving air stability is to design SiPc molecules with more electron withdrawing groups by either peripheral fluorination or the incorporation fluoroalkyl chains to the axial position in order to lower the LUMO energy level. Peripheral fluorination has been demonstrated as a method to achieve air stable SiPc based OTFTs fabricated by thermal evaporation,[5] but not yet successfully employed for solution processable SiPc derivatives. Additionally, the air stability of SiPc devices could be improved through device engineering by employing the use of electron-injecting interlayers such as low work function metal oxides,[6–8] or encapsulation layers[9–11].

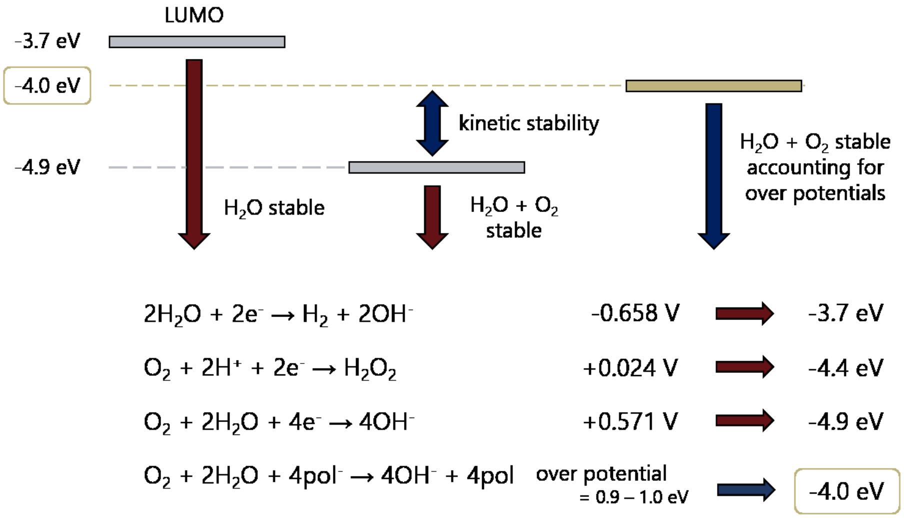

Figure 7.1. Schematic diagram of the LUMO level stability requirements for an n-type material and the key reduction equations that cause inherent n-type instability. Adapted from reference 1. Copyright © 2021 the Authors under the Creative Commons Attribution 3.0 Licence.

References

1 Griggs, S., Marks, A., Bristow, H. & McCulloch, I. n-Type organic semiconducting polymers: stability limitations, design considerations and applications. J. Mater. Chem. C 9, 8099–8128 (2021).

2 Quinn, J. T. E., Zhu, J., Li, X., Wang, J. & Li, Y. Recent progress in the development of n-type organic semiconductors for organic field effect transistors. J. Mater. Chem. C 5, 8654–8681 (2017).

3 Zaumseil, J. & Sirringhaus, H. Electron and Ambipolar Transport in Organic Field-Effect Transistors. Chem. Rev. 107, 1296–1323 (2007).

4 Yan, H. et al. A high-mobility electron-transporting polymer for printed transistors. Nature 457, 679–686 (2009).

5 King, B. et al. Peripherally Fluorinated Silicon Phthalocyanines: How Many Fluorine Groups Are Necessary for Air-Stable Electron Transport in Organic Thin-Film Transistors? Chem. Mater. 35, 8517–8528 (2023).

6 Greiner, M. T. & Lu, Z.-H. Thin-film metal oxides in organic semiconductor devices: their electronic structures, work functions and interfaces. NPG Asia Mater. 5, e55–e55 (2013).

7 Peng, J. et al. Efficient Indium-Doped TiO x Electron Transport Layers for High-Performance Perovskite Solar Cells and Perovskite-Silicon Tandems. Adv. Energy Mater. 7, (2017).

8 Cho, S., Seo, J. H., Lee, K. & Heeger, A. J. Enhanced Performance of Fullerene n-Channel Field-Effect Transistors with Titanium Sub-Oxide Injection Layer. Adv. Funct. Mater. 19, 1459–1464 (2009).

9 Iqbal, H. F. et al. Suppressing bias stress degradation in high performance solution processed organic transistors operating in air. Nat. Commun. 12, 2352 (2021).

10 Sang, M., Kim, K., Shin, J. & Yu, K. J. Ultra-Thin Flexible Encapsulating Materials for Soft Bio-Integrated Electronics. Adv. Sci. 9, (2022).

11 Lu, Q. et al. A Review on Encapsulation Technology from Organic Light Emitting Diodes to Organic and Perovskite Solar Cells. Adv. Funct. Mater. 31, (2021).

Chapter 8. Additional Contributions

Thin-Film Characterization

I contributed to the following publications by performing a combination of AFM imaging, Raman microscopy, and synchrotron experiments including GIWAXS, STXM and NEXAFS on organic thin-films to characterize their microstructural properties for myriad of research objectives. Additionally, I assisted in preparing these works for publication by editing and proofreading all manuscripts. **Work 1** explored the use of novel multi-phenyl molecules as templating layers for the formation of highly ordered SiPc thin films by physical vapour deposition. Multi-phenyl molecules can be used for the weak epitaxial growth of organic films allowing for the precise control of microstructure properties. This work focused on the importance of template layer selection and the optimization of deposition conditions on film properties and OTFTs performance. For this work I assisted in GIWAXS and Raman microscopy experiments to characterize SiPc film formation on the different template layers.

Works 2, 5 and **6** investigated the use of MPc based OTFTs as sensors for the detection of primary cannabinoids Δ^9-tetrahydrocannabinol (THC) and cannabidiol (CBD) in both liquid and gas phases. Cannabis producers, consumers, and regulators require point-of-use sensors that can provide rapid speciation and detection while maintaining low manufacturing costs and ease of use. These works focused on engineering MPc thin films by altering deposition conditions, and the molecular engineering of MPcs to determine the relationship between physical film characteristics and analyte interactions to ultimately improve device sensitivity and OTFT sensing response. For these works I assisted in GIWAXS experiments and conducted AFM imaging on thin-films pre and post exposure to THC and CBD to determine changes in film microstructure and morphology.

Work 4 examined the use of a strong magnetic field as a non-destructive post deposition process for the improvement of MPc thin-film microstructures and OTFT performance. Common post deposition processes used to alter film properties, such as thermal and solvent vapour annealing, can be destructive or incompatible with certain semiconductor and substrate materials. MPc films exposed to a strong magnetic field exhibited increased concentrations of oxygen-induced radicals within the film, lending to a paramagnetic character and altered thin-film microstructure that favourably improved charge transport characteristics in OTFTs. For this work

I performed GIWAXS and AFM experiments on films to elucidate the effect of a strong magnetic field on the physical properties of MPc thin-films.

Different from previous works, **works 3, 7** and **8** focused on the self-assembly and nanostructure formation of poly(3-hexylthiophene) polymer thin films. Poly(3-hexylthiophene) based polymers are some of the most prevalent and promising conjugated polymers for use in organic electronic devices. These works looked at the influence of polymer molecular weight and film deposition conditions on the self-assembly behaviour of poly(3-hexylthiophene) in films. For **work 3** I assisted in the experimental design of the project, OTFT fabrication, and Raman microscopy characterization, along with conducting GIWAXS, STXM and NEXAFS experiments. For **works 7** and **8** I performed GIWAXS experiments on films with analysis of results.

1. Ewenike, R. B. *et al.* Engineering the Template Layer for Silicon Phthalocyanine Based Organic Thin Film Transistors. *Adv. Funt. Mater.* (2024) DOI:10.1002/adfm.202408779
2. Lamontagne, H. R. *et al.* Axial Phenoxylation of Aluminum Phthalocyanines for Improved Cannabinoid Sensitivity in OTFT Sensors. *Adv. Sci.* (2024) DOI:10.1002/advs.202305515
3. Dickson, L. E. *et al*. Blade Coating Poly(3-hexylthiophene): The Importance of Molecular Weight on Thin-Film Microstructures. *ACS Appl. Mater. Interfaces.* 15, 55109–55118 (2023) DOI:10.1021/acsami.3c12335
4. Comeau, Z. J., Cranston, R. R., Lamontagne, H. R., Shuhendler, A. J. & Lessard, B. H. Strong Magnetic Field Annealing for Improved Phthalocyanine Organic Thin-Film Transistors. *Small*. 19, 2206792 (2023) DOI:10.1002/smll.202206792
5. Comeau, Z. J. *et al*. Surface Engineering of Zinc Phthalocyanine Organic Thin-Film Transistors Results in Part-Per-Billion Sensitivity Towards Cannabinoid Vapor. *Commun. Chem*. 5, 178 (2022) DOI:10.1038/s42004-022-00797-y
6. Lamontagne, H. R. *et al*. Chloro Aluminum Phthalocyanine-Based Organic Thin-Film Transistors as Cannabinoid Sensors: Engineering the Thin Film Response. *Sensors & Diagnostics.* 1, 1165–1175 (2022) DOI:10.1039/d2sd00071g
7. Li, S., Cranston, R., Lessard, B. H. & Seferos, D. S. Poly(3-hexylthiophene)- stat -poly(3-dodecylselenophenes): Conjugated Statistical Copolymers and Their Gels. *ACS Appl. Polym. Mater.* 4, 6030–6037 (2022) DOI:10.1021/acsapm.2c00841
8. Hicks, G. E. J. *et al*. Dopant-Stabilized Assembly of Poly(3-hexylthiophene). *J. Am. Chem. Soc.* (2022) DOI:10.1021/jacs.2c04984

Metal Phthalocyanine OTFTs

My contributions to the following works included the fabrication and characterization of MPc based OTFTs by both physical vapour deposition and solution processing, along with preparing the manuscripts for publication by editing and proof reading. **Work 9** used two novel ruthenium phthalocyanine (RuPc) derivatives containing axial pyridine substituents with aliphatic chains as the organic semiconductors in solution fabricated OTFTs. RuPcs are multipurpose compounds characterized by their remarkable reactivity and photoelectronic properties, however they remain relatively underexplored for use in organic electronic devices. The first RuPc derivative displayed comparable p-type device performance to other MPc OTFTs of similar design, while the second derivative was found to be non-functional likely as a result of significant differences in the thin-film formation between the two materials. For this work I fabricated and characterized all OTFTs, performed AFM and XRD measurements on thin films, and wrote a signification portion of the manuscript.

Work 10 incorporated solution processable axially substituted tin (IV) phthalocyanines (SnPcs) in OPV and OTFT devices to study their utility as ternary additives and semiconductors respectively. In OPVs, all SnPc derivatives decreased the power conversion efficiency of devices, however exhibited comparable performance in OTFTs to the previously studied SiPc analogues in **Chapter 2**. The difference in electrical performance between OTFT and OPV devices was attributed to the low photostability of SnPcs. For this work I fabricated and characterized all SnPc OTFTs, performed AFM measurements on thin films, and wrote a signification portion of the manuscript.

Works 11 and **12** investigated the use of a variety of MPcs with different metal inclusions as semiconductors in OTFTs for applications in DNA and temperature sensing. MPc thin films were fabricated by physical vapour deposition with OTFTs characterized under varying temperatures (25°C to 150°C), environmental conditions (air and vacuum, $P < 0.1$ Pa) and exposure to DNA in different hybridization states. For these works I fabricated all MPc OTFTs and performed the electrical characterization of baseline devices pre-exposure to DNA, and devices operated at elevated temperatures in different environments. Additionally, I analyzed all OTFT data and summarized the findings for publication.

9. García-Calvo, J., Cranston, R. R., López-Duarte, I., Torres, T. & Lessard, B. H. Soluble Ruthenium Phthalocyanines as Semiconductors for Organic Thin-Film Transistors. *ChemElectroChem*. 10, (2023) DOI:10.1002/celc.202300286

10. Cranston, R. R. *et al*. N-Type Solution-Processed Tin versus Silicon Phthalocyanines: A Comparison of Performance in Organic Thin-Film Transistors and in Organic Photovoltaics. *ACS Appl. Electron. Mater*. 3, 1873–1885 (2021) DOI:10.1021/acsaelm.1c00114

11. Boileau, N. T., Cranston, R., Mirka, B., Melville, O. A. & Lessard, B. H. Metal Phthalocyanine Organic Thin-Film Transistors: Changes in Electrical Performance and Stability in Response to Temperature and Environment. *RSC Adv*. 9, 21478–21485 (2019) DOI:10.1039/c9ra03648b

12. Boileau, N. T., Melville, O. A., Mirka, B., Cranston, R. & Lessard, B. H. P and N Type Copper Phthalocyanines as Effective Semiconductors in Organic Thin-Film Transistor Based DNA Biosensors at Elevated Temperatures. *RSC Adv*. 9, 2133–2142 (2019). DOI:10.1039/c8ra08829b

Copyright Permissions

Chapter 1:

Cranston, R. R. & Lessard, B. H. Metal phthalocyanines: thin-film formation, microstructure, and physical properties. RSC Adv. 11, 21716–21737 (2021). DOI: 10.1039/d1ra03853b

Copyright © 2021 The Authors. The Royal Society of Chemistry

Chapter 2:

Cranston, R. R. et al. Thin-Film Engineering of Solution-Processable n-Type Silicon Phthalocyanines for Organic Thin-Film Transistors. ACS Appl. Mater. Interfaces 13, 1008–1020 (2021). DOI:10.1021/acsami.0c17657

Copyright © 2020 American Chemical Society

Chapter 3:

Cranston, R. R. et al. Highlighting the processing versatility of a silicon phthalocyanine derivative for organic thin-film transistors. J. Mater. Chem. C 10, 485–495 (2022). DOI: 10.1039/d1tc05238a

Copyright © 2021 The Royal Society of Chemistry

Chapter 4:

Cranston, R. R. et al. High Performance Solution Processed n-Type OTFTs through Surface Engineered F–F Interactions Using Asymmetric Silicon Phthalocyanines. Adv. Electron. Mater. 8, (2022). DOI: 10.1002/aelm.202200696

Copyright © 2022 The Authors. Advanced Electronic Materials

Chapter 5:

Cranston, R. R. et al. Polarized Raman Microscopy to Image Microstructure Changes in Silicon Phthalocyanine Thin-Films. Small Sci. (2024) DOI:10.1002/smsc.202300350.

Copyright © 2024 The Authors. Small Science published by Wiley-VCH GmbH

Chapter 6:

Unpublished work